

# **Molecular imaging of mouse brain tissue using Cluster Time-of-Flight Secondary Ion Mass Spectrometry**

---

A thesis submitted to The University of Manchester for the degree of Doctor of  
Philosophy in the Faculty of Engineering and Physical Sciences

**Irma Berrueta Razo**

2015

The University of Manchester  
Faculty of Engineering and Physical Sciences  
School of Chemistry

## Contents

Contents .....	2
List of Figures.....	7
List of Tables .....	22
List of Equations .....	23
Abbreviations.....	24
Abstract .....	26
Declaration.....	27
Copyright Statement .....	27
Acknowledgements .....	28
1 Introduction .....	29
1.1 Aim of the study.....	30
2 Literature review.....	31
2.1 Secondary ion mass spectrometry (SIMS).....	31
2.1.1 SIMS basic experimental parameters.....	31
2.1.2 Damage cross section .....	32
2.2 SIMS methodologies.....	33
2.2.1 Static SIMS .....	33
2.2.2 Dynamic SIMS .....	34
2.2.3 Molecular imaging with SIMS.....	34
2.3 ToF-SIMS.....	36
2.3.1 Analysis beams used in ToF-SIMS.....	36
2.3.2 Physics of polyatomic projectiles .....	37
2.3.3 Time-of-Flight mass analysers.....	39
2.4 Data processing for ToF-SIMS.....	41
2.4.1 Multivariate analysis.....	41
2.5 ToF-SIMS imaging of biological systems .....	44
2.5.1 Complementary techniques in mass spectrometry imaging for the analysis of biological systems.....	45

2.5.2	Targeted and untargeted metabolomic studies with MSI .....	52
2.5.3	ToF-SIMS imaging of mouse brain tissue .....	57
2.5.4	Sample preparation workflow for mouse brain imaging with ToF-SIMS.....	61
2.5.5	Bio-medical applications of ToF-SIMS imaging .....	63
2.5.6	Challenges of analysis of bio-systems with ToF-SIMS.....	66
2.5.7	Water cluster primary ion beams.....	68
2.5.8	Sputtering studies .....	69
2.6	Summary.....	70
2.7	References.....	70
3	Instrumentation .....	92
3.1	Mass resolution.....	92
3.1.1	Obtainable mass resolution with different ToF-SIMS configurations .....	93
3.2	Mass accuracy.....	94
3.3	The duty cycle.....	94
3.4	The J105-3D Chemical imager .....	94
3.4.1	Operation of the J105 instrument.....	95
3.5	Analysis beams in the J105-3D Chemical Imager .....	97
3.5.1	40 keV C <sub>60</sub> ion gun.....	98
3.5.2	20 keV Gas cluster ion beam.....	101
3.6	References.....	105
4	Materials and methods.....	109
4.1	Analysis of biomolecules.....	109
4.1.1	Studied biomolecular standards .....	109
4.1.2	Preparation of spin-coated films for ToF-SIMS analysis.....	113
4.2	Sample preparation of mouse brain tissue and brain total lipid extract .....	116
4.2.1	Preparation of brain total lipid extract.....	116
4.2.2	Preparing mouse brain tissue sections for ToF-SIMS analysis.....	116
4.2.3	Lipid standards for ion suppression/enhancement studies .....	118

4.3	Methodology for correlation of multi-modal imaging techniques: ToF-SIMS imaging and fluorescence microscopy.....	119
4.3.1	Sample preparation of 3xTg-AD brain tissue.....	120
4.3.2	Thioflavin S staining protocol .....	121
4.3.3	Fluorescence microscopy imaging .....	123
4.3.4	Handling brain sections for ToF-SIMS imaging .....	123
4.3.5	Synthetic Amyloid- $\beta$ peptide (1-40).....	123
4.4	References.....	124
5	Comparative studies on biomolecule models .....	129
5.1	Molecular profiling and the steady-state region.....	129
5.2	Aim of the experiments .....	131
5.3	ToF-SIMS analysis.....	131
5.4	Comparative secondary ion yield studies with $\text{Ar}_n^+$ and $(\text{H}_2\text{O})_n^+$ clusters on standard biomolecules .....	132
5.4.1	Results and discussion .....	132
5.4.2	Ionisation mechanisms and the influence of the cluster size.....	141
5.4.3	Study of the $(\text{H}_2\text{O})_n^+$ mechanism: $\text{D}_2\text{O}$ studies on trehalose and DPPC.....	144
5.4.4	Secondary ion detection per $1 \mu\text{m}^2$ .....	148
5.5	Generation of water-doped argon clusters for analysis of biomolecular systems: comparative studies on trehalose and DPPC .....	150
5.5.1	Results and discussion .....	151
5.6	Summary.....	156
5.7	References.....	157
6	Molecular imaging of mouse brain tissue sections using Cluster ToF-SIMS.....	161
6.1	Overview of the mouse brain anatomy.....	161
6.2	Presence of cholesterol in the grey and white matter .....	164
6.3	Aim of the experiments .....	165
6.4	ToF-SIMS analysis.....	166
6.4.1	Analysis of brain total lipid extract.....	166
6.4.2	Molecular imaging of mouse brain sections.....	166



6.4.3	Matrix effect experiments.....	167
6.5	Results and discussion.....	168
6.5.1	Analysis of total lipid brain extract with 20 keV $C_{60}^+$ , $Ar_n^+$ , $(H_2O)_n^+$ and $(H_2O)Ar_n^+$ clusters.....	168
6.5.2	Cluster ToF-SIMS imaging of the brain striatum.....	171
6.5.3	Molecular imaging of the brain cerebellum with cluster ToF-SIMS.....	177
6.5.4	Cluster ToF-SIMS imaging studies on the brain cerebellum with using 20 keV $C_{60}^+$ , $Ar_{2000}^+$ , $(H_2O)Ar_{2000}^+$ and $(H_2O)_{6000}^+$ .....	182
6.5.5	Study of the ion suppression effect on Cholesterol.....	202
6.6	Summary.....	206
6.7	References.....	207
7	Application of cluster ToF-SIMS imaging to the analysis of a transgenic mouse model infected with Alzheimer's disease.....	213
7.1	Amyloid- $\beta$ plaques in Alzheimer's disease.....	213
7.2	Transgenic mouse models in Alzheimer's disease.....	215
7.3	Detection of neuritic plaques with ThioS labelling and fluorescence microscopy.....	217
7.4	Aim of the experiments.....	218
7.5	ToF-SIMS imaging conditions.....	218
7.5.1	<i>In-situ</i> localisation of Amyloid- $\beta$ plaques in brain sections from a triple transgenic mouse model infected with Alzheimer's disease.....	219
7.5.2	Fluorescence microscopy and ToF-SIMS image registration.....	221
7.5.3	Study of Amyloid- $\beta$ plaques <i>in situ</i> .....	223
7.5.4	Detection of cholesterol in areas with A $\beta$ plaques.....	230
7.6	Summary.....	234
7.7	References.....	235
8	Conclusions and future work.....	239
8.1	Comparative background studies on biomolecule models.....	240
8.2	Molecular imaging of mouse brain sections using cluster ToF-SIMS.....	241

8.2.1	Application of cluster ToF-SIMS imaging to the analysis of a clinical case: a transgenic mouse model infected with Alzheimer's disease.....	243
8.3	Future work.....	244
8.3.1	Cluster ToF-SIMS imaging of mouse brain sections.....	244
8.3.2	Analysis of AD brain tissue .....	245
8.4	References.....	246
Appendix I .....		249
Appendix II.....		250
Appendix III .....		251

Final word count 70,850

## List of Figures

Figure 1.1: Schematic of ToF-SIMS imaging of tissue. The sample is probed with a primary ion beam, desorbing secondary ion particles from the surface. Secondary ions are extracted into a time-of-flight tube where the ions fly according to their masses before reaching the detector [11].....	29
Figure 2.1: Schematic of the desorption-ionisation process in SIMS. A primary ion beam is scanned across the sample's surface. During this process, the analysis beam breaks bonds and causes desorption of multiple species. The majority of species emitted are neutral atoms (not included in the diagram) or molecules and only a small number of them are charged. The size of the primary ion beam is much larger in reality [16]. .....	31
Figure 2.2: The two modalities in SIMS. (A) Static mode provides information about the outermost atomic layer of the sample. (B) Dynamic mode uses high primary ion dose to remove material to obtain 3D information resulting in the formation of an etched crater [16].....	34
Figure 2.3: Schematic illustrating the dynamic SIMS method. This approach obtains information from the variation of the chemical composition below the surface [11]....	34
Figure 2.4: Illustration of SIMS imaging. The primary particles are scanned in X and Y directions to obtain chemical map where each pixel corresponds to a mass spectrum [7].....	35
Figure 2.5: ToF-SIMS 3D-imaging of the cerebellum area of a mouse brain section with sagittal orientation. A small region from this region was depth-profiled by acquiring one hundred 2D-images until enough material was removed to generate an etched crater. (A) Initial total ion image acquired with 40 keV $C_{60}^+$ of the cerebellum area. (B) Total ion image of the same area after depth profiling.....	35
Figure 2.6: MD simulations of atomic, polyatomic and cluster bombardment on Ag (111) substrate. The projectiles used are 15 keV Ga, $Au_3$ , $C_{60}$ and $Ar_{872}$ . The top row of images shows 1.5 nm of the atoms from the sample. The substrate has an interlayer spacing of 0.23 nm. The light grey region starts after a depth of 4.6 nm. The following two rows (from top to bottom) of images, shows the effects of the projectile impacts after 3 ps and 29 ps. The numbers included on the third row of images relate to the average secondary ion yields calculated from 32 impacts in the case of Ga and 16 impacts for $Au_3$ , $C_{60}$ and $Ar_{872}$ . The bottom row of images displays the damage caused	

by the projectiles on the bombarded areas viewed from the top down. Reproduced with permission from reference [41].	38
Figure 2.7: Illustration of PCA geometric projection. (A) 3-dimensional data set with data points (observations). (B) Three orthogonal principal components generated according to the variance. (C) The projection of the data points into the first two principal components [26].	42
Figure 2.8: Data visualisation from a total ion image acquired with ToF-SIMS. The total ion image can be thought of as a data-cube [26], [27]. According to the size, both the sample and primary ion beam can be scanned in X and Y directions and a series of pixels projected. Each pixel is a mass spectrum containing thousands of mass channels and each channel can be displayed as a single ion image [61], [64].	43
Figure 2.9: Score and loading result from the PCA analysis of the total ion image shown in Figure 2.8. The score image displays the chemical differences between the grey and white matter areas of the brain. The loading indicates which ions belong to each of these regions.	44
Figure 2.10: Workflow of a ToF-SIMS imaging experiment [67].	45
Figure 2.11: Diagram comparing three MSI techniques: SIMS, MALDI and DESI [76]. The chemical specificity for each technique is ruled by the mass range detectable for each method and it is divided into elements, lipids and proteins. Also shown are the best spatial resolutions currently available for (A) DESI [71], (B) SIMS [11] and (C) MALDI [70].	46
Figure 2.12: (A) MALDI image from a horizontal mouse brain section with a pixel size of 5 $\mu\text{m}$ . (B) Image of a horizontal mouse brain section acquired with a pixel size of 50 $\mu\text{m}$ . (C) Image of the intestinal tract of a rat with a pixel size of 200 $\mu\text{m}$ . The three images show the distribution of phospholipids in green and red. Reprinted with permission from reference [70].	47
Figure 2.13: (A) DESI mass spectrum from a coronal brain section highlighting different lipid species. (B) 2D DESI image overlay of PS (40:6) at $m/z$ 834.4 in green and ST (24:1) at $m/z$ 888.8 in red. (C) 3D reconstruction of serial 2D images showing the spatial localisation of the ions highlighted in (B). Reprinted with permission from reference [79].	47
Figure 2.14: Microprobe and microscope imaging modalities for MSI [69].	49

Figure 2.15: Two imaging modalities combined for tissue analysis. The section is imaged with ToF-SIMS first and then stained with a fluorophore. Optical images are obtained with fluorescence microscopy after SIMS.....	50
Figure 2.16: Image fusion of MSI and microscopy. An ion image from PE (P-40:4) at m/z 778.5 with 100 $\mu\text{m}$ pixel size is registered with and H&E image (10 $\mu\text{m}$ pixel size) obtained with optical microscopy. This registration will predict the distribution of the lipid at the highest spatial resolution. Reprinted with permission from reference [86].	51
Figure 2.17: Whole-body DESI-MSI in neonate mouse doped with clozapine. (a) Distribution of clozapine $[\text{M}+\text{H}]^+$ at m/z 327.14, (b) Single ion image of N-oxide metabolite at m/z 343.14 and (c) H&E stain on the same tissue section. Organs and anatomical features are highlighted with numbers: 1-brain, 2-adipose tissue (brown), 3- spinal cord, 4- adipose tissue (white), 5- liver, 6- lung, 7- heart ventricle and 7'- heart atrium. Reprinted with permission from reference [155].	53
Figure 2.18: Separation between tissue types found in the brain. Grey matter contains the cell bodies and nuclei whereas the white matter contains the axons and myelin sheets [145], [146].....	56
Figure 2.19: Single ion images from an Aplysia neuron obtained with ToF-SIMS: (A) Vitamin E $[\text{M}+\text{H}]^+$ at m/z 430.3, (B) Hydrocarbon at m/z 128.1, (C) Cholesterol $[\text{M}-\text{OH}]^+$ at m/z 369.3, (D) Phosphocholine head group at m/z 184, (E) PC (16:0e/18:1) fragment at m/z 709.6 and (F) Sum of PC (16:0e/18:1) related peaks (Scale bar= 100 $\mu\text{m}$ ). Reprinted with permission from reference [165].	56
Figure 2.20: Lipid ion images and overlaid images obtained with positive ToF-SIMS analysis of a mouse brain section using $\text{Ar}_{1700}^+$ . Images displayed in (a1), (a2) and (a3) belong to PC(32:0) $[\text{M}+\text{H}]^+$ , $[\text{M}+\text{Na}]^+$ and $[\text{M}+\text{K}]^+$ respectively. Single ion images of PC(34:0) $[\text{M}+\text{H}]^+$ , $[\text{M}+\text{Na}]^+$ and $[\text{M}+\text{K}]^+$ are shown as (b1), (b2) and (b3). The distribution of cholesterol $[\text{M}-\text{OH}]^+$ can be observed on (c) . Image overlay of PC(34:3) in blue, cholesterol in turquoise and glucosyl ceramide (d18:1/16:0) in yellow are displayed on (d). The major structures of the brain are also indicated (co-corpus callosum, cerebellum, hi-hippocampus, in-internal capsule). Image (e) contains the overlay of a DAG ion and PC(36:3). Reprinted with permission from reference [35].	58
Figure 2.21: Mouse brain image overlay of 30 minutes TFA exposed (a) and control (b) samples, respectively. Single ion images of m/z 570.53 (red), m/z 863.65 (green) and m/z 1096.90 (blue) are overlaid in each image. The rows below display single ion image	

comparison of ions with different mass-to-charge ratio. Signal intensities are lower for the control sample, especially for ions at $m/z$ 1096.90 and $m/z$ 1116.90. The distribution of cholesterol $m/z$ 369.35 is specific to the white matter in the control sample whereas it is also located across the grey matter on the sample exposed to TFA. Reproduced from reference [23].	60
Figure 2.22: Sample preparation workflow of a mouse brain for ToF-SIMS analysis.	61
Figure 2.23: ToF-SIMS images in negative ion mode with added intensities of sulfatides from a mass range $m/z$ 778.5-934.6 (a). (b) Distribution of cholesterol ( $m/z$ 385) in white matter in green. Image overlay of (a) and (b), showing the localisation of sulfatides mainly at the border of the white matter. Reprinted and modified with permission from reference [192].	65
Figure 2.24: (a) Confocal microscopy and (b), (d) ToF SIMS images from the areas occupied by A $\beta$ deposits. Images (c) and (e) are the overlay of the two techniques to correlate the location of the plaques. ToF-SIMS images were acquired with Bi $_3^+$ and a spatial resolution of 3-5 $\mu$ m. Reprinted with permission from reference [193].	66
Figure 2.25: Secondary ion signal comparison between 10 keV (H $_2$ O) $_n^+$ and 10 keV Ar $_n^+$ for the analysis of L-arginine, haloperidol, DPPC and Angiotensin II pure compounds. Reproduced from [36].	68
Figure 2.26: Sputter yield measurements obtained with argon, water and C $_{60}$ ion beam clusters. The samples presented are Irganox 1010 and L-arginine films. The data obtained using water clusters was compared to that presented by Seah [46] and Shard [203]. The sputtering yields are plotted as Y nm $^3$ /n as a function of E/atom or molecule [202].	69
Figure 3.1: Illustration of two peaks with similar masses. The minimum difference between the masses of two different ion peaks close to each other is used to calculate the mass resolution in Equation 3.1. The peaks are not necessarily on the baseline.	93
Figure 3.2: Diagram of the J105 3D-Chemical imager [7].	95
Figure 3.3: Schematic of the buncher-ToF mass analyser in the J105-3D chemical imager [2].	96
Figure 3.4: Schematic of an electron bombardment source [11].	98
Figure 3.5: Measurement of the beam diameter for 40 ke C $_{60}^+$ beam using a 30 $\mu$ m adjustable aperture. A line profile is manually drawn on one of the grid bars of the SEM	

image (left). The lateral resolution is 1.3 $\mu\text{m}$ , provided by the line scan profile 20- 80%.	99
Figure 3.6: Schematic of a Wien filter [11].	101
Figure 3.7: Schematic of a GCIB source [4].	102
Figure 3.8: Illustration of the water cluster ion beam [24]. A boiler assembly was fitted within the first vacuum chamber to produce a water steam. Cluster formation and selection are achieved in the same manner as argon clusters [32].	103
Figure 3.9 Graphical representation of the size range distribution of the clusters obtained with the GCIB primary ion beam. For example, if the desired cluster is $(\text{H}_2\text{O})_{2000}$ , the size of the clusters obtained will be $\pm 100$ i.e. $(\text{H}_2\text{O})_{1900-2100}$ .	104
Figure 3.10: SEM images from a 300 copper grid covering a 300 $\mu\text{m}^2$ area using 256 X 256 pixels. (a) The spatial resolution measured for 20 keV $\text{Ar}_{2000}^+$ is 13 $\mu\text{m}$ . (b) A line profile is drawn manually over a sharp edge to determine the beam diameter from image (a). (c) The spatial resolution of 20 keV $(\text{H}_2\text{O})\text{Ar}_{2000}^+$ is 11 $\mu\text{m}$ . (d) The spatial resolution of 20 keV $(\text{H}_2\text{O})_{6000}^+$ is 11 $\mu\text{m}$ .	105
Figure 4.1: Chemical structure of Arginine [20].	110
Figure 4.2: Fragments obtained from human angiotensin II (DRVYIHPF) with ToF-SIMS analysis [11].	111
Figure 4.3: Chemical structure of trehalose dehydrate [2].	111
Figure 4.4: Parts of a phospholipid molecule. This figure displays the chemical structure of a phospholipid (DPPC) and their polar (hydrophilic) head and non-polar (hydrophobic) tail. Phospholipids build arrangements in aqueous environments forming bilayers. These type of bilayers can be observed in biological cell membranes [26], [27].	112
Figure 4.5: Chemical structure of DPPC.	113
Figure 4.6: Schematic representation of the spin coating process to get uniform films with different compounds [37].	114
Figure 4.7: Methodology used for the preparation of brain total lipid extract. The snap-frozen brain is first homogenised in a 1:1 $\text{MeOH}:\text{CHCl}_3$ (v/v) solution. The brain homogenate is then sonicated until a separation of phases is produced. The extracted lipid will be contained in the aqueous part of the two-phase solution.	116

Figure 4.8: (A) Part of a mouse brain embedded to the cryo-microtome sample holder with CMC. (B) Specimen ready for sectioning in the cryostat microtome. (C) Serial section with sagittal orientation thaw-mounted on a silicon substrate.....	117
Figure 4.9: Chemical structure of cholesterol.....	118
Figure 4.10: Methodology followed for the analysis of 3xTg-AD brain mirror sections. First, the brain is sectioned in serial mirror sections to obtain almost identical surfaces in two sections. Section 1 is stained with 1% thioflavin S and analysed with fluorescence microscopy to locate the A $\beta$ plaques. Once identified in section 1, the areas containing A $\beta$ plaques are analysed in section 2 using ToF-SIMS. To validate the presence of A $\beta$ aggregates, section 2 is also stained with 1% thioflavin S and analysed with fluorescence microscopy. ....	119
Figure 4.11: Developed staining protocol for Thioflavin S. All solutions are placed in glass sample tubes. The procedure starts by submerging the brain section in solution (A) and ends with solution (M). Solutions (A-E) are applied to fix and re-hydrate the tissue sample. Solution (F) is the staining step of the protocol. Solutions (G-M) are applied to rinse the excess of dye in the sample. Incubation times are specified below every solution. ....	123
Figure 5.1: Different situations encountered during organic depth profiling. (A-C) depth profiling of thin films and (D) depth profiling a bulk sample. (A) example of a profile under ideal conditions. (B) and (C) depth profiles under non-optimum conditions showing the accumulation of damage. The damage exhibit in (B) is greater than (C). The three regions observed in plots (A-C) are: 1) the initial signal decay observed in the surface transient region of the depth profile, 2) steady-state region and 3) interfacial region with a significant decrease of the ion signal and increase in the substrate signal. (D) example of depth profiling bulk materials when there is loss of signal intensity after high primary ion dose exposure [4]. ....	130
Figure 5.2: Trehalose, angiotensin II, arginine and DPPC spectra acquired with (a) 20 keV Ar <sub>4000</sub> <sup>+</sup> and (b) 20 keV (H <sub>2</sub> O) <sub>4000</sub> <sup>+</sup> cluster ion beams with a primary ion dose of $5 \times 10^{11}$ ions cm <sup>-2</sup> . All spectra are normalised to their base peak.....	133
Figure 5.3: Plots (a) 20 keV Ar <sub>2000</sub> <sup>+</sup> ; (b) 20 keV Ar <sub>4000</sub> <sup>+</sup> ; (c) 20 keV (H <sub>2</sub> O) <sub>2000</sub> <sup>+</sup> and (d) 20 keV (H <sub>2</sub> O) <sub>4000</sub> <sup>+</sup> secondary ion signal variation in trehalose as a function of primary ion dose. The signal was normalised to the total in all plots. ....	134
Figure 5.4: Secondary ion signal plot after exposing the trehalose sample to $5 \times 10^{11}$ ions cm <sup>-2</sup> . The signal was normalised to the highest value obtained from the quasi-	



molecular ion  $[M+H]^+$  with 20 keV  $(H_2O)_{7000}^+$ . The secondary ion signal is plotted as a function of E/atom or molecule. The experiments were acquired with 20 keV  $Ar_n^+$  (dashed lines) and  $(H_2O)_n^+$  (solid lines) clusters. The green line shows the signal variation of the trehalose quasi-molecular ion  $[M+H]^+$ ;  $[M-OH]^+$  is highlighted with blue lines; the sodiated molecular ion adduct  $[M+Na]^+$  is plotted in red lines and finally the fragment  $[C_6H_{11}O_5]^+$  at m/z 163 is represented with purple lines. Error bars are also included in the  $[M-OH]^+$  plot to show the data uncertainty between multiple measurements. This signal variation,  $\sim 10\%$ , is the same for all the ions from different experiments..... 135

Figure 5.5: Trehalose secondary ion signal plot after an accumulated primary ion dose of  $3 \times 10^{13}$  ions  $cm^{-2}$ . The plots were normalised to the  $[M+H]^+$  signal obtained with 20 keV  $(H_2O)_{7000}^+$ . The signal intensity is plotted against E/atom or molecule.. The plots include 20 keV  $Ar_n^+$  (dashed lines) and  $(H_2O)_n^+$  (solid lines) clusters. Signal variation of the trehalose quasi-molecular ion  $[M+H]^+$  is represented with green lines;  $[M-OH]^+$  signal is plotted with blue lines; the sodiated molecular ion adduct  $[M+Na]^+$  is highlighted with red lines and the fragment  $[C_6H_{11}O_5]^+$  at m/z 163 is denoted by purple lines. Error bars are included to show the variation ( $\sim 10\%$ ) in measurements from multiple experiments..... 136

Figure 5.6: Plot of the secondary ion signal from the arginine film after a primary ion dose of  $5 \times 10^{11}$  ions  $cm^{-2}$  and  $3 \times 10^{13}$  ions  $cm^{-2}$ , respectively. Signal intensities from  $[M+H]^+$  at m/z 175,  $[2M+H]^+$  at m/z 349 and  $[M+Na]^+$  at m/z 197 ions are plotted against their E/atom or molecule. Argon cluster experiments are denoted by dashed lines whereas water cluster are plotted with solid lines. The signal values are normalised to the  $[M+H]^+$  signal acquired with  $(H_2O)_{8000}^+$ . Error bars are omitted since the level of uncertainty is the same to that observed in trehalose ( $\sim 10\%$ )..... 137

Figure 5.7: Secondary ion yield plot for Angiotensin II after a primary ion dose of  $5 \times 10^{11}$  ions  $cm^{-2}$  and  $2 \times 10^{13}$  ions  $cm^{-2}$ , respectively. The experiments acquired with 20 keV  $Ar_n^+$  are highlighted with dashed lines) and those acquired with 20 keV  $(H_2O)_n^+$  are represented with solid lines. The secondary ion signal from ions  $[M+H]^+$  at m/z 1031,  $[M+Na]^+$  at m/z 1053 (multiplied by 10) and the fragment  $[b_2-NH_3]^+$  at m/z 254 were normalised to the  $[M+H]^+$  signal obtained with 20 keV  $(H_2O)_{7000}$ . Error bars are omitted since the level of uncertainty is the same to that observed in trehalose ( $\sim 10\%$ )..... 138

Figure 5.8: Analysis of DPPC with 20 keV  $(H_2O)_{7000}^+$  showing the presence of water peak adducts in the red rectangle. This water peaks are only observed in DPPC spectra analysed with cluster sizes  $> 7000$ . ..... 139

Figure 5.9: Secondary ion signal from DPPC with a total primary ion dose of $5 \times 10^{11}$ ions $\text{cm}^{-2}$ and $1.5 \times 10^{13}$ ions $\text{cm}^{-2}$ . The experiments were carried out using 20 keV $\text{Ar}_n^+$ (dashed lines) and 20 keV $(\text{H}_2\text{O})_n^+$ (solid lines). The ion signal from $[\text{M}+\text{H}]^+$ at $m/z$ 735 (green lines), $[\text{M}+\text{Na}]^+$ at $m/z$ 757 (red line) and the phosphocholine fragment $[\text{C}_5\text{H}_{15}\text{NO}_4\text{P}]^+$ at $m/z$ 184 /100 (blue line) were normalised to the maximum signal $[\text{M}+\text{H}]^+$ with 20 keV $(\text{H}_2\text{O})_{6000}^+$ . The level of uncertainty is the same to that observed in trehalose ( $\sim 10\%$ ).	140
Figure 5.10: Plot of the signal ratio $[\text{M} + \text{Na}]^+ / [\text{M} + \text{H}]^+$ in trehalose as a function of $E/\text{atom}$ or molecule. The plots include analysis with 20 keV $\text{Ar}_n^+$ (dotted blue line) and 20 keV $(\text{H}_2\text{O})_n^+$ clusters (red solid line).	142
Figure 5.11: Ratio of $[\text{M}-\text{OH}]^+$ at $m/z$ 325 and $[\text{C}_6\text{H}_{11}\text{O}_5]^+$ at $m/z$ 163 to $[\text{M}+\text{H}]^+$ at $m/z$ 379 as a function of $E/\text{atom}$ or molecule for trehalose using $(\text{H}_2\text{O})_n^+$ clusters as primary ion beams.	142
Figure 5.12: Ratio of $[\text{M}-\text{OH}]^+$ at $m/z$ 325 and $[\text{C}_6\text{H}_{11}\text{O}_5]^+$ at $m/z$ 163 to $[\text{M}+\text{H}]^+$ at $m/z$ 379 as a function of $E/\text{atom}$ or molecule for trehalose using $(\text{Ar})_n^+$ clusters as primary ion beams.	143
Figure 5.13: $[\text{M}+\text{H}]^+$ (green line) and $[\text{M}-\text{OH}]^+$ (blue line) ion signal from trehalose, generated by water beam analysis. The ion yield obtained with clusters having $E/\text{atom}$ or molecule $\sim 3$ eV was plotted as a function of cluster size and normalised to $[\text{M}+\text{H}]^+$ yield obtained with 20 keV $(\text{H}_2\text{O})_{7000}^+$ .	144
Figure 5.14: DPPC isotope ratios for the DPPC $[\text{M}+\text{H}]^+$ ion and its related $^{13}\text{C}$ isotope at $m/z$ 735/734 (blue columns) and the phosphocholine fragment ion $[\text{C}_5\text{H}_{15}\text{NO}_4\text{P}]^+$ and its related $^{13}\text{C}$ isotope at $m/z$ 185/184 (red columns). The expected ratios were calculated from the natural abundance of $^{13}\text{C}$ isotopes and are compared to the ratios obtained with $(\text{D}_2\text{O})_n^+$ and $(\text{H}_2\text{O})_n^+$ . The primary ion dose used in these experiments was $5 \times 10^{11}$ ions $\text{cm}^{-2}$ .	146
Figure 5.15: Trehalose secondary ion yields obtained with $(\text{H}_2\text{O})_n^+$ and $(\text{D}_2\text{O})_n^+$ analysis with a total primary ion dose of $5 \times 10^{11}$ ions $\text{cm}^{-2}$ . All yields were normalised to $[\text{M}+\text{H}]^+$ obtained with 10 keV $(\text{H}_2\text{O})_{4000}^+$ . The secondary ion yields were calculated from $[\text{M}+\text{H}]^+$ at $m/z$ 343 and the isotopes at $m/z$ 344, 345, 346, 347 and 348.	147
Figure 5.16: Detected secondary ion signal per $1 \mu\text{m}^2$ area with 20 keV $\text{Ar}_{2000}^+$ and $(\text{H}_2\text{O})_{7000}^+$ under static primary ion dose conditions ( $5 \times 10^{11}$ ions $\text{cm}^{-2}$ ) and in the steady-state ( $1.5 \times 10^{13}$ ions $\text{cm}^{-2}$ ). The results from the experiments are displayed for (a) Arginine $[\text{M}+\text{H}]^+$ and $[2\text{M}+\text{H}]^+$ , (b) Trehalose $[\text{M}+\text{H}]^+$ , (c) DPPC $[\text{M}+\text{H}]^+$ and fragment	

m/z 184 and (d) Angiotensin II  $[M+H]^+$ . (e) Secondary ion signal enhancement specified by the ratio of the signal detected with water is steady state divided by the signal detected with argon clusters in static. \* In the DPPC chart specifies that the data was acquired with 20 keV  $(H_2O)_{4000}^+$ . The values are rounded to a 10 % error. .... 150

Figure 5.17: Secondary ion signal comparison from the analysis of trehalose.  $(H_2O)_n^+$  (blue line),  $Ar_n^+$  (red line) and  $(H_2O)Ar_n^+$  (green line) cluster ion beams were used for analysis. Secondary ion signal intensities are plotted against E/nucleon. Intensity values were normalised to the signal of the  $[M+H]^+$  ion produced by 20 keV  $Ar_{2000}^+$ . The two plots presented correspond to the ions: A)  $[M+H]^+$  at m/z 343 and B)  $[M-OH]^+$  at m/z 325..... 152

Figure 5.18: Secondary ion signal comparison from the analysis of DPPC.  $(H_2O)_n^+$  (blue line),  $Ar_n^+$  (red line) and  $(H_2O)Ar_n^+$  (green line) cluster ion beams were used for analysis. Secondary ion intensities from  $[M+H]^+$  at m/z 735 and the phosphocholine fragment  $[C_5H_{15}NO_4P]^+$  at m/z 184 are plotted against E/nucleon. The phosphocholine fragment was divided by ten to fit the plots and all ion intensities were normalised to the signal of the  $[M+H]^+$  ion produced by 20 keV  $Ar_{2000}^+$ ..... 153

Figure 5.19: Ion signal ratios from the DPPC experiments. The ratios were calculated for m/z 735/734 and m/z 185/184. The expected ratios are calculated from the  $^{13}C$  isotopic abundance (44.36 % for the DPPC molecule and 5.54% for the phosphocholine fragment). The experiments we acquired with 20 keV  $(H_2O) Ar_{2000}^+$ ,  $(D_2O)Ar_{2000}^+$  and 20 keV  $(D_2O)_{2000,4000}^+$  under static conditions ( $5 \times 10^{11}$  ions  $cm^{-2}$ )..... 155

Figure 6.1: Visualisation of the sagittal plane on a mouse brain. .... 162

Figure 6.2: Sagittal sections obtained from the left hemisphere of the mouse brain. This hemisphere is sectioned in nine sections from the outside (section A) up to the central axis (section I). Here, it is possible to locate many of the main brain structures: the cerebellum area with pons and medulla underneath, the midbrain, the cerebral cortex; the two hippocampal areas; caudate putamen; thalamus; internal capsule and amygdala [11]. .... 163

Figure 6.3: Mouse brain anatomy from a sagittal plane perspective. The identified anatomical structures from this sagittal section belong to the region close to the central axis [11]..... 164

Figure 6.4: (A) Membrane structure found in the cell bodies located in the grey matter area of the brain. (B) Lipids located in the myelin sheath of the neuron's axons; the

myelin sheath wraps up the axon. Axons are the main components of the white matter of the brain [19], [20].	165
Figure 6.5: Secondary ion spectra of brain extract acquired with (A) 20 keV $(\text{H}_2\text{O})_{2000}^+$ and (B) 20 keV $(\text{H}_2\text{O})_{6000}^+$ . Both spectra were normalised to the total ion counts.	169
Figure 6.6: Plots of secondary ion signal of GPCho C32:0 $[\text{M}+\text{H}]^+$ at $m/z$ 734; GPCho C34:0 $[\text{M}+\text{H}]^+$ at $m/z$ 762; Sphingolipid Ch 24:1 $[\text{M}+\text{H}]^+$ at $m/z$ 826 and cholesterol $[\text{M}-\text{H}_2\text{O}+\text{H}]^+$ ion at $m/z$ 369. The experiments were acquired using 20 keV $(\text{H}_2\text{O})_n^+$ (blue line), 20 keV $(\text{H}_2\text{O})\text{Ar}_n^+$ (green line) and 20 keV $\text{Ar}_n^+$ (red line). All signal intensities are plotted relative to the ion signal observed with 20 keV $\text{Ar}_{2000}^+$ and as a function of $E/\text{nucleon}$ .	170
Figure 6.7: Localisation of the brain striatum in a total ion SIMS image of a sagittal section of a mouse brain. This image was acquired with 20 keV $\text{C}_{60}^+$ and a pixel size of 7 $\mu\text{m}$ . The mass range recorded was $m/z$ 100- 1000. The striated appearance is one of the main characteristics of this brain region.	171
Figure 6.8: ToF-SIMS imaging of the brain striatum in positive ion mode. The same area was analysed with 20 keV $\text{C}_{60}^+$ and 20 keV $(\text{H}_2\text{O})_{3000}^+$ with a 650 $\mu\text{m}^2$ field of view. (A) Total ion spectrum and image after a primary ion dose of $2.5 \times 10^{12}$ ions $\text{cm}^{-2}$ with 20 keV $\text{C}_{60}^+$ . The beam diameter was 7 $\mu\text{m}$ and it is possible to observe the white matter striated features commonly found in this area of the brain. The ion peaks in mass range in which most intact phospholipids can be found (500-1000 Da) are zoomed in. (B) Same area analysed with 20 keV $(\text{H}_2\text{O})_{3000}^+$ after $\text{C}_{60}$ bombardment. The accumulated ion dose was $5 \times 10^{11}$ ions $\text{cm}^{-2}$ with a spot size 9 $\mu\text{m}$ .	173
Figure 6.9: ToF-SIMS positive images of two different regions of the brain striatum using (A) 20 keV $(\text{H}_2\text{O})_{3000}^+$ and (B) 20 keV $(\text{H}_2\text{O})_{4500}^+$ . Both analysed were acquired over a 650 $\mu\text{m}^2$ area with $\sim 10$ $\mu\text{m}$ of beam diameter.	174
Figure 6.10: Total ion spectra comparison between the image acquired with 20 keV $\text{C}_{60}^+$ only (top, blue line) and the image obtained from the same area with 20 keV $\text{C}_{60}^+$ and 20 keV $(\text{H}_2\text{O})_{3000}^+$ on dc simultaneously (bottom, red line). Total ion images are also displayed for comparison.	175
Figure 6.11: Cholesterol ion peak $[\text{M}+\text{H}-\text{H}_2\text{O}]^+$ comparison between the image acquired with 20 keV $\text{C}_{60}^+$ (top, blue line) and the image obtained from the same area with 20 keV $\text{C}_{60}^+$ and 20 keV $(\text{H}_2\text{O})_{3000}^+$ on dc simultaneously (bottom, red line)[26].	176
Figure 6.12: Total ion images of the mouse brain cerebellum acquired with 20 keV $\text{C}_{60}^+$ and a mass range $m/z$ 100-1000. (A) Localisation of the cerebellum in a sagittal mouse	

brain section. (B) General anatomy and main regions within the cerebellar area. (C) Amplification of a small region of the ansiform lobule to visualise the different cerebellum layers: the molecular layer; the granular layer; and the Purkinje layer (not shown), localised between the molecular and granular layers..... 178

Figure 6.13: Total ion spectra from the tissue region (ROI), excluding the silicon substrate. (A) 20 keV  $\text{Ar}_{2000}^+$  spectrum and (B) 20 keV  $(\text{H}_2\text{O})_{4000}^+$  spectrum. Both experiments were run with  $1 \times 10^{12}$  ions  $\text{cm}^{-2}$  as the primary ion dose..... 181

Figure 6.14: Spectrum derived from the subtraction of 20 keV  $\text{Ar}_{2000}^+$  from 20 keV  $(\text{H}_2\text{O})_{4000}^+$ . The total ion spectra used in the subtraction were obtained from the ROI of tissue area to exclude interference peaks from the substrate..... 182

Figure 6.15: Total ion count (TIC) images and total ion spectra acquired from the cerebellar area of serial sagittal mouse brain sections. The primary ion dose applied was  $1 \times 10^{12}$  ions  $\text{cm}^{-2}$ . The cluster primary ion beams used are: (A) 20 keV  $\text{C}_{60}^+$ , (B) 20 keV  $\text{Ar}_{2000}^+$ , (C) 20 keV  $(\text{H}_2\text{O})\text{Ar}_{2000}^+$  and (D) 20 keV  $(\text{H}_2\text{O})_{6000}^+$ ..... 183

Figure 6.16: Score images generated with ROI-PCA applied to the normalised TIC images of the brain cerebellum. The images were normalised to the total ion counts prior to PCA analysis. (A) 20 keV  $(\text{H}_2\text{O})_{6000}^+$  score image, (B) 20 keV  $(\text{H}_2\text{O})\text{Ar}_{2000}^+$  score image, (C) 20 keV  $\text{Ar}_{2000}^+$  score image and (D) 20 keV  $\text{C}_{60}^+$ . These images show the grey and white matter areas in green and red, respectively. .... 184

Figure 6.17: Anatomical features observed in the score image obtained from the 20 keV  $\text{C}_{60}^+$  image on the cerebellar area. .... 184

Figure 6.18: Loading plot corresponding to the image score obtained from the ROI-PCA analysis on the image analysed with 20 keV  $(\text{H}_2\text{O})_{6000}^+$ . This loading was calculated for the 3<sup>rd</sup> principal component (PC3)..... 185

Figure 6.19: Overlaid spectra from images obtained with 20 keV  $(\text{H}_2\text{O})_{6000}^+$ (purple line),  $(\text{H}_2\text{O})\text{Ar}_{2000}^+$  (green line) and  $\text{Ar}_{2000}^+$  (red line). White matter (A) and grey matter (B) regions were identified according to the PCA analysis. The mass ranges included are 500-900 Da and 369-370 Da for intact lipid detection and cholesterol detection, respectively. Data collected with 20 keV  $\text{C}_{60}^+$  is not included due to the low secondary ion signal obtained. Some lipid ion peaks have been labelled as a reference for each region. Black labels refer to ion peaks observed in both brain regions, ion peaks with red labels were observed only in the white matter region and lipids with blue labels were only detected in the grey matter. .... 187

Figure 6.20: Single ion images from different lipids obtained from the tissue area (ROI). The total ion images were normalised to the total number of counts before generating the single ion images. Image showing the localisation of cholesterol  $[M-H_2O+H]^+$  at  $m/z$  369 with (A)  $(H_2O)Ar_{2000}$  and (B)  $(H_2O)_{6000}$ . Single ion image of the lipid PC36:1  $[M+H]^+$  at  $m/z$  788.6 obtained with (C)  $(H_2O)Ar_{2000}$  and (D)  $(H_2O)_{6000}$ . Image (E) displays the distribution of the glycosphingolipids GalCer(32:1  $[M+H]^+$  at  $m/z$  672.5, GalCer(d18:0/16:0)  $[M+H]^+$  at  $m/z$  702.5 and GalCer(d18:2/20:1)  $[M+H]^+$  at  $m/z$  752.5 with  $(H_2O)_{6000}$ . The white line was drawn to highlight the location of the white matter.

..... 189

Figure 6.21: Total ion spectra obtained with (A) 20 keV  $Ar_{2000}^+$  and B)  $(H_2O)_{6000}^+$  from a cholesterol mixture of sphingomyelin/ DPPC (1:1). The total primary ion dose used was  $1 \times 10^{12}$  ions  $cm^{-2}$ .

..... 202

Figure 6.22: Secondary ion yields obtained from a  $400 \mu m^2$  area from the images previously presented. Secondary ion yields of stearic acid  $[M+H]^+$  ion from sphingomyelin and cholesterol  $[M-H_2O+H]^+$  ion from grey matter and white matter regions are presented. The primary ion beams used were 20 keV  $(H_2O)_{6000}^+$ , 20 keV  $(H_2O)Ar_{2000}^+$ , 20 keV  $Ar_{2000}^+$  and 20 keV  $C_{60}^+$  under a primary ion fluence of  $1 \times 10^{12}$  ions  $cm^{-2}$ . The presence of both lipids is in a ratio 1:0.3 (cholesterol/SM) [13]. The secondary ion yields of SM were multiplied by ten for better visualisation.

..... 203

Figure 6.23: Cholesterol/SM ratio obtained from the secondary ion yields from the analysis of the brain cerebellum. The primary ion beams used were 20 keV  $(H_2O)_{6000}^+$ , 20 keV  $(H_2O)Ar_{2000}^+$ , 20 keV  $Ar_{2000}^+$  and 20 keV  $C_{60}^+$  under a primary ion fluence of  $1 \times 10^{12}$  ions  $cm^{-2}$ . The ratios are calculated for grey matter (top) and white matter (bottom).

..... 205

Figure 6.24: Cholesterol/sphingomyelin peak ratios from the analysis of a mixture of cholesterol/SM (1:1). The primary ion beams used were 20 keV  $(H_2O)_{6000}^+$ , 20 keV  $(H_2O)Ar_{2000}^+$ , 20 keV  $Ar_{2000}^+$  and 20 keV  $C_{60}^+$  under a primary ion fluence of  $1 \times 10^{12}$  ions  $cm^{-2}$ .

..... 206

Figure 7.1: (A) Diseased neuron with Alzheimer's disease (AD). (B) Non-diseased (healthy) neuron. Illustration (A) displays the effects of the disease on the generation of neurofibrillary tangles inside the neuron and the extracellular deposition of A $\beta$  protein in plaques around the cortical and hippocampal regions [10].

..... 214

Figure 7.2: The 3xTg-AD mouse model is generated from the expression of three mutant genes identified in AD: APP, PSEN1 and Tau. The name of each mouse strain is

also included next to the gene: M146V for PSEN1, SWE for APP and P301L for Tau. [12].

.....215

Figure 7.3: Progression of AD in a mouse model brain. This mouse model is the combination of three genetic mutations: APP, PS1 and Tau. APP and PS1 have been identified as the genes responsible of encoding the proteins deposited in A $\beta$  plaques. The tau mutant mouse model reproduces the formation of neurofibrillary tangles. The combination of the three mutant genes leads to the generation of a 3xTg-AD mouse model. This mouse model develops plaques and tangles in hippocampus and cortex areas. These brain lesions get more prominent with the progression of the disease [12]......216

Figure 7.4: Fluorescence microscopy image from a mouse brain section labelled with Thioflavin S. From the scale, it is possible to observe that the A $\beta$  plaques are less than 30  $\mu$ m in diameter. Modified and reprinted with permission from [19]. .....217

Figure 7.5: Fluorescence microscopy image of a complete 3xTg-AD sagittal section labelled with 1% thioflavin S. The sample was imaged with fluorescence microscopy with magnification of x10 and a spatial resolution of 0.86  $\mu$ m per pixel.....219

Figure 7.6: Neuritic plaques labelled with thioS found on the frontal brain cortex. The plaques are classified as: type 1, type 2b and 2c with an average diameter of 10-20  $\mu$ m. The image was obtained using a fluorescent microscope with x20 magnification and 0.53  $\mu$ m per pixel resolution.....220

Figure 7.7: A $\beta$  plaques dyed with 1% thioS and localised in frontal and superior (above hippocampus) brain cortex. (A) Cored plaques type 2b localised in superior cortex. (B) Cored plaques (Type 2b and 2c) localised above hippocampus. (C) Diffuse plaque type 1 and a group of 3 plaques type 2b localised in frontal cortex. (D) Plaque type 2a found in superior cortex. These images were acquired in a fluorescent microscope with the following magnification: (A) x40, (B) x40, (C) x 20 and (D) x20. Images with x40 magnification have 0.27  $\mu$ m per pixel spatial resolution and x20 images have 0.53  $\mu$ m per pixel spatial resolution.....221

Figure 7.8: (A) Selection of control points for the geometric transformation according to specific features of the brain's anatomy: foliation patterns in the cerebellum, superior cortex, inferior cortex and internal capsule. The points selected on the microscopy image are fixed points and the points selected on the SIMS fixed are moving points. (B) Registered image generated by overlapping of the fixed image

(SIMS) and the image geometrically transformed (microscopy). The areas containing neuritic plaques are highlighted with white boxes and arrows. ....222

Figure 7.9: Selected regions-of-interest of areas from the cortex with and without the presence of A $\beta$  plaques. The areas of interest were selected on the registered image (SIMS and fluorescence microscopy) and total ion spectra were extracted from both regions. The regions-of-interest are identical in size and were deliberately selected in close proximity to minimise the chemical variation caused by different anatomical features.....224

Figure 7.10: Spectrum resulting from the spectra from ROI with plaques minus the ROI without plaques. The labels refer to possible ions identified: phosphocholine ion [C<sub>5</sub>H<sub>15</sub>NO<sub>4</sub>P]<sup>+</sup> at m/z 184, Leu or Ile at m/z 86, Ala-Gly , Gln or Lys at m/z 128, Gly-Val at m/z 156 and Asp-Al at m/z 222.....225

Figure 7.11: Overlaid spectra obtained from four different ROIs with A $\beta$  plaques. The areas were selected to cover the plaques and the least possible amount of surrounding tissue. The observed ions peaks are similar than those observed in the subtracted spectrum (Figure 7.10). The labels refer to possible ions identified: phosphocholine ion [C<sub>5</sub>H<sub>15</sub>NO<sub>4</sub>P]<sup>+</sup> at m/z 184, Leu or Ile at m/z 86, Ala-Gly , Gln or Lys at m/z 128, Gly-Val at m/z 156 and Asp-Al at m/z 222.....225

Figure 7.12: Total ion spectrum of Amyloid- $\beta$  synthetic peptide (1-40) acquired with 40 keV C<sub>60</sub><sup>+</sup>. The primary ion dose used was 2 x 10<sup>12</sup> ions cm<sup>-2</sup>. ....226

Figure 7.13: Spectrum resulting from the ROI with plaques minus the spectrum taken from the region without plaques. The areas of interest were selected on the registered image (SIMS and fluorescence microscopy) and total ion spectra were extracted from both regions. The labels refer to possible ions identified: phosphocholine ion [C<sub>5</sub>H<sub>15</sub>NO<sub>4</sub>P]<sup>+</sup> at m/z 184, cholesterol fragment [M-H<sub>2</sub>O+H]<sup>+</sup> at m/z 369], the ion m/z 104.1 relates to a Gly-Gly or Asn, the peak at m/z 236.2 is Ala-Glu and the ion at m/z 329.3 could be assigned as Arg-His. ....229

Figure 7.14: Score image from PC2 generated from the ROI-PCA analysis of a 40 keV C<sub>60</sub><sup>+</sup> image. This image covers a 500 x 400  $\mu$ m region of the cortex located above the hippocampus. The score shows the distribution of the cholesterol fragment [C<sub>16</sub>H<sub>21</sub>]<sup>+</sup> at m/z 213 in red and a phosphocholine fragment [C<sub>2</sub>H<sub>6</sub>PO<sub>4</sub>]<sup>+</sup> at m/z 125. The localisation of the A $\beta$  plaques is highlighted in white and magnified for better visualisation. The concentration of the cholesterol ions is higher towards the white matter. Cholesterol is



not specifically localised around the plaques, as showed by Solé-Domènech et al. [24].

.....231

Figure 7.15: Score image and loading from PC2 on the 20 keV  $(\text{H}_2\text{O})\text{Ar}_{2000}^+$  image from a region of the frontal cortex. The score shows the distribution of the cholesterol fragment  $[\text{M}-\text{H}_2\text{O}+\text{H}]^+$  at  $m/z$  369 in red and the phosphocholine fragment  $[\text{C}_5\text{H}_{15}\text{NO}_4\text{P}]^+$  at  $m/z$  184 in green. The localisation of the  $\text{A}\beta$  plaques is drawn in white according to the registered SIMS-microscopy image and it is highlighted in white circles.....233

Figure 7.16: Single ion image of the cholesterol ion  $[\text{M}-\text{H}_2\text{O}+\text{H}]^+$  at  $m/z$  369. The area shown on this image is the frontal cortex of the brain. The distribution of this molecule is uniform across grey and white matter, thus, the anatomical structures are not visible.

.....234

Figure 8.1: Cholesterol  $[\text{M}-\text{H}_2\text{O}+\text{H}]^+$  spectra comparison between 20 keV  $(\text{H}_2\text{O})_{6000}^+$ ,  $(\text{H}_2\text{O})\text{Ar}_{2000}^+$  and  $\text{Ar}_{2000}^+$  in the grey and white matter regions. The secondary ion signal intensity is similar in both regions with  $(\text{H}_2\text{O})_{6000}^+$  and  $(\text{H}_2\text{O})\text{Ar}_{2000}^+$ . With  $\text{Ar}_{2000}^+$ , the signal detected is considerably lower in the white matter and close to zero in the grey matter.....241

Figure 8.2: Single ion images of the distribution of cholesterol  $[\text{M}-\text{H}_2\text{O}+\text{H}]^+$  at  $m/z$  369 with (A)  $(\text{H}_2\text{O})\text{Ar}_{2000}$  and (B)  $(\text{H}_2\text{O})_{6000}$ .....242

Figure 8.3:  $[\text{M}+\text{H}]^+$  (green line) and  $[\text{M}-\text{OH}]^+$  (blue line) ion signal from trehalose, generated by water beam analysis. The ion yield obtained with clusters having  $E/\text{molecule} \sim 3$  eV was plotted as a function of cluster size and normalised to  $[\text{M}+\text{H}]^+$  yield obtained with 20 keV  $(\text{H}_2\text{O})_{7000}^+$ . .....245

## List of Tables

Table 2.1: Chemical structure of lipids that are most commonly found in mouse brain tissue analysis with ToF-SIMS [141].	54
Table 2.2: Lipid composition of myelin, white matter, grey matter and the whole brain in rats and humans. The total lipid* figure is presented in percent dry weight whilst all others are mentioned in percent total lipid weight [167].	55
Table 3.1: Diameters of adjustable apertures to focus the 40 kV C60 beam and the lateral resolution obtained on each one [8], [9].	100
Table 6.1: ROI-PCA score images (top) showing the separation between grey and white matter tissue areas of the brain. The score from the first principal component (PC1) is shown for every experiment. Single ion images are also displayed for a cholesterol fragment, the phospholipid GPCho C34:0, a phosphorylethanolamine ion and the sphingolipid Ch24:1. All images were normalised to the total number of counts. The counts recorded per $\mu\text{m}^2$ are included under each image.	180
Table 6.2: Lipid ion peaks observed in the spectra from white matter and grey matter (Figure 6.19). Peak assignments were obtained using references [1], [36], [38] and were based on measurements with 10 ppm of precision. Columns on the right show the ratios result from the comparison of secondary ion yields between water-containing clusters and $\text{Ar}_{2000}$ . ‘(H <sub>2</sub> O) only’ refers to peaks only detected with water-containing clusters such as $(\text{H}_2\text{O})\text{Ar}_{2000}$ and $(\text{H}_2\text{O})_{6000}$ ; ‘ND’ refers to not- observed ion peaks. Lipid abbreviations included are: PE-Phosphatidylethanolamine, PC-Phosphatidylcholine, PI-Phosphatidylinositol, GalCer-Galactosylceramide, SM-Sphingomyelin, DAG-Diacylglyceride, TAG-Triacylglyceride, Cer-Ceramide and Chol-Cholesterol (Chol).	190
Table 6.3: List of lipids ion observed with $(\text{H}_2\text{O})_{6000}^+$ , $(\text{H}_2\text{O})\text{Ar}_{2000}^+$ and $\text{Ar}_{2000}^+$ . ‘✓’ indicates a detected ion whereas ‘ND’ refers to not-observed species.	201
Table 7.1: Possible amino acid fragments observed in the Amyloid- $\beta$ synthetic peptide (1-40) standard acquired with 40 keV $\text{C}_{60}^+$ and 20 keV $(\text{H}_2\text{O})\text{Ar}_{2000}^+$ [25]–[27].	228

## List of Equations

Equation 2.1.....	32
Equation 2.2.....	32
Equation 2.3.....	33
Equation 2.4.....	39
Equation 3.1.....	92
Equation 3.2.....	97
Equation 3.3.....	100

## Abbreviations

3xTg-AD	Triple-transgenic mouse model of Alzheimer's disease
ACE	Angiotensin-converting Enzyme
AD	Alzheimer's disease
APP	Amyloid precursor protein
A $\beta$	Amyloid-beta
BTLE	Brain total lipid extract
CNS	Central nervous system
Cer	Ceramide
Chol	Cholesterol
CMC	Carboxymethyl cellulose
DAG	Diacylglyceride
DC	Direct current
DESI	Desorption electrospray ionisation
DMD	Duchenne muscular dystrophy
DMSO	Dimethyl sulfoxide
DPPC	Dipalmitoylphosphatidylcholine
ESA	Electrostatic analyser
FAD	Familial Alzheimer's disease
FTIR	Fourier transform infrared spectroscopy
GalCer	Galactosylceramide
GCIB	Gas cluster ion beam
H&E	Hematoxylin and eosin
HPLC	High-performance liquid chromatography
ITO	Indium tin oxide-coated
LMIG	Liquid metal ion gun
MALDI	Matrix assisted laser desorption/ionisation
MAPT	Microtubule-associated protein tau
MD	Molecular dynamics
ME-SIMS	Matrix-enhanced secondary ion mass spectrometry
Met-A-SIMS	Metal-assisted secondary ion mass spectrometry
MRSI	Magnetic resonance spectroscopic imaging
MS	Mass spectrometry
MSI	Mass spectrometry imaging

MS-MS	Tandem mass spectrometry
NAFLD	Non-alcoholic fatty liver disease
OCT	Optimal cutting temperature compound
PC	Phosphatidylcholine
PCA	Principal component analysis
PE	Phosphatidylethanolamine
PI	Phosphatidylinositol
PS	Phosphatidylserine
PSEN 1	Presenilin 1
PSEN 2	Presenilin 2
RF	Radio-frequency
ROI	Region-of-interest
SAC	Sample analysis chamber
SED	Secondary electron detector
SEM	Scanning electron microscope
SIMS	Secondary ion mass spectrometry
SM	Sphingomyelin
ST	Sterol lipid
TAG	Triacylglyceride
TFA	Trifluoroacetic acid
ThioS	Thioflavin S
TIC	Total ion count
ToF-SIMS	Time-of-flight secondary ion mass spectrometry
WT	Wild type

# Abstract

The University of Manchester

Candidate's name: Irma Berrueta Razo

Degree title: Doctor of Philosophy

Thesis title: Molecular imaging of mouse brain tissue using Cluster Time-of-Flight Secondary Ion Mass Spectrometry

September 2015

ToF-SIMS imaging has been drawing attention due to the wide range of applications in the biological and biomedical fields. These applications include the acquisition of quantitative and qualitative data that ranges in scale from single cells to organs, image visualisation and interpretation of biomarkers for diagnosis and development of pharmaceuticals.

This study focused on molecular imaging of mouse brain tissue sections using cluster primary ion beams. First, cluster ion beams were applied to comparative background studies of biomolecules and brain total lipid extract. Enhancement of the secondary ion signal was observed using water-containing cluster primary ion beams, especially for  $[M+H]^+$  type secondary ions.

Water-containing clusters were then used to acquire ToF-SIMS images from the cerebellar area of serial mouse brain tissue sections. Again, water-containing cluster beams produced the highest secondary ion yields in both grey and white matter, gaining a new level of insight into the lipid compositions of both types of tissue in the brain.

A clinical case was also evaluated with ToF-SIMS imaging, using cluster beams for the analysis of 3xTg-AD mouse brain tissue. SIMS images were registered with fluorescence microscopy images for the *in situ* identification and co-localisation of the Amyloid- $\beta$  plaques on the SIMS images. Spectra from regions of interest were analysed to identify possible ion fragments derived from the A $\beta$  protein. The co-localisation of cholesterol was also studied from images obtained with different primary ion beams.

The results presented show that cluster ToF-SIMS can be successfully applied to brain tissue imaging. New primary ion beam technologies allow us to acquire data with more useful secondary ion yield for clinical applications and biological research. Nevertheless, future technological improvements are required for specialised applications e.g. cellular imaging. Moreover, processing the data obtained is still challenging and more data processing tools are also needed for interpretation.

## Declaration

No portion of the work referred to in the thesis has been submitted in support of an application for another degree or qualification of this or any other university or other institute of learning.

## Copyright Statement

i. The author of this thesis (including any appendices and/or schedules to this thesis) owns certain copyright or related rights in it (the "Copyright") and s/he has given The University of Manchester certain rights to use such Copyright, including for administrative purposes.

ii. Copies of this thesis, either in full or in extracts and whether in hard or electronic copy, may be made **only** in accordance with the Copyright, Designs and Patents Act 1988 (as amended) and regulations issued under it or, where appropriate, in accordance with licensing agreements which the University has from time to time. This page must form part of any such copies made.

iii. The ownership of any patents, designs, trademarks and any and all other intellectual property rights except for the Copyright (the "Intellectual Property Rights") and any reproductions of copyright works, for example graphs and tables ("Reproductions"), which may be described in this thesis, may not be owned by the author and may be owned by third parties. Such Intellectual Property Rights and Reproductions cannot and must not be made available for use without the prior written permission of the owner(s) of the relevant Intellectual Property Rights and/or Reproductions.

iv. Further information on the conditions under which disclosure, publication and commercialisation of this thesis, the Copyright and any Intellectual Property and/or Reproductions described in it may take place is available in the University IP Policy (see <http://documents.manchester.ac.uk/DocuInfo.aspx?DocID=487>), in any relevant Thesis restriction declarations deposited in the University Library, The University Library's regulations (see <http://www.manchester.ac.uk/library/aboutus/regulations>) and in The University's policy on Presentation of Theses.

## Acknowledgements

I would like to acknowledge the Mexican council of science and technology (CONACYT) for funding my PhD studies with the studentship number 214961.

I would like to thank my supervisors at the University of Manchester Dr Nick Lockyer and Professor John Vickerman for their guidance and support during my PhD project.

I am very grateful for all the support received from present and former group members of the surface analysis research centre (SARC). Special thanks to Dr Sadia Sheraz for providing guidance and training, Taylor Kohn for his help in sample handling and preparation and Giles Edwards for his advice on instrumentation issues. Many thanks to Dr Alex Henderson for all the advice and help provided for data processing.

Thanks to Dr Herve Boutin for the mouse brain samples provided for this project as well as advice. Thanks to Dr Duncan Forster and Fiona Henderson from the Wolfson Molecular Imaging Centre (WMIC) for the training in brain sample preparation. I would like to acknowledge Professor Peter Gardner and the members of his lab for facilitating the use of equipment. I am also grateful to Professor Andrew Doig and Maria Priscila del Castillo Frias for providing peptide samples.

Last but not least, I am truly grateful to my family and friends from Mexico and Manchester. Thanks to Nick O'Meara for providing unconditional support and advice. I could not have done it without their love and support.



# 1 Introduction

Chemical imaging, in particular mass spectrometry imaging, has been drawing attention due to the wide range of applications in the biological and biomedical fields. These applications include image visualisation and interpretation of biomarkers for diagnosis, development of pharmaceuticals for therapeutic purposes and acquisition of quantitative and qualitative information that ranges in scale from cellular to whole small animals such as mice [1]–[5].

Mass spectrometry imaging (MSI) offers unique capabilities, including the detection of molecules *in situ* from the surface of samples [3], [6]–[8]. Time-of-Flight secondary ion mass spectrometry (ToF-SIMS) imaging is a MSI technique capable of providing images with high spatial resolution. It involves the ionisation of sputtered molecules and their fragments from a sample under primary ion beam bombardment and operates with a time-of-flight analyser [9]–[11], as illustrated in Figure 1.1 .

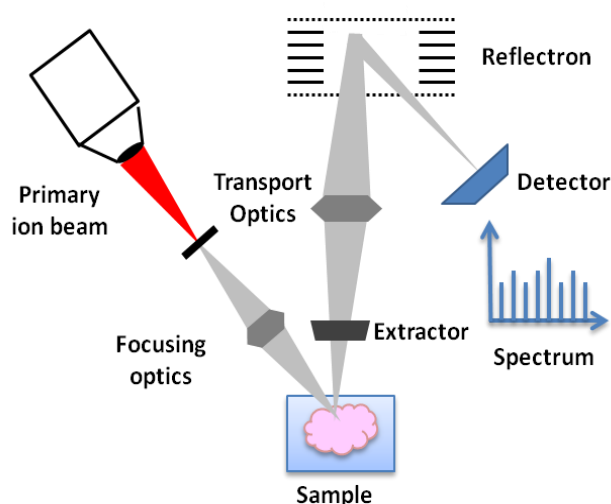


*Figure 1.1: Schematic of ToF-SIMS imaging of tissue. The sample is probed with a primary ion beam, desorbing secondary ion particles from the surface. Secondary ions are extracted into a time-of-flight tube where the ions fly according to their masses before reaching the detector [11].*

ToF-SIMS can image biological surfaces with spatial resolution up to 400 nm and with a mass accuracy comparable to <5 ppm. In ToF-SIMS, samples are label-free and do not require preparation with complex protocols [9], [11]. Along with the advantages associated with the technique, there are also significant challenges to overcome. The low secondary ion yield and matrix effects observed in biological samples are important issues that limit the scope of ToF-SIMS in the biomedical field [7]. These

issues are discussed later in section 2.5.6. Efforts from the SIMS community to try to increase the low secondary ion yield obtained from biological samples include the addition of metallic nanoparticles, MALDI type matrix compounds that aid the formation of cations and the analysis of samples under frozen-hydrated conditions [11]–[15].

## 1.1 Aim of the study

In light of previous studies focused on the addition of water during the analysis to increase the proton ionisation [28], [58], [200], [201], the research presented in this thesis studies the application of a prototype gas cluster ion beam (GCIB) capable of providing  $\text{Ar}_n^+$ ,  $(\text{H}_2\text{O})_n^+$  and  $(\text{H}_2\text{O}) \text{Ar}_n^+$  clusters for brain tissue imaging. The experiments presented include comparative studies applying different primary ion cluster beams on model compounds and mouse brain. More importantly, cluster beams which provided the highest secondary ion yields were then applied to 2D molecular imaging of mouse brain tissue. A medical case is likewise explored with ToF-SIMS and Fluorescent microscopy, the multi-modal imaging of a transgenic mouse model infected with Alzheimer's disease.

The development of an experimental protocol for 2D imaging and characterisation of mouse brain tissue sections was performed using the Ionoptika J105 – 3D Chemical Imager ToF-SIMS instrument. Background studies on spin-coated films of model bio-compounds such as L-arginine, human angiotensin II, D-(+)-trehalose dehydrate, dipalmitoylphosphatidylcholine (DPPC) and brain total lipid extract (BTLE) provided an insight into the secondary ion yields obtained when using clusters of different composition, size and energy as primary ion beams. The analysis beams that provided the best results were then applied to mouse brain imaging.

Imaging experiments carried out on mouse brain samples aimed to study the advantages and limitations of gas cluster analysis beams, particularly  $(\text{H}_2\text{O})_n^+$  clusters and establish reliable experimental parameters. Biological tissue models are particularly complex to characterise with ToF-SIMS due to their insulating nature and the low yield obtained with most analysis beams; hence the need for technology capable of providing more chemical information and better spatial resolution. Moreover, multi-modal imaging is explored as a biomedical application in the study of Alzheimer's disease. The causes of this pathology still remain unknown and the detection of biomarkers with MSI is still under intensive research. The composition of amyloid- $\beta$  ( $\text{A}\beta$ ) aggregates was studied *in situ* on a triple-transgenic mouse model of

AD (3xTg- AD) using  $(\text{H}_2\text{O})\text{Ar}_{2000}^+$  and  $\text{C}_{60}^+$  clusters in high spatial resolution ToF-SIMS images. The co-localisation of plaques was obtained by correlating fluorescent microscopy and ToF-SIMS images from the same sample. Images from both techniques were then registered to obtain the location of the plaques. This experiment aimed to identify diagnostic fragment ions from the  $\text{A}\beta$  aggregates thus gaining more information about the disease.

## 2 Literature review

### 2.1 Secondary ion mass spectrometry (SIMS)

Secondary ion mass spectrometry (SIMS) is a surface-sensitive technique used in the analysis of ionised particles (or secondary ions) desorbed from the surface of a sample after primary ion bombardment. The primary particles can be monatomic, polyatomic or clusters e.g.  $\text{Ar}_n^+$ ,  $\text{C}_{60}^+$ ,  $(\text{H}_2\text{O})_n^+$ ,  $\text{Au}_n^+$ ,  $\text{Bi}_n^+$ ,  $\text{Ga}^+$  [11], [20]. Emitted secondary ions are extracted and enable chemical analysis of the surface, as shown in Figure 2.1.

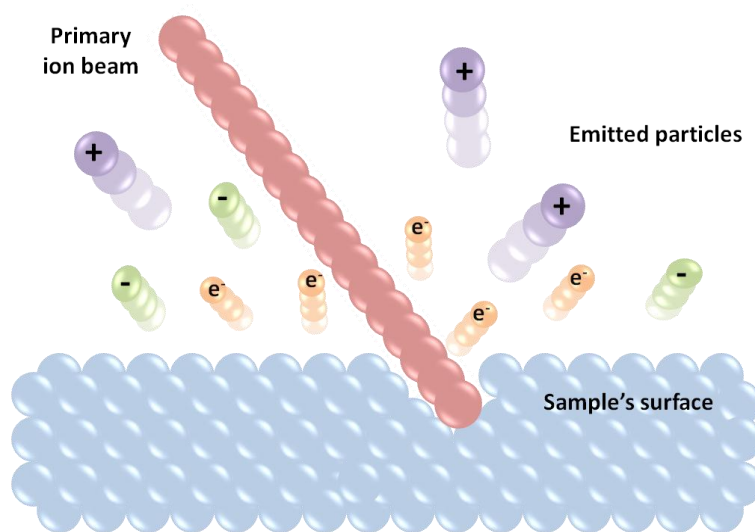


*Figure 2.1: Schematic of the desorption-ionisation process in SIMS. A primary ion beam is scanned across the sample's surface. During this process, the analysis beam breaks bonds and causes desorption of multiple species. The majority of species emitted are neutral atoms (not included in the diagram) or molecules and only a small number of them are charged. The size of the primary ion beam is much larger in reality [16].*

#### 2.1.1 SIMS basic experimental parameters

The ionisation of secondary particles occurs when they are emitted from the surface. Consequently, the electronic state of the analyte will have an effect on the secondary

ion generation which makes quantitative analysis difficult [17]. The basic equation in SIMS can be described as shown in Equation 2.1 [17]:

*Equation 2.1*

$$I_m = I_p \gamma_m \alpha^+ \theta_m \eta$$

Where  $I_m$  is the secondary ion current from the sample  $m$ ;

$I_p$  is the primary ion flux;

$\gamma_m$  is the sputter yield;

$\alpha^+$  is the positive ion ionisation probability;

$\theta_m$  is the fractional concentration of the chemistry  $m$  on the surface layer of the sample;

$\eta$  is the transmission of the analysis system

The parameter  $\gamma_m$  refers to the sputter yield of species  $m$ . The sputtered particles can be either neutral or ionic and their yield also increases with primary ion mass, energy and charge although not in a linear manner [17].

### **2.1.2 Damage cross section**

When a primary ion particle impacts a sample, its surface is significantly modified. Particles are desorbed generating neutral and charged particles as well as fragments derived from the molecular structure of the sample [17]–[19]. The damage caused by primary ions can be characterised by estimating the size of the area modified by the impact. This measurement is called damage cross-section ( $\sigma$ ). Damage-cross section can be defined as the average size of the surface area per single ion impact from which the analysed sputtered ions are excluded [17].

A primary ion beam of several keV of energy can cause damage of several nanometres around its impact point, depending on the chemistry of the sample and the nature of the primary particles. The secondary ion intensity is related to damage cross-section; this relation can be described using Equation 2.2 [23] :

*Equation 2.2*

$$I_m = I_{m0} \exp(-\sigma I_p)$$

Where  $I_m$  is the secondary ion current from sample  $m$  after primary ion irradiation;

$I_{mo}$  is the initial secondary ion yield of  $m$  and  $I_p$  is the primary ion flux.

The parameter  $\sigma$  determines the surface area modified with each impact. The secondary ion yield from  $\sigma$  will indicate the efficiency ( $E$ ). Efficiency can be defined as the number of secondary ions detected when the whole sample surface is bombarded [18], [19]. Under static conditions, secondary ion species arise from different impact points, retaining the molecular information by never striking the same place twice.  $\geq 10^{13}$  impacts/cm<sup>2</sup> would affect all of the atoms from the topmost layer of the specimen, thus the static limit is determined by a primary ion dose  $< 10^{13}$  ions/cm<sup>2</sup>.

The primary ion dose can be calculated with the following equation [19]:

*Equation 2.3*

$$\text{Primary ion dose} = \frac{I_p t}{A}$$

Where  $I_p$  is the primary ion flux (ions/s);  $t$  is the analysis time (s); and  $A$  is the analysis area (cm<sup>2</sup>). To specify primary ion doses, the analysis areas are specified in cm since that unit is commonly found in the SIMS literature.

## **2.2 SIMS methodologies**

### **2.2.1 Static SIMS**

When a flux of ions impacts a surface, the ions transfer energy to the atoms of the specimen causing a cascade of collisions. These collisions result in the emission of particles from the surface, some of which are charged when desorbed [10],[11], as shown in Figure 2.2, (A). Each emitted ion is a molecule or fragment of the sample's molecular structure and will be recorded as an ion peak in the mass spectrum.

In static SIMS, the flux of primary ions is limited to a dose less than or equal to the static limit ( $10^{13}$  ions cm<sup>-2</sup>) so that less than 1% of the sample's topmost layer of atoms is bombarded by the primary ion beam. This condition minimises the damage to the structure of the sample and limits the area of desorption to a maximum of 10 nm<sup>2</sup> per primary ion impact. For surface analysis purposes, this ensures that sputtered particles are emitted from an area that has not experienced previous bombardment [11],[16],[17].

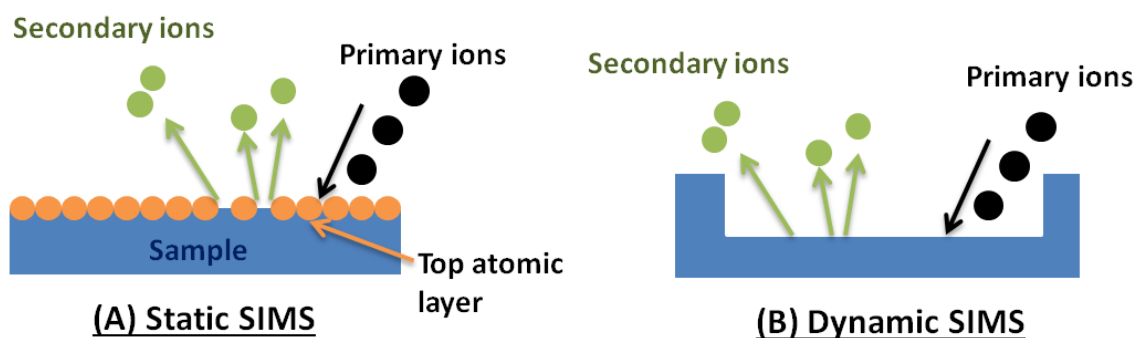


Figure 2.2: The two modalities in SIMS. (A) Static mode provides information about the outermost atomic layer of the sample. (B) Dynamic mode uses high primary ion dose to remove material to obtain 3D information resulting in the formation of an etched crater [16].

### 2.2.2 Dynamic SIMS

The dynamic SIMS mode relies on the study of the sub-surface of a matrix. Whereas static SIMS only investigates the uppermost atom layers of a sample, the dynamic mode involves the analysis of the specimen under ion irradiation as a function of depth, as illustrated in Figure 2.2 (B) and Figure 2.3. This experimental approach enables the characterisation of three-dimensional chemical distribution and structural changes under high primary ion beam exposure [10], [11], [20].

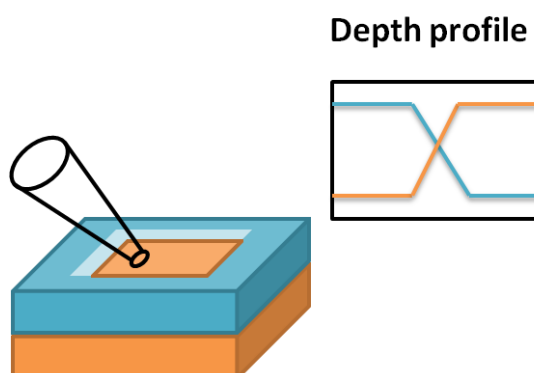
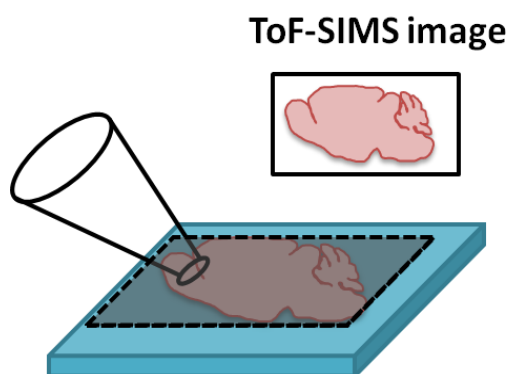


Figure 2.3: Schematic illustrating the dynamic SIMS method. This approach obtains information from the variation of the chemical composition below the surface [11].

### 2.2.3 Molecular imaging with SIMS

The aim of SIMS imaging is to obtain a compositional image by rastering a primary ion beam across a sample's surface, as illustrated in Figure 2.4. Each pixel from the image corresponds to spatial coordinates and has an associated mass spectrum. The brightness of each pixel is given by the secondary ion intensity detected in each mass spectrum. In this technique, the primary ion flux and spot size will be limited by the

type of primary ion beam applied to the analysis. The image could be acquired with a primary ion dose beyond the static limit to maximise the ion yield obtained per pixel [7], [9]–[11], [21]. One of the main challenges is to obtain both high spatial resolution and high sensitivity in order to detect intact molecules over a wide mass range [11], [22], [23].



*Figure 2.4: Illustration of SIMS imaging. The primary particles are scanned in X and Y directions to obtain chemical map where each pixel corresponds to a mass spectrum [7].*

Molecular images can also be acquired which have compositional information as a function of depth. SIMS 3D-imaging is now attracting more attention since it is capable of generating 3D high spatial resolution images with chemical specificity. It is applied to biological systems to study their structure and major components [9], [10], [24]. Figure 2.5 shows a depth profile in the cerebellum area of a mouse brain section. This experiment shows the initial image (A) and the removal of material after depth-profiling a smaller region resulting in an etched crater (B).

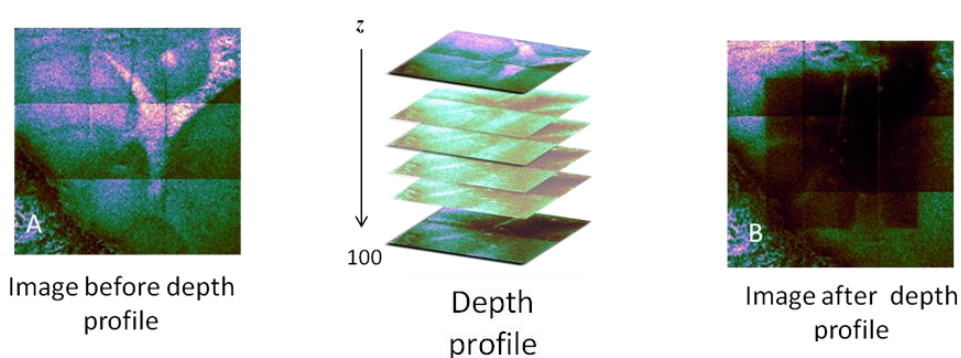


*Figure 2.5: ToF-SIMS 3D-imaging of the cerebellum area of a mouse brain section with sagittal orientation. A small region from this region was depth-profiled by acquiring one hundred 2D-images until enough material was removed to generate an etched crater. (A) Initial total ion image acquired with 40 keV  $C_{60}^+$  of the cerebellum area. (B) Total ion image of the same area after depth profiling.*

## 2.3 ToF-SIMS

The material desorbed from a sample's surface during SIMS is very little, especially if the sample is analysed in static mode. Thus, Time-of-Flight (ToF) analysers were successfully coupled in SIMS systems since the late 1980's to increase the efficiency and decrease the amount of lost information. The high sensitivity of ToF analysers lead to the application of ToF-SIMS in molecular imaging using focused primary ion beams [25]. A summary of the primary ion beams applied in ToF-SIMS is included in the following section.

### 2.3.1 Analysis beams used in ToF-SIMS

The primary ion beam used in a ToF-SIMS experiment will determine important analytical parameters, including spatial resolution, damage-cross section and secondary ion yield [7], [8], [10], [25], [26]. The desired characteristics of a primary ion beam will be determined by the type of experiment to be acquired. For example, high spatial resolution and good mass accuracy might be needed for biological imaging, while the analysis of semiconductors may only require an elemental mass range but higher mass resolution [26]. The accessible mass range, among other factors, can be limited by the size of molecules sputtered during the desorption process as well as the instrumentation used for analysis [27].

A primary ion beam usually contains several keV of energy (5- 30 keV). If more atoms or molecules are contained in the projectile, the energy per atom/molecule will be less. Consequently, the energy deposited on the sample's surface after the collision will remain closer to the topmost atomic layer. Sputtered particles will be generated as a consequence of the energy deposition on the solid's surface. If the projectile penetrates too deep from the surface, fewer particles will be ejected and ionised for detection. Furthermore, higher energy per atom/molecule will induce more damage to the structure of the analyte and more fragments will be emitted instead of intact molecules, restricting the accessible mass range [26].

Monoatomic and polyatomic liquid metal ion guns e.g.  $\text{Cs}^+$ ,  $\text{Au}_n^+$ ,  $\text{Ga}_n^+$ ,  $\text{Bi}_n^+$  deliver the highest spatial resolution ( $\sim 50$  nm) although they contain high energy per atom, causing significant bombardment-induced damage. Polyatomic ion beams such as  $\text{SF}_5^+$  and  $\text{C}_{60}^+$  cause reduced damage to the matrix. However, the spatial resolution for biological imaging obtained with  $\text{SF}_5^+$  and  $\text{C}_{60}^+$  is lower [7], [26]. Nowadays, the beam diameter of a 40 keV  $\text{C}_{60}^+$  beam can be focused down to 500 nm [6], [28], [29].



With the introduction of giant gas cluster ion beams such as  $\text{Ar}_n^+$ , the damage induced by each collision was ameliorated and secondary ion yields are enhanced. Clusters containing thousands of atoms or molecules are currently used for analysis, especially since experiments are no longer limited to static limit conditions [21], [29]–[33]. Nowadays, the scope of GCIB sources has expanded to the use of hydrogen-containing molecules to form giant clusters such as  $(\text{H}_2\text{O})_n^+$  or the doping of argon clusters with compounds like  $\text{CH}_4$ . It has been demonstrated that the presence of hydrogen enhances the secondary ion yield of protonated intact molecules [35], [36]. The biggest challenge for gas clusters is their low spatial resolution which at the moment is still in the order of microns due to limitations in instrumentation ( $\sim 4 \mu\text{m}$  [35]). This is explained in detail in section 3.5.2.

### 2.3.2 Physics of polyatomic projectiles

#### 2.3.2.1 Molecular dynamics

Molecular dynamics (MD) computer simulations provide a representation of the interaction between the energetic particles from the primary ion beam and the sample's atomic structure. These simulations explain the energy-transfer process that occurs after the projectile impacts the surface [37]–[39]. MD simulations have shown that an atomic projectile induces an atomic collision cascade when it hits the surface of a sample. On the other hand, cluster ion beams initiate a motion in the sample, which resembles a meteor impacting a surface [40]. The effect of atomic, polyatomic and cluster projectiles are shown in Figure 2.6. The average yields are also included in this figure (Figure 2.6, 3<sup>rd</sup> row from top to bottom) to visualise the effect of each projectile. Gallium (Ga) is the monoatomic projectile that produces the lowest secondary ion yield, thus, numerous impacts are required to produce useful data. Ga produces a collision cascade with each impact and penetrates the sample  $\sim 5.2 \text{ nm}$ . In contrast, when  $\text{C}_{60}$  hits the surface, most of its kinetic energy is deposited close to the surface, ejecting energised particles and producing higher secondary ion yield than Ga ( $> 3.5 \text{ nm}$  from the surface) [41].

The effects of  $\text{Au}_3$  are similar to those caused by Ga, although the penetration of this projectile is less deep.  $\text{Au}_3$  also yields more secondary particles than Ga, since the energy is deposited closer to the surface, allowing ejection of more material. When the  $\text{Ar}_{872}$  impacts the surface, the atoms present in the cluster form a cloud that prevents the ejection of the particles close to the surface. Once this cloud disappears, particles from the surface are ejected [41]. The argon cluster has lower energy per atom than

$C_{60}$ , but with the same kinetic energy. Hence,  $Ar_{872}$  has a gentler interaction with the atoms in the sample, causing less fragmentation of the material when compared to  $C_{60}$  [42], [43].

Argon clusters can be generated with a wide range of sizes. In general, the yield produced by  $Ar_n$  clusters depends on both kinetic energy and cluster size [42]–[45]. This dependence and its impact on the sputtering yield has been studied and parameterised by different SIMS groups [46], [47].

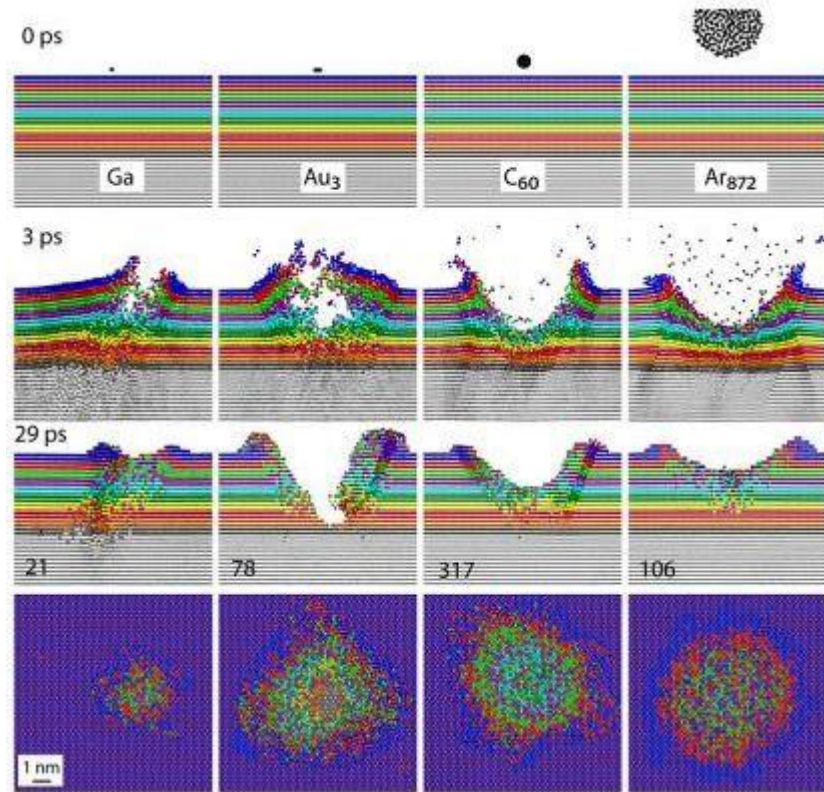


Figure 2.6: MD simulations of atomic, polyatomic and cluster bombardment on Ag (111) substrate. The projectiles used are 15 keV Ga,  $Au_3$ ,  $C_{60}$  and  $Ar_{872}$ . The top row of images shows 1.5 nm of the atoms from the sample. The substrate has an interlayer spacing of 0.23 nm. The light grey region starts after a depth of 4.6 nm. The following two rows (from top to bottom) of images, shows the effects of the projectile impacts after 3 ps and 29 ps. The numbers included on the third row of images relate to the average secondary ion yields calculated from 32 impacts in the case of Ga and 16 impacts for  $Au_3$ ,  $C_{60}$  and  $Ar_{872}$ . The bottom row of images displays the damage caused by the projectiles on the bombarded areas viewed from the top down. Reproduced with permission from reference [41].

### 2.3.2.2 Kinetic energy in a polyatomic ion beam

Polyatomic ion beams distribute their total incident energy among the atoms present in the projectile. This energy can be calculated with the following equation:

#### Equation 2.4

$$E/\text{atom or molecule} = \frac{\text{Beam energy}}{\text{Number or atoms or molecules}}$$

For instance, each atom from a 40 keV  $\text{C}_{60}^+$  ion beam will have 666.6 eV of kinetic energy.

This  $E/\text{atom}$  is higher than the energy needed to break a single C-C bond ( $\sim 3.6$  eV). Hence, the atoms in this projectile disassociate with the impact, causing sixty separate collisions of 666.6 eV on the sample's surface. The sputtering and damage are considerably different than monoatomic projectiles, since the incident energy of several atoms is deposited over a larger area [30], [48], as shown in Figure 2.6.

The energy of a primary ion beam can also be visualised as energy per nucleon. A nucleon can be defined as one of the particles found in the atom's nucleus i.e. protons and neutrons. Their energy can be defined with the equation below:

$$\frac{E}{\text{nucleon}} = \frac{E/\text{atom or molecule}}{\text{Atomic mass number}}$$

In a gas cluster composed by several atoms or molecules, each particle will have a specific energy or  $E/\text{atom}$  or  $E/\text{molecule}$  [48]. The kinetic energies will vary from meV to several eV. If the kinetic energy is  $> 1$  eV, this energy is the same order as the energy found in covalent bonds. A study by Moritani *et al.* [48] showed that by selecting the size of  $\text{Ar}_n^+$  clusters, the fragmentation produced by the analysis of a polystyrene thin film was dependant on the cluster's kinetic  $E/\text{atom}$ . They also showed that by controlling the  $E/\text{atom}$ , the dissociation of energy could be specific for a certain bond in the sample's molecular structure [49].

### 2.3.3 Time-of-Flight mass analysers

There is an increasing variety of commercially available ToF-SIMS systems comprising diverse primary ion sources [28], [50], [51]. After secondary ions are generated, they have to be separated according to their masses. In mass spectrometry, a mass analyzer measures the mass-to-charge ratio ( $m/z$ ) of an ion [52]; the separation of masses can be based on different principles e.g kinetic energy, velocity, momentum.

A ToF analyser measures the  $m/z$  of ions according to their velocity, requiring their generation in bunches and allowing their simultaneous transmission [52], [53]. This type of mass analyser has evolved over the years with the implementation of delayed

extraction and the introduction of the reflectron. However, the analysis of particles from continuous ionisation is currently possible with the introduction of orthogonal acceleration techniques [52], [53]

The ToF analyser concept was introduced in 1946 by Stephens [54] and was later developed into the first commercial linear ToF mass spectrometer by Wiley and McLaren in the 1950's [55]. ToF mass spectrometers can be linear type, coupled with reflectrons or orthogonal injection. In linear ToF systems, ions are accelerated by an electric field and drift in the flight tube according to their masses directly into the detector. This mass analyser allows very fast data acquisition with high sensitivity but poor mass resolution [52].

Implementation of a reflectron is a way to improve mass resolution in a ToF system. A reflectron is an optical device that deflects the ions, creating a retarding field [52]. If a packet containing ions with a given  $m/z$  but different kinetic energies, the reflectron compensates for the spread in the flight times of the ions, due to different kinetic energies. According to their complexity and characteristics, reflectrons are classified into three main types: single-stage, two-stage and non-linear (higher order) [52], [53].

To improve the ion formation time and extraction, the delayed extraction mode is used in conventional ToF-SIMS instruments [52], [56]. Pulsed delayed extraction introduces a time lag between the ion formation and the ion extraction. A conventional SIMS instrument, like the BioToF-SIMS instrument (Kore Technology Ltd, Cambridgeshire), comprises a ToF tube with a reflectron at the end of the field-free region and operates with a delayed extraction system. With this configuration, a short primary ion beam pulse impacts a surface; then there is a time delay for secondary ion formation and finally the extraction is triggered. The primary ion beam pulse and the extraction time can be extended to improve mass resolution. For example, short beam pulses are chosen to maximise the extraction time and improve mass resolution, although this results in poor spatial resolution [25], [56].

A new configuration for SIMS instruments result by decoupling the mass analyser and the sputtering process. With this new configuration, mass spectra are not influenced by primary ion beam conditions or the sample's topography. This allows acquisition of data with both, high mass resolution and high spatial resolution. Moreover, the analysis can be performed with a primary ion beam on DC mode, leading to fast data acquisition in 2D and 3D [57], [58]. A new SIMS instrument with these characteristics, the J105-3D chemical imager, was developed by the SIMS group in Manchester in collaboration with

Ionoptika Ltd. This instrument comprises a specific type of arrangement with a ToF analyser orthogonally mounted after a quadrupole and an electrostatic analyser [58]. After primary ion beam bombardment, the secondary ions are extracted and collisionally cooled in a quadrupole. Once cooled, the secondary ions are electrostatically filtered in an electrostatic analyser, before being orthogonally injected into a linear buncher. A packet of ions is then generated by the buncher. This tight ion packet will determine the mass resolution, in the same way the primary ion pulse determines the mass resolution in delayed extraction mode. This ion packet enters the quadratic field ToF analyser, where the ions will travel according to their masses and charge [52], [57], [58]. Details of the J105-3D chemical imager are explained in chapter 3.

## **2.4 Data processing for ToF-SIMS**

ToF-SIMS experiments can generate a great amount of data, depending of the type of analysis performed. The extraction of specific information from the spectra can be a complex task, especially when analysing large data sets. The implementation of multivariate analysis techniques for data reduction and comparison is essential for quantitative analysis. Qualitative interpretation can be carried out by focusing on the correlation between the chemistry of the sample and the detected secondary ions represented on the mass spectrum [59].

### **2.4.1 Multivariate analysis**

Information obtained from SIMS data can be very detailed and challenging to interpret. Advances in instrumentation and improvement in mass resolution, sensitivity and acquisition speed are reflected in the vast amount of data collected from a single experiment [10], [60]. Many researchers choose to employ statistical approaches to reduce the complexity of the data analysis. Advanced variate statistical methods are normally used to study ToF-SIMS spectra [59]. There are many multivariate algorithms available yet this section will focus on the multivariate technique applied to the work presented in this thesis: Principal Component Analysis (PCA).

#### **2.4.1.1 Principal component analysis (PCA)**

Principal Component Analysis (PCA) is a statistical method implemented to calculate the variance and expose strong patterns in a dataset by reducing the dimensions with minimal data loss [61]. ToF-SIMS data is multivariate: each experiment can contain multiple spectra and each spectrum has various mass channels with different signal

intensities. Thus, PCA is routinely used for simultaneous statistical analysis of all these variables. It is useful for the discrimination and classification of information based on differences in the spectra [60], [62].

Figure 2.7 explains PCA in a geometric projection. This projection includes a series of observations or data points from a three-dimensional data set (Figure 2.7, A). To describe the direction in which most variance can be found, the first three orthogonal principal components are drawn according to the variance within the data set (Figure 2.7, B) [60]–[62].

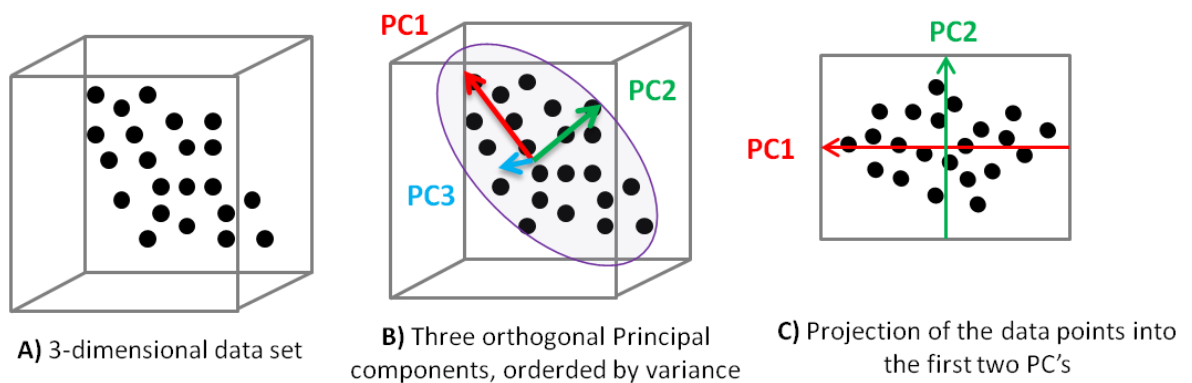


*Figure 2.7: Illustration of PCA geometric projection. (A) 3-dimensional data set with data points (observations). (B) Three orthogonal principal components generated according to the variance. (C) The projection of the data points into the first two principal components [26].*

The more the data points are spread out relative to the principal component, the larger the variance. For instance if we look at the projection of the first two principal components (Figure 2.7, C) the first principal component (PC1) has a larger variance compared to the second principal component (PC2). Unlike this example, principal components are not drawn with lines but calculated based on eigenvectors and eigenvalues. The direction of the principal component is given by a vector and the variance within the data set is given by an eigenvalue. Each eigenvector has a corresponding eigenvalue [60]–[62]. In Figure 2.7 there are three eigenvectors and three eigenvalues, one for each principal component.

PCA also applies dimensionality reduction to the data set. Reducing dimensions simplifies the information and makes interpretation more practicable [59]. This can be done by re-arranging and rotating the axes to the number of dimensions needed to represent the greater eigenvalues. The observations can then be projected onto the new axes called factors. This projection of factors onto the original variables is assigned

as loadings while the observations projected onto the factors are scores [11], [61], [63].

There are many approaches used for PCA but the work presented as part of this thesis will focus on PCA applied to image analysis.

#### 2.4.1.2 PCA applied to image analysis

Data obtained from ToF-SIMS images can be visualised as a cube (as shown in Figure 2.8). A SIMS image is a pixel map with X and Y coordinates where each pixel contains a mass spectrum and every spectrum contains a collection of mass channels. A single ion image is a matrix that contains values from a single mass channel [60], [61], [63].

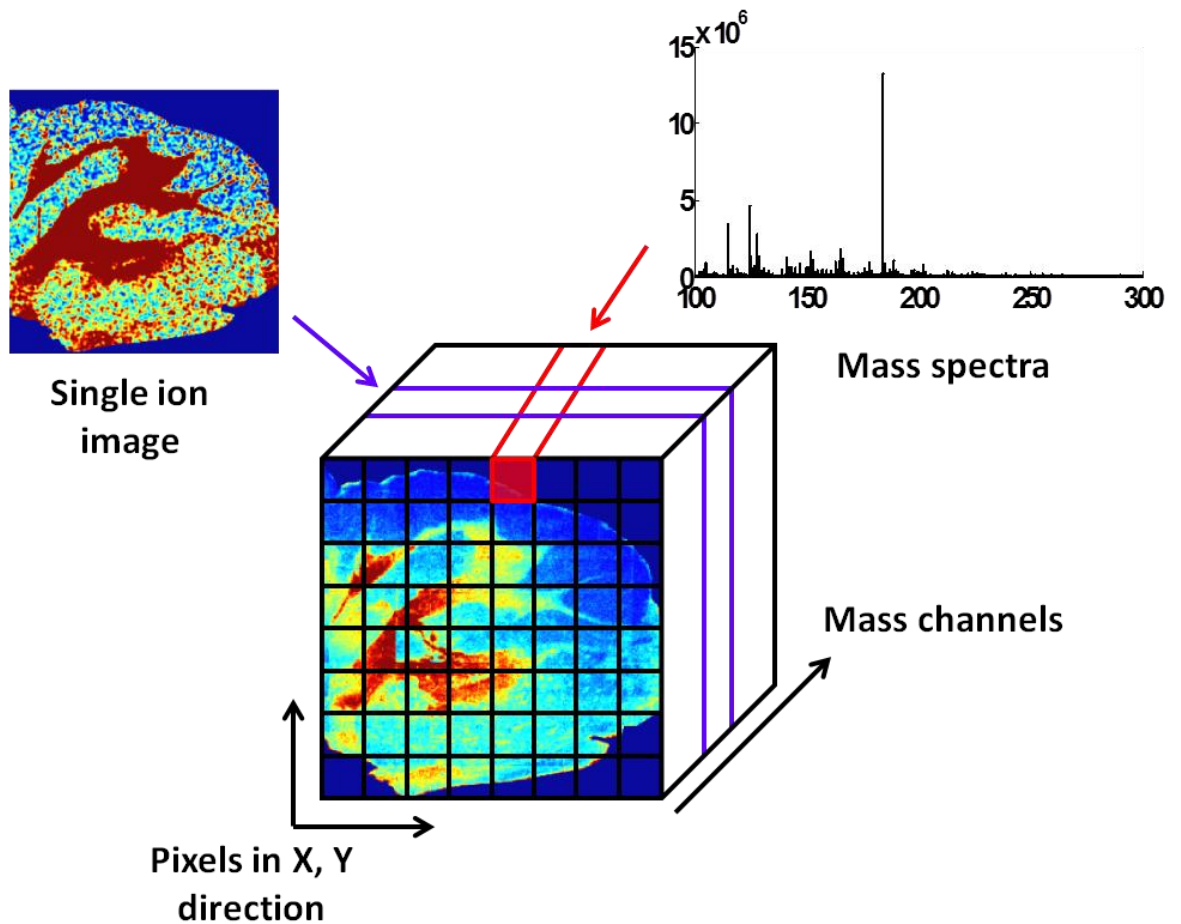


Figure 2.8: Data visualisation from a total ion image acquired with ToF-SIMS. The total ion image can be thought of as a data-cube [26], [27]. According to the size, both the sample and primary ion beam can be scanned in X and Y directions and a series of pixels projected. Each pixel is a mass spectrum containing thousands of mass channels and each channel can be displayed as a single ion image [61], [64].

In PCA analysis this data cube is rearranged into a two-dimensional data set, i.e. a series of vectors. Results from PCA analysis of these vectors are displayed in image scores. Each score is a density contour plot that shows the variance between each pixel i.e. the variance between mass spectra. Loadings are plots with positive or negative values obtained from the calculated variance of every pixel exposed in the scores [60], [63]. Figure 2.9 shows one score image and one loading plot from PCA analysis applied to the total ion image from Figure 2.8. In the score image, pixels with similar chemistry are coloured red or green according to their positive or negative loading value. Consequently, the score image highlights the chemical distinction between the grey matter and white matter of the brain cerebellum and the loadings indicate the ions (mass channels) present in each cerebral region.

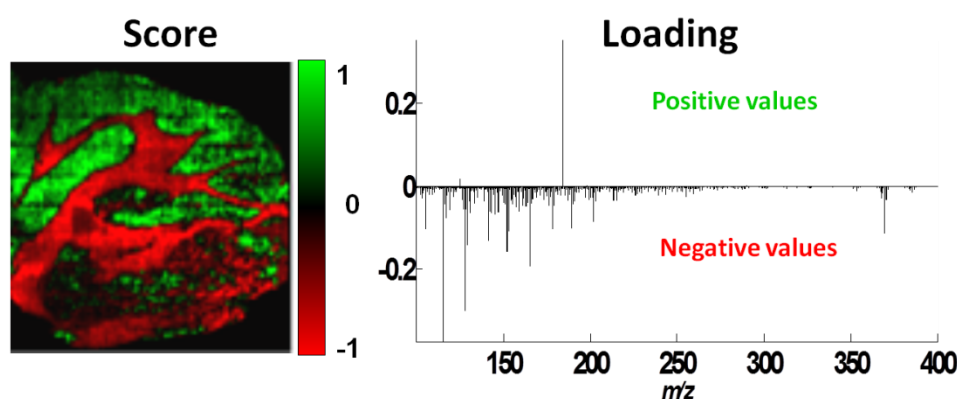


Figure 2.9: Score and loading result from the PCA analysis of the total ion image shown in Figure 2.8. The score image displays the chemical differences between the grey and white matter areas of the brain. The loading indicates which ions belong to each of these regions.

## 2.5 ToF-SIMS imaging of biological systems

The starting point for the application of ToF-SIMS within the biological field was the study of apolipoproteins back in 1986 [65]. Ever since, this technique has been used to study many other microscopic and macroscopic systems including cells and organs. This is likely due to instrumental developments, such as new primary ion sources capable of providing higher spatial resolution and new sample preparation methods implemented to keep the integrity of the sample under high vacuum [66].

There are many considerations for ensuring the successful analysis of biological systems. The ToF-SIMS imaging workflow is illustrated in Figure 2.10. Prior to analysis, the process requires the correct sample handling and preparation techniques since there are special requirements for maintaining the integrity of the material and for



avoiding molecule migration and biological decay [8], [21], [50]. Once the sample is prepared, the analytical conditions will be chosen according to the experimental design. For instance, the primary ion beam will be selected based on the objectives of study i.e. 2D or 3D analysis and the desired spatial resolution [11], [21], [67]. Once the sample has been analysed, the data is processed and interpreted. This involves applying statistical methods in order to obtain the required information, for example, applying principal component analysis (PCA) to emphasize the patterns of the variance within the data set. [62]. This section will review the contemporary ToF-SIMS imaging applications in biology and the considerations involved in this approach.

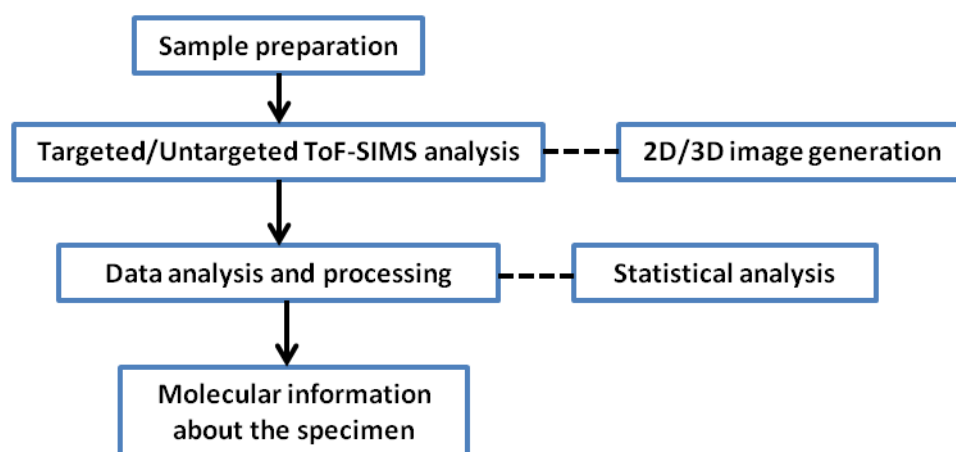


Figure 2.10: Workflow of a ToF-SIMS imaging experiment [67].

### 2.5.1 Complementary techniques in mass spectrometry imaging for the analysis of biological systems

Mass spectrometry imaging (MSI) is a powerful analytical tool capable of providing *in situ* chemical information and spatial distribution of a wide range of molecules without the need for sample labelling or extensive preparation protocols [3], [8], [25], [68]–[70]. Biomedical applications demand specialised instrumentation for the acquisition of data with high mass resolution, spatial resolution and mass accuracy. Fast acquisitions from large biological areas and robust data infrastructure are also preferred for better experimentation in MSI [67]. In addition to ToF-SIMS, other MSI techniques have proven to be successful for the analysis of bio-samples, such as Matrix-Assisted Laser Desorption Ionisation (MALDI) and Desorption Electro Spray Ionisation (DESI). These two techniques can detect molecules within the mass range occupied by proteins [3], [8], [21], [68]–[70]. Mass range and spatial resolution for SIMS, MALDI and DESI are compared in Figure 2.11. ToF-SIMS is capable of providing submicron spatial resolution  $\sim 50$  nm [26] whereas MALDI and DESI are capable of resolving

features as small as 10  $\mu\text{m}$  [70] and 50  $\mu\text{m}$  [71], [72], respectively. ToF-SIMS is certainly superior to MALDI and DESI in terms of spatial resolution, and the capability of analysing a single sample in 3D by depth profiling [1], [67]. However, SIMS is limited in the type of fragments and molecules it is able to study. MALDI and DESI are able to detect high mass molecules such as lipids and low-mass proteins or protein fragments, whereas SIMS is only able to detect elements, small molecules like lipids and some small peptides [73]–[76]. The analysis mass range for ToF-SIMS is usually below  $m/z$  2500 [11].

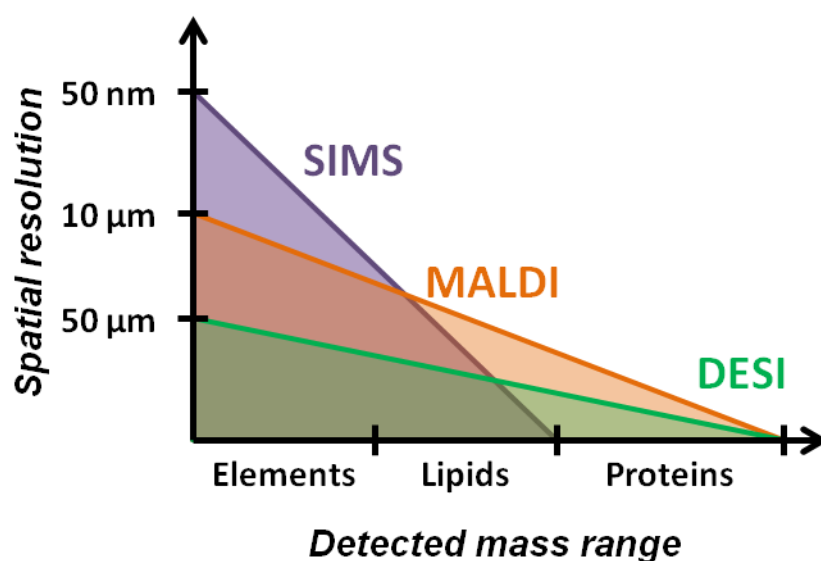


Figure 2.11: Diagram comparing three MSI techniques: SIMS, MALDI and DESI [76]. The chemical specificity for each technique is ruled by the mass range detectable for each method and it is divided into elements, lipids and proteins. Also shown are the best spatial resolutions currently available for (A) DESI [71], (B) SIMS [11] and (C) MALDI [70].

In MALDI imaging, a sample is covered with a matrix compound and it is probed with a laser beam in order to allow desorption and ionisation of molecules from the surface. The resulting ions are then transferred into a mass analyser, resulting in a chemical map of the sample [21], [63], [69], [70].

An example of the capabilities of MALDI imaging is displayed in Figure 2.12. This figure contains a MALDI image of a coronal mouse brain section (A and B) and mouse intestinal tract (C) acquired by Römpp *et al.* [70]. This image contains pixels with 5, 50 and 200  $\mu\text{m}$  and shows the distribution of two phospholipids in green and red.

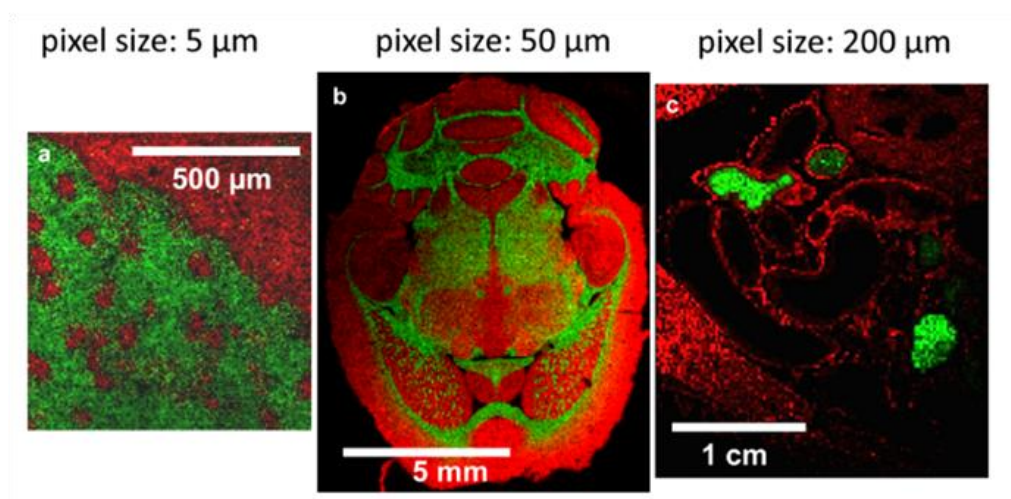


Figure 2.12: (A) MALDI image from a horizontal mouse brain section with a pixel size of 5  $\mu\text{m}$ . (B) Image of a horizontal mouse brain section acquired with a pixel size of 50  $\mu\text{m}$ . (C) Image of the intestinal tract of a rat with a pixel size of 200  $\mu\text{m}$ . The three images show the distribution of phospholipids in green and red. Reprinted with permission from reference [70].

DESI is a recently developed ambient ionisation technique. It works by ionising the surface of an analyte with an electrically charged spray under atmospheric pressure. Once generated, ions are directed to a mass spectrometer [21], [69], [75], [77], [78]. DESI is considered to be less challenging in terms of sample preparation and instrumental features. However, the effects of some of the parameters involved in analysis are still under research. The analysis is not carried out in vacuum and it has been increasingly applied to 2D and 3D imaging of biological tissues [79]. For example, DESI has been used for 2D lipid imaging leading to a 3D reconstruction of mouse brain serial sections as seen in Figure 2.13. This 3D model provides comprehensive information about the morphology of the lateral corpus callosum and its correlation with the distribution of lipids within the brain [79], [80].

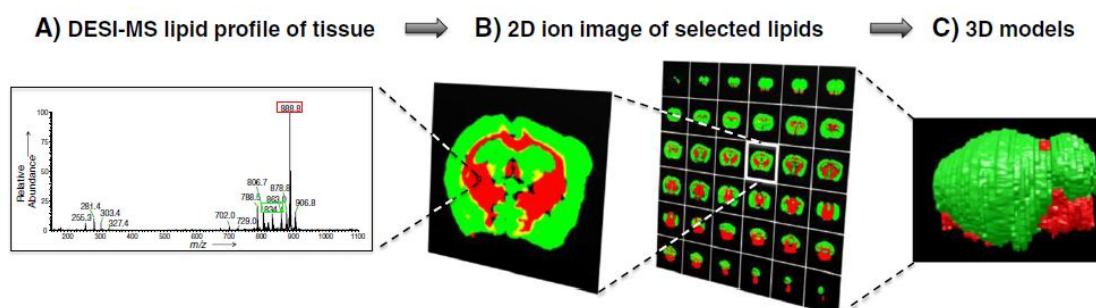


Figure 2.13: (A) DESI mass spectrum from a coronal brain section highlighting different lipid species. (B) 2D DESI image overlay of PS (40:6) at  $m/z$  834.4 in green and ST (24:1) at  $m/z$  888.8 in red. (C) 3D reconstruction of serial 2D images showing the spatial localisation of the ions highlighted in (B). Reprinted with permission from reference [79].

Interest in the application of ToF-SIMS to biomedical studies has been growing among bio-medical researchers[11], [21], [76], [78]. Examples of biological applications will be discussed in detail in the following section.

Despite its excellent sensitivity and spatial resolution, ToF-SIMS is limited to the detection of elements and small molecules such as lipids, drugs and metabolites. On the other hand, MALDI and DESI cover a broader range of molecules like protein fragments and nucleotides and it has been extensively applied to bio-medical and pharmaceutical research as well as biomarker discovery [76] [81]. However, proteins are not the only cell components. Recent biological studies have focused on the emerging field of lipidomics and researchers have employed SIMS to characterise cells and tissues, with ToF-SIMS benefiting from its unique sub-micron spatial resolution and mass accuracy [10], [11], [22], [76].

#### ***2.5.1.1 MSI imaging modalities***

Two acquisition modes can be distinguished in MSI: microprobe and microscope modes [69], [78]. Both modalities are shown in Figure 2.14. Microprobe mode is the most common mode in MSI. Here, the sample is probed with a desorption-ionisation beam and a mass spectrum is generated at each raster point. The focused beam moves relative to the sample position and an image is generated with a pixel size defined by the beam size. This approach allows the analysis of localised regions by focusing an ion beam (SIMS) or a laser (MALDI). One spectrum is recorded in each position or pixel and images of specific ions can be reconstructed. This mode is commonly employed in MALDI and SIMS [21], [69], [78], [81].

Contrastingly, microscope mode induces desorption-ionisation from the whole of the sample's surface. This mode does not require scanning the sample in different positions. Ions are extracted into an ion-microscope and imaged with a position-sensitive detector. This results in a mass-resolved projection which contains the spatial distribution of the ions. In this mode, the obtained spatial resolution is independent of the beam size and the lateral resolution will be dependent on the ion optics and the position-sensitive detector [78], [82]. The best spatial resolution observed in this imaging mode is 600 nm, although the analysis area is restricted to 400  $\mu\text{m}$ . This mode has been developed and applied to MALDI and DESI experiments since both techniques offer spatial resolutions in the micrometric range [80], [83].

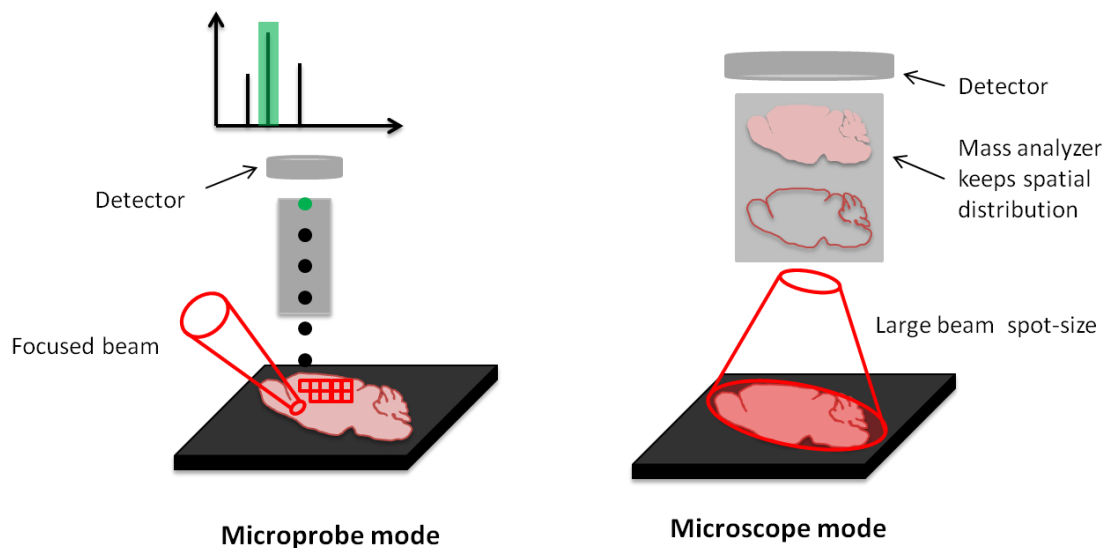


Figure 2.14: Microprobe and microscope imaging modalities for MSI [69].

#### 2.5.1.2 Multimodal MSI for characterisation of biological samples

When designing an MSI experiment, it is crucial to consider that all techniques have advantages and limitations. It is unlikely that a single technique will provide all the required information for targeted or untargeted analyses [4], [22], [68], [84]–[87]. Due to the complexity of biological systems, it is desirable to compare and complement data from different techniques to gain a better understanding of the specimen [84], [88], [89].

MSI has been applied to a vast number of tissue analyses, targeting the study of specific neurodegenerative pathologies like Parkinson's [90]–[92] and Alzheimer's diseases [93]–[97], metabolic disorders like non-alcoholic fatty liver condition [98]–[102] and Fabry disease [103]–[108], *musculoskeletal* disorders [109]–[112], kidney pathologies [113]–[116]. Several different cancer types like breast [2], [117]–[120], prostate [121]–[125], ovary [74], [126]–[129], lung [130]–[134] and colon cancer [135]–[138] have also been studied with MSI. MSI has played an important role in identifying biomarkers of disorders when coupled with other methodologies. For instance, magnetic resonance spectroscopic imaging (MRSI), MALDI and pathological assessment by histological staining (H&E) were combined for multi-modal mass spectrometric imaging of signature lipids for different metastatic breast tumour models. As part of this study, different tumorous regions were identified by their distinctive molecular signatures [139].

MSI can be combined with microscopy imaging with the aim of obtaining the mass spectrometric chemical specificity and high resolution capabilities from optical images [4], [89], [140]. This will be discussed in the following section.

Within the context of mapping small molecules from a tissue surface, TOF-SIMS has the advantage of investigating a sample without pre-treatment and with minimum potential damage to the surface, depending on the selected primary ion beam for experimentation. The destruction of the specimen can be minimised by restricting the primary ion dose to the static limit, reducing the damage to less than 1% of the topmost atomic layer [141]. Since the sample integrity can be preserved, a specimen that has been characterised with ToF-SIMS may be subjected to further experimentation with other methodologies e.g. histological staining or another MSI technique like MALDI [142].

For instance, SIMS imaging has been combined with histological or immunohistochemical staining to obtain fluorescence microscopy images [143]–[145]. Techniques to dye biological specimens, such as fluorescence dyes, are applied after the sample's analysis with ToF-SIMS, allowing the acquisition of images in two modalities (Figure 2.15).

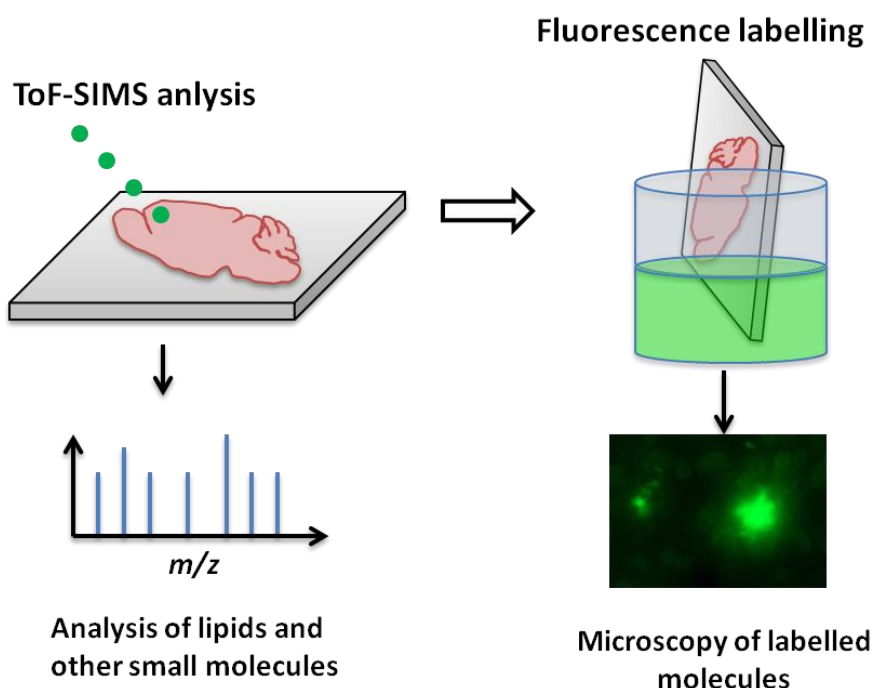


*Figure 2.15: Two imaging modalities combined for tissue analysis. The section is imaged with ToF-SIMS first and then stained with a fluorophore. Optical images are obtained with fluorescence microscopy after SIMS.*

### 2.5.1.3 Image registration and image fusion

Image fusion of two modalities has proven to be a powerful approach for fully exploiting the capabilities of different methodologies [86], [146]. MSI creates images rich with chemical data, sometimes with low spatial resolution, that can be registered to an optical image of higher resolution enabling the molecular interpretation with high chemical specificity at high spatial resolution [86].

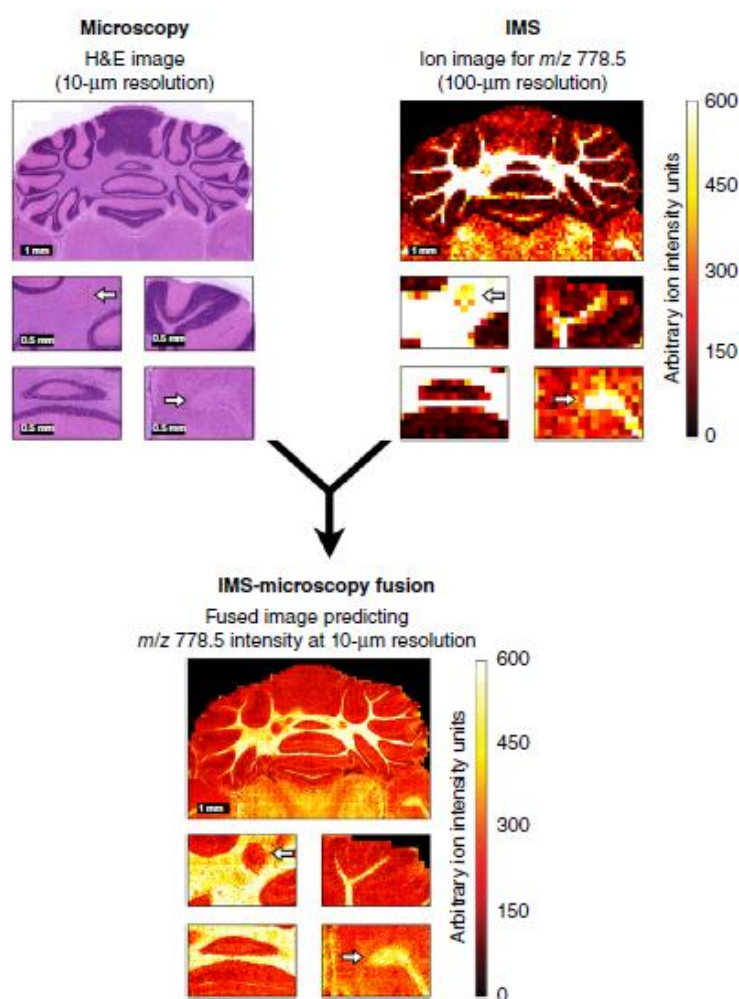


Figure 2.16: Image fusion of MSI and microscopy. An ion image from PE (P-40:4) at  $m/z$  778.5 with 100  $\mu$ m pixel size is registered with and H&E image (10  $\mu$ m pixel size) obtained with optical microscopy. This registration will predict the distribution of the lipid at the highest spatial resolution. Reprinted with permission from reference [86].

Total or single ion images generated with MSI can be registered with microscopy images, allowing the visualisation of molecular signatures contained in cells or organs [146]. For this purpose, images from different techniques can be obtained for registration or fusion from one single sample.



The use of the same sample in multiple techniques will be limited by the chemical pre-treatment applied to the sample, which could cause significant changes to its chemical composition e.g. addition of matrices [2]. The sample's chemistry can also be affected by damage during MSI analysis e.g. depth profiling a specimen [147], [148].

For example, samples analysed with ToF-SIMS under static conditions are label-free, allowing the use of the same specimen in complementary histochemical techniques, other MSI techniques such as MALDI or DESI or spectroscopy techniques such as FTIR or Raman [67], [84], [86], [88], [149], [150].

An example of this image combination approach is shown schematically in Figure 2.16. This illustration contains an MSI image of  $m/z$  778.5 with 100  $\mu\text{m}$  of spatial resolution, fused with an optical image with a pixel size of 10  $\mu\text{m}$ . The resulting image predicts the distribution of this lipid with a resolution of 10  $\mu\text{m}$  [86].

Image registration can be conducted using MatLab® since there is no specific software capable of executing this approach automatically [146]. In this thesis, an image registration approach was implemented using ToF-SIMS and fluorescence microscopy images and will be discussed in the following chapters.

### 2.5.2 Targeted and untargeted metabolomic studies with MSI

Metabolomic studies can be divided into two categories: targeted and untargeted [151]. Targeted studies are designed to localise and quantify known metabolites. One of the major applications of targeted analysis is the detection and determination of the bio-distribution of drugs within cells and tissues for therapeutic purposes [152]–[154]. The molecular distribution of a drug in a specimen is required for pharmacokinetics studies. One of the preferred methodologies is the whole-body distribution study of drugs in animals with MALDI and DESI, as shown by Figure 2.17 [155].

Non-targeted or global experiments aim to obtain a complete metabolite profile. This approach requires less experimental preparation, but involves more data analysis [156]. One crucial application of non-targeted MSI is the investigation of pathologies and biomarker discovery. The determination of molecular changes in disease progression involves the comparison of different ions associated to the disease. These molecules are usually unknown but can be related to the disease information obtained from histological tests and developed symptoms [157]–[160]. Untargeted MSI studies are not limited to *a priori* knowledge of the molecules present in the system since they can be located and identified from diagnostic ions [66].



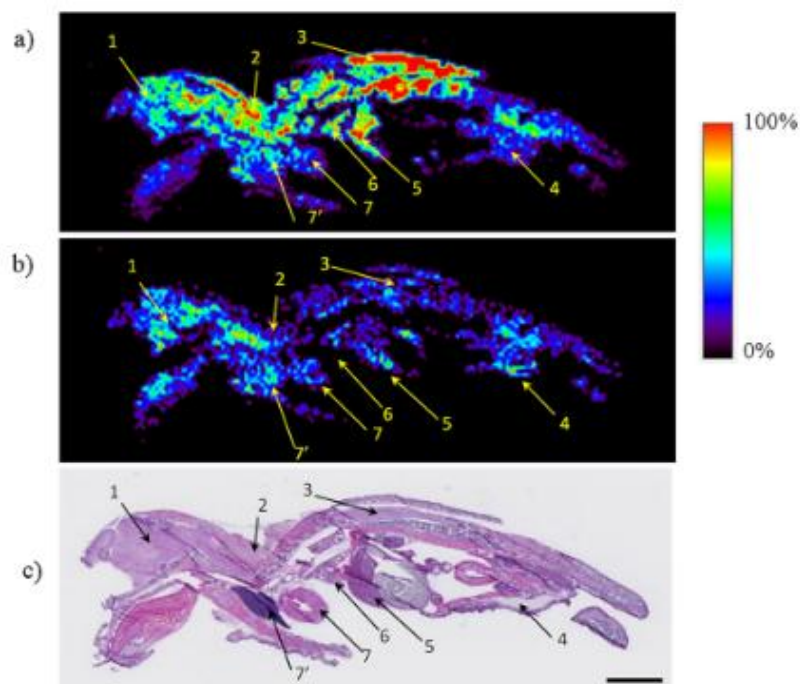


Figure 2.17: Whole-body DESI-MSI in neonate mouse doped with clozapine. (a) Distribution of clozapine  $[M+H]^+$  at  $m/z$  327.14, (b) Single ion image of N-oxide metabolite at  $m/z$  343.14 and (c) H&E stain on the same tissue section. Organs and anatomical features are highlighted with numbers: 1-brain, 2-adipose tissue (brown), 3- spinal cord, 4- adipose tissue (white), 5- liver, 6- lung, 7- heart ventricle and 7'- heart atrium. Reprinted with permission from reference [155].

### 2.5.2.1 Classification and study of lipids in the mouse brain

Lipidomics refers to the study and characterisation of different lipid species and their role in different biological functions. It is a relatively new field, emerging ten years after proteomics, that has been driven by emerging biological questions and new instrumental capabilities, particularly in mass spectrometry imaging [161].

Lipids are relatively small molecules (up to  $\sim 1000$  Daltons) which makes them accessible by SIMS. Recent instrumental advances allow the *in situ* characterisation of intact lipids with sub-micron resolution from a diverse range of biological structures, especially from tissues and single cells [162], [163]. SIMS is a widely accepted technique for lipidomic studies due to its sensitivity, mass accuracy and spatial resolution [76], [163].

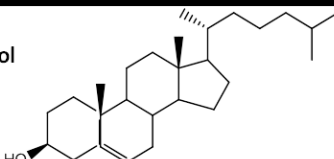
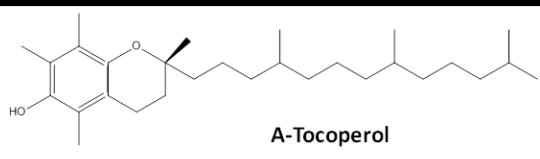
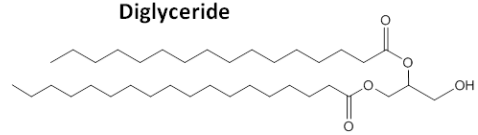
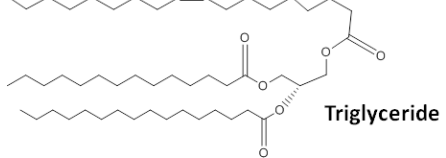
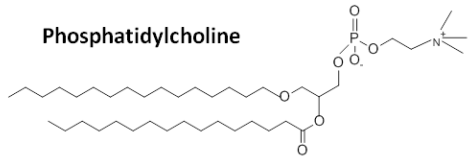
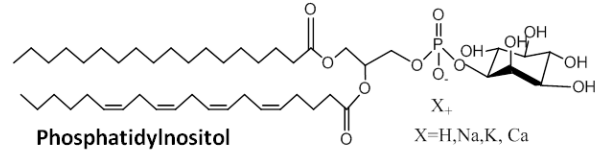
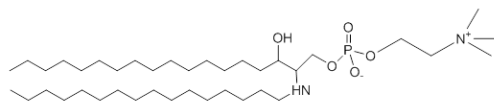
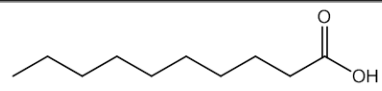
Sterol lipids			
Cholesterol		A-Tocopherol	
Glycerolipids			
Diglyceride		Triglyceride	
Glycerophospholipids			
Phosphatidylcholine		Phosphatidylinositol	
Sphingolipids			
Sphingomyelin			
Fatty acyls			
Fatty acid			

Table 2.1: Chemical structure of lipids that are most commonly found in mouse brain tissue analysis with ToF-SIMS [141].

According to the LIPID MAPS initiative [164], a lipid is any molecule with both hydrophilic and lipophilic properties. Biological lipids refer to a wide range of natural molecules classified in eight main categories, including fatty acyls, glycerolipids, glycerophospholipids, sphingolipids, saccharolipids and polyketides, sterol lipids and prenol lipids [155]. Their main biological roles are energy storage, as a structural component in cell membranes and in signalling. There are many sub-classes and sub-groups within each of the eight categories [164]. Table 2.1 shows the structure and classification of the most abundant lipids in mouse brain detected with ToF-SIMS in positive and negative ion mode [76]. Examples of these lipid molecules in mouse brains are fatty acyls, glycerophospholipids, sphingomyelins, triglycerides, diglycerides,  $\alpha$ -tocopherol (vitamin E) and cholesterol [76], [141], [165], [166].

The mouse brain is an extensively used animal model for mass spectrometry since 90% of the genes responsible of its operation are identical to those in human brains. Its lipid composition percentage in dry weight is summarised in Table 2.2 [167].

Substance	Myelin		White matter	Grey matter	Whole brain
	Human	Rat	Human	Human	Rat
<b>Total lipid*</b>	70	70.5	54.9	32.7	37
<b>Sterol lipids/Cholesterol</b>	27.7	27.3	27.5	22	23
<b>Total sphingolipids: sphingomyelin, cerebrosides, sulfatides and galactolipids.</b>	27.5	31.5	26.4	7.3	21.3
<b>Total glycerophospholipids: phosphatidylcholine, phosphoethanolamines, phosphatidylserine and phosphatidylinositol</b>	43.1	44	45.9	69.5	57.6

*Table 2.2: Lipid composition of myelin, white matter, grey matter and the whole brain in rats and humans. The total lipid\* figure is presented in percent dry weight whilst all others are mentioned in percent total lipid weight [167].*

The brain, like the rest of the central nervous system (CNS), is composed of two kinds of tissue: grey matter and white matter. Grey matter contains the nerve soma, dendrites and axon terminals of neurons (as illustrated on Figure 2.18) and this is where synapses take place. On the other hand, white matter is mainly composed of axons wrapped in myelin sheath, connecting different parts of the grey matter to each other [167].

The major structures in the white matter of the brain are glial cells, axons and myelin sheaths. It has been estimated that in a human, 50 % of the white matter is myelin and approximately 60% percent of the lipids in all the white matter are in myelin, while the remaining 40% are in extra-myelin structures [168].

Over the years, lipids were regarded only as structural constituents of the cells and energy-storage units. More recently research has revealed that lipids have active signalling and neurotransmitting functions as well as other important metabolic regulations [169].

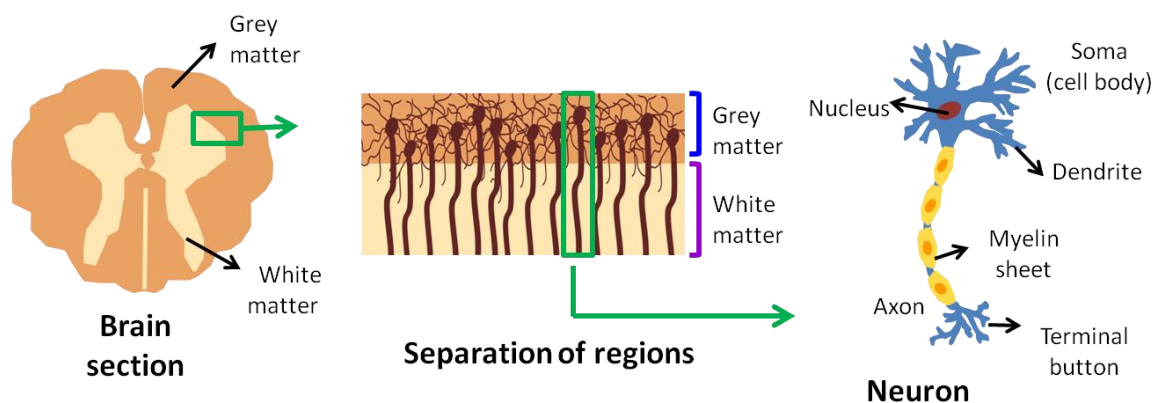


Figure 2.18: Separation between tissue types found in the brain. Grey matter contains the cell bodies and nuclei whereas the white matter contains the axons and myelin sheets [145], [146].

ToF-SIMS is widely applied to the investigation of lipids and their functions on the brain [35], [147], [170]–[172]. For example, Passarelli *et al.* [165] investigated single-cell lipidomics on *Aplysia californica* neurons with cluster ToF-SIMS. This research was based upon the detection and classification of several lipid classes from the neuron's surface using  $C_{60}^+$  clusters on a modified Q-STAR ToF-SIMS instrument. Figure 2.19 displays images with the distribution of vitamin E, cholesterol and phospholipids in an *Aplysia* neuron.

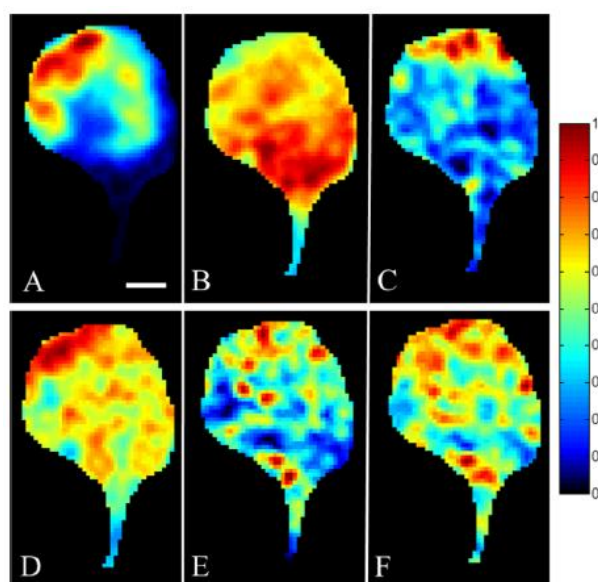


Figure 2.19: Single ion images from an *Aplysia* neuron obtained with ToF-SIMS: (A) Vitamin E  $[M+H]^+$  at  $m/z$  430.3, (B) Hydrocarbon at  $m/z$  128.1, (C) Cholesterol  $[M-OH]^+$  at  $m/z$  369.3, (D) Phosphocholine head group at  $m/z$  184, (E) PC (16:0e/18:1) fragment at  $m/z$  709.6 and (F) Sum of PC (16:0e/18:1) related peaks (Scale bar= 100  $\mu$ m). Reprinted with permission from reference [165].

Lipids share similar chemical and physical properties as a class such as their amphiphilic behaviour and the fact that they are entirely or partly formed by carbanion-based condensations of thioesters. Lipid molecules are probably the least understood in the biomolecule world. With the expansion of the metabolomics field to the study of lipids, scientists are gaining more knowledge while raising more questions regarding lipidomics and its influence on metabolic processes. The answers to these questions can influence our understanding of biology and biochemical pathways as well as guiding biotechnology towards the development of more effective healthcare treatments [76], [161], [164], [169].

### 2.5.3 ToF-SIMS imaging of mouse brain tissue

Mouse brain is a well established biological model for SIMS and has been employed to illustrate the imaging potential of ToF-SIMS [34], [35], [76], [163], [170]–[175]. Ever since the introduction of polyatomic ion beam sources to the technique, detection of intact lipids has been possible in both positive and negative ion modes. Due to the high lipid content in cell membranes, if a tissue sample is exposed to primary ion bombardment, most of the secondary ions detected in the mass spectrum are lipid ions or will correspond to their fragments. With the introduction of new cluster primary beams, it is possible to detect intact lipids and dimers up to  $m/z$  2000 although their low yield still remains a challenge [23], [166], [176]. Due to developments in beam and data processing technology, ToF-SIMS is now a well-established technique for tissue analysis.

As mentioned in the analysis beams section, liquid metal ion guns are capable of providing outstanding spatial resolution for biological imaging but cause extensive fragmentation and damage to the tissue sample.  $C_{60}^+$  clusters generate lower fragmentation and less surface damage and can be effectively applied to 2D and 3D biological imaging even though the beam is more difficult to focus [35], [163], [166]. With the use of giant gas cluster ion beams (GCIB) e.g.  $Ar_n^+$ ,  $(H_2O)_n^+$ , the secondary ion generation can be enhanced and the damage caused to the sample is minimised [7].

To draw an example, Tian *et al.* [35] demonstrated the capabilities of 20 kV  $Ar_{1700}^+$  by imaging coronal mouse brain sections with 7  $\mu m$  spatial resolution (Figure 2.20). Different species of lipid molecular ions and their sodium and potassium adducts were identified. The single ion images shown in Figure 2.20 display the distribution of glycerophospholipids PC(32:0) and PC(34:0) and their molecular ions  $[M+H]^+$ , sodium adducts  $[M+Na]^+$  and potassium adducts  $[M+K]^+$  (Figure 2.20, a and b). The third row of

images includes a cholesterol fragment ( $[M-OH]^+$ ) with very specific encapsulated localisation around hippocampus and corpus callosum (Figure 2.20, c).

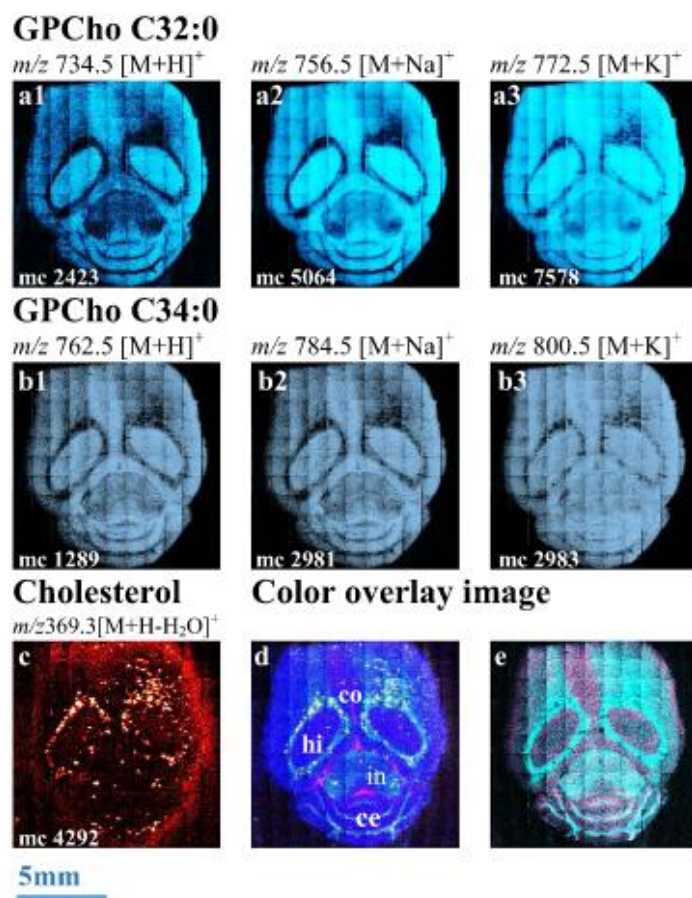


Figure 2.20: Lipid ion images and overlaid images obtained with positive ToF-SIMS analysis of a mouse brain section using  $Ar_{1700}^+$ . Images displayed in (a1), (a2) and (a3) belong to PC(32:0)  $[M+H]^+$ ,  $[M+Na]^+$  and  $[M+K]^+$  respectively. Single ion images of PC(34:0)  $[M+H]^+$ ,  $[M+Na]^+$  and  $[M+K]^+$  are shown as (b1), (b2) and (b3). The distribution of cholesterol  $[M-OH]^+$  can be observed on (c). Image overlay of PC(34:3) in blue, cholesterol in turquoise and glucosyl ceramide (d18:1/16:0) in yellow are displayed on (d). The major structures of the brain are also indicated (co-corpus callosum, cerebellum, hi-hippocampus, in-internal capsule). Image (e) contains the overlay of a DAG ion and PC(36:3). Reprinted with permission from reference [35].

The contrast in distribution of phospholipids, sphingolipids and sterol lipids is shown in overlaid images (Figure 2.20, c, d and e). This is a good example of improved lipid detection obtained with GCIB for mouse brain analysis. The spatial resolution obtained is not critical in this example since sub-micron resolution is not crucial for the analysis of tissues, in contrast to cell analysis.

Lipids from the eight categories established by LIPID MAPS [164] can be extracted, identified and quantified accurately from a tissue sample with gas/liquid chromatography analysis. Nevertheless, chromatographic techniques involve the loss

of spatial distribution information, whereas ToF-SIMS offers direct sampling from discrete regions of the surface [11]. This technique also offers a dual functionality for lipid imaging. If there is a macro-scale interest, the analysis can cover a large area with a defocused beam. For micro-scale analysis, a more detailed study can be achieved by probing the tissue sample with high spatial resolution to obtain anatomical features and molecular signatures [76].

#### ***2.5.3.1 Tissue sample preparation: protocols and considerations***

There are a variety of sample preparation methods for ToF-SIMS imaging of tissues samples. The techniques are designed to preserve the native state of the sample and to minimise molecule migration [125]–[127], [132], [140], [141]. SIMS instruments work under high vacuum conditions thus subjecting the sample to stresses associated with a vacuum environment. Moreover, the low concentration of molecules of interest and the low secondary ion yield obtained from biological matrices drive the application of sample preparation protocols that promote the ion formation of all or certain molecules. For example, Angerer and co-workers [23] exposed a mouse brain tissue section to trifluoroacetic acid (TFA) vapour for varying periods of time, enhancing the detection of certain intact lipids like phospholipids, sphingolipids and glycerides but suppressing or evaporating of specific prenol lipids like cholesterol. This example is illustrated in Figure 2.21, where a control mouse section and a sample exposed to TFA for 30 minutes are compared.

Even though it is not ideal to modify the sample chemically, some approaches are practiced successfully e.g. matrix-enhanced SIMS (ME-SIMS) or metal-assisted SIMS (Met-A-SIMS) [66]. There are a vast number of biological systems that can be imaged with SIMS and this section will focus only in the most common sample preparation protocols for mouse brain tissue, the main sample type used for this project.

Vacuum plays an important role during analysis since volatile molecules will be removed from the system, including water. The rapid removal of water can cause structural damage to the specimen and can lead to the migration of compounds, modifying the sample's native state. Researchers have different methods for quick water removal or preservation in a frozen-hydrated state. These methods are discussed in the following sections.



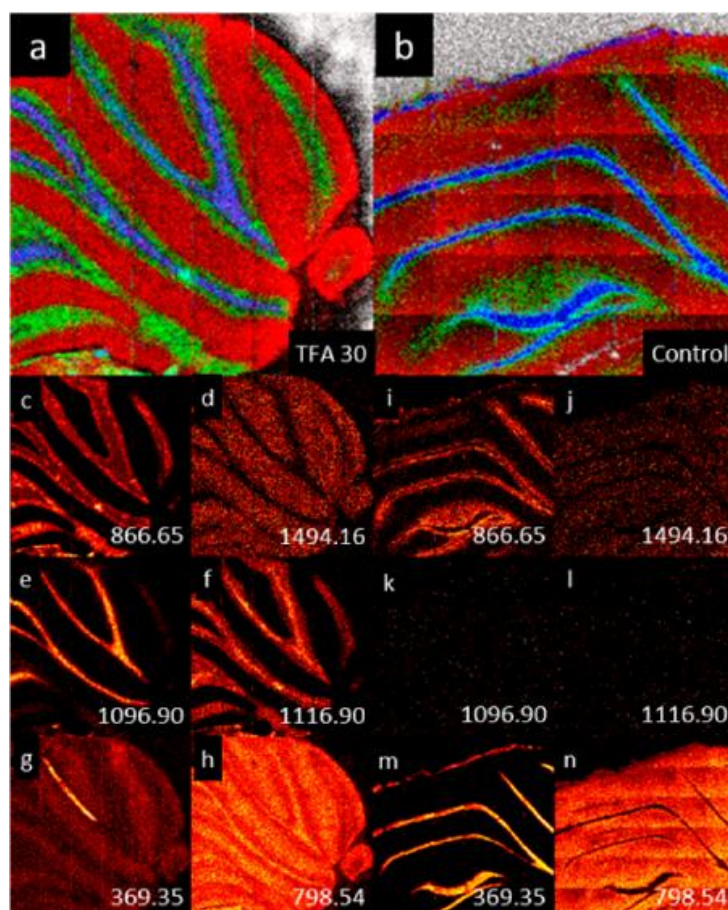


Figure 2.21: Mouse brain image overlay of 30 minutes TFA exposed (a) and control (b) samples, respectively. Single ion images of  $m/z$  570.53 (red),  $m/z$  863.65 (green) and  $m/z$  1096.90 (blue) are overlaid in each image. The rows below display single ion image comparison of ions with different mass-to-charge ratio. Signal intensities are lower for the control sample, especially for ions at  $m/z$  1096.90 and  $m/z$  1116.90. The distribution of cholesterol  $m/z$  369.35 is specific to the white matter in the control sample whereas it is also located across the grey matter on the sample exposed to TFA. Reproduced from reference [23].

Specific sample preparation strategies have to be considered when analysing brain tissue samples. Nygren and co-workers have demonstrated that sample preparation of brain tissue is the key to detecting higher/lower cholesterol signal from a brain sample [204]. When the sample was treated with high-pressure freezing and freeze fracturing, there was a higher detection of  $[M+H]^+$  and  $[M+H-H_2O]^+$  cholesterol ions whilst the tissue's integrity was preserved. Moreover, temperature-controlled ToF-SIMS experiments on mouse brain have revealed cholesterol migration to the surface of the sections when the sample is kept under vacuum conditions at room temperature [170]. This can be avoided by analysing the sample in frozen-hydrated conditions at temperatures  $<0^\circ\text{C}$ . If the sample is analysed at room temperature, the analysis has to be carried out as soon as the sample is inserted in the vacuum chamber to prevent migration of cholesterol [170], [204].



#### 2.5.4 Sample preparation workflow for mouse brain imaging with ToF-SIMS

Figure 2.22 illustrates the traditional sample preparation methodology for mouse brain. A complete brain ( ~ 0.8- 1 cm in length, 0.5-0.8 cm in height) is dissected from the animal and cryo-fixed to avoid biodegradation. The whole organ is kept in liquid nitrogen or in a freezer at -80°C until sectioning. For sectioning purposes, the brain is mounted with media e.g. optimal cutting temperature compound (OCT), carboxymethyl cellulose (CMC) or gelatine on a cryostat disc [179]. This mounting media is only used to support the organ on the cryo-microtome holder, and does not penetrate the tissue. Soon after, the organ is sectioned using a cryo-microtome at -22°C and each section is mounted on a substrate. The samples are kept under cryogenic conditions until desiccation or analysis in a hydrated state. It has not been investigated if cellular disruption takes place during this process.

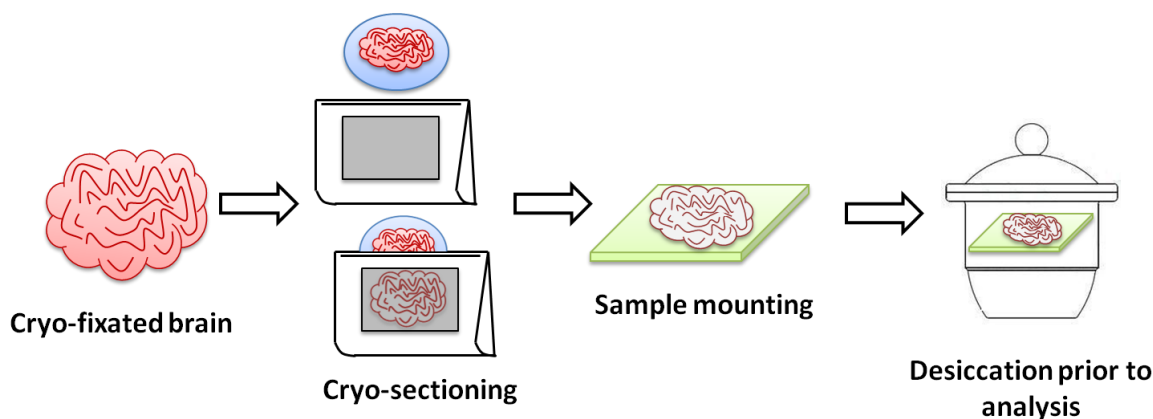


Figure 2.22: Sample preparation workflow of a mouse brain for ToF-SIMS analysis.

##### 2.5.4.1 Cryo-fixation

To minimise sample degradation, fixation is required immediately after an organ is dissected from the animal. Chemical-based fixatives should be avoided in SIMS; the consequences of such procedures are the migration of molecules and the addition of external compounds that can significantly modify the system [76], [180]. Instead of a chemical fixation, cryo-fixation is employed to preserve the sample's chemistry and integrity. Cryo-fixation is a fixation method that requires ultra-cooling of a biological specimen to stop any metabolic activity. This rapid ultra cooling technique is also known as snap-freezing [181]. In this approach the specimen is plunged into liquid propane or ethane cooled with liquid nitrogen and kept at temperatures close to their melting points (85 and 89 K, respectively). These liquid hydrocarbons cool down the sample fast enough allowing the transition of the sample's water to amorphous ice.

With rapid cooling, the formation of crystals that could disrupt the molecular structure is avoided. This method is widely used for brain preparation; this way brain sections retain their native distributions of ions such as Na<sup>+</sup>, K<sup>+</sup> and Ca<sup>+</sup> which subsequently form adducts with other molecular species during the ionisation process [76], [180]. If the presence of diffusible ions and the formation of adducts is to be avoided, washing the complete organ in ammonium formate or ammonium acetate should be carried out before cryo-fixation. This ammonium formate or ammonium acetate treatment will remove the salt precipitates by perfusion [165].

#### ***2.5.4.2 Cryo-sectioning and freeze- drying***

After fixation, tissue samples are sectioned with a cryo-microtome. The whole brain is embedded on a cryostat disc with media e.g. OCT, CMC, gelatine or water. During sectioning, the tissue is brought to -20°C in the cryostat microtome and sliced into thin sections. The thickness of the sections varies according to the experimental design; for brain specimens is typically between 5-50 µm [182]. The slices are usually thaw-mounted onto substrates like indium tin oxide-coated (ITO-coated) slides, silicon wafers, steel plates or microscope slides, among others. During the cryo-sectioning process, the sections obtained are often incomplete, leading to the loss of the integrity of the samples. Sample mounting is also a critical step, since thin sections can get folded very easily, compromising the integrity of the section.

Once mounted, the samples are kept in a freezer at -80°C until analysis. Prior to analysis, the samples are freeze-dried to sublimate the sample's water content [44-59], [62-74]. The dehydration of the tissue is usually carried out by exposing the sample to low vacuum using a desiccator at room temperature for one to two hours. It has not been explained how this process influences the tissue's structure since water loss can lead to the collapse of the material or the re-distribution of molecules due to the changes in the sample's temperature.

#### ***2.5.4.3 Frozen-hydrated sample analysis***

As previously mentioned, one of the main experimental requirements for SIMS is the vacuum compatibility of the sample. Biological samples are usually dehydrated but they can also be analysed in a hydrated state. This can be achieved by keeping the sample under cryogenic conditions at all times, including during analysis. This approach has been explored for the analysis of frozen-hydrated HeLa cells [6], [28], [177] demonstrating enhanced molecular ion signals from phospholipids due to the presence of a larger number of protons in the water contained in the sample. In this

approach, cells are snap-frozen and kept in liquid nitrogen avoiding contact with air; this prevents molecule diffusion while keeping the sample's morphology. The analysis stage in the SIMS instrument is also cooled with liquid nitrogen throughout the experiment.

Although this approach has been very successful for cells, it has not been widely used for macro-structures like tissue samples. Specific instrument features are needed for this experiment to be successful since the time required to image a tissue sample is longer meaning a constant liquid nitrogen supply is required to keep the sample stage at cryogenic temperature.

#### **2.5.4.4 Freeze-fracturing**

This type of sample preparation is usually applied to cellular analyses [183]–[186] but it can also be implemented in tissue analysis [3]. In freeze-fracturing, a specimen is sandwiched in between two substrates and subsequently cryo-fixed by snap freezing. The sandwich is then fractured on a plane through the tissue. The fracture occurs mainly in membranes or organelle's surfaces, exposing the content of cells for analysis.

#### **2.5.5 Bio-medical applications of ToF-SIMS imaging**

MALDI-ToF has been the main MSI technique practised in medical research due to its ability to detect molecules over a high mass range [119]. Nevertheless, the application of ToF-SIMS to biomedical research has been growing considerably in the past few years. Although medical applications are still relatively novel to the technique [187], there are a number of diseases that have been investigated with ToF-SIMS so far. Genetic and chronic metabolic disorders such as cystic fibrosis in colonic mucosa [135], atherosclerotic aorta [188], [189], cirrhotic liver [98], [149], fabry disease [103]–[105], non-alcoholic fatty liver [101], [190] and duchenne muscular dystrophy [109], [191] among others, are examples of the successful application of ToF-SIMS imaging to medical studies.

Fabry disease was studied in kidney biopsies from patients with this condition [108]. This rare genetic disease affects the metabolism of glycosphingolipids, hence accelerating the accumulation of digalactosylceramides and globotriasylceramides in the skin and kidneys. These biomarkers have been observed in skin biopsies using MALDI-MSI, but kidney specimens were too small for MALDI imaging ( $\sim 500\ \mu\text{m}$  of diameter). ToF-SIMS was found to be suitable for this analysis due to its sub-micron resolution and the mass range required to detect the biomarkers ( $m/z$  800-1200).

Duchenne muscular dystrophy (DMD) is a genetic condition that causes muscular fibrosis inducing muscle dystrophy. A mouse model and human biopsies from muscle affected with DMD have been studied with ToF-SIMS using  $\text{Au}_3^+$  and  $\text{Bi}_3^+$  for imaging [109], [191]. As the condition advances, necrotic musculoskeletal cells are replaced by adipose tissue. Images from muscle fibres mixed with adipose and conjunctive tissue were successfully acquired with ToF-SIMS in positive and negative ion modes and several lipids were characterised. Specific distribution of fatty acyls, phospholipids, triglycerides, prenol lipids and coenzymes allowed the identification of the cells from the affected areas [109], [191]. In negative ion mode, areas with muscular dystrophy contained a higher amount of chloride ions and saturated C18 fatty acyls. Vitamin E was also an indicator of oxidation stress. In positive ion mode diglycerides and triglycerides were biomarkers of adipocytes from the degenerated area whereas sphingomyelin, phosphatidylcholine and vitamin E evidenced the presence of myofibers.

ToF-SIMS imaging has also been utilised for studying non-alcoholic fatty liver disease (NAFLD) with the purpose of evaluating cholesterol, accumulation of fatty acyls, triglycerides and diglycerides in livers. These lipids were detected as small droplet patterns in hepatocytes [101], [190] and demonstrated the presence of diglycerides (DAG's) of different chain lengths and saturation degree for the first time with ToF-SIMS [101],[204].

ToF-SIMS studies in rodent brain sections have focused on the spatial distribution of lipids of different classes. The cerebellum area of the brain has provided information about the distribution of cholesterol, fatty acyls and sulfatides with hydrocarbon chains of different lengths [3], [192]. Ions corresponding to sulfatides have been found in the granular layer and paranodal area of the white matter of the cerebellum, with higher a concentration at the border (As seen in Figure 2.23, a and c). The same results were obtained from sections prepared under different conditions: cryo-sectioning, high-pressure freezing, freeze-fracturing and freeze-drying [76].

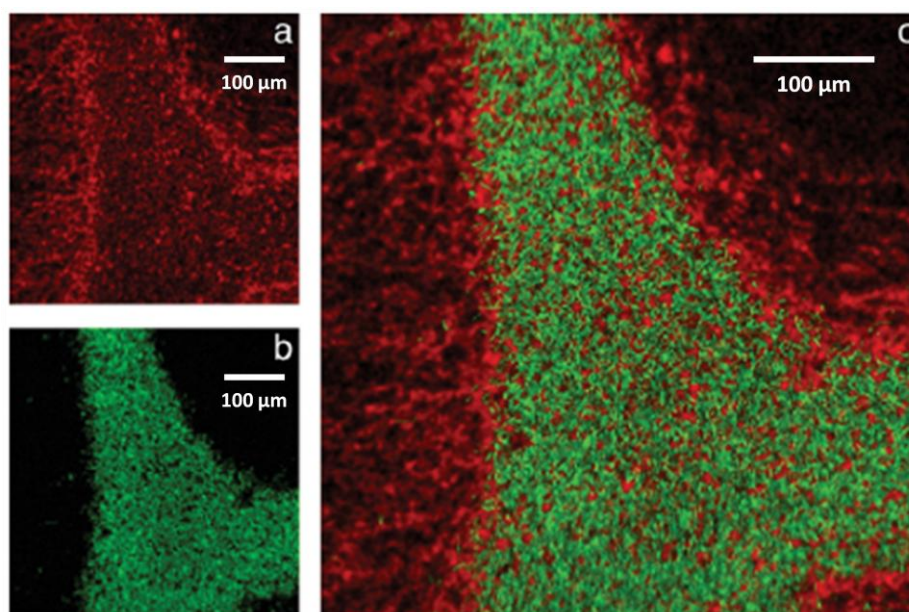


Figure 2.23: ToF-SIMS images in negative ion mode with added intensities of sulfatides from a mass range  $m/z$  778.5-934.6 (a). (b) Distribution of cholesterol ( $m/z$  385) in white matter in green. Image overlay of (a) and (b), showing the localisation of sulfatides mainly at the border of the white matter. Reprinted and modified with permission from reference [192].

#### 2.5.5.1 ToF-SIMS imaging studies on Alzheimer's disease

ToF-SIMS imaging has recently been applied to research related to neurodegenerative diseases, specifically Alzheimer's disease (AD). Specimens analysed with this pathology include brain sections from transgenic mouse models and human biopsies infected with the condition [97], [193]. AD is a chronic neurodegenerative condition which is not fully understood. The progress of the disease is associated with the presence of accumulated amyloid beta protein, also known as  $A\beta$  plaques, and abnormal aggregation of tau protein in neurofibrillary tangles [194].

Efforts to understand the causes of this condition have led to the application of ToF-SIMS imaging on sections from transgenic infected mouse models with AD [193]. Solé-Domènech *et al.* studied brain sections from two transgenic mice strains, localising the  $A\beta$  accumulations and identifying cholesterol deposits surrounding the plaques. The  $A\beta$  plaques were spatially located using immunohistochemistry and characterised in situ with ToF-SIMS. Multi-modal imaging was applied for spatial and chemical characterisation, providing a lipid profile of specific  $A\beta$  regions, as illustrated in Figure 2.24.

Lazar and co-workers [97] analysed post-mortem biopsies from different patients. Their study also focused on the distribution of cholesterol relative to the areas with  $A\beta$

plaques and neurofibrillary tangles. Results showed an uneven distribution of cholesterol around the cortical area, being more abundant in the lower half of the cortex in AD samples when compared to control samples. This is an indication of cholesterol alteration in the cerebral cortex; however, the mechanism of this accumulation is yet to be elucidated.

None of the studies mentioned previously were able to identify any diagnostic ions from A $\beta$  aggregations. The detection of A $\beta$  *in situ* still remains a challenge and it is one of the aims presented in this thesis (Section 7). Multi-modal analysis of AD samples will be presented in the results chapters as a bio-medical application of ToF-SIMS imaging, in combination with fluorescent microscopy.

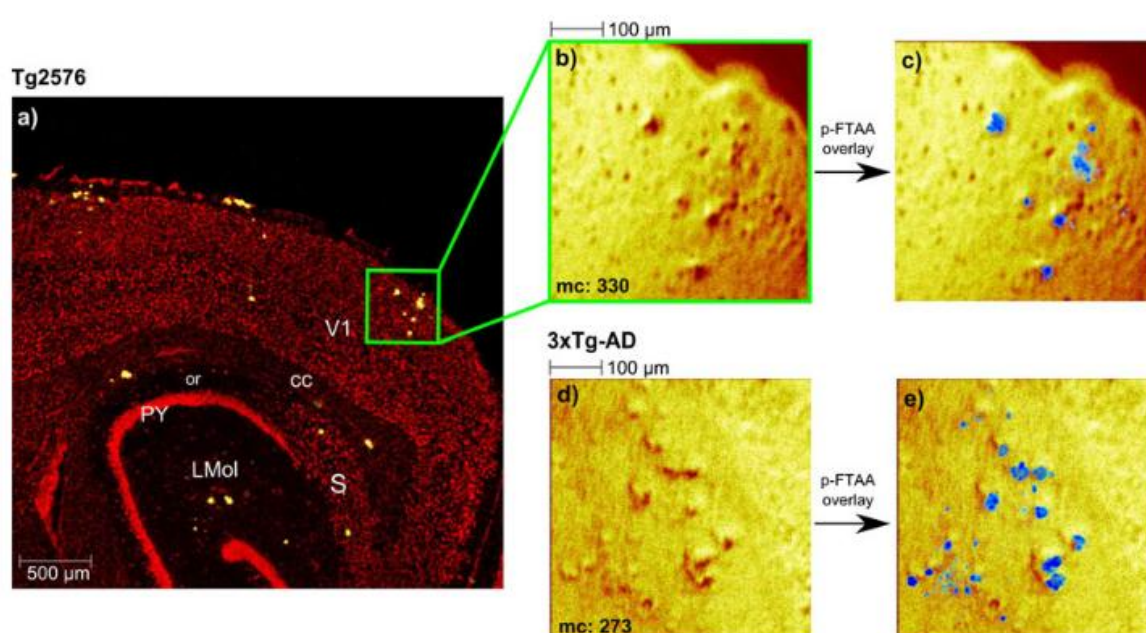


Figure 2.24: (a) Confocal microscopy and (b), (d) ToF SIMS images from the areas occupied by A $\beta$  deposits. Images (c) and (e) are the overlay of the two techniques to correlate the location of the plaques. ToF-SIMS images were acquired with Bi $_3^+$  and a spatial resolution of 3-5  $\mu$ m. Reprinted with permission from reference [193].

## 2.5.6 Challenges of analysis of bio-systems with ToF-SIMS

ToF-SIMS analysis offers important features such as high mass accuracy and high spatial resolution; however, there are important limitations to be overcome. One of the main limitations is the narrow detection mass range. ToF-SIMS is a high impact energy surface technique that produces abundant fragmentation thus the mass range of commercial instruments is usually limited to 0 to 2500 Daltons [11].

When analysing biological systems, ion suppression/enhancement effects might take place based on the molecular environments. These effects cause significant issues relating to the quantification and identification of the molecules distributed in a complex system. The ionisation of a molecule is severely influenced by its chemical environment [138], [176]. Reported experiments have demonstrated that some chemical environments like gelatine [196] or water [28], [58], [186] aid the ionisation of sputtered particles. Other molecules such as DPPC, which has been proven to suppress amino acids and drugs [21], can suppress ion formation. Studies have also established an association between the protonation of ions and the basicity of molecules [197]. Despite all the efforts to understand the ion enhancement/suppression mechanisms, the relationship between ion formation and the surrounding chemical environment in a biological system is not yet fully understood. Understanding this process will guide researchers to improved ion identification.

Ion suppression issues have also been related to the presence of contaminants in the sample. Ions from inorganic molecules act as interference in the mass spectrum by re-combining with the biological molecules, forming adducts. Contaminants are usually transferred to analytes during the handling and preparation processes. To avoid this type of contamination, improper lab techniques should be avoided and great care must be taken during sample handling and preparation [147], [198].

#### ***2.5.6.1 Analysis of insulating samples and sample preparation issues***

Tissues samples are insulating materials mounted onto semi-conductive surfaces for analysis purposes. The thickness of the tissue section and the media used to embed it are critical factors that can affect experimentation, especially imaging. If the volume of non-conductive material increases, the balance between the fluence of primary ions and the extraction of secondary ions may cause the accumulation of surface charge that affects the secondary ion emission and mass detection. This will be reflected in the secondary ion image by reduced signal intensity (brightness) of the pixels [141].

These issues are to be considered when analysing any type of biological sample with SIMS. For the purpose of this thesis, considerations for brain tissue handling and preparation will be explained in the methodology section.

### 2.5.7 Water cluster primary ion beams

The SIMS group at the University of Manchester in collaboration with Ionoptika Ltd have developed a prototype water cluster ion beam to try to increase the low secondary ion yields obtained from biological sample [36]. This ion beam works under the basis that increasing the density of water in the impact zone during analysis would increase  $[M+H]^+$  type ions. The mechanism and operation of this beam is explained in section 3.5.2.

The first experiments acquired with this prototype cluster ion beam, involved the comparison of 10 keV  $(H_2O)_n^+$  and 10 keV  $Ar_n^+$  clusters for the analysis of arginine, haloperidol, dipalmitoylphosphatidylcholine (DPPC) and angiotensin II in static and high dose conditions. Results showed an enhancement in secondary ion yields on the order of 10 or more when water clusters were applied to the analysis of all compounds (Figure 2.25). When the counts obtained per  $1\ \mu m^2$  with water clusters were calculated, they were as high as 20 relative to 0.05 counts obtained with argon clusters [36].

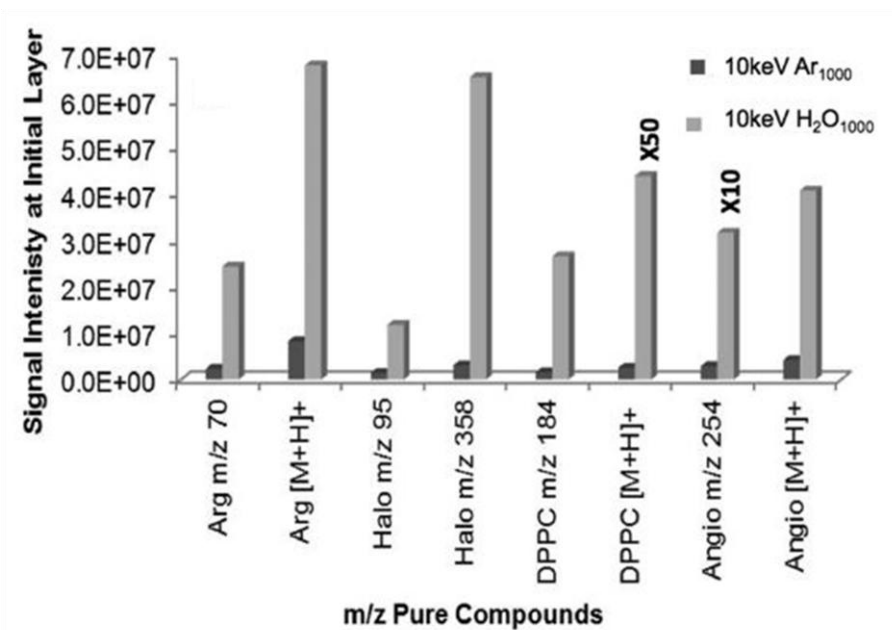


Figure 2.25: Secondary ion signal comparison between 10 keV  $(H_2O)_n^+$  and 10 keV  $Ar_n^+$  for the analysis of L-arginine, haloperidol, DPPC and Angiotensin II pure compounds. Reproduced from [36].

Besides the secondary ion yield enhancement, it was also reported that the ion suppression effect that prevented the formation of haloperidol  $[M+H]^+$  ions when mixed with DPPC [197], [199] was ameliorated when using water clusters for analysis. These results show that water clusters could potentially enhance the useful secondary ion yields obtained from the analysis of biological samples, although future



developments and studies are required to assess the application of this water cluster ion beams [36].

### 2.5.8 Sputtering studies

Sputtering studies were performed by Kohn *et al.* [202] to compare the performance of water cluster ion beams when compared to  $C_{60}$  and Argon. These studies were carried out on 50 nm thick Irganox 1010 films and L-arginine films. The films were sputtered using 10, 20 or 40 keV  $C_{60}$ , 20 keV Ar and 10 or 20 keV  $H_2O$  cluster beams. The sputter yields were calculated by measuring the volume removed from a  $250 \mu m^2$  area divided by the number of ions bombarding the analysis area.

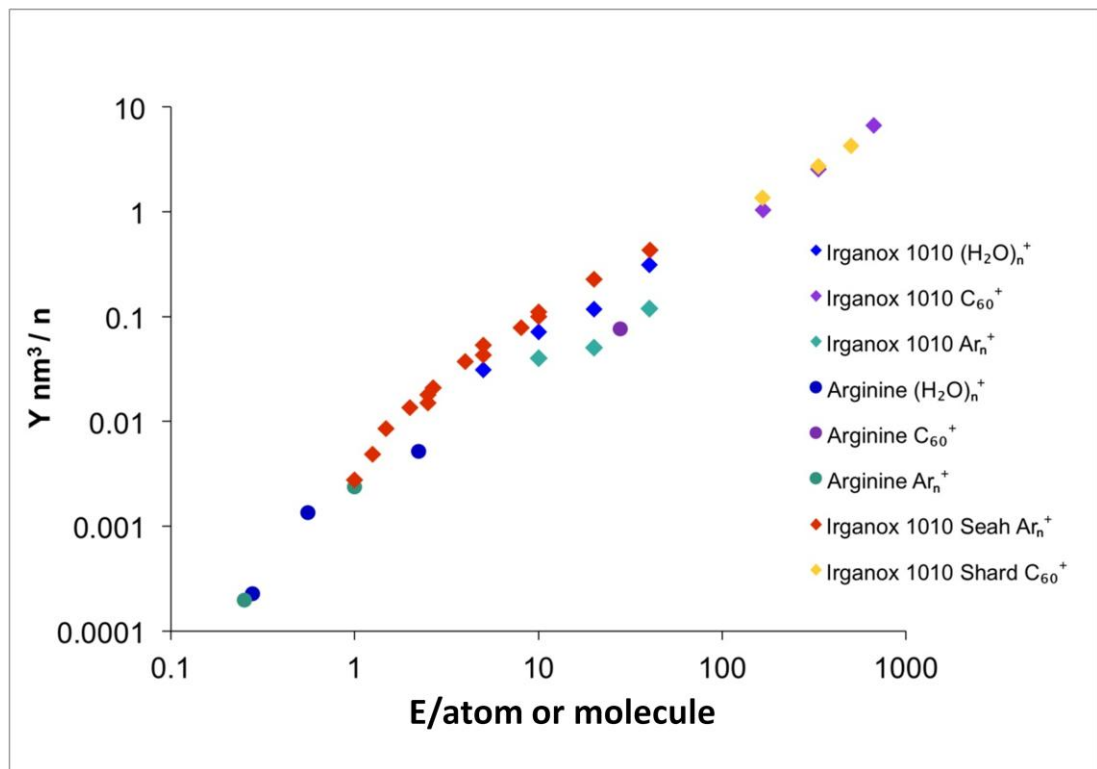


Figure 2.26: Sputter yield measurements obtained with argon, water and  $C_{60}$  ion beam clusters. The samples presented are Irganox 1010 and L-arginine films. The data obtained using water clusters was compared to that presented by Seah [46] and Shard [203]. The sputtering yields are plotted as  $Y \text{ nm}^3/n$  as a function of  $E/\text{atom or molecule}$  [202].

The measurements obtained with water cluster ion beams were compared to those obtained by Shard *et al.* [203] and Seah *et al.* [46]. This comparison is illustrated with Figure 2.26. This plot shows the sputter yields ( $Y$ ) data in  $\text{nm}^3/n$  as a function of energy per atom or molecule. This data shows that the sputter yields obtained under water cluster bombardment are not so different from other clusters ( $C_{60}$  or argon) of similar

size. Figure 2.26 shows the close alignment of the sputtering obtained with water, argon and C<sub>60</sub>.

## 2.6 Summary

ToF-SIMS imaging is successfully applied to the characterisation of biological tissue samples. Studies on mouse brain tissue samples have shown that SIMS can detect different lipid species and other metabolites, enabling the biological study of different diseases and genetic conditions.

Clearly, there are limitations still to overcome to fully exploit ToF-SIMS capabilities for imaging. Low secondary ion yield generated from biological samples and the suppression effects on different ions are among the main challenges. In addition, experimental parameters and sample preparation of insulating samples are key factors to obtain the best possible results from SIMS imaging.

There is a clear need for the development of new primary ion sources capable of enhancing the ionisation of sputtered particles with minimum damage to the analyte. Giant gas cluster ion beams, seem to be the best candidates to sputter bigger intact molecules with less damage caused to the sample. Spatial resolution is also very critical for the feasibility of sub-micron bioimaging, especially when small structures are studied.

Different mass spectrometry techniques offer various advantages and limitations in terms of spatial resolution, and mass range detected. It is very unlikely that one single technique (SIMS, MALDI or DESI) will provide all the answers to targeted or untargeted biological questions. Multi-modal studies seem to be the best approach to obtain as much information as possible from one sample. With this approach, images obtained from two different techniques e.g. mass spectrometry and microscopy can be correlated by image registration to fully exploit the capabilities of both methods.

## 2.7 References

- [1] J. Liu and Z. Ouyang, "Mass spectrometry imaging for biomedical applications," *Anal. Bioanal. Chem.*, vol. 405, no. 17, pp. 5645–5653, 2013.
- [2] M. Aichler and A. Walch, "MALDI Imaging mass spectrometry: current frontiers and perspectives in pathology research and practice," *Lab. Investig.*, vol. 95, no. 4, pp. 422–431, 2015.

- [3] K. Börner, P. Malmberg, J. E. Månsson, and H. Nygren, "Molecular imaging of lipids in cells and tissues," *Int. J. Mass Spectrom.*, vol. 260, pp. 128–136, 2007.
- [4] S. Chughtai, K. Chughtai, B. Cillero-Pastor, A. Kiss, P. Agrawal, L. MacAleese, and R. M. a Heeren, "A multimodal mass spectrometry imaging approach for the study of musculoskeletal tissues," *Int. J. Mass Spectrom.*, vol. 325–327, pp. 150–160, 2012.
- [5] J. H. Jungmann and R. M. A. Heeren, "Emerging technologies in mass spectrometry imaging," *J. Proteomics*, vol. 75, no. 16, pp. 5077–5092, 2012.
- [6] J. S. Fletcher, S. Rabbani, A. Henderson, N. P. Lockyer, and J. C. Vickerman, "Three-dimensional mass spectral imaging of HeLa-M cells - Sample preparation, data interpretation and visualisation," *Rapid Commun. Mass Spectrom.*, vol. 25, no. January, pp. 925–932, 2011.
- [7] J. S. Fletcher, N. P. Lockyer, and J. C. Vickerman, "Molecular SIMS imaging; Spatial resolution and molecular sensitivity: Have we reached the end of the road? Is there light at the end of the tunnel?," *Surf. Interface Anal.*, vol. 43, no. May 2010, pp. 253–256, 2011.
- [8] N. P. Lockyer, "Bioimaging of elements and small molecules using MS.," *Bioanalysis*, vol. 3, pp. 1047–1051, 2011.
- [9] J. S. Fletcher, "Latest applications of 3D ToF-SIMS bio-imaging," *Biointerphases*, vol. 10, p. 018902, 2015.
- [10] J. S. Fletcher, J. C. Vickerman, and N. Winograd, "Label free biochemical 2D and 3D imaging using secondary ion mass spectrometry," *Curr. Opin. Chem. Biol.*, vol. 15, no. 5, pp. 733–740, 2011.
- [11] A. G. Shard and I. S. Gilmore, *TOF-SIMS: Materials analysis by mass spectrometry*, 2nd ed. Manchester: IM Publications, 2013.
- [12] L. Adriaensen, F. Vangaeveer, and R. Gijbels, "Metal-assisted secondary ion mass spectrometry: Influence of Ag and Au deposition on molecular ion yields," *Anal. Chem.*, vol. 76, no. 22, pp. 6777–6785, 2004.
- [13] J. J. D. Fitzgerald, P. Kunnath, and A. V. Walker, "Matrix-Enhanced Secondary Ion Mass Spectrometry (ME SIMS) Using Room Temperature Ionic Liquid Matrices," *Technology*, vol. 82, no. 11, pp. 4413–4419, 2010.

- [14] A. Heile, D. Lipinsky, N. Wehbe, A. Delcorte, P. Bertrand, A. Felten, L. Houssiau, J. J. Pireaux, R. De Mondt, L. Van Vaeck, and H. F. Arlinghaus, "Metal-assisted SIMS and cluster ion bombardment for ion yield enhancement," *Appl. Surf. Sci.*, vol. 255, pp. 941–943, 2008.
- [15] N. Wehbe, A. Heile, H. F. Arlinghaus, P. Bertrand, and A. Delcorte, "Effects of metal nanoparticles on the secondary ion yields of a model alkane molecule upon atomic and polyatomic projectiles in secondary ion mass spectrometry," *Anal. Chem.*, vol. 80, no. 16, pp. 6235–6244, 2008.
- [16] J. C. Vickerman, "Surface Analysis: The principal techniques," 1997.
- [17] J. C. Vickerman, "Prologue: ToF-SIMS- An evolving mass spectrometry of materials," in *TOF-SIMS: Materials analysis by mass spectrometry*, 2nd ed., D. Vickerman, John C., Briggs, Ed. Manchester: IM Publications, 2013, pp. 1–38.
- [18] Y. Abe, "Evaluation of Damage Cross Sections by Au Cluster Ion Bombardment," vol. 12, no. 2, 2005.
- [19] U. Oran, "Surface Chemical Characterization of Plasma-Chemically Deposited Polymer Films by Time of Flight Static Secondary Ion Mass Spectrometry," 2005.
- [20] A. Shard, I. Gilmore, and A. Wucher, "Molecular depth profiling," in *TOF-SIMS: Materials analysis by mass spectrometry*, 2nd ed., J. C. V. and D. Briggs, Ed. IM Publications, 2013, pp. 311–334.
- [21] J. C. Vickerman, "Molecular imaging and depth profiling by mass spectrometry--SIMS, MALDI or DESI?," *Analyst*, vol. 136, pp. 2199–2217, 2011.
- [22] A. Brunelle and O. Laprévôte, "Lipid imaging with cluster time-of-flight secondary ion mass spectrometry," *Anal. Bioanal. Chem.*, vol. 393, pp. 31–35, 2009.
- [23] T. B. Angerer, M. P. Dowlatsahi, P. Malmberg, and J. S. Fletcher, "Improved Molecular Imaging in Rodent Brain with Time-of-Flight Secondary Ion Mass Spectrometry using Gas Cluster Ion Beams and Reactive Vapour Exposure," *Anal. Chem.*, p. 150323220819005, 2015.
- [24] G. Gillen, A. Fahey, M. Wagner, and C. Mahoney, "3D molecular imaging SIMS," *Appl. Surf. Sci.*, vol. 252, pp. 6537–6541, 2006.
- [25] J. C. Vickerman and N. Winograd, "SIMS-A precursor and partner to contemporary mass spectrometry," *Int. J. Mass Spectrom.*, vol. 377, pp. 568–579, 2014.

- [26] J. S. Fletcher and C. Szakal, "Cluster and polyatomic primary ions beams," in *TOF-SIMS: Materials analysis by mass spectrometry*, 2nd ed., J. C. Vickerman and D. Briggs, Eds. Manchester: IM Publications, 2013, pp. 291–310.
- [27] J. P. Speir, G. S. Gorman, and I. Jonathan Amster, "Laser desorption and chemical ionization applications for Fourier transform mass spectrometry," in *Mass Spectrometry in the Biological Sciences: A Tutorial*, M. . Gross, Ed. Media, Springer Science & Business, 2012.
- [28] A. M. Piwowar, S. Keskin, M. O. Delgado, K. Shen, J. J. Hue, I. Lanekoff, A. G. Ewing, and N. Winograd, "C60-ToF SIMS imaging of frozen hydrated HeLa cells," *Surf. Interface Anal.*, vol. 45, no. February, pp. 302–304, 2013.
- [29] S. Rabbani, J. S. Fletcher, N. P. Lockyer, and J. C. Vickerman, "Exploring subcellular imaging on the buncher-ToF J105 3D chemical imager," *Surf. Interface Anal.*, vol. 43, no. 1–2, pp. 380–384, 2011.
- [30] S. Rabbani, A. M. Barber, J. S. Fletcher, N. P. Lockyer, and J. C. Vickerman, "TOF-SIMS with argon gas cluster ion beams: A comparison with C 60 +," *Anal. Chem.*, vol. 83, no. 10, pp. 3793–3800, 2011.
- [31] K. Mochiji, M. Hashinokuchiy, M. Kousuke, and N. Toyoda, "Matrix-free detection of intact ions from proteins in argon-cluster secondary ion mass spectrometry," *Rapid Commun. Mass Spectrom.*, vol. 23, no. 23, pp. 648–652, 2009.
- [32] A. G. Shard, R. Havelund, M. P. Seah, S. J. Spencer, I. S. Gilmore, N. Winograd, D. Mao, T. Miyayama, E. Niehuis, D. Rading, and R. Moellers, "Argon Cluster Ion Beams for Organic Depth Pro fi ling : Results from a," 2012.
- [33] J. Bailey, R. Havelund, A. G. Shard, I. S. Gilmore, M. R. Alexander, J. S. Sharp, and D. J. Scurr, "3D ToF-SIMS Imaging of Polymer Multilayer Films Using Argon Cluster Sputter Depth Profiling," *ACS Appl. Mater. Interfaces*, vol. 7, no. 4, pp. 2654–2659, 2015.
- [34] C. Bich, D. Touboul, and A. Brunelle, "Cluster TOF-SIMS Imaging as a tool for micrometric histology of lipids in tissue," *Mass Spectrom. Rev.*, no. 33, pp. 442–451, 2013.
- [35] H. Tian, A. Wucher, and N. Winograd, "Molecular imaging of biological tissue using gas cluster ions," *Surf. Interface Anal.*, vol. 46, no. S1, pp. 115–117, 2014.

- [36] S. Sheraz, A. Barber, J. S. Fletcher, N. P. Lockyer, and J. C. Vickerman, "Enhancing secondary ion yields in ToF-SIMS using water cluster primary beams .," *Anal. Chem.*, pp. 2–3, 2013.
- [37] B. J. Garrison, "Molecular ions in cluster bombardment: What clues do the molecular dynamics simulations provide?," *Surf. Interface Anal.*, vol. 43, no. 1–2, pp. 134–136, 2011.
- [38] N. Winograd and B. J. Garrison, "Biological cluster mass spectrometry.," *Annu. Rev. Phys. Chem.*, vol. 61, pp. 305–322, 2010.
- [39] B. J. Garrison and Z. Postawa, "Computational view of surface based organic mass spectrometry," *Mass Spectrom. Rev.*, vol. 27, no. 27, pp. 289– 315, 2008.
- [40] Z. Postawa, B. Czerwinski, M. Szewczyk, E. J. Smiley, N. Winograd, and B. J. Garrison, "Enhancement of sputtering yields due to C<sub>60</sub> versus Ga bombardment of Ag{111} as explored by molecular dynamics simulations," *Anal. Chem.*, vol. 75, no. 17, pp. 4402–4407, 2003.
- [41] B. J. Garrison and Z. Postawa, "MD simulations, the theoretical partner to dynamic cluster SIMS experiments," in *TOF-SIMS: Materials analysis by mass spectrometry*, 2nd, Ed. Manchester: IM Publications, 2013, pp. 151–192.
- [42] L. Rzeznik, B. Czerwinski, B. J. Garrison, N. Winograd, and Z. Postawa, "Microscopic insight into the sputtering of thin polystyrene films on Ag{111} induced by large and slow Ar clusters," *J. Phys. Chem. C*, vol. 112, no. 2, pp. 521–531, 2008.
- [43] S. Ninomiya, K. Ichiki, H. Yamada, Y. Nakata, T. Seki, T. Aoki, and J. Matsuo, "The effect of incident energy on molecular depth profiling of polymers with large Ar cluster ion beams," *Surf. Interface Anal.*, vol. 43, no. 1–2, pp. 221–224, 2011.
- [44] C. Anders, H. M. Urbassek, and R. E. Johnson, "Linearity and additivity in cluster-induced sputtering: A molecular-dynamics study of van der Waals bonded systems," *Phys. Rev. B - Condens. Matter Mater. Phys.*, vol. 70, no. 15, pp. 1–6, 2004.
- [45] N. P. Barradas and C. Pascual-Izarra, "Double scattering in RBS analysis of PtSi thin films on Si," *Nucl. Instruments Methods Phys. Res. Sect. B Beam Interact. with Mater. Atoms*, vol. 228, no. 1–4 SPEC. ISS., pp. 378–382, 2005.
- [46] M. P. Seah, "Universal equation for argon gas cluster sputtering yields," *J. Phys. Chem. C*, vol. 117, no. 24, pp. 12622–12632, 2013.

- [47] C. Anders and H. M. Urbassek, "Effect of binding energy and mass in cluster-induced sputtering of van-der-Waals bonded systems," *Nucl. Instruments Methods Phys. Res. Sect. B Beam Interact. with Mater. Atoms*, vol. 228, no. 1–4 SPEC. ISS., pp. 84–91, 2005.
- [48] K. Moritani, G. Mukai, M. Hashinokuchi, and K. Mochiji, "Site-Specific Fragmentation of Polystyrene Molecule Using Size-Selected Ar Gas Cluster Ion Beam," *Appl. Phys. Express*, vol. 2, no. APRIL, p. 046001, 2009.
- [49] N. K. Dzhemilev, a. M. Goldenberg, I. V. Veriovkin, and S. V. Verkhoturov, "Fragmentation of cluster ions in SIMS: cluster distributions over lifetime, excitation energy and kinetic energy release," *Nucl. Instruments Methods Phys. Res. Sect. B Beam Interact. with Mater. Atoms*, vol. 114, no. 3–4, pp. 245–251, 1996.
- [50] B. Rocha, B. Cillero-Pastor, G. Eijkel, A. L. Bruinen, C. Ruiz-Romero, R. M. A. Heeren, and F. J. Blanco, "Characterization of lipidic markers of chondrogenic differentiation using mass spectrometry imaging," *Proteomics*, vol. 15, pp. 702–713, 2015.
- [51] P. Malmberg and H. Nygren, "Methods for the analysis of the composition of bone tissue, with a focus on imaging mass spectrometry (TOF-SIMS)," *Proteomics*, vol. 8, pp. 3755–3762, 2008.
- [52] E. de Hoffman and V. Stroobant, "Mass Analysers," in *Mass Spectrometry Principles and Applications*, 3rd ed., John Wiley & Sons, Ltd, 2007, pp. 85–167.
- [53] B. W. Schueler, "Time-of-flight mass analysers," in *TOF-SIMS: Materials analysis by mass spectrometry*, 2nd ed., J. C. Vickerman and D. Briggs, Eds. Manchester: IM Publications, 2013, pp. 247–270.
- [54] W. E. Stephens, "A Pulsed Mass Spectrometer with Time Dispersion," vol. 69, p. 691, 1946.
- [55] W. C. Wiley and I. H. McClaren, "Time-of-flight mass spectrometer with improved resolution," *Rev. Sci. Instrum.*, vol. 26, pp. 1150–1157, 1955.
- [56] R. Hill, "Analysis beams used in ToF-SIMS," in *TOF-SIMS: Materials analysis by mass spectrometry*, 2nd ed., J. C. Vickerman and D. Briggs, Eds. Manchester: IM Publications, 2013, pp. 271–290.

- [57] J. S. Fletcher, N. P. Lockyer, and J. C. Vickerman, "Developments in Molecular Sims Depth Profiling and 3d Imaging of Biological Systems Using Polyatomic Primary Ions," *Mass Spectrom. Rev.*, vol. 30, no. 30, pp. 142–174, 2011.
- [58] J. S. Fletcher, S. Rabbani, A. Henderson, P. Blenkinsopp, S. P. Thompson, N. P. Lockyer, and J. C. Vickerman, "A New Dynamic in Mass Spectral Imaging of Single Biological Cells," *Anal. Chem.*, vol. 80, no. 23, pp. 9058–9064, 2008.
- [59] A. Henderson, "Multivariate analysis of SIMS spectra," in *TOF-SIMS: Materials analysis by mass spectrometry*, 2nd ed., D. Vickerman, John C., Briggs, Ed. Manchester: IM Publications, 2013, pp. 449–484.
- [60] A. Henderson, J. S. Fletcher, and J. C. Vickerman, "A comparison of PCA and MAF for ToF-SIMS image interpretation," *Surf. Interface Anal.*, vol. 41, no. 8, pp. 666–674, 2009.
- [61] B. M. Wise and P. Geladi, "A Brief Introduction to Multivariate Image Analysis (MIA)," *Newsl. North Am. Chapter Int. Chemom. Soc.*, vol. 22, pp. 3–7, 2000.
- [62] D. J. Graham, M. S. Wagner, and D. G. Castner, "Information from complexity: Challenges of TOF-SIMS data interpretation," *Appl. Surf. Sci.*, vol. 252, no. 19, pp. 6860–6868, 2006.
- [63] M. Mudrov and a Proch, "Principal component analysis in image processing," *Inst. Chem. Technol. Prague ...*, no. 3, pp. 2–5, 2005.
- [64] J. Lee and I. S. Gilmore, "A Guide to the Practical Use of Multivariate Analysis in SIMS," 2010.
- [65] H. U. Jabs, G. Assmann, D. Greifendorf, and a Benninghoven, "High performance liquid chromatography and time-of-flight secondary ion mass spectrometry: a new dimension in structural analysis of apolipoproteins," *J. Lipid Res.*, vol. 27, no. 6, pp. 613–621, 1986.
- [66] A. Piwowar and N. Winograd, "Application of SIMS to study of biological systems," in *TOF-SIMS: Materials analysis by mass spectrometry*, 2013.
- [67] J. H. Jungmann and R. M. A. Heeren, "Emerging technologies in mass spectrometry imaging," *J. Proteomics*, vol. 75, no. 16, pp. 5077–5092, 2012.
- [68] E. R. Amstalden van Hove, D. F. Smith, and R. M. A. Heeren, "A concise review of mass spectrometry imaging," *J. Chromatogr. A*, vol. 1217, no. 25, pp. 3946–3954, 2010.



- [69] J. Pól, M. Strohalm, V. Havlíček, and M. Volný, "Molecular mass spectrometry imaging in biomedical and life science research," *Histochem. Cell Biol.*, vol. 134, no. 5, pp. 423–443, 2010.
- [70] A. Römpf and B. Spengler, "Mass spectrometry imaging with high resolution in mass and space," *Histochem. Cell Biol.*, vol. 139, no. 6, pp. 759–783, 2013.
- [71] R. E. O'brien, T. B. Nguyen, A. Laskin, J. Laskin, P. L. Hayes, S. Liu, J. L. Jimenez, L. M. Russell, S. a. Nizkorodov, and A. H. Goldstein, "Probing molecular associations of field-collected and laboratory-generated soa with nano-desi high-resolution mass spectrometry," *J. Geophys. Res. Atmos.*, vol. 118, no. 2, pp. 1042–1051, 2013.
- [72] J. Oetjen, K. Veselkov, J. Watrous, J. S. McKenzie, M. Becker, L. Hauberg-Lotte, J. H. Kobarg, N. Strittmatter, A. K. Mróz, F. Hoffmann, D. Trede, A. Palmer, S. Schiffler, K. Steinhorst, M. Aichler, R. Goldin, O. Guntinas-Lichius, F. von Eggeling, H. Thiele, K. Maedler, A. Walch, P. Maass, P. C. Dorrestein, Z. Takats, and T. Alexandrov, "Benchmark datasets for 3D MALDI- and DESI-imaging mass spectrometry," *Gigascience*, vol. 4, no. 1, 2015.
- [73] D. M. G. Anderson, Z. Ablonczy, Y. Koutalos, J. Spraggins, R. K. Crouch, R. M. Caprioli, and K. L. Schey, "High resolution MALDI imaging mass spectrometry of retinal tissue lipids," *J. Am. Soc. Mass Spectrom.*, vol. 25, no. 8, pp. 1394–1403, 2014.
- [74] M. El Ayed, D. Bonnel, R. Longuespée, C. Castelier, J. Franck, D. Vergara, A. Desmons, A. Tasiemski, A. Kenani, D. Vinatier, R. Day, I. Fournier, and M. Salzet, "MALDI imaging mass spectrometry in ovarian cancer for tracking, identifying, and validating biomarkers," *Med. Sci. Monit.*, vol. 16, no. 8, pp. BR233–R245, 2010.
- [75] M. Dhunna, "Desorption Electrospray Ionization Mass Spectrometry Imaging : Instrumentation , Optimization and Capabilities," 2014.
- [76] M. K. Passarelli and N. Winograd, "Lipid imaging with time-of-flight secondary ion mass spectrometry (ToF-SIMS)," *Biochim. Biophys. Acta - Mol. Cell Biol. Lipids*, vol. 1811, no. 11, pp. 976–990, 2011.
- [77] E. Claude and E. A. Jones, "Multiple , Sequential DESI Images from a Single Tissue Section at Different Spatial Resolution."
- [78] D. Gode and D. A. Volmer, "Lipid imaging by mass spectrometry - a review," *Analyst*, vol. 138, no. 5, pp. 1289–315, 2013.

- [79] L. S. Eberlin, C. R. Ferreira, A. L. Dill, D. R. Ifa, and R. G. Cooks, "Desorption electrospray ionization mass spectrometry for lipid characterization and biological tissue imaging," *Biochim. Biophys. Acta - Mol. Cell Biol. Lipids*, vol. 1811, no. 11, pp. 946–960, 2011.
- [80] L. S. Eberlin, D. R. Ifa, C. Wu, and R. G. Cooks, "Three-dimensional visualization of mouse brain by lipid analysis using ambient ionization mass spectrometry," *Angew. Chem. Int. Ed. Engl.*, vol. 49, no. 5, pp. 873–876, 2010.
- [81] A. Svatoš, "Mass spectrometric imaging of small molecules," *Trends Biotechnol.*, vol. 28, no. 8, pp. 425–434, 2010.
- [82] H. Ye, T. Greer, and L. Li, "From pixel to voxel: a deeper view of biological tissue by 3D mass spectral imaging," *Bioanalysis*, vol. 3, no. 3, pp. 313–332, 2011.
- [83] J. Stauber and R. M. Heeren, "Biological tissue imaging at different levels: MALDI and SIMS imaging combined," in *Surface analysis and techniques in Biology*, V. S. Smentkowski, Ed. NY: Springer International Publishing.
- [84] T. Porta, "Multimodal Molecular Mass Spectrometry Imaging – Development and Applications in Plant Biology and Forensic Toxicology," University of Geneva, 2013.
- [85] S. Takamori, K. Kong, S. Varma, I. Leach, H. C. Williams, and I. Nottingher, "Optimization of multimodal spectral imaging for assessment of resection margins during Mohs micrographic surgery for basal cell carcinoma," *Biomed. Opt. Express*, vol. 6, no. 1, p. 98, 2014.
- [86] R. Van de Plas, J. Yang, J. Spraggins, and R. M. Caprioli, "Image fusion of mass spectrometry and microscopy: a multimodality paradigm for molecular tissue mapping," *Nat. Methods*, vol. 12, no. 4, pp. 4–6, 2015.
- [87] E. H. Seeley and R. M. Caprioli, "Molecular imaging of proteins in tissues by mass spectrometry," *Proc. Natl. Acad. Sci. U. S. A.*, vol. 105, no. 47, pp. 18126–18131, 2008.
- [88] A. Römpf, J.-P. Both, A. Brunelle, R. M. a. Heeren, O. Laprévotte, B. Prideaux, A. Seyer, B. Spengler, M. Stoeckli, and D. F. Smith, "Mass spectrometry imaging of biological tissue: an approach for multicenter studies," *Anal. Bioanal. Chem.*, pp. 2329–2335, 2015.

- [89] E. R. A. Van Hove, T. R. Blackwell, I. Klinkert, G. B. Eijkel, R. M. a Heeren, and K. Glunde, "Multimodal mass spectrometric imaging of small molecules reveals distinct spatio-molecular signatures in differentially metastatic breast tumor models," *Cancer Res.*, vol. 70, no. 22, pp. 9012–9021, 2010.
- [90] J. Pierson, J. L. Norris, H. Aerni, P. Svenningsson, R. M. Caprioli, P. E. Andre, and P. E. Andrén, "Molecular Profiling of Experimental Parkinson's Disease: Direct Analysis of Peptides and Proteins on Brain Tissue Sections by MALDI Mass Spectrometry," *J. Proteome Res.*, vol. 3, no. 2, pp. 289–295, 2004.
- [91] A. Ljungdahl, J. Hanrieder, M. Fälth, J. Bergquist, and M. Andersson, "Imaging mass spectrometry reveals elevated nigral levels of dynorphin neuropeptides in L-DOPA-induced dyskinesia in rat model of Parkinson's disease," *PLoS One*, vol. 6, no. 9, 2011.
- [92] J. Hanrieder, A. Ljungdahl, and M. Andersson, "MALDI Imaging Mass Spectrometry of Neuropeptides in Parkinson's Disease," *J. Vis. Exp.*, no. 60, pp. 1–7, 2012.
- [93] L. Carlred, A. Gunnarsson, S. Solé-Domènech, B. Johansson, V. Vukojević, L. Terenius, A. Codita, B. Winblad, M. Schalling, F. Höök, and P. Sjövall, "Simultaneous imaging of amyloid- $\beta$  and lipids in brain tissue using antibody-coupled liposomes and time-of-flight secondary ion mass spectrometry," *J. Am. Chem. Soc.*, vol. 136, no. 28, pp. 9973–9981, 2014.
- [94] D. M. Forster, "Investigation of a transgenic model of Alzheimer's Disease, the TASTPM mouse, using magnetic resonance spectroscopy and matrix assisted laser desorption imaging," 2010.
- [95] S. S. Domènech, *Combining mass spectrometric tissue imaging with conventional histology: focus on Alzheimer's disease*. 2012.
- [96] Y. Liu, H. Qing, and Y. Deng, "Biomarkers in Alzheimer's disease analysis by mass spectrometry-based proteomics," *Int. J. Mol. Sci.*, vol. 15, no. 5, pp. 7865–7882, 2014.
- [97] A. N. Lazar, C. Bich, M. Panchal, N. Desbenoit, V. W. Petit, D. Touboul, L. Dauphinot, C. Marquer, O. Laprèvote, A. Brunelle, and C. Duyckaerts, "Time-of-flight secondary ion mass spectrometry (TOF-SIMS) imaging reveals cholesterol overload in

the cerebral cortex of Alzheimer disease patients,” *Acta Neuropathol.*, vol. 125, no. 1, pp. 133–144, 2013.

[98] F. Le Naour, M. P. Bralet, D. Debois, C. Sandt, C. Guettier, P. Dumas, A. Brunelle, and O. Laprévote, “Chemical imaging on liver steatosis using synchrotron infrared and ToF-SIMS microspectroscopies,” *PLoS One*, vol. 4, no. 10, 2009.

[99] D. Debois, M. Bralet, A. Brunelle, and O. Lapre, “In Situ Lipidomic Analysis of Nonalcoholic Fatty Liver by Cluster TOF-SIMS Imaging,” vol. 81, no. 8, pp. 2823–2831, 2009.

[100] K. Nishikawa, M. Hashimoto, Y. Itoh, S. Hiroi, A. Kusai, F. Hirata, T. Sakamoto, and K. Iwaya, “Detection of changes in the structure and distribution map of triacylglycerol in fatty liver model by MALDI-SpiralTOF,” *FEBS Open Bio*, vol. 4, pp. 179–184, 2014.

[101] D. Debois, M. Bralet, L. Naour, A. Brunelle, and O. Lapre, “In Situ Lipidomic Analysis of Nonalcoholic Fatty Liver by Cluster TOF-SIMS Imaging ac research In Situ Lipidomic Analysis of Nonalcoholic Fatty Liver by Cluster TOF-SIMS Imaging,” *Anal. Chem.*, vol. 81, no. 8, pp. 2823–2831, 2009.

[102] A. Seyer, M. Cantiello, J. Bertrand-Michel, V. Roques, M. Nauze, V. Bézirard, X. Collet, D. Touboul, A. Brunelle, and C. Coméra, “Lipidomic and Spatio-Temporal Imaging of Fat by Mass Spectrometry in Mice Duodenum during Lipid Digestion,” *PLoS One*, vol. 8, no. 4, 2013.

[103] L. Kuchar, H. Faltyskova, L. Krasny, R. Dobrovolny, H. Hulkova, J. Ledvinova, M. Volny, M. Strohalm, K. Lemr, L. Kryspinova, B. Asfaw, J. Rybová, R. J. Desnick, and V. Havlicek, “Fabry disease: renal sphingolipid distribution in the  $\alpha$ -Gal A knockout mouse model by mass spectrometric and immunohistochemical imaging,” *Anal. Bioanal. Chem.*, vol. 407, no. 8, pp. 2283–2291, 2014.

[104] K. Onoue, N. Zaima, Y. Sugiura, T. Isojima, S. Okayama, M. Horii, Y. Akai, S. Uemura, G. Takemura, H. Sakuraba, Y. Sakaguchi, M. Setou, and Y. Saito, “Using Imaging Mass Spectrometry to Accurately Diagnose Fabry’s Disease,” *Circ. J.*, vol. 75, no. 1, pp. 221–223, 2011.

[105] R. Madonna, C. Cevik, and N. Cocco, “Multimodality imaging for pre-clinical assessment of Fabry’s cardiomyopathy,” *Eur. Heart J. Cardiovasc. Imaging*, pp. 1094–1100, 2014.

- [106] N. Zaima, N. Goto-Inoue, and T. Moriyama, "Matrix-Assisted Laser Desorption/Ionization Imaging Mass Spectrometry: New Technology for Vascular Pathology," *J. Vasc. Res.*, vol. 51, no. 2, pp. 144–148, 2014.
- [107] S. Mas, D. Touboul, A. Brunelle, P. Aragoncillo, J. Egido, O. Laprévotte, and F. Vivanco, "Lipid cartography of atherosclerotic plaque by cluster-TOF-SIMS imaging," *Analyst*, vol. 132, no. 1, pp. 24–26, 2007.
- [108] D. Touboul, S. Roy, D. P. Germain, P. Chaminade, A. Brunelle, and O. Laprévotte, "MALDI-TOF and cluster-TOF-SIMS imaging of Fabry disease biomarkers," *Int. J. Mass Spectrom.*, vol. 260, no. 2–3, pp. 158–165, 2007.
- [109] N. Tahallah, A. Brunelle, S. De La Porte, and O. Laprévotte, "Lipid mapping in human dystrophic muscle by cluster-time-of-flight secondary ion mass spectrometry imaging," *J. Lipid Res.*, vol. 49, no. 2, pp. 438–454, 2008.
- [110] M. J. Peffers, B. Cillero-Pastor, G. B. Eijkel, P. D. Clegg, and R. M. Heeren, "Matrix assisted laser desorption ionization mass spectrometry imaging identifies markers of ageing and osteoarthritic cartilage," *Arthritis Res. Ther.*, vol. 16, no. 3, p. R110, 2014.
- [111] E. Q. Blatherwick, G. J. Van Berkel, K. Pickup, M. K. Johansson, M.-E. Beaudoin, R. O. Cole, J. M. Day, S. Iverson, I. D. Wilson, J. H. Scrivens, and D. J. Weston, "Utility of spatially-resolved atmospheric pressure surface sampling and ionization techniques as alternatives to mass spectrometric imaging (MSI) in drug metabolism," *Xenobiotica*, vol. 41, no. 8, pp. 720–734, 2011.
- [112] O. Klein, K. Strohschein, H. Thiele, T. Alexandrov, S. Geissler, P. Giavalisco, P. Von Roth, and J. Klose, "MALDI-Imaging mass spectrometry: Discrimination of pathophysiological regions in traumatized skeletal muscle by characteristic peptide signatures," pp. 1–27, 2014.
- [113] M. Lalowski, F. Magni, and E. Monogioudi, "Imaging mass spectrometry : a new tool for kidney disease investigations," no. April, pp. 1648–1656, 2013.
- [114] M. Lalowski, F. Magni, V. Mainini, E. Monogioudi, A. Gotsopoulos, R. Soliymani, C. Chinello, and M. Baumann, "Imaging mass spectrometry: a new tool for kidney disease investigations," *Nephrol. Dial. Transplant*, vol. 28, no. 7, pp. 1648–56, 2013.
- [115] A. Nilsson, B. Forngren, S. Bjurström, R. J. Goodwin, E. Basmaci, I. Gustafsson, A. Annas, D. Hellgren, A. Svanhagen, P. E. Andrén, and J. Lindberg, "In Situ Mass Spectrometry Imaging and Ex Vivo Characterization of Renal Crystalline Deposits

Induced in Multiple Preclinical Drug Toxicology Studies," *PLoS One*, vol. 7, no. 10, pp. 1–10, 2012.

[116] H. Ruh, T. Salonikios, J. Fuchser, M. Schwartz, and C. Sticht, "MALDI imaging MS reveals candidate lipid markers of polycystic kidney disease Abstract Autosomal recessive polycystic kidney disease is a severe , monogenetically inherited kidney and liver."

[117] M. Kawashima, N. Iwamoto, N. Kawaguchi-Sakita, M. Sugimoto, T. Ueno, Y. Mikami, K. Terasawa, T. A. Sato, K. Tanaka, K. Shimizu, and M. Toi, "High-resolution imaging mass spectrometry reveals detailed spatial distribution of phosphatidylinositols in human breast cancer," *Cancer Sci.*, vol. 104, no. 10, pp. 1372–1379, 2013.

[118] D. Calligaris, D. Caragacianu, X. Liu, I. Norton, C. J. Thompson, a. L. Richardson, M. Golshan, M. L. Easterling, S. Santagata, D. a. Dillon, F. a. Jolesz, and N. Y. R. Agar, "Application of desorption electrospray ionization mass spectrometry imaging in breast cancer margin analysis," *Proc. Natl. Acad. Sci.*, vol. 111, no. 42, pp. 15184–15189, 2014.

[119] T. J. A. Dekker, B. D. Ballu, E. A. Jones, D. Scho, M. Schmitt, M. Aubele, J. R. Kroep, V. T. H. B. M. Smit, R. A. E. M. Tollenaar, W. E. Mesker, A. Walch, and L. A. McDonnell, "Multicenter Matrix-Assisted Laser Desorption / Ionization Mass Spectrometry Imaging ( MALDI MSI ) Identifi es Proteomic Di ff erences in Breast-Cancer-Associated Stroma," 2014.

[120] S. Rauser, C. Marquardt, B. Balluff, C. Albers, E. Belau, R. Hartmer, D. Suckau, K. Specht, M. P. Ebert, M. Schmitt, M. Aubele, H. Ho, and A. Walch, "Classification of HER2 Receptor Status in Breast Cancer Tissues by MALDI Imaging Mass Spectrometry research articles," *J. Proteome Res.*, vol. 9, pp. 1854–1863, 2010.

[121] S. Steurer, C. Borkowski, S. Odinga, M. Buchholz, C. Koop, H. Huland, M. Becker, M. Witt, D. Trede, M. Omid, O. Kraus, A. S. Bahar, a S. Seddiqi, J. M. Singer, M. Kwiatkowski, M. Trusch, R. Simon, M. Wurlitzer, S. Minner, T. Schlomm, G. Sauter, and H. Schlüter, "MALDI mass spectrometric imaging based identification of clinically relevant signals in prostate cancer using large-scale tissue microarrays.," *Int. J. Cancer*, vol. 133, no. 4, pp. 920–8, 2013.

- [122] E.-M. Spur, E. a Decelle, and L. L. Cheng, "Metabolomic imaging of prostate cancer with magnetic resonance spectroscopy and mass spectrometry.," *Eur. J. Nucl. Med. Mol. Imaging*, vol. 40 Suppl 1, pp. S60–71, 2013.
- [123] L. S. Eberlin, A. L. Dill, A. B. Costa, D. R. Ifa, L. Cheng, T. Masterson, M. Koch, T. L. Ratliff, and R. . G. Cooks, "Letters to Analytical Chemistry Cholesterol Sulfate Imaging in Human Prostate Cancer Tissue by Desorption Electrospray Ionization Mass Spectrometry," *Society*, vol. 82, no. 9, pp. 3430–3434, 2010.
- [124] D. Miura, Y. Fujimura, and H. Wariishi, "In situ metabolomic mass spectrometry imaging: Recent advances and difficulties," *J. Proteomics*, vol. 75, no. 16, pp. 5052–5060, 2012.
- [125] P. Chaurand, M. A. Rahman, T. Hunt, J. A. Mobley, G. Gu, J. C. Latham, R. M. Caprioli, and S. Kasper, "Monitoring mouse prostate development by profiling and imaging mass spectrometry.," *Mol. Cell. Proteomics*, vol. 7, no. 2, pp. 411–423, 2008.
- [126] M. A. Merlos Rodrigo, O. Zitka, S. Krizkova, A. Moulick, V. Adam, and R. Kizek, "MALDI-TOF MS as evolving cancer diagnostic tool: A review," *J. Pharm. Biomed. Anal.*, vol. 95, pp. 245–255, 2014.
- [127] S. Meding, K. Martin, O. J. R. Gustafsson, J. S. Eddes, S. Hack, M. K. Oehler, and P. Hoffmann, "Tryptic peptide reference data sets for MALDI imaging mass spectrometry on formalin-fixed ovarian cancer tissues," *J. Proteome Res.*, vol. 12, no. 1, pp. 308–315, 2013.
- [128] F. Leung, N. Musrap, E. P. Diamandis, and V. Kulasingam, "Advances in mass spectrometry-based technologies to direct personalized medicine in ovarian cancer," *Transl. Proteomics*, vol. 1, no. 1, pp. 74–86, 2013.
- [129] R. Longuespee, C. Boyon, O. Kerdraon, D. Vinatier, I. Fournier, R. Day, and M. Salzet, "Ovarian Cancer Biomarkers," pp. 3–11.
- [130] N. Desbenoit, E. Saussereau, C. Bich, M. Bourderioux, J. Fritsch, A. Edelman, A. Brunelle, and M. Ollero, "Localized lipidomics in cystic fibrosis: TOF-SIMS imaging of lungs from *Pseudomonas aeruginosa*-infected mice," *Int. J. Biochem. Cell Biol.*, vol. 52, pp. 77–82, 2014.
- [131] G. Marko-Varga, T. E. Fehniger, M. Rezeli, B. Döme, T. Laurell, and Á. Végvári, "Drug localization in different lung cancer phenotypes by MALDI mass spectrometry imaging," *J. Proteomics*, vol. 74, no. 7, pp. 982–992, 2011.

- [132] Á. Végvári, T. E. Fehniger, M. Rezeli, T. Laurell, B. Döme, B. Jansson, C. Welinder, and G. Marko-Varga, "Experimental models to study drug distributions in tissue using MALDI mass spectrometry imaging," *J. Proteome Res.*, vol. 12, no. 12, pp. 5626–5633, 2013.
- [133] S. Ocak, P. Chaurand, and P. P. Massion, "Mass spectrometry-based proteomic profiling of lung cancer," *Proc. Am. Thorac. Soc.*, vol. 6, no. 2, pp. 159–170, 2009.
- [134] F. Taguchi, B. Solomon, V. Gregorc, H. Roder, R. Gray, K. Kasahara, M. Nishio, J. Brahmer, A. Spreafico, V. Ludovini, P. P. Massion, R. Dziadziuszko, J. Schiller, J. Grigorieva, M. Tsypin, S. W. Hunsucker, R. Caprioli, M. W. Duncan, F. R. Hirsch, P. a. Bunn, and D. P. Carbone, "Mass spectrometry to classify non-small-cell lung cancer patients for clinical outcome after treatment with epidermal growth factor receptor tyrosine kinase inhibitors: a multicohort cross-institutional study," *J. Natl. Cancer Inst.*, vol. 99, no. 11, pp. 838–846, 2007.
- [135] M. Brulet, A. Seyer, A. Edelman, A. Brunelle, J. Fritsch, M. Ollero, and O. Laprévote, "Lipid mapping of colonic mucosa by cluster TOF-SIMS imaging and multivariate analysis in cfr knockout mice," *J. Lipid Res.*, vol. 51, no. 10, pp. 3034–3045, 2010.
- [136] K. a Veselkov, R. Mirnezami, N. Strittmatter, R. D. Goldin, J. Kinross, A. V. M. Speller, T. Abramov, E. a Jones, A. Darzi, E. Holmes, J. K. Nicholson, and Z. Takats, "Chemo-informatic strategy for imaging mass spectrometry-based hyperspectral profiling of lipid signatures in colorectal cancer," *Proc. Natl. Acad. Sci. U. S. A.*, vol. 111, no. 3, pp. 1216–21, 2014.
- [137] S. Shimma, Y. Sugiura, T. Hayasaka, Y. Hoshikawa, T. Noda, and M. Setou, "MALDI-based imaging mass spectrometry revealed abnormal distribution of phospholipids in colon cancer liver metastasis," *J. Chromatogr. B Anal. Technol. Biomed. Life Sci.*, vol. 855, no. 1 SPEC. ISS., pp. 98–103, 2007.
- [138] P. H. Pevsner, J. Melamed, T. Remsen, A. Kogos, F. Francois, P. Kessler, A. Stern, and S. Anand, "Mass spectrometry MALDI imaging of colon cancer biomarkers: a new diagnostic paradigm," *Biomark. Med.*, vol. 3, no. 1, pp. 55–69, 2009.
- [139] K. Chughtai, L. Jiang, T. R. Greenwood, K. Glunde, and R. M. A. Heeren, "Mass Spectrometry Images Acylcarnitines, Phosphatidylcholines and Sphingomyelin in MDA-MB-231 Breast Tumor Models," *J. Lipid Res.*, vol. 54, pp. 333–344, 2012.



- [140] G. De Sio, A. J. Smith, M. Galli, M. Garancini, C. Chinello, F. Bono, F. Pagni, and F. Magni, "A MALDI-Mass Spectrometry Imaging method applicable to different formalin-fixed paraffin-embedded human tissues," *Mol. BioSyst.*, vol. 11, pp. 1507–1514, 2015.
- [141] D. Touboul, O. Laprevote, and A. Brunelle, "Medical and biological applications of cluster ToF-SIMS," in *TOF-SIMS: Materials analysis by mass spectrometry*, 2nd ed., D. Vickerman, John C., Briggs, Ed. Manchester: IM Publications, 2013, pp. 583–612.
- [142] C. Bich, S. Vianello, V. Guérineau, D. Touboul, S. De La Porte, and a. Brunelle, "Compatibility between TOF-SIMS lipid imaging and histological staining on a rat brain section," *Surf. Interface Anal.*, vol. 45, no. 1, pp. 260–263, 2013.
- [143] M. Angelo, S. C. Bendall, R. Finck, M. B. Hale, C. Hitzman, A. D. Borowsky, R. M. Levenson, J. B. Lowe, S. D. Liu, S. Zhao, Y. Natkunam, and G. P. Nolan, "Multiplexed ion beam imaging of human breast tumors.," *Nat. Med.*, vol. 20, no. 4, pp. 436–42, 2014.
- [144] A. Bloom and N. Winograd, "Dye-enhanced imaging of mammalian cells with SIMS," *Surf. Interface Anal.*, vol. 46, no. S1, pp. 177–180, 2014.
- [145] C.-Y. Lee, G. M. Harbers, D. W. Grainger, L. J. Gamble, and D. G. Castner, "Fluorescence, XPS, and TOF-SIMS surface chemical state image analysis of DNA microarrays," *J. Am. Chem. Soc.*, vol. 129, no. 30, pp. 9429–9438, 2007.
- [146] W. M. Abdelmoula, K. Skrášková, B. Balluff, R. J. Carreira, E. a Tolner, B. F. P. Lelieveldt, L. van der Maaten, H. Morreau, A. M. J. M. van den Maagdenberg, R. M. a Heeren, L. a McDonnell, and J. Dijkstra, "Automatic Generic Registration of Mass Spectrometry Imaging Data to Histology using Nonlinear Stochastic Embedding," *Anal. Chem.*, 2014.
- [147] E. A. Jones, N. P. Lockyer, and J. C. Vickerman, "Depth profiling brain tissue sections with a 40 keV C60 + primary ion beam," *Anal. Chem.*, vol. 80, no. 6, pp. 2125–2132, 2008.
- [148] J. S. Fletcher, X. A. Conlan, E. A. Jones, G. Biddulph, N. P. Lockyer, and J. C. Vickerman, "TOF-SIMS Analysis Using C 60 . Effect of Impact Energy on Yield and Damage," vol. 78, no. 6, pp. 1827–1831, 2006.
- [149] V. W. Petit, M. Réfrégiers, C. Guettier, F. Jamme, K. Sebanayakam, A. Brunelle, O. Laprévote, P. Dumas, and F. Le Naour, "Multimodal spectroscopy combining time-of-flight-secondary ion mass spectrometry, synchrotron-FT-IR, and synchrotron-UV

microspectroscopies on the same tissue section," *Anal. Chem.*, vol. 82, no. 9, pp. 3963–3968, 2010.

[150] J. Hanrieder, L. Carlred, A. G. Ewing, and S. Syvänen, "Multimodal Imaging Mass Spectrometry for Probing A  $\beta$  - Plaque Pathology in Transgenic Alzheimer ' s Disease Mice," vol. 84, no. 1, pp. 2–3, 2011.

[151] D. Y. Lee, B. P. Bowen, and T. R. Northen, "Mass spectrometry-based metabolomics, analysis of metabolite-protein interactions, and imaging," *Biotechniques*, vol. 49, no. 2, pp. 557–565, 2010.

[152] J. G. Swales, J. W. Tucker, N. Strittmatter, A. Nilsson, D. Cobice, M. R. Clench, C. L. Mackay, and P. E. Andren, "Mass Spectrometry Imaging of Cassette-Dosed Drugs for Higher Throughput Pharmacokinetic and Biodistribution Analysis," *Anal. Chem.*, vol. 86, no. 8, p. 8473–8480, 2014.

[153] T. Greer, R. Sturm, and L. Li, "Mass spectrometry imaging for drugs and metabolites," *J. Proteomics*, vol. 74, no. 12, pp. 2617–2631, 2011.

[154] S. Nimesh, S. Mohottalage, R. Vincent, and P. Kumarathasan, "Current status and future perspectives of mass spectrometry imaging," *Int. J. Mol. Sci.*, vol. 14, no. 6, pp. 11277–11301, 2013.

[155] J. Liu, J. Gingras, K. P. Ganley, R. Vismeh, Y. Teffera, and Z. Zhao, "Whole-body tissue distribution study of drugs in neonate mice using desorption electrospray ionization mass spectrometry imaging," *Rapid Commun. Mass Spectrom.*, vol. 28, no. 2, pp. 185–90, 2014.

[156] N. Vinayavekhin and A. Saghatelian, "Untargeted metabolomics," *Curr. Protoc. Mol. Biol.*, no. SUPPL. 90, pp. 1–24, 2010.

[157] M. Sideris and S. Papagrigoriadis, "Molecular biomarkers and classification models in the evaluation of the prognosis of colorectal cancer.," *Anticancer Res.*, vol. 34, no. 5, pp. 2061–8, 2014.

[158] H. D. Bean, J. E. Hill, and J.-M. D. Dimandja, "Improving the quality of biomarker candidates in untargeted metabolomics via peak table-based alignment of comprehensive two-dimensional gas chromatography-mass spectrometry data," *J. Chromatogr. A*, vol. 1394, pp. 111–117, 2015.

- [159] E. Gorrochategui, J. Casas, C. Porte, S. Lacorte, and R. Tauler, "Chemometric strategy for untargeted lipidomics: Biomarker detection and identification in stressed human placental cells," *Anal. Chim. Acta*, vol. 854, pp. 20–33, 2015.
- [160] R. D. Smith, "Mass spectrometry in biomarker applications: From untargeted discovery to targeted verification, and implications for platform convergence and clinical application," *Clin. Chem.*, vol. 58, no. 3, pp. 528–530, 2012.
- [161] H. C. Köfeler, A. Fauland, G. N. Rechberger, and M. Trötz Müller, "Mass Spectrometry Based Lipidomics: An Overview of Technological Platforms," *Metabolites*, vol. 2, no. 1, pp. 19–38, 2012.
- [162] J. L. Denbigh and N. P. Lockyer, "ToF-SIMS as a tool for profiling lipids in cancer and other diseases," *Mater. Sci. Technol.*, vol. 31, no. 2, pp. 137–147, 2015.
- [163] D. Touboul and A. Brunelle, "Mass Spectrometry Imaging of Small Molecules," vol. 1203, 2015.
- [164] K. Schmelzer, E. Fahy, S. Subramaniam, and E. a. Dennis, "The Lipid Maps Initiative in Lipidomics," *Methods Enzymol.*, vol. 432, no. 07, pp. 171–183, 2007.
- [165] M. K. Passarelli, A. G. Ewing, and N. Winograd, "Single-cell lipidomics: Characterizing and imaging lipids on the surface of individual *Aplysia californica* neurons with cluster secondary ion mass spectrometry," *Anal. Chem.*, vol. 85, no. 4, pp. 2231–2238, 2013.
- [166] D. Touboul, A. Brunelle, and O. Laprévote, "Mass spectrometry imaging: Towards a lipid microscope?," *Biochimie*, vol. 93, no. 1, pp. 113–119, 2011.
- [167] G. J. Siegel, B. W. Agranoff, R. W. Albers, S. K. Fisher, and M. D. Uhler., *Basic Neurochemistry, Molecular, Cellular and Medical Aspects*, 6th ed. Philadelphia: Lippincott-Raven, 1999.
- [168] J. S. O'Brien and E. L. Sampson, "Lipid composition of the normal human brain: gray matter, white matter, and myelin.," *J. Lipid Res.*, vol. 6, no. 4, pp. 537–544, 1965.
- [169] J. B. German, L. A. Gillies, J. T. Smilowitz, A. M. Zivkovic, and S. M. Watkins, "Lipidomics and lipid profiling in metabolomics.," *Curr. Opin. Lipidol.*, vol. 18, no. 1, pp. 66–71, 2007.

- [170] P. Sjövall, B. Johansson, and J. Lausmaa, "Localization of lipids in freeze-dried mouse brain sections by imaging TOF-SIMS," *Appl. Surf. Sci.*, vol. 252, no. 19, pp. 6966–6974, 2006.
- [171] L. A. McDonnell, S. R. Piersma, A. F. MaartenAltelaar, T. H. Mize, S. L. Luxembourg, P. D. E. M. Verhaert, J. van Minnen, and R. M. A. Heeren, "Subcellular imaging mass spectrometry of brain tissue.," *J. Mass Spectrom.*, vol. 40, no. 2, pp. 160–168, 2005.
- [172] T. B. Angerer, P. Blenkinsopp, and J. S. Fletcher, "High energy gas cluster ions for organic and biological analysis by time-of-flight secondary ion mass spectrometry," *Int. J. Mass Spectrom.*, vol. 377, pp. 591–598, 2015.
- [173] A. Bodzon-kulakowska, A. Kiss, K. Chughtai, and R. M. A. Heeren, "DISTRIBUTION OF CHOLESTEROL IN THE BRAIN TISSUE AS AN EXAMPLE OF TOF-SIMS ANALYSIS," vol. 3, no. 1, pp. 1–11, 2011.
- [174] L. a. McDonnell, R. M. a Heeren, R. P. J. de Lange, and I. W. Fletcher, "Higher Sensitivity Secondary Ion Mass Spectrometry of Biological Molecules for High Resolution, Chemically Specific Imaging," *J. Am. Soc. Mass Spectrom.*, vol. 17, no. 9, pp. 1195–1202, 2006.
- [175] A. Brunelle, D. Touboul, and O. Laprévotte, "Biological tissue imaging with time-of-flight secondary ion mass spectrometry and cluster ion sources," *J. Mass Spectrom.*, vol. 40, no. 8, pp. 985–999, 2005.
- [176] I. Berrueta Razo, S. Sheraz, A. Henderson, N. P. Lockyer, and J. C. Vickerman, "Comparing C<sub>60</sub><sup>+</sup> and (H<sub>2</sub>O)<sub>n</sub><sup>+</sup> clusters for mouse brain tissue analysis," *Surf. Interface Anal.*, no. November 2013, p. n/a–n/a, 2014.
- [177] J. Brison, M. A. Robinson, D. S. W. Benoit, S. Muramoto, P. S. Stayton, and D. G. Castner, "TOF-SIMS 3D imaging of native and non-native species within hela cells," *Anal. Chem.*, vol. 85, no. 22, pp. 10869–10877, 2013.
- [178] B. Spengler, "Mass spectrometry imaging of biomolecular information.," *Anal. Chem.*, 2015.
- [179] M. D. Pour, "Optimizing Sample Preparation Protocols for Multi- Modal Imaging Mass Spectrometry (IMS)," no. xxxx, 2013.

- [180] M. Robinson and D. G. Castner, "Characterization of sample preparation methods of NIH/3T3 fibroblasts for ToF-SIMS analysis," *Biointerphases*, vol. 8, no. 1, p. 15, 2013.
- [181] J. Malm, D. Giannaras, M. O. Riehle, N. Gadegaard, and P. Sjövall, "Fixation and drying protocols for the preparation of cell samples for time-of-flight secondary ion mass spectrometry analysis," *Anal. Chem.*, vol. 81, no. 17, pp. 7197–7205, 2009.
- [182] A. Matros and H.-P. Mock, "Mass spectrometry based imaging techniques for spatially resolved analysis of molecules," *Front. Plant Sci.*, vol. 4, no. April, p. 89, 2013.
- [183] T. P. Roddy, D. M. Cannon, S. G. Ostrowski, N. Winograd, and A. G. Ewing, "Identification of cellular sections with imaging mass spectrometry following freeze fracture," *Anal. Chem.*, vol. 74, no. 16, pp. 4020–4026, 2002.
- [184] M. Fartmann, S. Dambach, C. Kriegeskotte, D. Lipinsky, H. P. Wiesmann, a. Wittig, W. Sauerwein, and H. F. Arlinghaus, "Subcellular imaging of freeze-fractured cell cultures by TOF-SIMS and Laser-SNMS," *Appl. Surf. Sci.*, vol. 203–204, pp. 726–729, 2003.
- [185] T. L. Colliver, C. L. Brummel, M. L. Pacholski, F. D. Swanek, a G. Ewing, and N. Winograd, "Atomic and molecular imaging at the single-cell level with TOF-SIMS," *Anal. Chem.*, vol. 69, no. 13, pp. 2225–2231, 1997.
- [186] T. P. Roddy, D. M. Cannon Jr., C. . Meserole, N. Winograd, and A. G. Ewing, "Imaging of freeze-fractured cells with in situ fluorescence and time-of-flight secondary ion mass spectrometry," *Anal Chem*, vol. 74, no. 16, pp. 4011–4019, 2002.
- [187] P. Malmberg, E. Jennische, D. Nilsson, and H. Nygren, "High-resolution, imaging TOF-SIMS: Novel applications in medical research," *Anal. Bioanal. Chem.*, vol. 399, no. 8, pp. 2711–2718, 2011.
- [188] E. S. Lee, H. K. Shon, T. G. Lee, S. H. Kim, and D. W. Moon, "The regional ratio of cholesteryl palmitate to cholesteryl oleate measured by ToF-SIMS as a key parameter of atherosclerosis," *Atherosclerosis*, vol. 226, no. 2, pp. 378–384, 2013.
- [189] P. Malmberg, K. Börner, Y. Chen, P. Friberg, B. Hagenhoff, J. E. Månsson, and H. Nygren, "Localization of lipids in the aortic wall with imaging TOF-SIMS," *Biochim. Biophys. Acta - Mol. Cell Biol. Lipids*, vol. 1771, no. 2, pp. 185–195, 2007.

- [190] C. Martel, D. Degli Esposti, A. Bouchet, C. Brenner, and A. Lemoine, "Non-Alcoholic Steatohepatitis: New Insights from OMICS Studies," *Curr. Pharm. Biotechnol.*, vol. 13, no. 5, pp. 726–735, 2012.
- [191] D. Touboul, A. Brunelle, F. Halgand, S. De La Porte, and O. Lapr  v  te, "Lipid imaging by gold cluster time-of-flight secondary ion mass spectrometry: application to Duchenne muscular dystrophy.," *J. Lipid Res.*, vol. 46, no. 7, pp. 1388–1395, 2005.
- [192] Z. Pernber, K. Richter, J. E. Mansson, and H. Nygren, "Sulfatide with different fatty acids has unique distributions in cerebellum as imaged by Time-Of-Flight Secondary Ion Mass Spectrometry (TOF-SIMS)," *Biochim. Biophys. Acta - Mol. Cell Biol. Lipids*, vol. 1771, no. 2, pp. 202–209, 2007.
- [193] S. Sol  -Dom  nech, P. Sj  vall, V. Vukojevi  , R. Fernando, A. Codita, S. Salve, N. Bogdanovi  , A. H. Mohammed, P. Hammarstr  m, K. P. R. Nilsson, F. M. Laferla, S. Jacob, P. O. Berggren, L. Gim  nez-Llort, M. Schalling, L. Terenius, and B. Johansson, "Localization of cholesterol, amyloid and glia in Alzheimer's disease transgenic mouse brain tissue using time-of-flight secondary ion mass spectrometry (ToF-SIMS) and immunofluorescence imaging," *Acta Neuropathol.*, vol. 125, no. 1, pp. 145–157, 2013.
- [194] C. L. Masters and D. J. Selkoe, "Biochemistry of amyloid beta-protein and amyloid deposits in Alzheimer disease," *Cold Spring Harb Perspect Med*, vol. 2, no. 6, p. a006262, 2012.
- [195] E. A. Jones, N. P. Lockyer, J. Kordys, and J. C. Vickerman, "Suppression and Enhancement of Secondary Ion Formation Due to the Chemical Environment in Static-Secondary Ion Mass Spectrometry," *J. Am. Soc. Mass Spectrom.*, vol. 18, no. 8, pp. 1559–1567, 2007.
- [196] C. M. John and R. W. Odom, "Static secondary ion mass spectrometry (SSIMS) of biological compounds in tissue and tissue-like matrices," *Int. J. Mass Spectrom. Ion Process.*, vol. 161, no. 1–3, pp. 47–67, 1997.
- [197] E. A. Jones, N. P. Lockyer, and J. C. Vickerman, "Mass spectral analysis and imaging of tissue by ToF-SIMS-The role of buckminsterfullerene, C60 +, primary ions," *Int. J. Mass Spectrom.*, vol. 260, no. 2–3, pp. 146–157, 2007.
- [198] A. M. Piwowar, N. P. Lockyer, and J. C. Vickerman, "Salt effects on ion formation in desorption mass spectrometry: An investigation into the role of alkali chlorides on

peak suppression in time-of-flight-secondary ion mass spectrometry," *Anal. Chem.*, vol. 81, no. 3, pp. 1040–1048, 2009.

[199] E. a. Jones, N. P. Lockyer, and J. C. Vickerman, "Suppression and enhancement of non-native molecules within biological systems," *Appl. Surf. Sci.*, vol. 252, no. 19, pp. 6727–6730, 2006.

[200] P. D. Piehowski, M. E. Kurczy, D. Willingham, M. L. Heien, N. Winograd, A. G. Ewing, and S. Parry, "Freeze-Etching and Vapor Matrix Deposition for ToF-SIMS Imaging of Single Cells Freeze-Etching and Vapor Matrix Deposition for ToF-SIMS Imaging of Single Cells," vol. 38, no. 8, pp. 7906–7911, 2008.

[201] X. A. . Conlan, N. P. Lockyer, and J. C. Vickerman, "Is proton cationization promoted by polyatomic primary ion bombardment during time-of-flight secondary ion mass spectrometry analysis of frozen aqueous solutions?," *Rapid Commun. Mass Spectrom.*, vol. 20, no. 8, pp. 1327–1334, 2006.

[202] S. Sheraz née Rabbani, I. Berrueta Razo, T. Kohn, N. P. Lockyer, and J. C. Vickerman, "Enhancing Ion Yields in Time-of-Flight-Secondary Ion Mass Spectrometry: A Comparative Study of Argon and Water Cluster Primary Beams," *Anal. Chem.*, vol. 87, no. 4, pp. 2367–2374, 2015

[203] A.G. Shard, R. Foster, I. S. Gilmore, J. L. S. Lee, S. Ray and L. Yang, " VAMAS interlaboratory study on organic depth profiling. Part I: Preliminary report", *Surf. Interface Anal.* 2011, vol. 43. pp 510-513.

[204] H. Nyren, K. Börner, P. Malmberg and B. Hagenhoff. "Localization of Cholesterol in Rat Cerebellum with Imaging TOF-SIMS. Effect of tissue preparation", SIMX XV proceedings paper, Manchester, 2005.

### 3 Instrumentation

ToF-SIMS analytical instrumentation is constantly under development to meet specific requirements for organic and inorganic research. Typically, a ToF-SIMS instrument consists of:

- One or more ion guns with which to produce the analysis beam
- A column to accelerate the primary ions and focus the analysis beam
- An analysis chamber under high vacuum
- A series of electrostatic lenses for secondary ion extraction
- A time-of-flight mass analyser with a particle detector.

Specific features of these components may vary according to the manufacturer and the type of study intended for each instrument [1]. Ionoptika Ltd. (Southampton, UK) and the SIMS group at the University of Manchester have collaborated to design and develop a high performance ToF-SIMS instrument for biological analysis. The J105 3D chemical imager is an instrument equipped with two primary ion guns. These provide 40 keV  $C_{60}^+$  and 20 keV  $Ar_n^+$ ,  $(H_2O)_n^+$  and  $(H_2O)Ar_n^+$  on continuum (dc) mode for high mass and spatial resolution and 3D analysis and a 1 keV electron gun (IOE 10 Electron Gun, Ionoptika) for charge neutralisation [3]. This chapter introduces the characteristics of this instrument and how these benefit the experiments presented in this thesis.

#### 3.1 Mass resolution

When two ion peaks have similar mass-to-charge ratios, high mass resolution may be required to distinguish them. For the analysis of complex molecules, high mass resolution is required for peak assignment due to the presence of many ion peaks with similar masses. The mass resolution can be calculated from two ion peaks with similar masses (Figure 3.1) using the following equation (Equation 3.1 [3]):

*Equation 3.1*

$$\text{Mass resolution (ppm)} = \frac{M}{\Delta M} = \frac{M}{M_1 - M_2} \times 10^6$$

Where  $M_1$  is the  $m/z$  from the first ion and  $M_2$  is the  $m/z$  from the second ion peak.



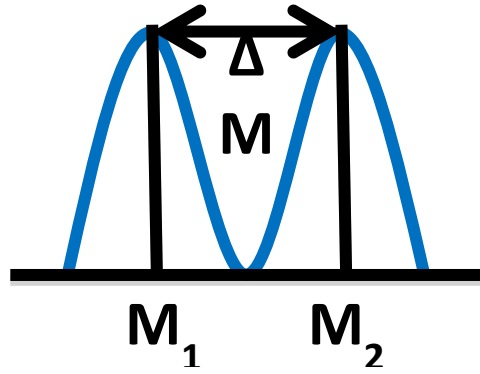


Figure 3.1: Illustration of two peaks with similar masses. The minimum difference between the masses of two different ion peaks close to each other is used to calculate the mass resolution in Equation 3.1. The peaks are not necessarily on the baseline.

### 3.1.1 Obtainable mass resolution with different ToF-SIMS configurations

In a conventional ToF-SIMS instrument, the mass resolution depends on the pulse duration of the analysis beam [4]. The sputtering of all the secondary ions should happen at the same time so that a good mass resolution can be obtained. With pulsed beams, data acquisition with high mass resolution is possible with short primary ion beam pulses  $\sim 1$  ns, although spatial resolution will be severely hampered due to the instability of the primary ion beam [4].

A long pulse would result in a more stable beam probe with a steady spot size rastering the sample, although in this case the ion peaks are less well resolved in time (mass). Consequently, it is not possible to have both high mass resolution and spatial resolution simultaneously with pulsed primary ion beams [5].

In, the J105-3D chemical imager (described in section 2.4), the primary ion beam is operated on DC mode and the secondary ion generation is separated from the mass spectrometry process. As such, the constant flux of secondary ions is extracted, collisionally cooled and filtered in a quadrupole and an electrostatic analyser (ESA) before being injected into a buncher with a 1 eV energy spread. The ion packet ejected from the buncher is then accelerated and focused into the reflectron where the secondary ions will travel according to their masses and charge before hitting the detector. All the ions are contained in the packet with the same energy spread, determined by their axial distribution in the buncher at the time of ion ejection. Thus high mass resolving power is maintained at all times ( $\frac{M}{\Delta M} \sim 6000$ ).

### 3.2 Mass accuracy

Mass accuracy is the similarity in mass the recorded  $m/z$  and the actual mass. It is usually measured in parts per million (ppm) [6]. In some ToF-SIMS mass spectrometers, mass accuracy is affected by the constant mass calibration in every experiment. For instance, if the specimen is not flat, the secondary ions will be extracted from different positions with different flight times and different energy spread, hence mass calibration is required in each spectrum[5]. The J105 mass spectrometer is capable of providing 5 ppm of mass accuracy due to the continuous particle sputtering and extraction and the subsequent injection of the secondary ions into the ToF [2], [5].

### 3.3 The duty cycle

The duty cycle is the percentage of real time in which the analysis beam is on. It is determined by the length and frequency of the beam pulses; it is a main factor when calculating the duration of an experiment [4].

In a conventional ToF-SIMS experiment the duty cycle is selected according to the desired experimental parameters such as mass resolution (pulse duration) and lateral resolution (beam current and pulse length). The primary ion dose conditions applied to the analysis will be determined by the useful secondary ion yield obtained from the sample i.e. the primary ion dose applied could exceed the static limit to obtain more secondary ion signal from the analyte [4].

The primary ion beams in the J105 instrument are not pulsed and the analysis speed is not limited by the duty cycle, reducing considerably the data acquisition time. Without time limitations, it is feasible to analyse the sample beyond the static limit such that the sample can be fully consumed during the experiment to obtain useful secondary ion signal. The analysis of samples beyond the static limit is possible with polyatomic beams, thus, this instrument has been designed to make optimum use of these type of beams [7].

### 3.4 The J105-3D Chemical imager

A schematic of the J105-3D chemical imager is illustrated by Figure 3.2. The sample is first inserted to the Preparation chamber through the sample entry port. This chamber has a provision for cold sample handling and freeze-fracture. The experimental setup is achieved by navigating the sample using camera-assisted sample positioning. The

specimen is then transferred to the sample analysis chamber (SAC) via software-controlled automated sample handling. Once on the analysis stage, the sample is sputtered by the analysis beam: 5-40 keV  $C_{60}^+$  and 5-20 kV  $Ar_n^+$ ,  $(H_2O)_n^+$  or  $(H_2O)Ar_n^+$ .

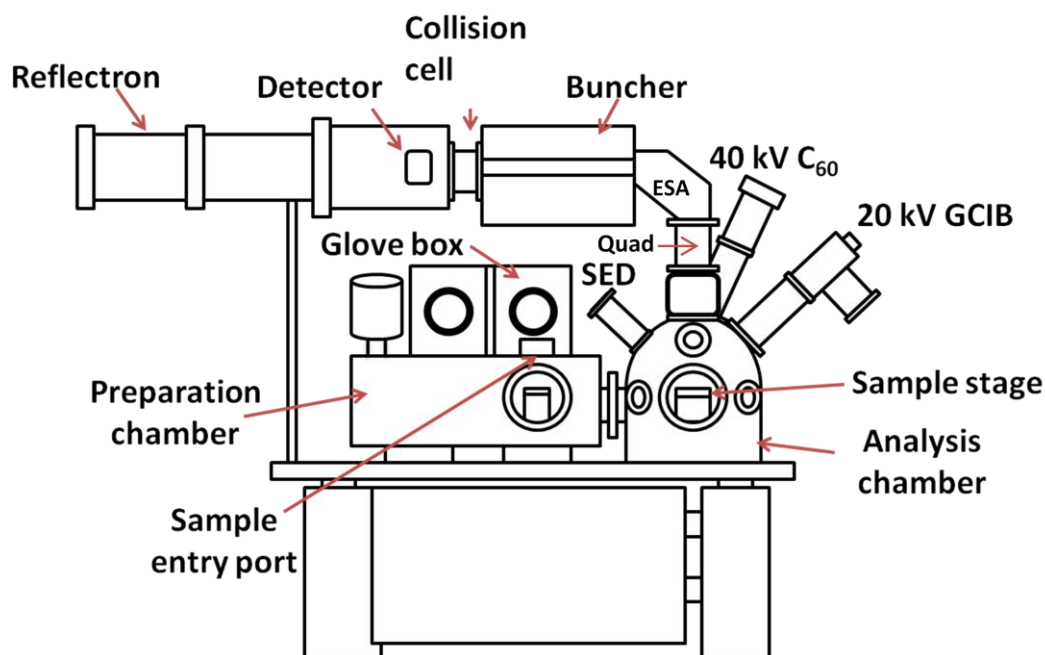


Figure 3.2: Diagram of the J105 3D-Chemical imager [7].

### 3.4.1 Operation of the J105 instrument

A buncher-ToF variant has been developed for the J105 instrument. Instead of extracting the secondary ions directly into the reflectron, as with other ToF systems, the J105 features apply secondary ion pre-treatment with a quadrupole and ESA arrangement, before being injected into the buncher-ToF. When particles are desorbed from the material, the secondary ion beam is extracted and cooled by collision gas ( $N_2$ ) in a RF-only mode quadrupole. Here, any light ions are blanked from the beam path. Any excess energy spread is filtered by an electrostatic analyser (ESA). This process results in the reduction of the secondary ion energy spread from 100 eV to 1 eV before the ions are injected into the linear buncher. Subsequently, the secondary ions are orthogonally injected into a linear buncher.

The buncher-ToF is illustrated in Figure 3.3. The linear buncher is  $\sim 30$  cm in length and accommodates 30 plates with 60 electrodes with 30 coupled apertures, one in each plate, which are pulsed every 100  $\mu s$  with a potential field arranged to form a time focus (ion packet) after the collision cell [2]. The voltage of each plate can be adjusted separately for the optimisation of the accelerating field which affects the spatial and temporal reduction of the primary ion packet [8].

In a SIMS experiment, the buncher collects secondary ions for 85  $\mu\text{s}$  and fires a packet within a 15  $\mu\text{s}$  interval [2], [8], [9]. During the 15  $\mu\text{s}$  period, an instantaneous accelerating field of 7 kV is applied at the entrance of the buncher and 1 kV at the exit. This accelerating field balances the kinetic energy of the ions and ensures that all ions are compressed in secondary ion pulse with high spread energy (6 keV). The spatial dimensions of the bunched ion pulse determine the mass resolution. Once outside the buncher, the ion packet is accelerated by a post-buncher acceleration voltage, which accelerates the ions into the ToF-mass analyser. Once the ion packet has been emitted, the cycle is repeated [10].

In the J105, the secondary ion pulse leaving the buncher has high spread energy of  $\sim 6$  keV, hence the need of a harmonic type reflectron to compensate for this high energy spread. A non-linear reflectron provides higher order energy focusing when very large secondary ion energy spreads have to be accommodated [11]. In this nonlinear “quadratic field” reflectron, the flight time of the secondary ions is independent of the initial energy spread of the bunched ions [11]. Here, the ions time-of-flight is decoupled from their kinetic energy by undergoing half a period of simple harmonic motion before reaching the detector. The ion mirror will have an electric potential proportional to the square of the distance to the mirror’s entrance. The time at which secondary ions reach the detector depends only on their  $m/z$  not their kinetic energy. [2], [11]–[13].

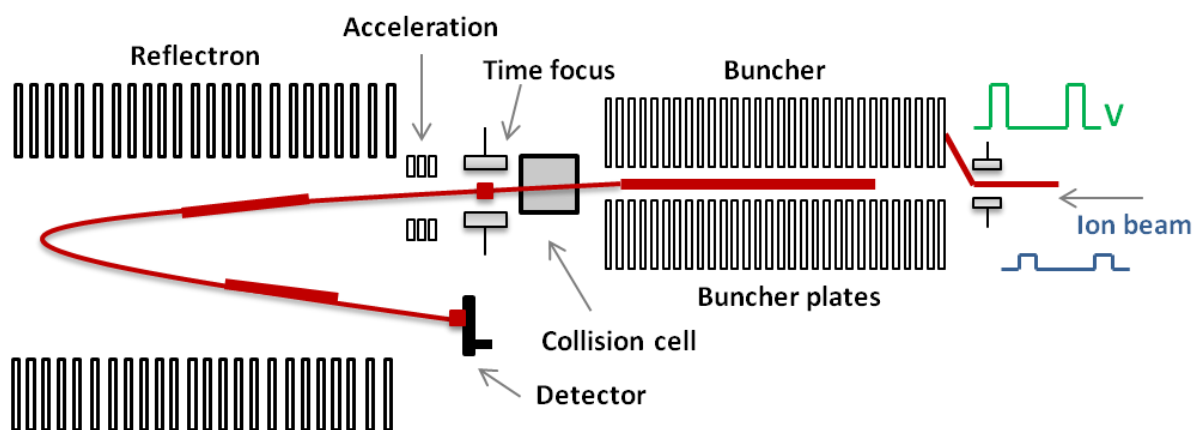


Figure 3.3: Schematic of the buncher-ToF mass analyser in the J105-3D chemical imager [2].

This configuration allows the use of tandem mass spectrometry (MS-MS) mode after the secondary ions exit the buncher [2]. The ion packet enters a gas collision cell situated between the buncher and the ToF-mass analyser (Figure 3.3) which fragments a selected parent ion for MS-MS mode. In normal MS mode, the collision cell rejects the ions that were not bunched [2], [9].

Secondary ion transmission refers to the number of produced ions that actually reach the detector [14]. In the J105, the transmission is related to the mass of the ions; some light ions passing through the buncher are blanked from the beam path. As a result, there is good transmission for bigger ions i.e. molecular ions and poor transmission of fragments [2]. The transmission in the buncher is given by the following equation:

*Equation 3.2*

$$Transmission = \frac{l}{t} \sqrt{\frac{m}{2Vq}} \times 100$$

Where:

$l$  = length of the buncher;

$t$  = buncher filling time;

$m$  = mass of the ion;

$V$  = transport voltage; and

$q$  = charge [2].

### **3.5 Analysis beams in the J105-3D Chemical Imager**

The ideal analysis beam would be able to deliver high spatial resolution with minimal damage to the material in any ToF-SIMS system. However, each ion beam has different characteristics depending on its chemical and physical nature and the instrument it is coupled with. Liquid Metal Ion Guns (LMIGs) provide the smallest spot diameters (~ 50 nm) but their use is limited by the static limit. Fullerene or large Gas Cluster Ion Beams (GCIB) can be applied to 3D analysis because bombardment-induced damage is comparatively low, although their spatial resolution is limited [4]. LMIGs are used in combination with GCIBs or C<sub>60</sub> guns to fully exploit their capabilities; a cluster ion beam is applied to sample etching while a liquid metal ion beam is used for sub-micrometric analysis [15].

In the J105-3D chemical imager, the selection of analysis beams was narrowed to 40 keV C<sub>60</sub> (IOG C60-40) and 20 keV GCIB (GCIB-20) beams. The system was initially supplied with and LMIG-40 that was later replaced with the GCIB-20 with the intention to explore the benefits of cluster analysis.

### 3.5.1 40 keV C<sub>60</sub> ion gun

The introduction of fullerene polyatomic sources is well suited to the analysis of organic materials due to their lower energy per atom, as explained in section 2.3.1.

The IOG C60-40 ion gun is an electron-bombardment type source capable of providing mass-selected C<sub>60</sub> ions with single, double or triple charge with up to 40 keV of beam energy. When the anode is run at 40 keV with a C<sub>60</sub><sup>3+</sup> cluster, an impact equivalent to 120 keV is generated [8].

The C<sub>60</sub><sup>+</sup> ions are produced by electron bombardment. The schematic of an electron bombardment ion source is illustrated in Figure 3.4. Electron ionisation of gases involves a filament cathode around a grid; a gas (C<sub>60</sub> vapour) is introduced while electrons from the cathode are orbiting the same region. The electrons are kept in the centre of the grid structure by an electric field generated by positive voltage from the grid and negative voltage from the repeller. Gas ions are then produced by electron bombardment; such ions are subsequently extracted by an electric field inside the grid (extractor)[11].

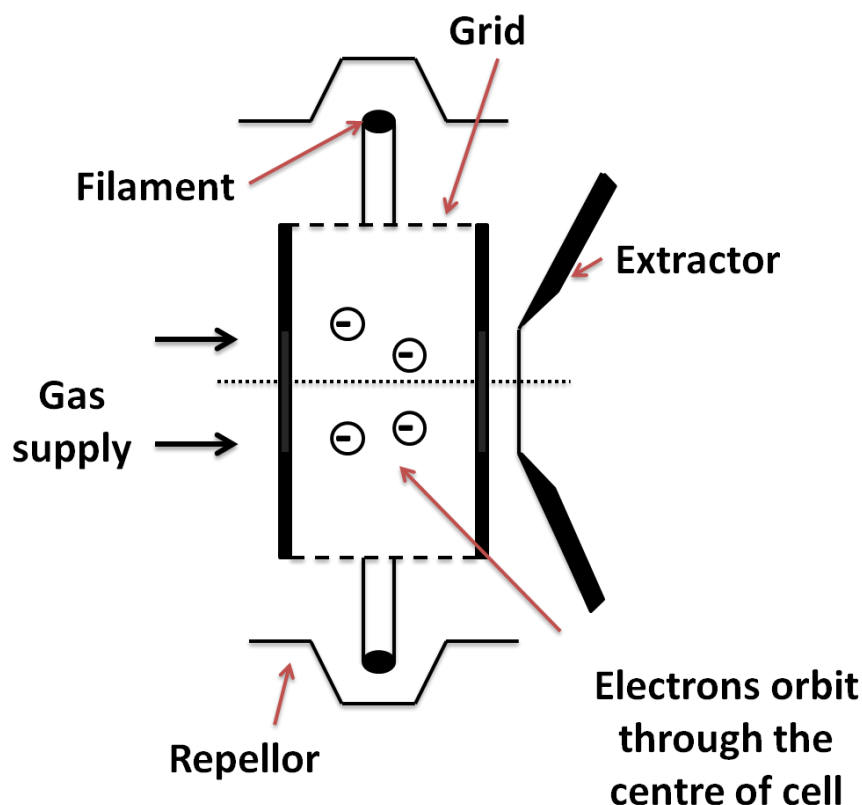


Figure 3.4: Schematic of an electron bombardment source [11].

Fullerene vapour is employed to produce  $C_{60}$  ions; this vapour is generated by heating  $C_{60}$  powder at a very high temperature ( $> 350^{\circ}\text{C}$ ). Positively charged  $C_{60}$  ions are selected with a Wien filter. This type of mass filtering enables mass-to-charge ratio filtering and excludes unwanted small species thus allowing the selection of single, double or triple charged clusters [4], [8], [11].

Mass-filtered  $C_{60}^{+}$  clusters are then extracted and accelerated further as they go through an ion column. The upper section of the column focuses the beam with a lens and further demagnification is achieved with a second lens.

The ion source is separated from the SAC chamber by a gate valve and ion optics are enclosed in a column under high vacuum conditions. The  $C_{60}$  ion gun can work with an anode voltage range of 5-40 kV [19].

### 3.5.1.1 Spatial resolution obtained with 40 keV $C_{60}$

The J105 instrument comprises a secondary electron detector (SED) capable of providing Scanning Electron Microscope (SEM) type images. This approach is used to measure the lateral resolution of a primary ion beam on a copper grid. This is achieved by generating a vertical or horizontal line-scan profile from one of the bars in the grid. The spot sizes are measured 20 to 80%.

The spatial resolution obtained for 40 keV  $C_{60}^{+}$  using a  $30\text{ }\mu\text{m}$  adjustable aperture on a 300 copper grid is displayed in Figure 3.5.

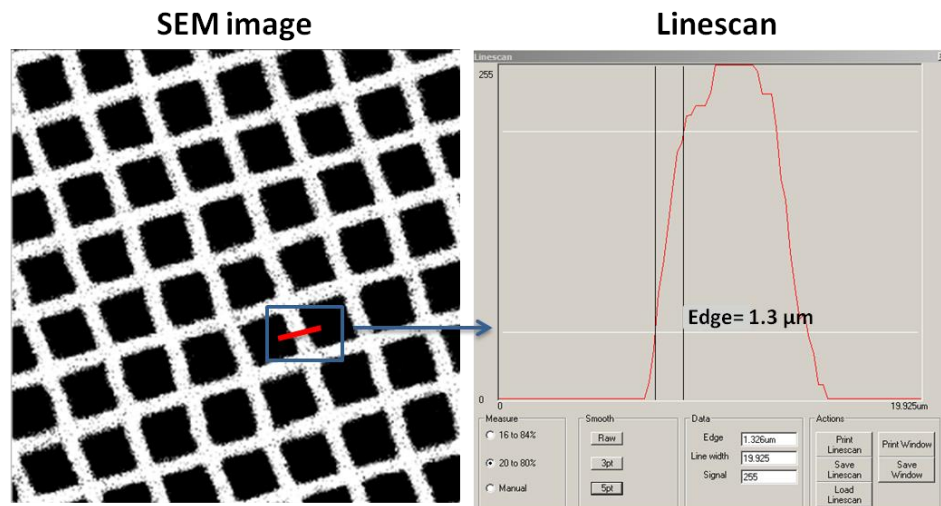


Figure 3.5: Measurement of the beam diameter for 40 ke  $C_{60}^{+}$  beam using a  $30\text{ }\mu\text{m}$  adjustable aperture. A line profile is manually drawn on one of the grid bars of the SEM image (left). The lateral resolution is  $1.3\text{ }\mu\text{m}$ , provided by the line scan profile 20- 80%.

The 40 keV C<sub>60</sub> beam can be focused down to 400 nm using an adjustable aperture [2], [9]. Table 3.1 summarises different beam spot sizes and current obtained with each adjustable aperture for the IOG C60-40 [8]. The beam currents are measured before every experiment to calculate primary ion doses.

Diameter of adjustable aperture (μm)	<i>I</i> (nA)	Beam diameter (μm)
1000	1.056	40
300	0.100	15
100	0.045	8
30	0.001	0.4-0.8

*Table 3.1: Diameters of adjustable apertures to focus the 40 kV C60 beam and the lateral resolution obtained on each one [8], [9].*

### 3.5.1.2 Mass filtering

A Wien filter is a velocity selector filter that comprises orthogonal electric and magnetic fields, as illustrated by Figure 3.6. It is mainly used for the selection of charged particles based on their mass and velocity. Particles obeying the condition determined by Equation 3.3 will be transmitted.

*Equation 3.3*

$$B \times q \times v = E \times q$$

Where:

*B* =magnetic flux;

*q* =electric charge;

*v* = velocity; and

*E* = electric field [4].

Ions with the incorrect speed will be deflected while the ones with the right speed will go through [11], [20], [21].



Clusters produced from an ion source can have a wide mass range. Usually, clusters entering a Wien filter undergo acceleration by electrostatic potential while they gain kinetic energy. Then, the mass separation is achieved according to the particle's velocity as a function of their mass [20]. The resulting ion beam is then directed into a Faraday cup for current measurement.

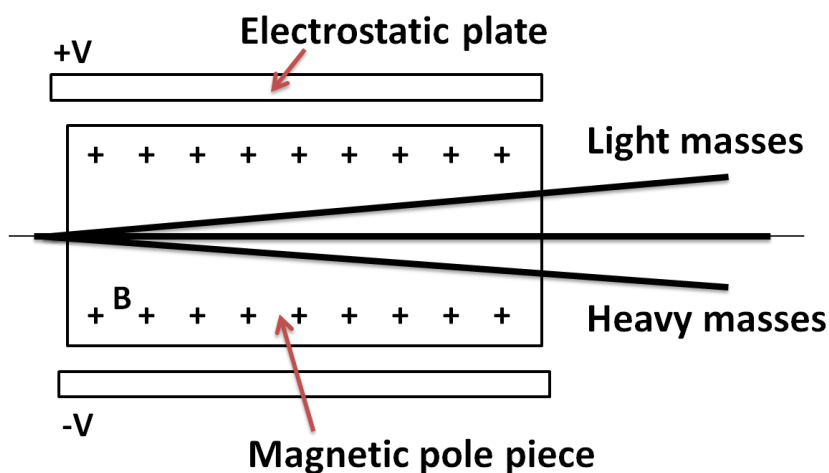


Figure 3.6: Schematic of a Wien filter [11].

### 3.5.2 20 keV Gas cluster ion beam

Clusters are homogeneous aggregates of atoms or molecules kept together by binding forces [22]. Clusters can be composed of a few to thousands of particles. Gas cluster ion beams (GCIBs) have recently been implemented in ToF-SIMS instruments, mainly for the generation of giant argon clusters [23]. Argon clusters are suitable for surface analysis, inducing low damage sputtering; they can range from small clusters ( $\sim 100$  atoms) to giant clusters ( $> 5000$  atoms) [11], [20], [22]–[27].

The gas cluster ion source contains two main regions, as illustrated by Figure 3.7. The cluster formation takes place within the first region, with a high pressure argon inlet (10 to 20 bar) fed through a nozzle into a low vacuum chamber where the gas goes through an adiabatic expansion process [4], [24]. The velocity of the argon atoms increases during this adiabatic expansion but the gas temperature decreases, leading to cluster formation. The skimmer aperture is placed right after the cluster formation point, allowing cluster selection and rejection of uncondensed atoms and divergent clusters (Figure 3.7) [4].

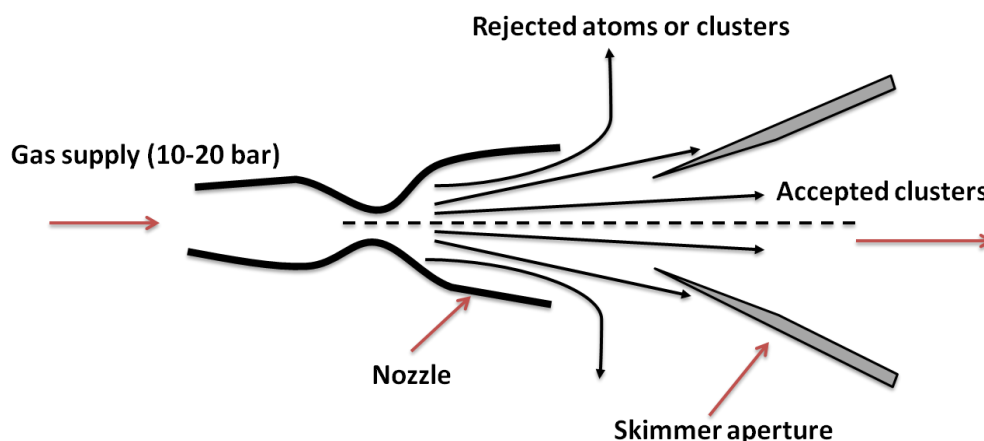


Figure 3.7: Schematic of a GCIB source [4].

During the formation process, the clusters are not ionised. They remain neutral until ionisation takes place after the skimmer aperture. The selected stream of neutral argon clusters enter the next vacuum chamber where the ionisation is achieved by electron bombardment ionisation [11], [24]. Charged clusters are then accelerated into an ion column, where the mass filter (Wien filter) will select clusters by size [24]. In the GCIB 20, there are four selectable apertures (30, 100, 300 and 1000  $\mu\text{m}$ ); they are used for current selection and beam diameter adjustment. The 20 keV argon cluster ion system was designed to produce different clusters sizes from  $\text{Ar}_2$  to  $\text{Ar}_{10000}$ , depending on the gas pressure (12- 24 bar) [24].

#### 3.5.2.1 Formation of water and water-doped argon clusters

The analysis of complex systems such as cells and tissues demands SIMS instrumentation capable of generating enough secondary ions from the target material. However, increasing secondary ion yield from biological samples is very challenging. Following the success of previous experiments, where ToF-SIMS analysis involved the presence of water [16], [28], the SIMS group in Manchester has developed and implemented a prototype water cluster ion beam (Figure 3.8) [29]. This GCIB enhances the protonation of secondary ions; it has been applied successfully to the analysis of model biomolecules and mouse brain tissue [29]–[32].

This prototype ion source includes an extra chamber which is attached to the GCIB 20. In addition, a water boiler assembly is placed before the expansion chamber. The boiler, heated above the water boiling point, generates water vapour which passes through a 30  $\mu\text{m}$  nozzle aperture for adiabatic expansion (as previously explained by Figure 3.7)[24].

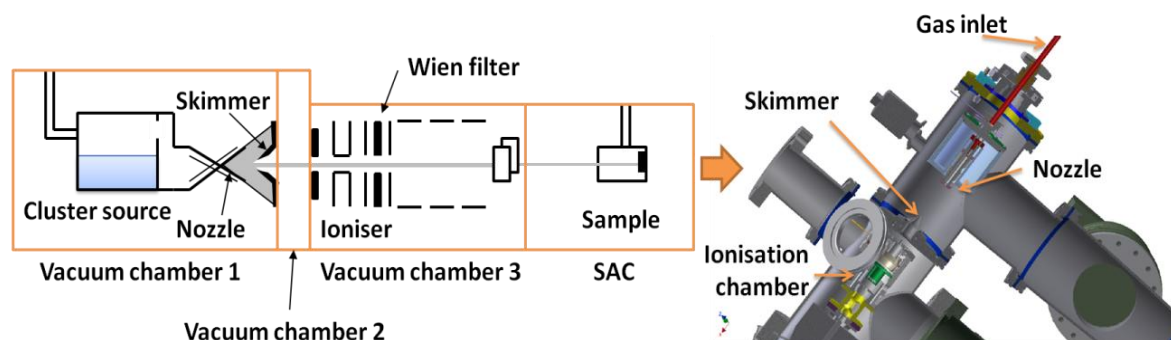


Figure 3.8: Illustration of the water cluster ion beam [24]. A boiler assembly was fitted within the first vacuum chamber to produce a water steam. Cluster formation and selection are achieved in the same manner as argon clusters [32].

The resulting neutral water cluster stream goes into another vacuum chamber (separately pumped) to be ionised by electron bombardment. To avoid water condensation due to reductions in temperature, the nozzle is heated at  $\sim 160^{\circ}\text{C}$ . To obtain stable water clusters, the water vapour pressure is kept  $\sim 3\text{--}4$  bar by boiling the water at  $\sim 145^{\circ}\text{C}$ , allowing the water intermolecular forces to aggregate [24], [32]. When the experiment requires argon cluster generation, only argon goes into the source and the boiler and the nozzle are kept at room temperature.

When water clusters are desired, the boiler is charged with HPLC grade or Millipore water.  $\text{D}_2\text{O}$  clusters can also be generated in the same way. The size of the clusters will be highly dependent on the pressure inside the expansion chamber, which is affected by the boiler's temperature. With this configuration, giant clusters with more than 10,000 molecules can be produced. Once the clusters are ionised, they are mass-selected by a Wien filter (Figure 3.6) [24].

Along with  $\text{Ar}_n$ ,  $(\text{H}_2\text{O})_n$  and  $(\text{D}_2\text{O})_n$  clusters, it is also possible to produce water-doped argon clusters  $((\text{H}_2\text{O})\text{Ar}_n)$ . For this type of cluster, the high-pressure argon inlet is passed over water contained in the boiler, which is heated  $\sim 85^{\circ}\text{C}$  [33]. The stream then passes through the nozzle aperture and then goes into the expansion chamber where the cluster formation takes place. Water-argon clusters are formed, ionised and selected for analysis.

The pressure of the water contained in the boiler is kept under 1 bar ( $\sim 0.8$  bar) with an argon pressure of 14–16 bar to avoid destabilisation of argon clusters. The nozzle is kept under  $100^{\circ}\text{C}$  ( $\sim 95^{\circ}\text{C}$ ) and the boiler temperature is held  $\sim 85^{\circ}\text{C}$  to avoid boiling of the water. As a result, stable  $(\text{H}_2\text{O})\text{Ar}_n$  clusters are generated. It is estimated that the composition of the clusters is 95% argon and 5% water. This percentage is obtained

based on the partial pressures of argon gas and water vapour in the system (16 bar of argon and 0.8 bar of water). The size range of  $(\text{H}_2\text{O})\text{Ar}_n$  clusters is  $n=1000$  to  $8000$ .

### 3.5.2.2 Cluster measurement

The cluster size distribution is selected by the Wien filter and verified by measuring the time-of-flight of the generated clusters. The cluster ion beam is pulsed, the cluster flight time between the pulser and the target is measured by the secondary electron detector[24].

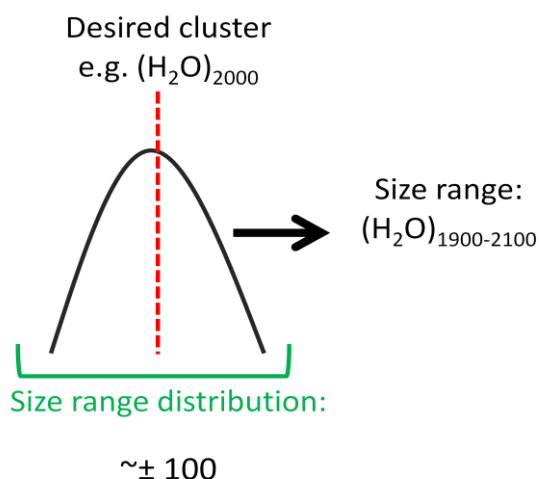


Figure 3.9 Graphical representation of the size range distribution of the clusters obtained with the GCIB primary ion beam. For example, if the desired cluster is  $(\text{H}_2\text{O})_{2000}$ , the size of the clusters obtained will be  $\pm 100$  i.e.  $(\text{H}_2\text{O})_{1900-2100}$ .

The time-of-flight can be converted to mass when the distance of the ion path and the energy of the projectile are known [26]. The size range distribution of clusters is then obtained for experimentation.

### 3.5.2.3 Spatial resolution obtained with different gas clusters

The spatial resolution obtained with different clusters can be measured from vertical and horizontal line profiles on SEM images, as previously explained in Figure 3.10. To measure the lateral resolution of GCIB 20 clusters, an Agar Scientific 300 copper finder grid (Agar scientific, Essex, UK) is used to obtain SEM images.

Beam current and spatial resolution are controlled by the adjustable apertures used for beam tuning. The diameters of the selectable apertures are 1 mm, 300  $\mu\text{m}$ , 100  $\mu\text{m}$  and 30  $\mu\text{m}$ . The chemistry of the gas particles will also affect the beam current and spatial resolution. The best lateral resolution achievable with the 100  $\mu\text{m}$  aperture is shown in

Figure 3.10. This figure shows  $\text{Ar}_{2000}$ ,  $(\text{H}_2\text{O})_{6000}$  and  $(\text{H}_2\text{O})\text{Ar}_{2000}$  clusters at their focal points, obtaining an optimum spatial resolution between 11 and 13  $\mu\text{m}$ .

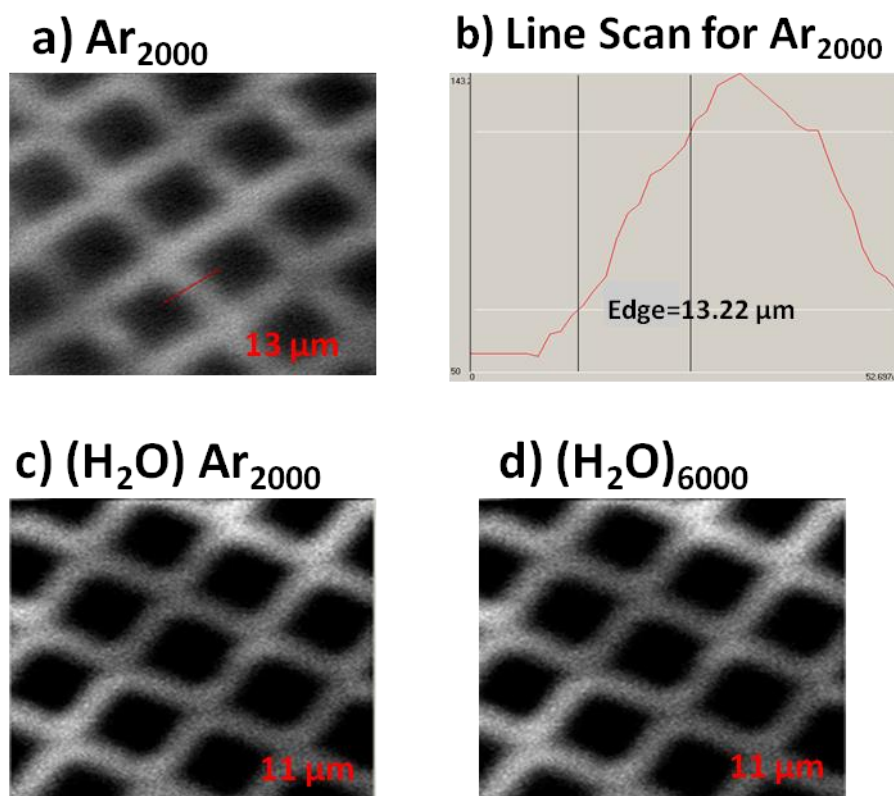


Figure 3.10: SEM images from a 300 copper grid covering a  $300 \mu\text{m}^2$  area using  $256 \times 256$  pixels. (a) The spatial resolution measured for 20 keV  $\text{Ar}_{2000}^+$  is 13  $\mu\text{m}$ . (b) A line profile is drawn manually over a sharp edge to determine the beam diameter from image (a). (c) The spatial resolution of 20 keV  $(\text{H}_2\text{O})\text{Ar}_{2000}^+$  is 11  $\mu\text{m}$ . (d) The spatial resolution of 20 keV  $(\text{H}_2\text{O})_{6000}^+$  is 11  $\mu\text{m}$ .

The beam diameter currently obtained with the GCIB source can be useful for micrometric molecular imaging of samples like biological tissues e.g. mouse brain. However, sub-micron spatial resolution for studies in biological systems such as cells is still under development.

Experiments demonstrating the application of different GCIB clusters on model compounds and tissue imaging are presented in the following chapters.

### 3.6 References

- [1] M. Guilhaus, "Principles and instrumentation in time-of-flight mass spectrometry: Physical and instrumental concepts," *J. Mass Spectrom.*, vol. 30, no. 11, pp. 1519–1532, 1995.

- [2] R. Hill, P. Blenkinsopp, S. Thompson, J. Vickerman, and J. S. Fletcher, "A new time-of-flight SIMS instrument for 3D imaging and analysis," *Surf. Interface Anal.*, vol. 43, no. 1–2, pp. 506–509, 2011.
- [3] E. de Hoffman and V. Stroobant, "Mass Analysers," in *Mass Spectrometry Principles and Applications*, 3rd ed., John Wiley & Sons, Ltd, 2007, pp. 85–167.
- [4] R. Hill, "Analysis beams used in ToF-SIMS," in *TOF-SIMS: Materials analysis by mass spectrometry*, 2nd ed., J. C. Vickerman and D. Briggs, Eds. Manchester: IM Publications, 2013, pp. 271–290.
- [5] J. S. Fletcher and J. C. Vickerman, "A new SIMS paradigm for 2D and 3D molecular imaging of bio-systems," *Anal. Bioanal. Chem.*, vol. 396, no. 1, pp. 85–104, 2010.
- [6] a. G. Brenton and a. R. Godfrey, "Accurate mass measurement: Terminology and treatment of data," *J. Am. Soc. Mass Spectrom.*, vol. 21, no. 11, pp. 1821–1835, 2010.
- [7] J. S. Fletcher, S. Rabbani, A. Henderson, P. Blenkinsopp, S. P. Thompson, N. P. Lockyer, and J. C. Vickerman, "A New Dynamic in Mass Spectral Imaging of Single Biological Cells," *Anal. Chem.*, vol. 80, no. 23, pp. 9058–9064, 2008.
- [8] H. Tian, "Visualisation and profiling of lipids in single biological cells using Time-of-Flight Secondary Ion Mass Spectrometry," University of Manchester, 2011.
- [9] S. Rabbani, "Advances in Time-of-Flight Secondary Ion Mass Spectrometry for the Analysis of Single Cells on Sub-Cellular Scale," 2010.
- [10] B. W. Schueler, "Time-of-flight mass analysers," in *TOF-SIMS: Materials analysis by mass spectrometry*, 2nd ed., J. C. Vickerman and D. Briggs, Eds. Manchester: IM Publications, 2013, pp. 247–270.
- [11] A. G. Shard and I. S. Gilmore, *TOF-SIMS: Materials analysis by mass spectrometry*, 2nd ed. Manchester: IM Publications, 2013.
- [12] V. M. Doroshenko and R. J. Cotter, "Ideal velocity focusing in a reflectron time-of-flight mass spectrometer," *J. Am. Soc. Mass Spectrom.*, vol. 10, no. 10, pp. 992–999, 1999.
- [13] J. Flensburg, D. Haid, J. Blomberg, J. Bielawski, and D. Ivansson, "Applications and performance of a MALDI-ToF mass spectrometer with quadratic field reflectron technology," *J. Biochem. Biophys. Methods*, vol. 60, no. 3, pp. 319–334, 2004.

- [14] C. H. Evans, "Introduction to mass spectrometry," *Trends Biochem. Sci.*, vol. 11, no. 3, pp. 124–125, 1986.
- [15] J. S. Fletcher and C. Szakal, "Cluster and polyatomic primary ion beams," in *TOF-SIMS: Materials analysis by mass spectrometry*, 2nd, Ed. Manchester: IM Publications, 2013, pp. 291–310.
- [16] A. M. Piwowar, S. Keskin, M. O. Delgado, K. Shen, J. J. Hue, I. Lanekoff, A. G. Ewing, and N. Winograd, "C60-ToF SIMS imaging of frozen hydrated HeLa cells," *Surf. Interface Anal.*, vol. 45, no. February, pp. 302–304, 2013.
- [17] E. A. Jones, N. P. Lockyer, and J. C. Vickerman, "Mass spectral analysis and imaging of tissue by ToF-SIMS-The role of buckminsterfullerene, C60 +, primary ions," *Int. J. Mass Spectrom.*, vol. 260, no. 2–3, pp. 146–157, 2007.
- [18] E. J. Lanni, S. J. B. Dunham, P. Nemes, S. S. Rubakhin, and J. V. Sweedler, "Biomolecular Imaging with a C60-SIMS/MALDI Dual Ion Source Hybrid Mass Spectrometer: Instrumentation, Matrix Enhancement, and Single Cell Analysis," *J. Am. Soc. Mass Spectrom.*, vol. 25, no. 11, pp. 1897–1907, 2014.
- [19] Ionoptika, "IOG C60-40 user manual," 2007.
- [20] K. Yano and Suck Hee Be, "Mass Analyses of Cluster Ion Beams By Wien Filter.," *Jpn. J. Appl. Phys.*, vol. 19, no. 6, pp. 1019–1025, 1980.
- [21] B. Wrenger and K. H. Meiwes-Broer, "The application of a Wien filter to mass analysis of heavy clusters from a pulsed supersonic nozzle source," *Rev. Sci. Instrum.*, vol. 68, no. 5, p. 2027, 1997.
- [22] S. Rabbani, A. M. Barber, J. S. Fletcher, N. P. Lockyer, and J. C. Vickerman, "TOF-SIMS with argon gas cluster ion beams: A comparison with C60 +," *Anal. Chem.*, vol. 83, no. 10, pp. 3793–3800, 2011.
- [23] N. Toyoda, J. Matsuo, T. Aoki, I. Yamada, and D. B. Fenner, "Secondary ion mass spectrometry with gas cluster ion beams," *Nucl. Instruments Methods Phys. Res. Sect. B Beam Interact. with Mater. Atoms*, vol. 190, no. 1–4, pp. 860–864, 2002.
- [24] A. M. Barber, "Development of Gas Cluster Ion Beams Table of Contents," 2012.
- [25] A. G. Shard, R. Havelund, M. P. Seah, S. J. Spencer, I. S. Gilmore, N. Winograd, D. Mao, T. Miyayama, E. Niehuis, D. Rading, and R. Moellers, "Argon Cluster Ion Beams for Organic Depth Profiling: Results from a," 2012.

- [26] H. Tian, A. Wucher, and N. Winograd, "Molecular imaging of biological tissue using gas cluster ions," *Surf. Interface Anal.*, vol. 46, no. S1, pp. 115–117, 2014.
- [27] K. Ichiki, S. Ninomiya, T. Seki, T. Aoki, and J. Matsuo, "Energy effects on the sputtering yield of Si bombarded with gas cluster ion beams," *AIP Conf. Proc.*, vol. 1321, no. 2011, pp. 294–297, 2010.
- [28] P. D. Piehowski, M. E. Kurczy, D. Willingham, M. L. Heien, N. Winograd, A. G. Ewing, and S. Parry, "Freeze-Etching and Vapor Matrix Deposition for ToF-SIMS Imaging of Single Cells Freeze-Etching and Vapor Matrix Deposition for ToF-SIMS Imaging of Single Cells," vol. 38, no. 8, pp. 7906–7911, 2008.
- [29] S. Sheraz née Rabbani, a. Barber, I. Berrueta Razo, J. S. Fletcher, N. P. Lockyer, and J. C. Vickerman, "Prospect of increasing secondary ion yields in ToF-SIMS using water cluster primary ion beams," *Surf. Interface Anal.*, no. November 2013, p. n/a–n/a, 2014.
- [30] S. Sheraz née Rabbani, I. Berrueta Razo, T. Kohn, N. P. Lockyer, and J. C. Vickerman, "Enhancing Ion Yields in Time-of-Flight-Secondary Ion Mass Spectrometry: A Comparative Study of Argon and Water Cluster Primary Beams," *Anal. Chem.*, vol. 87, no. 4, pp. 2367–2374, 2015.
- [31] I. Berrueta Razo, S. Sheraz, A. Henderson, N. P. Lockyer, and J. C. Vickerman, "Comparing C<sub>60</sub><sup>+</sup> and (H<sub>2</sub>O)<sub>n</sub><sup>+</sup> clusters for mouse brain tissue analysis," *Surf. Interface Anal.*, no. November 2013, p. n/a–n/a, 2014.
- [32] S. Sheraz, A. Barber, J. S. Fletcher, N. P. Lockyer, and J. C. Vickerman, "Enhancing secondary ion yields in ToF-SIMS using water cluster primary beams .," *Anal. Chem.*, pp. 2–3, 2013.
- [33] I. Berrueta Razo, S. Sheraz, A. Henderson, N. P. Lockyer, and J. C. Vickerman, "Mass Spectrometric Imaging of Brain Tissue by ToF-SIMS – How do polyatomic primary beams C<sub>60</sub><sup>+</sup>, Ar<sub>2000</sub><sup>+</sup>, water doped Ar<sub>2000</sub><sup>+</sup> and (H<sub>2</sub>O)<sub>6000</sub><sup>+</sup> compare?," 2015.



## 4 Materials and methods

Samples analysed with ToF-SIMS analysis must be vacuum-compatible solids i.e. exposing the sample to high vacuum will cause the removal of volatile solvents, including water [1]. ToF-SIMS instruments usually work with ultra-high vacuum ( $10^{-9}$ - $10^{-10}$  Torr); with this high vacuum specimens have to be stabilised prior to analysis to prevent sample rupture and delocalisation of molecules e.g. samples are analysed dehydrated or frozen hydrated [2]. Ideally, specimens should also have a flat surface since this can affect the angle of incidence of the ion beam, affecting the secondary ion yield [3].

In some cases, non-flat surfaces with specific topography like *Xenopus laevis* [4] have been imaged with ToF-SIMS using the J105-3D Chemical Imager which decouples the secondary ion extraction and detection from the sample's topography due to the specific buncher-ToF design [5]. The loss of secondary ion yield from the edges of the specimen is also reduced due to the dynamic emittance matching (DEM's) featured in this instrument. Charging compensation is usually applied using a 1 keV electron gun. However, the electron beam was not available during any of the experiments presented in this thesis.

The conductivity of the samples is also an important experimental factor [6]. Samples that are electrically conducting (or semi-conductive) give generally better results when compared to insulating specimens. Insulators generate a sample-charging effect during analysis and need some kind of charge compensation e.g. electron gun or external voltage applied to the analysis stage. Sample charging diffuses the analysis beam and disturbs the transmission of secondary ion emission. This is why the substrate and sample thickness are crucial for successful data acquisition [7].

### 4.1 Analysis of biomolecules

#### 4.1.1 Studied biomolecular standards

The standard compounds used in this study have been successfully analysed in ToF-SIMS experiments in the past. L-arginine films have been widely used as a basic amino acid models for sputtering studies [8]–[10]; its fragmentation patterns have been observed under different sputtering conditions. Angiotensin I, II and III from humans and mice are amino acid sequences used for peptide structural analysis. Their molecular weight is  $\sim 1000$  Da and they are useful to evaluate the detection of large ion fragments and  $[M+H]^+$  ions with cluster ion beam analysis [11]–[13]. The

disaccharide trehalose has been implemented as a matrix for the analysis of macrophages and glial cells in addition to sputtering studies with  $\text{Bi}_n^+$  and  $\text{C}_{60}^+$  primary ion beams. This type of sugar can preserve the structure of biological cells and tissues even after desiccation [2], [14], [15]. The phospholipid DPPC is probably one of the most applied standard lipids in ToF-SIMS [16]–[19]. DPPC is an important structural component of the cell membrane thus the importance of its characterisation in studies of complex biological systems e.g. cells and tissues [19].

#### 4.1.1.1 Arginine

Arginine (Arg) is a natural amino acid present in humans as part of the structure of the messenger ribonucleic acid (mRNA). It plays an important role in cell division, wound healing, immune functions and hormone release, among others [20].

L-arginine was bought from Sigma Aldrich (Gillingham, Dorset, UK). It has a molecular weight of 174.20 Da and its chemical structure is shown in Figure 4.1. This essential amino acid has a positively charged guanidine group. The fragmentation patterns of Arginine were observed and simulated under  $\text{Cs}^+$  analysis by Kato and co-workers [8].

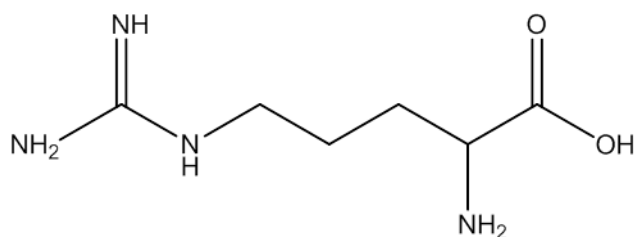


Figure 4.1: Chemical structure of Arginine [20].

#### 4.1.1.2 Angiotensin II (human)

Angiotensinogen is an alpha globulin, part of the group of globular proteins in plasma. These proteins are mobile electrically charged solutions, released to the circulation stream from the liver. The decapeptide angiotensin I is synthesised by the action of angiotensinogenase (produced by kidneys) on angiotensinogen. Angiotensin I is the precursor of angiotensin II. The angiotensin-converting enzyme (ACE) converts angiotensin I into the octapeptide sequence named angiotensin II. In the human body, angiotensin II regulates the secretion of the hormone aldosterone. This hormone increases the blood pressure by regulating the absorption of water and ions of kidneys [21].

Synthetic angiotensin II (human) was bought from Cambridge Bioscience Ltd (Cambridge, UK). The peptide sequence for this compound is: NRVYVHPF [Asn<sup>1</sup>Val<sup>5</sup>]

with a molecular weight of 1031.18 Da. This peptide chain has been studied with SIMS using  $\text{Bi}_n^+$ ,  $\text{C}_{60}^+$  and  $\text{Ar}_n^+$  ion beams. From these experiments molecular ions and large fragment ions representing multiple amino acid residues have been identified [11], [22], [23].

To understand the angiotensin II structure and fragments obtained from its analysis, the fragmentation patterns of this biomolecule are illustrated in Figure 4.2. These patterns and the characterisation of this peptide are discussed in reference [11].

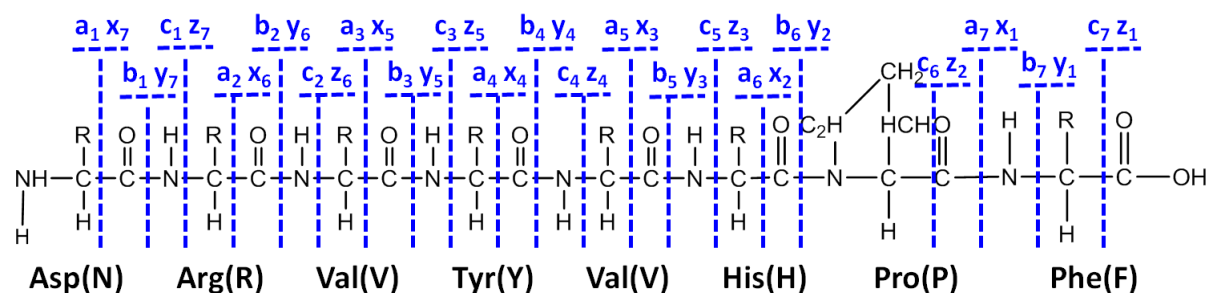


Figure 4.2: Fragments obtained from human angiotensin II (DRVYIHPF) with ToF-SIMS analysis [11].

#### 4.1.1.3 Trehalose

Trehalose is an alpha-linked disaccharide formed by two  $\alpha$ -glucose units linked by an  $\alpha$ ,  $\alpha$ -1, 1-glucoside bond. It has high water retention capabilities and can be synthesised by bacteria, fungi, plants and animals. This sugar prevents disruption of cells by keeping them in position by forming a gel phase as they dehydrate/rehydrate [24].

D-(+)-trehalose dehydrate was purchased from Sigma Aldrich (Gillingham, Dorset, UK). Its molecular weight is 378.33 Da and its chemical structure is illustrated in Figure 4.3. The structure includes two molecules of water added to the trehalose structure.

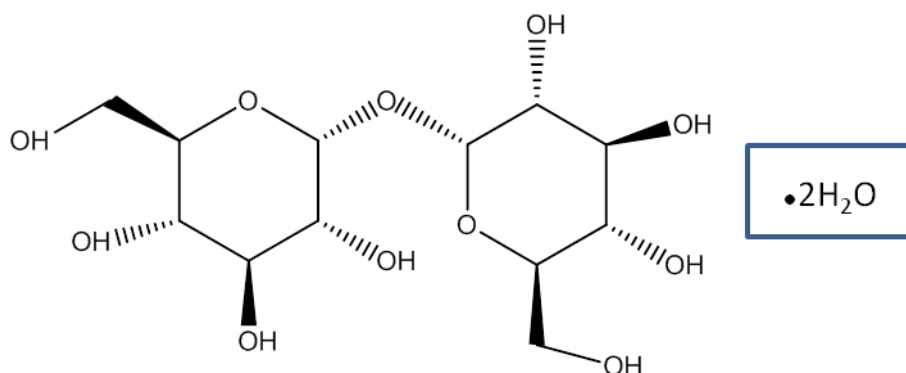
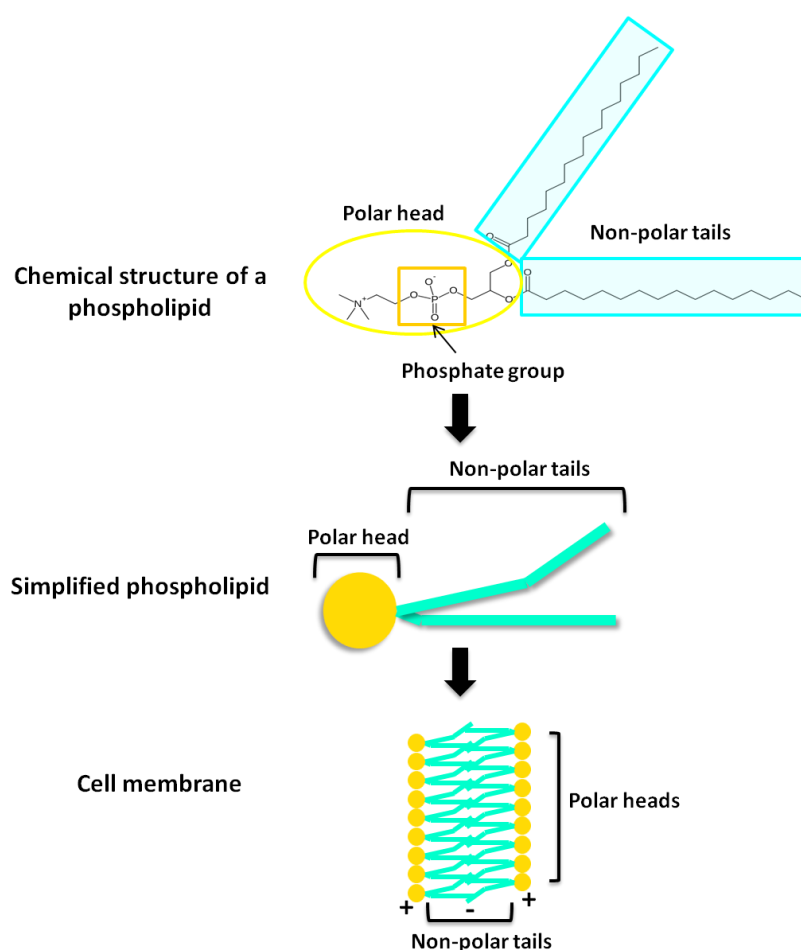


Figure 4.3: Chemical structure of trehalose dehydrate [2].

Trehalose is a standard molecule that has been analysed with ToF-SIMS under single and dual beam bombardment ( $\text{Bi}_n^+$  and  $\text{C}_{60}^+$ ) to evaluate the effect of increasing ion beam dose in depth profiles [15]. It has also been applied as a matrix to preserve and analyse Eukaryotic cells successfully [2]. The molecular and fragment ions from this model molecule have been observed and reported in different molecular environments [2], [14], [15], [25].

#### 4.1.1.4 Dipalmitoylphosphatidylcholine (DPPC)

DPPC is a phospholipid built by two fatty acids and a phosphocholine head group. It is a major component of lung surfactants, acting as a surface active and decreasing the surface tension. It is widely used in liposomes, lipid bilayers and biomembrane models for research [26].



*Figure 4.4: Parts of a phospholipid molecule. This figure displays the chemical structure of a phospholipid (DPPC) and their polar (hydrophilic) head and non-polar (hydrophobic) tail. Phospholipids build arrangements in aqueous environments forming bilayers. These type of bilayers can be observed in biological cell membranes [26], [27].*

Phospholipids are a main lipid class that acts as structural components of biological membranes. As illustrated in Figure 4.4, most phospholipids contain a diglyceride (two fatty acid chains), a phosphate group and a choline molecule. One of the main features in phospholipids is their amphiphilic character; they are formed by a hydrophilic 'head' and a hydrophobic 'tail'. The head is composed by a negative phosphate group whereas the tail is built by two fatty acid chains. When placed in aqueous-based environments, the tails line up against each other forming bilayer structures with the hydrophilic heads in direct contact with water. Phospholipid bilayers are the main components of cell membranes [26], [27].

Synthetic 1,2-dipalmitoyl-*sn*-glycero-3-phosphocholine was purchased from Sigma Aldrich (Gillingham, Dorset, UK). The chemical structure of this lipid can be seen in Figure 4.5. The molecular weight of this compound is 734.04 Da. DPPC has been applied to the investigation of model membrane systems; films made of pure DPPC and mixed with other model compounds e.g. proteins [23] were successfully studied with SIMS in the past [19]. Several other SIMS experiments involving DPPC were designed to investigate the function of the pulmonary surfactants [16], [29], [30].

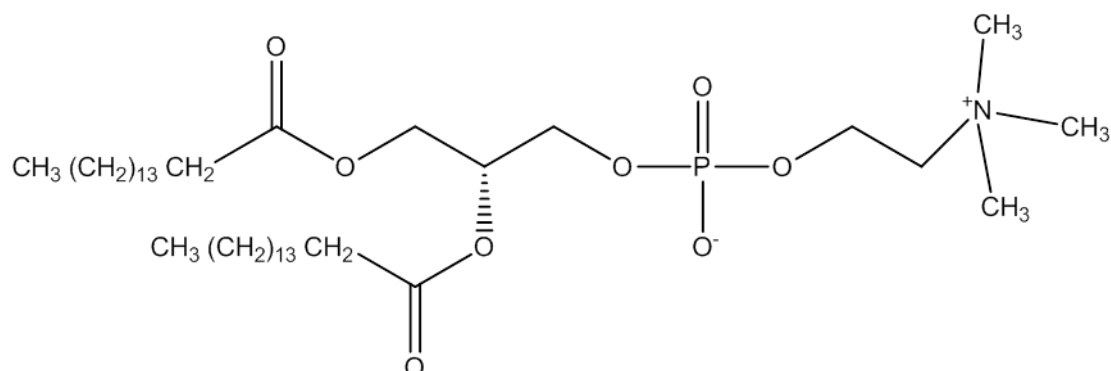


Figure 4.5: Chemical structure of DPPC.

DPPC was also analysed in the first set of experiments that aimed to explore the effect of water clusters as a primary ion beam [23].

#### 4.1.2 Preparation of spin-coated films for ToF-SIMS analysis

Preparation of films by spin coating has proven to be a practical method for fundamental studies involving depth profiling studies with ToF-SIMS [31]–[35]. A wide variety of molecules with different chemical composition can be used to prepare spin-coated films. Spin-coated films and *Langmuir–Blodgett* films have been widely used in SIMS experiments [31]–[33], [36].

Spin coating is used to prepare homogeneous films of different materials. The methodology to obtain films is displayed in Figure 4.6. The film deposition process starts when a droplet of the compound, dissolved in a liquid, is deposited on a solid substrate (Figure 4.6, 1 and 2). Dispensing of the solution can be done in static mode (static substrate) or dynamic mode (rotating substrate). This substrate is then placed on a rotating spin-coater. Once dispensed, the surface tension of the solvent is enough to keep the solution together on the surface. This solution will spread according to the solvent, the surface, temperature and rotation speed (rpm), drying out the solvent by evaporation and forming a film of a certain thickness and morphology [37] (Figure 4.6, 3-5).

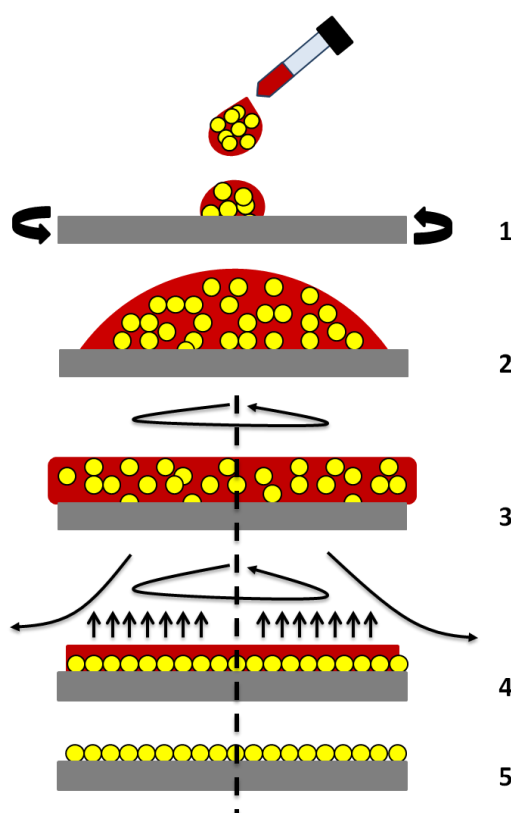


*Figure 4.6: Schematic representation of the spin coating process to get uniform films with different compounds [37].*

#### **4.1.2.1 Substrate preparation**

Any kind of contamination present on the surface of the substrate, specially surfactants, can lead to a lower surface tension of the solvent and will result in a non-uniform film or will prevent the deposition of the film [38].

The substrates used for film deposition are low-resistivity silicon chips (Agar Scientific, UK); each wafer is  $5 \times 5 \text{ mm}^2$  and  $460\text{--}530 \text{ }\mu\text{m}$  thick. The silicon wafers are polished on

one side with silicon dioxide top coating and have surface properties similar to those found in glass. Their surface roughness is less than 1nm and their crystallographic orientation is (111). To remove any chance of contamination, all chips were cleaned with solvents in an ultrasonic bath. The solvents used were HPLC grade and purchased from Fisher scientific (Loughborough, UK). The cleaning protocol is as follows:

1. Ultrasonic cleaning in hexane for two hours to eliminate oil organic residues.
2. Two hours of ultrasonic cleaning in HPLC water.
3. Finally, two extra hours of sonication in methanol.
4. As an optional step, the silicon wafers are rinsed in deionised water when a hydrophilic surface is desired i.e. when preparing arginine or trehalose films.

#### ***4.1.2.2 Preparation of L-arginine, trehalose, angiotensin II and DPPC spin-coated films***

The steps followed for the preparation of spin-coated films are described next:

*Arginine-* Films of L-arginine were prepared from a 3 mM solution. 7  $\mu$ L from this solution were static-dispensed onto clean silicon (the cleaning protocol is explained in section 4.1.2.1). A uniform film is obtained after a few seconds of rotation, with a rotation speed of 6700 rpm (revolutions per minute). After the initial film is formed, two subsequent dispenses in dynamic mode were added, accumulating 21  $\mu$ L in total..

*Trehalose-* Thin trehalose films were obtained from a 15 mM D-(+)-trehalose dehydrate solution. As in arginine, a film was produced by static dispensing 10  $\mu$ L of the solution and then adding two more aliquots with the same volume. The speed used was 6700 rpm.

*Angiotensin II-* 5 mg of synthetic human angiotensin II were mixed with 200  $\mu$ L of ethanol resulting in a 23  $\mu$ M solution. 10  $\mu$ L from this solution dispensed in static mode were spin-casted onto a clean silicon chip for a few minutes until a yellow film was produced. The rotation speed was 700 rpm

*DPPC-* 3 mg of synthetic 1, 2-dipalmitoyl-*sn*-glycero-3-phosphocholine were dissolved in a 10:1, chloroform:methanol solution. The result is an 8  $\mu$ M DPPC solution; 5 $\mu$ L from this mixture were then dispensed onto a clean wafer in static mode. The spin-coating process for DPPC requires a speed of 1700 rpm. The initial dispensing is followed by subsequent dynamic dispensing of 5  $\mu$ L each, accumulating 100  $\mu$ L in total.

## 4.2 Sample preparation of mouse brain tissue and brain total lipid extract

### 4.2.1 Preparation of brain total lipid extract

Brain total lipid extract (BTLE) is a mimic sample of the lipid content of the mouse brain. It is the most similar to actual brain tissue in terms of lipid composition [39]. The preparation of this sample is relatively straight forward, as indicated in Figure 4.7. A 50 mg sample of complete cryo-fixed mouse brain (previously stored at  $-80^{\circ}\text{C}$ ) was homogenised in a mortar with an ice-cold 1:1 solution of  $\text{MeOH}:\text{CHCl}_3$  (v/v). The brain homogenate was then placed in an ultrasonic bath for 1 hour. This process results in a two phase solution containing an organic and aqueous part. The extracted lipids can be found in the aqueous solution. An aliquot of  $10\ \mu\text{L}$  in volume was drop-cast onto a clean silicon wafer. The droplet was left to air-dry in a fume cupboard and was analysed only after the solvent evaporated completely, leaving the solute deposit on the substrate. Drop casting is a simple method to produce thin deposits of analytes on substrates for SIMS analysis [40].

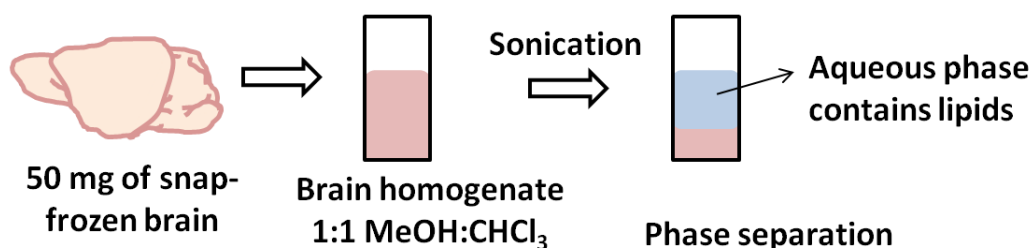


*Figure 4.7: Methodology used for the preparation of brain total lipid extract. The snap-frozen brain is first homogenised in a 1:1  $\text{MeOH}:\text{CHCl}_3$  (v/v) solution. The brain homogenate is then sonicated until a separation of phases is produced. The extracted lipid will be contained in the aqueous part of the two-phase solution.*

### 4.2.2 Preparing mouse brain tissue sections for ToF-SIMS analysis

A whole brain was obtained from the Faculty of Life Sciences, The University of Manchester using ethically approved procedures (Animals (Scientific Procedures) Act 1986). A mouse was euthanized with an anaesthetic overdose with isoflurane. The body was decapitated and the head was dissected to obtain the brain. The complete brain was snap-frozen by rapid immersion in isopentane cooled with liquid nitrogen ( $-161^{\circ}\text{C}$ ) to avoid chemical degradation. Biological degradation starts immediately after oxygen stops circulating through the animal's body and metabolites stop being produced [41]. The purpose of snap-freezing is the cryo-fixation of the tissue block. Once fixated, the brain is kept in a freezer at  $-80^{\circ}\text{C}$  until sectioning.



For sectioning, the whole brain is mounted on the sample holder of the cryo-microtome using *carboxymethyl cellulose* (CMC) as the embedding media (Figure 4.8, A). This viscous compound derived from cellulose has a low freezing point, consequently it freezes immediately when it gets in contact with the sample holder, kept at -22°C [42]. The brain was sectioned using a cryostat microtome *Leica CM3050 S* at the Wolfson Molecular Imaging Centre, The University of Manchester (Figure 4.8, B). Serial sections obtained in a sagittal plane were cut with 8 µm of thickness. Each section was thaw-mounted onto a clean silicon wafer (Figure 4.8, C). The thaw-mounting process involves picking up each section and depositing it onto the substrate [43]. The silicon wafers are kept at room temperature (~ 20°C) which is at a considerably warmer temperature than the sections (-22°C). Consequently, the section melts on the silicon, adhering to the surface without the need of mounting media or adhesives. The use of mounting media is avoided since it can induce contamination or interference peaks in the mass spectrum.

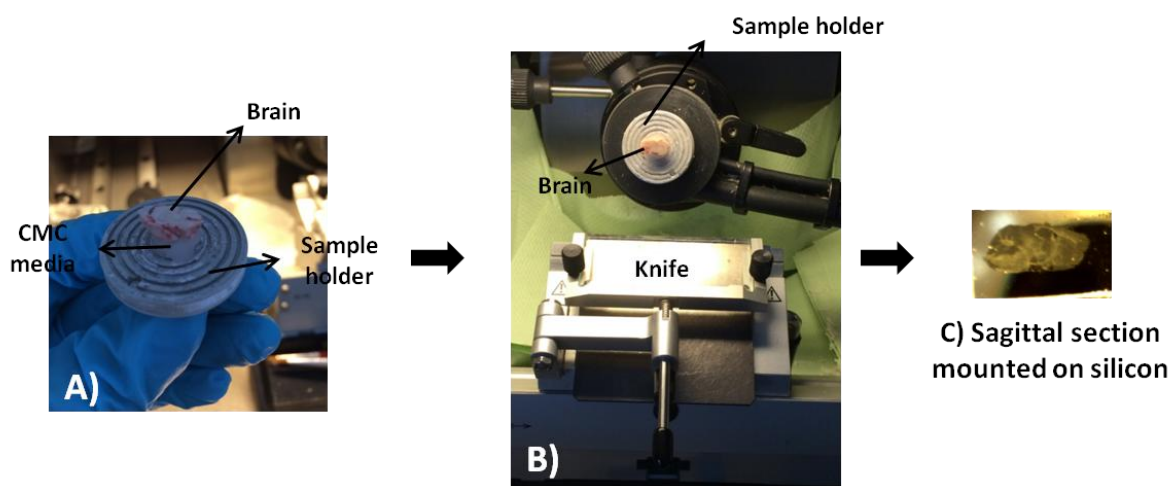


*Figure 4.8: (A) Part of a mouse brain embedded to the cryo-microtome sample holder with CMC. (B) Specimen ready for sectioning in the cryostat microtome. (C) Serial section with sagittal orientation thaw-mounted on a silicon substrate.*

The mounted serial sections are kept in a freezer at -80°C until the day of analysis. Prior to each ToF-SIMS experiment, the section to be analysed is desiccated for 1 hour at room temperature in a polypropylene vacuum desiccator connected to a low-vacuum rotary pump. The main purpose is to evaporate the water contained in the tissue. Dehydration aims to avoid cellular disruption by high-vacuum exposure during analysis [44], [45].

### 4.2.3 Lipid standards for ion suppression/enhancement studies

Experiments to study the ion suppression/enhancement observed in the ToF-SIMS images of specific lipids were performed on lipid mixtures. Three lipid standards were used in this experiment: the sterol lipid cholesterol which is one of the main lipids present in the white matter of the brain; the phospholipid DPPC, mainly found in the brain's grey matter; and sphingomyelin, which is a mixture of sphingophospholipids also present in both grey and white matter brain tissue.

Cholesterol sigma grade ( $\geq 99\%$ ) was purchased from Sigma Aldrich (Gillingham, Dorset, UK) and has a molecular weight of 386.65 Da. This lipid molecule is classified as a sterol lipid and its chemical structure is displayed in Figure 4.9. This lipid molecule is a structural component of mammalian cell membranes and has an important role in cell lipid exchange, cell signalling membrane permeability and protein diffusion [46]. In the central nervous system, the brain is the organ with the highest cholesterol content. Around 70% of the cholesterol present in the central nervous system can be found in the myelin sheath of oligodendroglia or myelin producing cells in the brain [47].

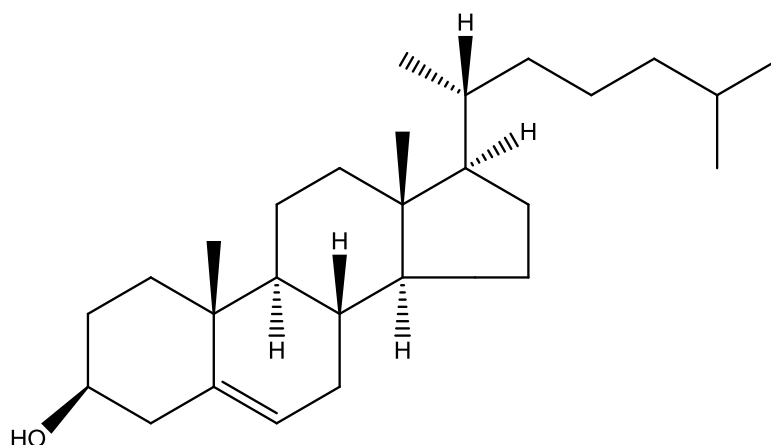


Figure 4.9: Chemical structure of cholesterol.

Sphingomyelin (SM) from bovine brain ( $\geq 97.0\%$ ) was bought from Sigma Aldrich (Gillingham, Dorset, UK). This compound is a mixture of different sphingophospholipids such as stearic acid C18:0, nervonic acid 24:1 (cis-15) and lignoceric acid C24:0. SM can be located in cell membranes and in the myelin sheath surrounding the axons [48].

The phospholipid DPPC was also purchased from Sigma Aldrich (Gillingham, Dorset, UK). The properties and chemical structure of this phospholipid molecule were introduced in section 4.1.1.4.

Each lipid standard was dissolved in chloroform to obtain solutions of similar concentrations (v/v). The obtained solutions were mixed in different ratios to obtain the following mixtures:

- Cholesterol: DPPC and Sphingomyelin (1:1).
- Cholesterol: Sphingomyelin (1:1).

A 10  $\mu$ L aliquot from each lipid mixture was drop-cast onto clean silicon and left to air-dry in a fume cupboard for a few minutes until the solvent evaporated completely.

#### 4.3 Methodology for correlation of multi-modal imaging techniques: ToF-SIMS imaging and fluorescence microscopy

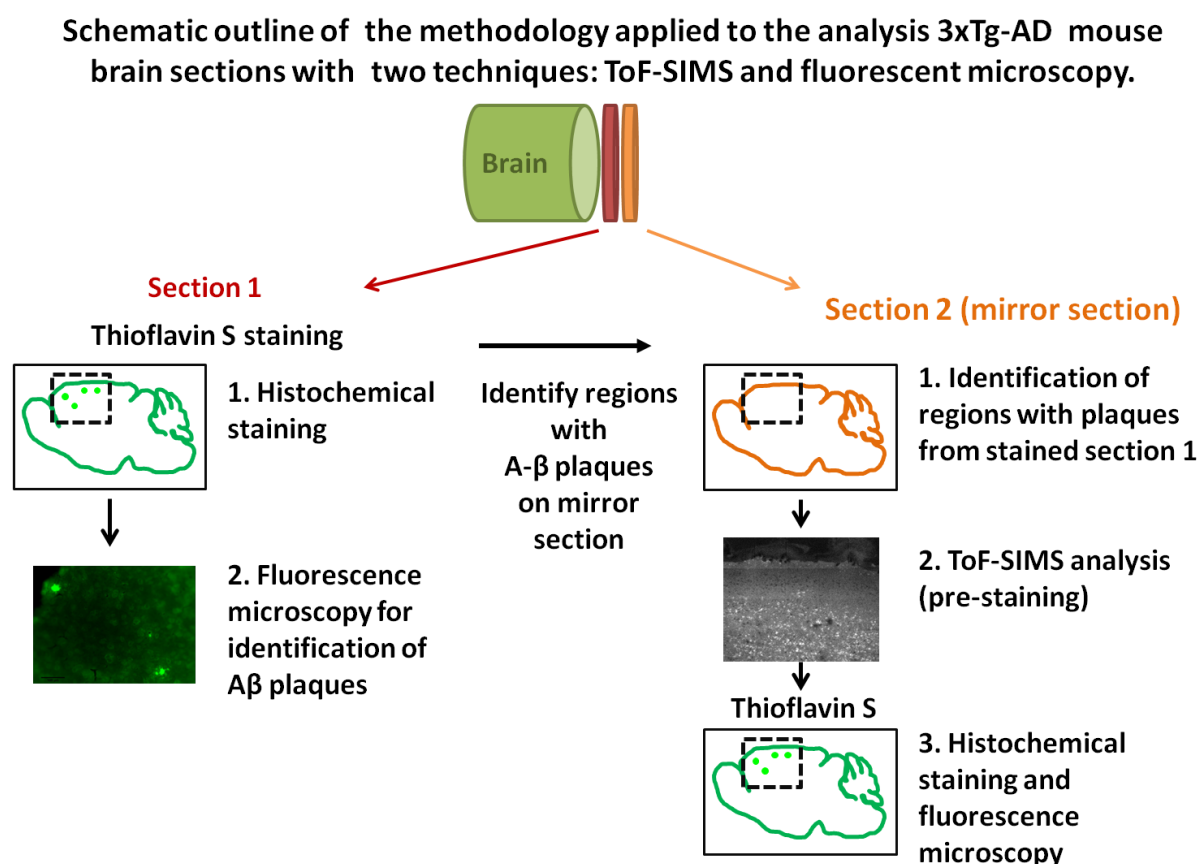


*Figure 4.10: Methodology followed for the analysis of 3xTg-AD brain mirror sections. First, the brain is sectioned in serial mirror sections to obtain almost identical surfaces in two sections. Section 1 is stained with 1% thioflavin S and analysed with fluorescence microscopy to locate the A $\beta$  plaques. Once identified in section 1, the areas containing A $\beta$  plaques are analysed in section 2 using ToF-SIMS. To validate the presence of A $\beta$  aggregates, section 2 is also stained with 1% thioflavin S and analysed with fluorescence microscopy.*

The methodology followed for the multi-modal analysis of 3xTg-AD brain sections is outlined in Figure 4.10. The methodology follows the sectioning of the tissue block into serial mirror sections. Mirror sections are obtained by mounting two sections in a way that their exposed surfaces correspond to immediate sections. In this way, both sections are identical.

The first section (section 1) is prepared for fluorescence microscopy by histological staining of the sample with 1% thioS. ThioS reveals the location A $\beta$  plaques under light excitation due to the fluorophores contained in the dye. Images are obtained with a fluorescence microscope and are used as reference to acquire ToF-SIMS of specific areas of the identical mirror section (section 2).

Specific regions of section 2 containing A $\beta$  plaques are imaged with 40 keV C<sub>60</sub><sup>+</sup> and 20 keV (H<sub>2</sub>O)Ar<sub>2000</sub><sup>+</sup>. After ToF-SIMS analysis, the sample is stained with 1% thioS to validate the presence of A $\beta$  plaques. Fluorescence microscopy images and SIMS images are correlated using image registration.

#### **4.3.1 Sample preparation of 3xTg-AD brain tissue**

Complete snap-frozen WT and 3xTg-AD brains were provided by Dr. Herve Boutin (Faculty of Life Sciences, The University of Manchester, UK). The brains were obtained following ethically approved procedures (Animals (Scientific Procedures) Act 1986). WT mice and 3xTg-AD adult mice were kept together under a 12 hour light-dark cycle (08:00/20:00h) at 22°C. Food and water were available at all times. The transgenes and strains of the 3xTg-AD mouse model are: PS1<sup>M146V</sup>, APP<sup>Swe</sup>, and tau<sup>P301L</sup>.

15 months old mice were euthanized with an anaesthetic overdose with isoflurane and were decapitated. Afterwards, the heads were dissected followed by the removal of the brains. The complete brains were cryo-fixed by submersion in isopentane cooled with liquid nitrogen (-161°C). After snap-freezing, the brains were kept in a freezer at -80°C until sectioning.

As described section 2.5.4, the whole tissue block was mounted on the cryo-microtome's sample holder using *carboxymethyl cellulose* (CMC) as the embedding media to keep it in position for sectioning (section 2.5.4.2). In the microtome, the brain sample is kept at -22°C at all times to avoid chemical degradation. The cryo-microtome used was a *Leica CM3050 S* at the (Wolfson Molecular Imaging Centre, The University of Manchester, UK). Serial sections were cut in a sagittal plane with ~ 9  $\mu$ m of thickness. Here, extreme care was taken to obtain pairs of mirror sections for fluorescence

microscopy and ToF-SIMS analyses. The sections were thaw-mounted on clean silicon wafers.

The sections were kept in pairs (corresponding mirror sections) in sealed sample tubes at -80°C until histochemical staining or ToF-SIMS analysis.

#### **4.3.2 Thioflavin S staining protocol**

Thioflavin S is a compound used as a dye in histochemistry. It is mainly used to stain amyloid  $\beta$  plaques [49]–[51]. This dye attaches to the amyloid protein fibrils (not the monomers) and produces a high fluorescence emission.

In order for the dying to be successful on thin samples obtained for SIMS analysis, a thioS protocol had to be developed. ThioS solutions of 0.01%, 0.1%, 1% and 2% of concentration and different incubation times were tested. Results showed different fluorescence intensity in the background tissue. The integrity of the tissue was also affected when the samples were incubated in EtOH solutions for a long time. The successful thioS protocol is described next:

##### *Reagents:*

- 1% ThioS solution. This is obtained by mixing 0.15 g of ThioS (from Sigma Aldrich, Gillingham, Dorset, UK) in 15 mL of milli-Q water (purified through a 0.22  $\mu\text{m}$  filter). Once prepared, the solution was filtered through a 0.2  $\mu\text{m}$  membrane to eliminate micelles that do not dissolve. The solution is kept in the dark to avoid photo-bleaching.
- 100%, 95%, 80% and 70% (vol/vol) ethanol solutions.
- Milli-Q water.

All solutions were prepared and kept in clean glass sample tubes. The silicon wafers were handled with clean tweezers.

##### *Procedure:*

1. The brain sections kept in the freezer are desiccated at room temperature for one hour before staining.
2. The solutions are labelled and organised in the following order:
  - A. 100% EtOH
  - B. 95% EtOH
  - C. 80% EtOH

- D. 70% EtOH
  - E. Milli-Q water
  - F. 1% ThioS solution
  - G. 70% EtOH
  - H. 80% EtOH
  - I. 95% EtOH
  - J. 100% EtOH
  - K. Milli-Q water
  - L. Milli-Q water
  - M. Milli-Q water
3. Submerge the brain sample in 100% EtOH for 1 min (A).
  4. Immediately after dip the sample in 95% EtOH (B) for one minute followed by one minute in 80% EtOH (C), and one more minute in 70% EtOH (D). These solutions are use to fix the tissue chemically and re-hydrate slowly.
  5. The section is submerged in milli-Q water (E) for a few seconds for re-hydration.
  6. Once re-hydrated, the sample is incubated during 25 to 30 minutes in a 1% thioS solution for staining (F). After this step, the tissue takes a distinctive yellow colour. During this process, the samples must be kept in the dark to avoid photo-bleaching.
  7. After staining, the sample is differentiated by incubation in 70% EtOH (G) for one minute, 80% EtOH (H) for one minute, 95% EtOH (I) for one minute and 100% EtOH (J) for an extra minute.
  8. The section is submerged in milli-Q water (K) for one minute to remove the excess of dye. Then it is rinsed by dipping the silicon wafer in milli-Q water twice (L and M). At this point, ethanol is no longer used to avoid loss of staining.
  9. After these steps, the sample is placed in the desiccator for an hour to dehydrate the sample before fluorescence microscopy analysis.

The steps of this protocol are summarised in Figure 4.11. A crucial consideration is the handling and storage of the sample in the dark after staining. The fluorophore contained in thioS slowly degrades, especially under light exposure.

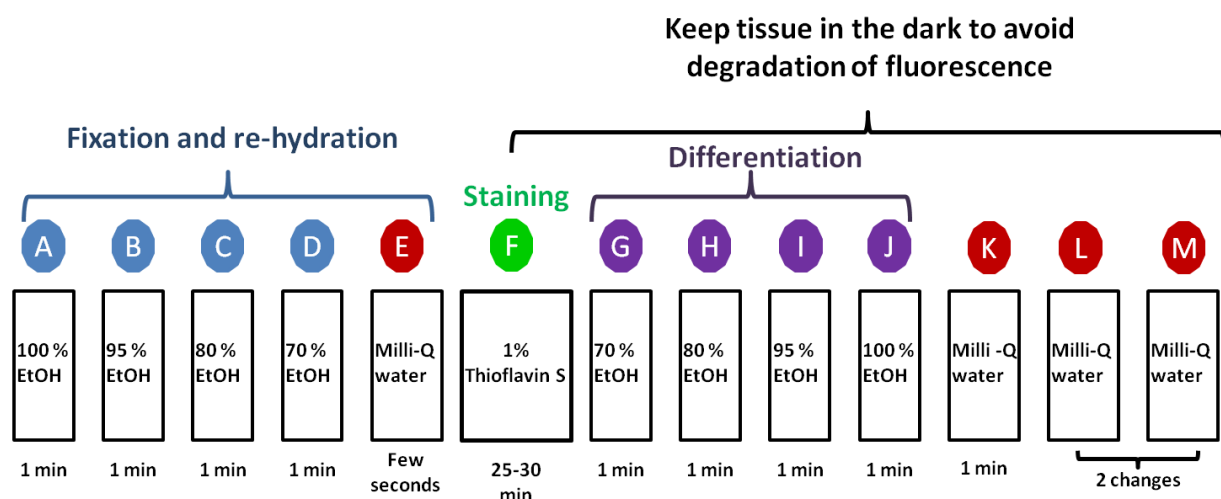


Figure 4.11: Developed staining protocol for Thioflavin S. All solutions are placed in glass sample tubes. The procedure starts by submerging the brain section in solution (A) and ends with solution (M). Solutions (A-E) are applied to fix and re-hydrate the tissue sample. Solution (F) is the staining step of the protocol. Solutions (G-M) are applied to rinse the excess of dye in the sample. Incubation times are specified below every solution.

#### 4.3.3 Fluorescence microscopy imaging

Fluorescence microscopy images were collected using a Nikon Eclipse 90i microscope equipped with a high-pressure mercury lamp that emits light in a broad spectrum. The sample is illuminated by epi-fluorescence illumination. For the excitation wavelength of thioS (430 nm), this microscope comprises a DAPI-FITC-TRITC filter set for detection of blue, green and red emission. The emission wavelength of thioS is 550 nm.

Tiled images were taken with a monochromatic DS-Qi1 camera. Images from the complete section were acquired with a resolution of 0.85  $\mu\text{m}$  per pixel. Images from single plaques were recorded with a resolution of 0.53  $\mu\text{m}$ /pixel.

#### 4.3.4 Handling brain sections for ToF-SIMS imaging

As previously mentioned, all sections were kept at  $-80^{\circ}\text{C}$ . When ToF-SIMS imaging is to be carried out on one of the sections, the brain sample has to be dehydrated for 1 hour prior to analysis. As described in section 4.2.2, this dehydration process allows the analysis of the sample under high-vacuum conditions i.e. in the ToF-SIMS instrument without disruption of the sample's structure.

#### 4.3.5 Synthetic Amyloid- $\beta$ peptide (1-40)

Synthetic peptide Amyloid-Beta (1-40), human was obtained from ANASPEC (Fremont, California), gifted by Prof Andrew Doig (Faculty of Life Sciences, Univ. Manchester).

This peptide (together with A $\beta$  1-42) is one of the two major variants of the A $\beta$  protein constituting the neuritic plaques found in AD brain. This molecule has a molecular weight of 4329.9 Da. The amino acid sequence is:



For ToF-SIMS analysis, 0.0001 g from this synthetic peptide was dissolved in 20  $\mu\text{L}$  of DMSO. 10  $\mu\text{L}$  of the solution was dispensed onto clean silicon. The wafer was left to air-dry for 10 minutes before analysis in a fume cupboard until the solvent evaporated completely.

#### 4.4 References

- [1] F. Reich, "Sample handling for ToF-SIMS," in *TOF-SIMS: Materials analysis by mass spectrometry*, J. C. Vickerman and D. Briggs, Eds. Manchester: IM Publications, 2013, pp. 397–416.
- [2] S. Parry and N. Winograd, "High-resolution TOF-SIMS imaging of eukaryotic cells preserved in a trehalose matrix," *Anal. Chem.*, vol. 77, no. 24, pp. 7950–7957, 2005.
- [3] K. E. Ryan, E. J. Smiley, N. Winograd, and B. J. Garrison, "Angle of incidence effects in a molecular solid," *Appl. Surf. Sci.*, vol. 255, no. 4, pp. 844–846, 2008.
- [4] H. Tian, J. S. Fletcher, R. Thuret, A. Henderson, N. Papalopulu, J. C. Vickerman, and N. P. Lockyer, "Spatiotemporal lipid profiling during early embryo development of *Xenopus laevis* using dynamic Time-of-Flight Secondary Ion Mass Spectrometry (ToF-SIMS) Imaging," *J. Lipid Res.*, vol. 55, 2014.
- [5] R. Hill, P. Blenkinsopp, S. Thompson, J. Vickerman, and J. S. Fletcher, "A new time-of-flight SIMS instrument for 3D imaging and analysis," *Surf. Interface Anal.*, vol. 43, no. 1–2, pp. 506–509, 2011.
- [6] D. Touboul, O. Laprevote, and A. Brunelle, "Medical and biological applications of ToF-SIMS," in *TOF-SIMS: Materials analysis by mass spectrometry*, 2nd, Ed. Manchester: IM Publications, 2013, pp. 583–612.
- [7] A. G. Shard and I. S. Gilmore, *TOF-SIMS: Materials analysis by mass spectrometry*, 2nd ed. Manchester: IM Publications, 2013.
- [8] N. Kato and M. Kudo, "Simulation of fragmentation of polyethylene glycol by quantum molecular dynamics for ToF-SIMS spectral analysis," *J. Surf. Anal.*, vol. 17, no. 3, pp. 208–211, 2011.



- [9] A. Piwowar, J. Fletcher, N. Lockyer, and J. Vickerman, "Investigating the effect of temperature on depth profiles of biological material using ToF-SIMS," *Surf. Interface Anal.*, vol. 43, no. 1–2, pp. 207–210, 2011.
- [10] S. EBook, *Basic Amino Acids—Advances in Research and Application: 2012 Edition*. Atlanta, Georgia: ScholarlyEditions, 2012.
- [11] S. Aoyagi, J. S. Fletcher, S. Sheraz, T. Kawashima, I. Berrueta Razo, A. Henderson, N. P. Lockyer, and J. C. Vickerman, "Peptide structural analysis using continuous Ar cluster and C60 ion beams," *Anal. Bioanal. Chem.*, vol. 405, no. 21, pp. 6621–6628, 2013.
- [12] J. D. DeBord, F. A. Fernandez-Lima, S. V. Verkhoturov, E. A. Schweikert, and S. Della-Negra, "Characteristics of positive and negative secondary ions emitted from and impacts," *Changes*, vol. 29, no. 6, pp. 997–1003, 2012.
- [13] A. Benninghoven, J. Okano, R. Shimizu, and H. W. Werner, *Secondary Ion Mass Spectrometry SIMS IV: Proceedings of the Fourth International Conference*. Osaka, Japan, 1983.
- [14] J. Cheng and N. Winograd, "Depth profiling of peptide films with TOF-SIMS and a C 60 probe," *Anal. Chem.*, vol. 77, no. 11, pp. 3651–3659, 2005.
- [15] S. Muramoto, J. Brison, and D. G. Castner, "ToF-SIMS depth profiling of trehalose: The effect of analysis beam dose on the quality of depth profiles," *Surf. Interface Anal.*, vol. 43, no. 1–2, pp. 58–61, 2011.
- [16] N. Bourdos, F. Kollmer, A. Benninghoven, M. Ross, M. Sieber, and H. J. Galla, "Analysis of lung surfactant model systems with time-of-flight secondary ion mass spectrometry," *Biophys. J.*, vol. 79, no. 1, pp. 357–369, 803.
- [17] E. Keating, A. J. Waring, F. J. Walther, F. Possmayer, R. A. W. Veldhuizen, and N. O. Petersen, "A ToF-SIMS study of the lateral organization of lipids and proteins in pulmonary surfactant systems," *Biochim. Biophys. Acta - Biomembr.*, vol. 1808, no. 3, pp. 614–621, 2011.
- [18] B. Vaezian, C. R. Anderton, and M. L. Kraft, "Discriminating and imaging different phosphatidylcholine species within phase-separated model membranes by principal component analysis of TOF-secondary ion mass spectrometry images," *Anal. Chem.*, vol. 82, no. 24, pp. 10006–10014, 2010.

- [19] A. G. Sostarecz, D. M. Cannon, C. M. McQuaw, S. Sun, A. G. Ewing, and N. Winograd, "Influence of molecular environment on the analysis of phospholipids by time-of-flight secondary ion mass spectrometry.," *Langmuir*, vol. 20, no. 12, pp. 4926–4932, 2004.
- [20] W. Belvedere, "Arginine : Biochemistry , Physiology , and Therapeutic Implications," pp. 227–238, 2015.
- [21] J. F. Riordan, "Angiotensin II: Biosynthesis, molecular recognition, and signal transduction," *Cell. Mol. Neurobiol.*, vol. 15, no. 6, pp. 637–651, 1995.
- [22] D. Touboul, A. Brunelle, and O. Laprévote, "Structural analysis of secondary ions by post-source decay in time-of-flight secondary ion mass spectrometry," *Rapid Commun. Mass Spectrom.*, vol. 20, no. 4, pp. 703–709, 2006.
- [23] S. Sheraz, A. Barber, J. S. Fletcher, N. P. Lockyer, and J. C. Vickerman, "Enhancing secondary ion yields in ToF-SIMS using water cluster primary beams .," *Anal. Chem.*, pp. 2–3, 2013.
- [24] E. P. Feofilova, a. I. Usov, I. S. Mysyakina, and G. a. Kochkina, "Trehalose: Chemical structure, biological functions, and practical application," *Microbiology*, vol. 83, no. 3, pp. 184–194, 2014.
- [25] S. Sheraz née Rabbani, I. Berrueta Razo, T. Kohn, N. P. Lockyer, and J. C. Vickerman, "Enhancing Ion Yields in Time-of-Flight-Secondary Ion Mass Spectrometry: A Comparative Study of Argon and Water Cluster Primary Beams," *Anal. Chem.*, vol. 87, no. 4, pp. 2367–2374, 2015.
- [26] B. Alberts, A. Johnson, J. Lewis, and E. Al., *Molecular Biology of the Cel*, 4th ed. New York: Garland Science, 2002.
- [27] J. M. Berg, T. J.L., and L. Stryer, *Biochemistry*, 5th ed. New York: W H Freeman, 2002.
- [28] S. Aoyagi, T. Shimanouchi, T. Kawashima, and H. Iwai, "ToF-SIMS observation for evaluating the interaction between amyloid  $\beta$  and lipid membranes," *Anal. Bioanal. Chem.*, pp. 2859–2863, 2015.
- [29] E. Keatinga, A. J. Waring, F. J. Walther, F. Possmayer, A. W. Ruud, V. Petersen, and O. Nils, "A ToF-SIMS study of the lateral organization of lipids and proteins in pulmonary surfactant systems," *Changes*, vol. 29, no. 6, pp. 997–1003, 2012.

- [30] D. Breitenstein, J. J. Batenburg, B. Hagenhoff, and H. J. Galla, "Lipid specificity of surfactant protein B studied by time-of-flight secondary ion mass spectrometry.," *Biophys. J.*, vol. 91, no. 4, pp. 1347–1356, 2006.
- [31] J. Bailey, R. Havelund, A. G. Shard, I. S. Gilmore, M. R. Alexander, J. S. Sharp, and D. J. Scurr, "3D ToF-SIMS Imaging of Polymer Multilayer Films Using Argon Cluster Sputter Depth Profiling," *ACS Appl. Mater. Interfaces*, vol. 7, no. 4, pp. 2654–2659, 2015.
- [32] J. Cheng, A. Wucher, and N. Winograd, "Molecular Depth Profiling with Cluster Ion Beams," vol. 110, no. 16, pp. 8329–8336, 2006.
- [33] X. Ren, L. T. Weng, C. M. Chan, and K. M. Ng, "Hollow interior structure of spin-coated polymer thin films revealed by ToF-SIMS three-dimensional imaging," *Anal. Chem.*, vol. 84, no. 20, pp. 8497–8504, 2012.
- [34] S. J. Hinder, C. Lowe, and J. F. Watts, "ToF-SIMS depth profiling of a complex polymeric coating employing a C 60 sputter source," *Surf. Interface Anal.*, vol. 39, no. 6, pp. 467–475, 2007.
- [35] D. J. Miller, L. Sun, M. J. Walzak, N. S. McIntyre, D. Chvedov, and a. Rosenfeld, "Static SIMS studies of fatty alcohols, amines and esters on gold and aluminium-magnesium alloy surfaces," *Surf. Interface Anal.*, vol. 37, no. 5, pp. 499–508, 2005.
- [36] L. Zheng, A. Wucher, and N. Winograd, "Chemically Alternating Langmuir-Blodgett Thin Films as a Model for Molecular Depth Profiling by Mass Spectrometry," *J. Am. Soc. Mass Spectrom.*, vol. 19, no. 1, pp. 96–102, 2008.
- [37] S. A. Jenekhe, "The rheology and spin coating of polyimide solutions," *Polym. Eng. Sci.*, vol. 23, no. 15, pp. 830–834, 1983.
- [38] S. Reuter, A. M. Hofmann, K. Busse, H. Frey, and J. Kressler, "Langmuir and Langmuir-Blodgett Films," *Society*, vol. 27, no. 5, pp. 1978–89, 2011.
- [39] M. A. Sani, J. D. Gehman, and F. Separovic, "Lipid matrix plays a role in Abeta fibril kinetics and morphology," *FEBS Lett.*, vol. 585, no. 5, pp. 749–754, 2011.
- [40] M. Cavallini, "Status and perspectives in thin films and patterning of spin crossover compounds," *Phys. Chem. Chem. Phys.*, vol. 14, no. 32, pp. 11867–11876, 2012.

- [41] A. E. Donaldson and I. L. Lamont, "Biochemistry changes that occur after death: Potential markers for determining post-mortem interval," *PLoS One*, vol. 8, no. 11, pp. 1–10, 2013.
- [42] C. Cocco, G. V. Melis, and G.-L. Ferri, "Embedding media for cryomicrotomy: an applicative reappraisal," *Appl. Immunohistochem. Mol. Morphol.*, vol. 11, no. 3, pp. 274–280, 2003.
- [43] T. J. Rahub, S. L. Douglas, G. W. Melchior, W. N. Charman, and W. Morozowich, "Assesing intestinal lymphatic transport," in *Lymphatic transport of drugs*, W. N. Charman and V. J. Stella, Eds. Boca Raton, Florida: CRC Press, 1992, pp. 63–112.
- [44] A. Piwowar and N. Winograd, "Application of SIMS to study of biological systems," in *TOF-SIMS: Materials analysis by mass spectrometry*, 2013.
- [45] M. K. Passarelli and N. Winograd, "Lipid imaging with time-of-flight secondary ion mass spectrometry (ToF-SIMS)," *Biochim. Biophys. Acta - Mol. Cell Biol. Lipids*, vol. 1811, no. 11, pp. 976–990, 2011.
- [46] E. Ikonen, "Cellular cholesterol trafficking and compartmentalization.," *Nat. Rev. Mol. Cell Biol.*, vol. 9, no. 2, pp. 125–138, 2008.
- [47] M. Orth and S. Bellosta, "Cholesterol: Its regulation and role in central nervous system disorders," *Cholesterol*, vol. 2012, 2012.
- [48] J. P. Slotte and B. Ramstedt, "The functional role of sphingomyelin in cell membranes," *Eur. J. Lipid Sci. Technol.*, vol. 109, no. 10, pp. 977–981, 2007.
- [49] T. Bussi re, F. Bard, R. Barbour, H. Grajeda, T. Guido, K. Khan, D. Schenk, D. Games, P. Seubert, and M. Buttini, "Morphological characterization of Thioflavin-S-positive amyloid plaques in transgenic Alzheimer mice and effect of passive Abeta immunotherapy on their clearance.," *Am. J. Pathol.*, vol. 165, no. 3, pp. 987–995, 2004.
- [50] A. Sun, X. V. Nguyen, and G. Bing, "Comparative analysis of an improved thioflavin-s stain, Gallyas silver stain, and immunohistochemistry for neurofibrillary tangle demonstration on the same sections.," *J. Histochem. Cytochem.*, vol. 50, no. 4, pp. 463–472, 2002.
- [51] G. Kel nyi, "Thioflavin S fluorescent and congo red anisotropic stainings in the histologic demonstration of amyloid," *Acta Neuropathol.*, vol. 7, no. 4, pp. 336–348, 1967.

## 5 Comparative studies on biomolecule models

One of the principal limitations for biological analysis with ToF-SIMS is the low secondary ion yield obtained from these type of samples [1], [2]. Based on the hypothesis that increasing the density of water-related ions impacting the analysis area would enhance the protonation of intact  $[M+H]^+$  ions, the SIMS group from the University of Manchester in collaboration with Ionoptika, Ltd have developed a prototype water cluster ion beam (described in section 3.5.2). The water clusters are generated by supersonic jet expansion and the boiler assembly and ion source has been coupled with the Ionoptika GCIB 20 already fitted in the J105 3D chemical imager [1]. This chapter will discuss the secondary ion yields generated from four biorelated compounds prepared in spin-coated films: L-arginine, angiotensin II, trehalose dehydrate and dipalmitoylphosphatidylcholine (DPPC). Data obtained with low and high primary ion dose conditions using 20 keV  $C_{60}^+$ , 20 keV  $Ar_n^+$ , 20 keV  $(H_2O)_n^+$  and 20 keV  $(H_2O)Ar_n^+$  were analysed and compared to obtain information about the secondary ion yields of  $[M+H]^+$  ions and diagnostic fragments. To obtain reproducible data and reliable results across different samples, secondary ion yields were calculated in steady-state conditions. Cluster ion beams that generate higher yields of intact molecules will be applied to the analysis of mouse brain tissue.

In the first series of experiments performed with this prototype water beam, a 10 keV  $(H_2O)_{1000}^+$  beam was compared to 10 keV  $Ar_{1000}^+$  [1] (see section 2.5.7). Secondary ion yields from arginine, haloperidol, DPPC, and angiotensin II were measured, obtaining an enhancement by a factor of 10 or more when using water clusters for analysis. The ion suppression effect on haloperidol when mixed in a 1:10 ratio with DPPC was also reduced with 10 keV  $(H_2O)_{1000}^+$  [1]. These preliminary results provided an evidence base to explore the use of water clusters with higher energy and larger sizes. This chapter will explain details of the experiments and the results obtained from new comparative experiments performed with 20 keV argon, water and water-doped argon clusters on different biomolecule models.

Results presented in this chapter were published in a scientific article included in a Appendix I.

### 5.1 Molecular profiling and the steady-state region

The concept of depth profiling was introduced in the literature review chapter (section 2.2.2). It was mentioned that atomic primary ion beams can cause damage beyond the

sample's surface, whereas the damage induced by polyatomic beams just affects the regions close to the top layer [3]. In the latter case, the chemical structure is mainly preserved and depth profiling can be enabled [4]. The energy of the polyatomic cluster impacting the surface causes a collision of atoms; this impact also produces a collisional spike which translates in a non-linear increase in sputtering and ion yield. An equilibrium state is achieved when the damage induced by the primary particles is removed and does not accumulate [4], [5].

Usually, depth-profiling an organic material will result in one of four scenarios described in Figure 5.1. In linear sputtering conditions scenario (A) can be observed. In region 1, a rapid exponential decay of the molecular signal is the result of the initial damage saturation. Within region 2 there is a constant signal intensity or steady-state where the damage accumulation is in equilibrium with the sputtering process. Finally, region 3 is an interfacial region where the molecular signal drops and the substrate signal arises. This is expected after getting through the organic layer and reaching the substrate [4].

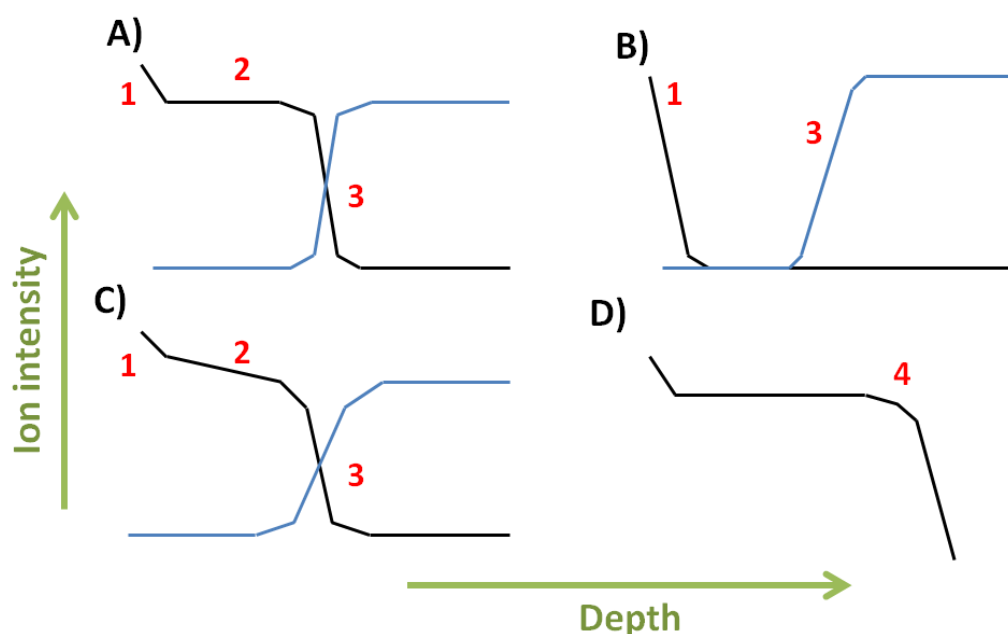


Figure 5.1: Different situations encountered during organic depth profiling. (A-C) depth profiling of thin films and (D) depth profiling a bulk sample. (A) example of a profile under ideal conditions. (B) and (C) depth profiles under non-optimum conditions showing the accumulation of damage. The damage exhibit in (B) is greater than (C). The three regions observed in plots (A-C) are: 1) the initial signal decay observed in the surface transient region of the depth profile, 2) steady-state region and 3) interfacial region with a significant decrease of the ion signal and increase in the substrate signal. (D) example of depth profiling bulk materials when there is loss of signal intensity after high primary ion dose exposure [4].

If the sputtering conditions are nonlinear, as shown in (B), the molecular signal decays immediately and the interface with the substrate is widened. There are some cases with intermediate behaviour, as depicted by (C) where the signal decreases steadily as a function of depth. (D) Illustrates the signal degradation under higher primary ion dose for depth profiling in bulk films.

## 5.2 Aim of the experiments

The aim of the experiments presented in this chapter is to analyse the compounds arginine, angiotensin II, trehalose dehydrate and DPPC and compare the secondary ion yields obtained during  $C_{60}^+$ ,  $Ar_n^+$ ,  $(H_2O)_n^+$  and  $(H_2O)Ar_n^+$  bombardment. The ultimate goal of the presented experiments is the identification of cluster primary ion beams that could potentially be applied to mouse brain tissue imaging, enabling the detection of intact lipid molecules. Cluster ion beams were evaluated according to the generation of secondary ion yield and the obtainable spatial resolution.

## 5.3 ToF-SIMS analysis

ToF-SIMS analysis was performed in a J105 3D chemical imager (Ionoptika Ltd, UK) previously described in the instrumentation chapter 3.

The studies presented will focus on the comparison of secondary ion yield generated by various water-containing clusters at room temperature. Data from all experiments was collected in positive ion mode. The prepared films were depth-profiled; an initial analysis of all compounds was carried out under static dose conditions using a primary ion dose of  $5 \times 10^{11}$  ions  $cm^{-2}$ . For arginine and trehalose, the initial dose was followed by a dose-dependent study of spectral changes, accumulating  $3 \times 10^{13}$  ions  $cm^{-2}$  where a steady-state was observed. The steady-state region for DPPC and angiotensin II was reached after a primary ion dose of  $2 \times 10^{13}$  ions  $cm^{-2}$ .

All ToF-SIMS data was acquired by scanning a  $350 \mu m^2$  area divided into  $16 \times 16$  pixels. The number of shots selected was dependant on the analysis beam current and so was the duty cycle. For a given ion beam current and a desired primary ion dose, the duty cycle can be selected. It will indicate the percentage of experimental time (0-100 %) during which the ion beam is on.

The ion current from each cluster beam is defined by the cluster size and type of cluster (water, argon or water-doped argon). During analysis, charging can be accumulated in the sample, preventing the extraction of secondary ions. This is mainly

observed in insulating thick samples, such as DPPC. To neutralise this charging effect, an external positive voltage of 2-4 Volts was connected to the sample stage when charge compensation was needed. Low mass range (50-1100 Da) was selected to acquire mass spectra.

The four reference samples were subjected to comparative analysis using 20 keV  $\text{Ar}_n^+$  with  $n=1000-6000$ , 20 keV  $(\text{H}_2\text{O})_n^+$  where  $n=1000-10000$  and 20 keV  $(\text{H}_2\text{O})\text{Ar}_n^+$  with  $n=1000-6000$ . Experiments acquired with different beam energies i.e. 10 and 20 keV are presented to study the secondary ion signal variation at a given cluster size.

For reference purposes, an initial 20 keV  $\text{C}_{60}^+$  analysis with a primary ion dose of  $3 \times 10^{13}$  ions  $\text{cm}^{-2}$  was performed on each sample before any other experiment was carried out. The total secondary ion yields from this experiment were used to normalise and correct the rest of the experiments for any instrumental variations in order to compare the ion yields obtained from similar samples in different days. From all the  $\text{C}_{60}$  analyses acquired, the calculated coefficient of signal variation as a percentage was 55.18%.

#### **5.4 Comparative secondary ion yield studies with $\text{Ar}_n^+$ and $(\text{H}_2\text{O})_n^+$ clusters on standard biomolecules**

##### **5.4.1 Results and discussion**

The spectra obtained from arginine, angiotensin II, trehalose and DPPC with 20 keV  $\text{Ar}_{4000}^+$  and  $(\text{H}_2\text{O})_{4000}^+$  after an ion dose of  $5 \times 10^{11}$  ions  $\text{cm}^{-2}$  are displayed in Figure 5.2. When comparing spectra acquired with  $\text{Ar}_{4000}^+$  and  $(\text{H}_2\text{O})_{4000}^+$  it is possible to observe qualitative differences. For example, sodiated adducts ( $[\text{M}+\text{Na}]^+$  ions) have higher relative signal intensity in the spectra obtained with  $\text{Ar}_{4000}^+$  whereas the quasi-molecular ions  $[\text{M}+\text{H}]^+$  are higher in intensity under  $(\text{H}_2\text{O})_{4000}^+$  bombardment. These results agree with the increased secondary ion signal observed in the first set of experiments performed with the prototype 10 keV water cluster ion beam [1]. These studies also agree with results from previous experiments that showed an increased  $[\text{M}+\text{H}]^+$  ion signal when ice matrices and water dosing of samples was implemented e.g. analysis of freeze-fractured and frozen hydrated samples [6]–[8].

To monitor the secondary ion signal as a function of the primary ion dose, the samples were exposed to a total primary ion dose of  $10^{13}$  ions  $\text{cm}^{-2}$ , where a steady-state was observed. The secondary ion signal from different ions was quantified and plotted relative to the total ion signal for  $\text{Ar}_{2000}$ , after  $5 \times 10^{11}$  ions  $\text{cm}^{-2}$  and 1.5 or  $3 \times 10^{13}$  ions  $\text{cm}^{-2}$  primary ion dose.



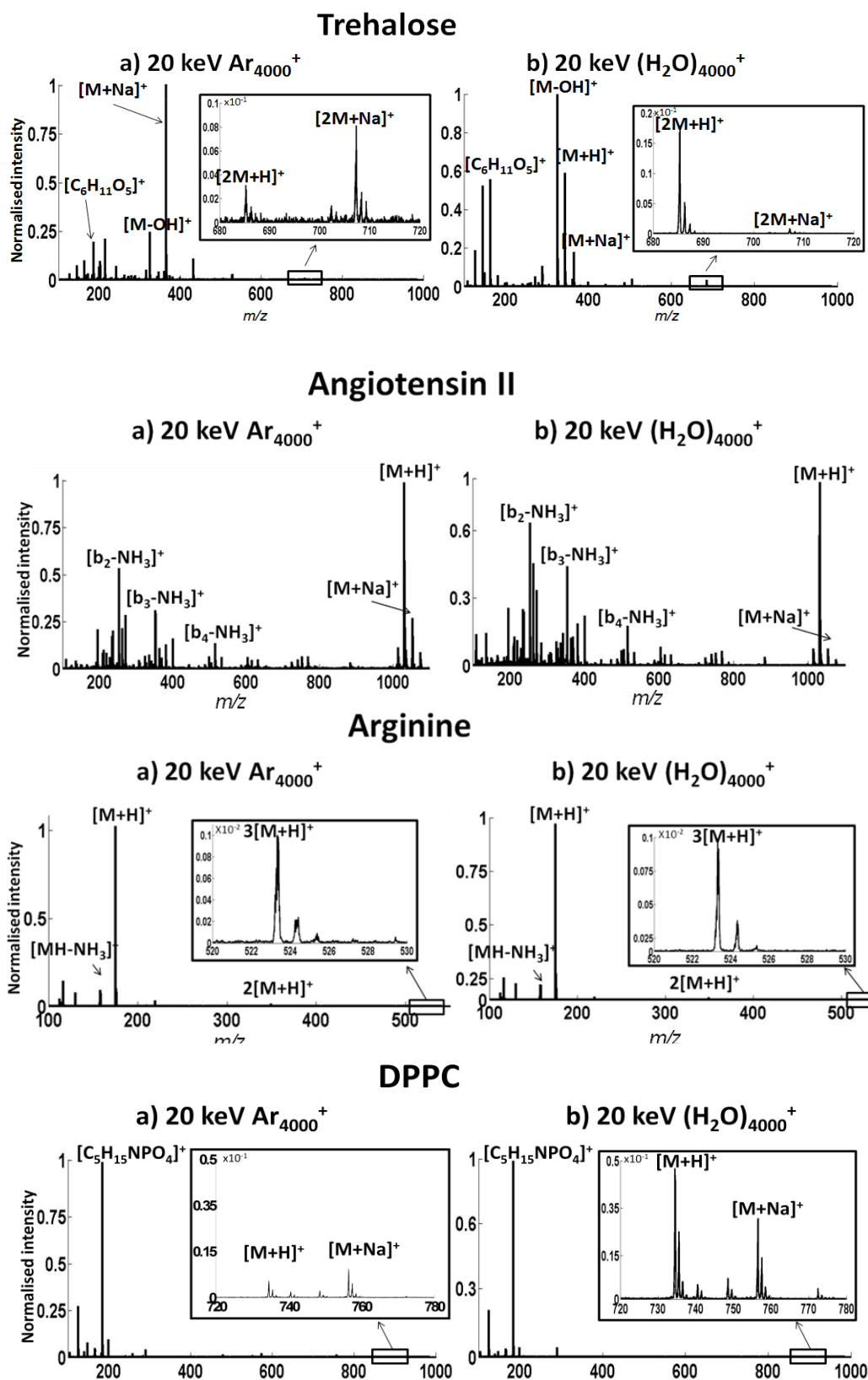


Figure 5.2: Trehalose, angiotensin II, arginine and DPPC spectra acquired with (a) 20 keV Ar<sub>4000</sub><sup>+</sup> and (b) 20 keV (H<sub>2</sub>O)<sub>4000</sub><sup>+</sup> cluster ion beams with a primary ion dose of  $5 \times 10^{11}$  ions cm<sup>-2</sup>. All spectra are normalised to their base peak.

Figure 5.3 displays the secondary ion yield comparison obtained from trehalose acquired with 20 keV  $\text{Ar}_{2000,4000}^+$  and 20 keV  $(\text{H}_2\text{O})_{2000}$  and  $(\text{H}_2\text{O})_{4000}^+$ .

Overall, the signal intensities do not decay under argon or water bombardment with  $3 \times 10^{13}$  ions  $\text{cm}^{-2}$ . However, it is noticeable that the signal of  $[\text{M}+\text{Na}]^+$  obtained with  $\text{Ar}_{2000}$  and  $\text{Ar}_{4000}$  predominates over  $[\text{M}+\text{H}]^+$  and  $[\text{M}-\text{OH}]^+$ . The signal obtained from the  $[\text{M}+\text{Na}]^+$  ion increases after an ion dose of  $5 \times 10^{12}$  ions  $\text{cm}^{-2}$ , remaining constant until the end. Under  $\text{Ar}_{2000}$  or  $\text{Ar}_{4000}$  bombardment, the intensity of the ions formed by protonation is less than 20% of the signal obtained from the sodiated adduct.  $[\text{M}-\text{OH}]^+$  is the most intense of these ions and it is formed when the protonated  $[\text{M}+\text{H}]^+$  loses a molecule of water. The ion intensity of the fragment  $[\text{C}_5\text{H}_{11}\text{O}_5]^+$  is the lowest.

On the other hand, the analysis acquired with 20 keV  $(\text{H}_2\text{O})_{4000}^+$  shows an enhanced ion intensity. Here, the highest signal is  $[\text{M}-\text{OH}]^+$  and  $[\text{M}+\text{Na}]^+$  is the least intense. The  $[\text{M}+\text{Na}]^+$  secondary ion signal is equivalent to approximately 20% of that obtained from the quasi-molecular ion. With 20 keV  $(\text{H}_2\text{O})_{2000}^+$  and low accumulated primary ion dose (up to  $\sim 5 \times 10^{12}$  ions  $\text{cm}^{-2}$ ) the signal from  $[\text{M}-\text{OH}]^+$  is the highest. After accumulating  $1 \times 10^{13}$  ions  $\text{cm}^{-2}$ , the  $[\text{M}+\text{Na}]^+$  yield overtakes the  $[\text{M}-\text{OH}]^+$  ion. In this case  $(\text{H}_2\text{O})_{2000}^+$  clusters produce higher signal from  $[\text{M}+\text{H}]^+$  when compared to  $\text{Ar}_{2000,4000}^+$  clusters.

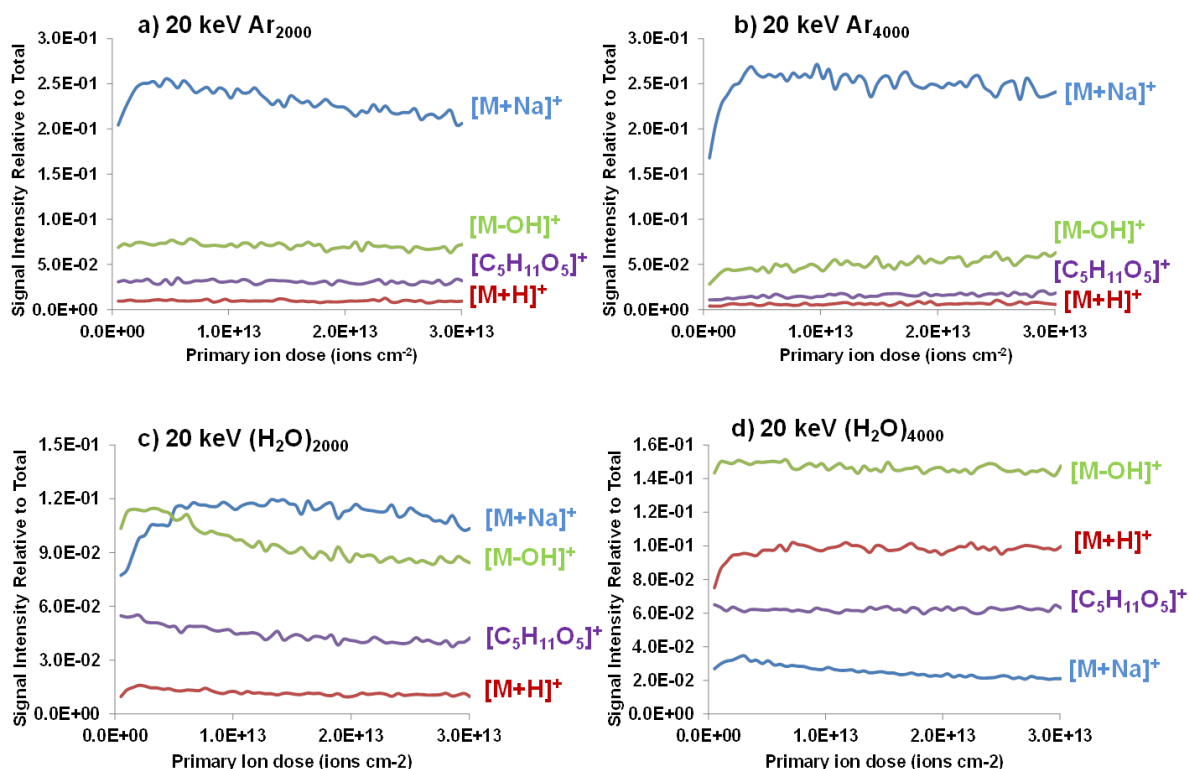


Figure 5.3: Plots (a) 20 keV  $\text{Ar}_{2000}^+$ ; (b) 20 keV  $\text{Ar}_{4000}^+$ ; (c) 20 keV  $(\text{H}_2\text{O})_{2000}^+$  and (d) 20 keV  $(\text{H}_2\text{O})_{4000}^+$  secondary ion signal variation in trehalose as a function of primary ion dose. The signal was normalised to the total in all plots.

These results indicate that the larger water cluster with  $E/\text{molecule} = 5$  eV produced more protonated ions whereas the cluster  $(\text{H}_2\text{O})_{2000}^+$  with  $E/\text{molecule} = 10$  eV behaves similarly to argon.

The rest of the standard compounds (arginine, angiotensin II and DPPC) studied under the same conditions showed a very similar behaviour. If the  $(\text{H}_2\text{O})_n^+$  cluster is larger, the decay of secondary yield in the steady-state region is smaller. If the energy per water molecule is  $\leq 10$  eV, the protonation of ions was increased.  $\text{Ar}_n^+$  clusters mainly favoured the formation of  $[\text{M}+\text{Na}]^+$  ions (Figure 5.2 and Figure 5.3).

For secondary ion signal comparison relative to  $E/\text{atom or molecule}$ , the variation of yields was plotted for each cluster where  $n=1000-10000$ . The secondary ion yields of the main ions from the four biomolecules were plotted using different argon and water clusters for bombardment. All clusters ion beams had 20 keV of energy.

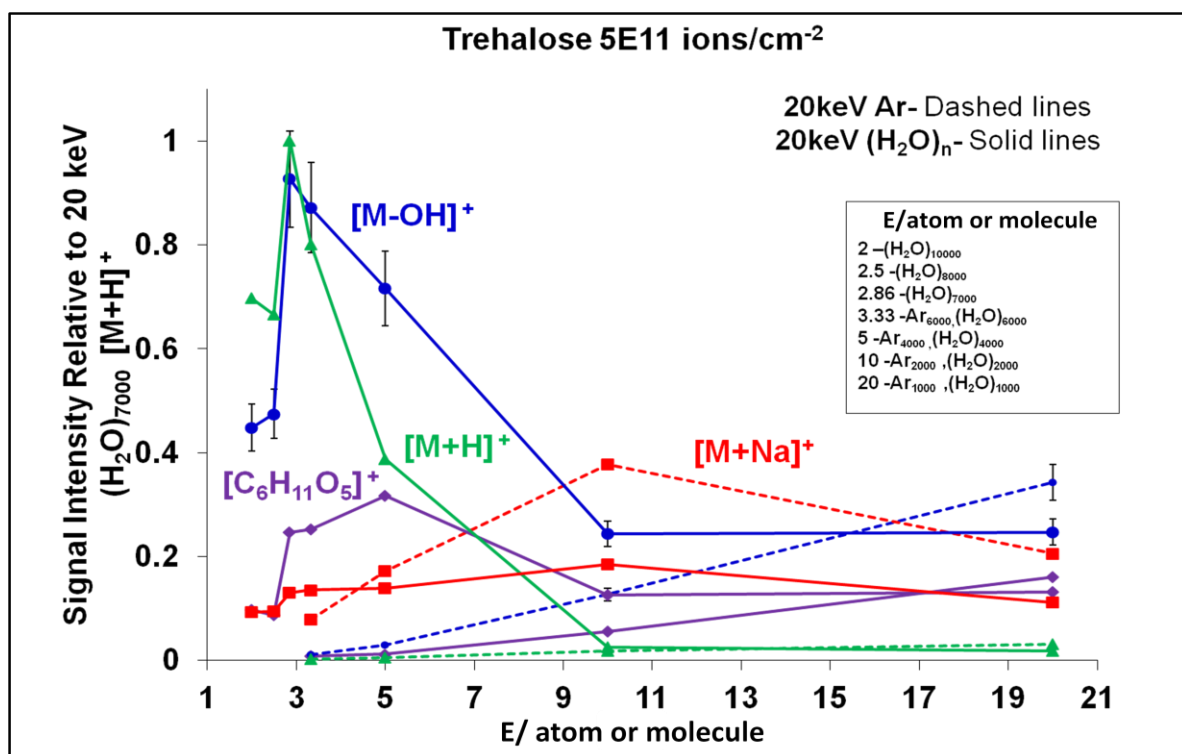


Figure 5.4: Secondary ion signal plot after exposing the trehalose sample to  $5 \times 10^{11}$  ions  $\text{cm}^{-2}$ . The signal was normalised to the highest value obtained from the quasi-molecular ion  $[\text{M}+\text{H}]^+$  with 20 keV  $(\text{H}_2\text{O})_{7000}^+$ . The secondary ion signal is plotted as a function of  $E/\text{atom or molecule}$ . The experiments were acquired with 20 keV  $\text{Ar}_n^+$  (dashed lines) and  $(\text{H}_2\text{O})_n^+$  (solid lines) clusters. The green line shows the signal variation of the trehalose quasi-molecular ion  $[\text{M}+\text{H}]^+$ ;  $[\text{M}-\text{OH}]^+$  is highlighted with blue lines; the sodiated molecular ion adduct  $[\text{M}+\text{Na}]^+$  is plotted in red lines and finally the fragment  $[\text{C}_6\text{H}_{11}\text{O}_5]^+$  at  $m/z$  163 is represented with purple lines. Error bars are also included in the  $[\text{M}-\text{OH}]^+$  plot to show the data uncertainty between multiple measurements. This signal variation,  $\sim 10\%$ , is the same for all the ions from different experiments.

Figure 5.4 and Figure 5.5 display two plots obtained from the analysis of trehalose following an ion dose of  $5 \times 10^{11}$  ions  $\text{cm}^{-2}$  and  $3 \times 10^{13}$  ions  $\text{cm}^{-2}$ , respectively. The plot from Figure 5.4 shows how the signal intensity from different trehalose ions varies as a function of energy per molecule. Here, it is possible to observe that the quasi-molecular ion  $[M+H]^+$  at  $m/z$  343 and the fragment  $[M-OH]^+$  at  $m/z$  325 have an opposite behaviour under water cluster and argon cluster bombardment.

The ion yield obtained with  $\text{Ar}_{2000}^+$  is close to zero and decreases in intensity as the cluster size increases up to  $\text{Ar}_{6000}^+$  ( $E/\text{atom}$  10- 3.3. eV). Signal intensity obtained from the same ions with water increased significantly (from about the same level as  $\text{Ar}_{2000}^+$ ) using  $(\text{H}_2\text{O})_{2000}^+$  to  $(\text{H}_2\text{O})_{7000}^+$ ; the rise of yield with  $(\text{H}_2\text{O})_{7000}^+$  is about x80 than the signal obtained with  $(\text{H}_2\text{O})_{2000}^+$ . These signals are plotted relative to the highest value which is the signal of the  $[M+H]^+$  ion obtained with  $(\text{H}_2\text{O})_{7000}^+$ .

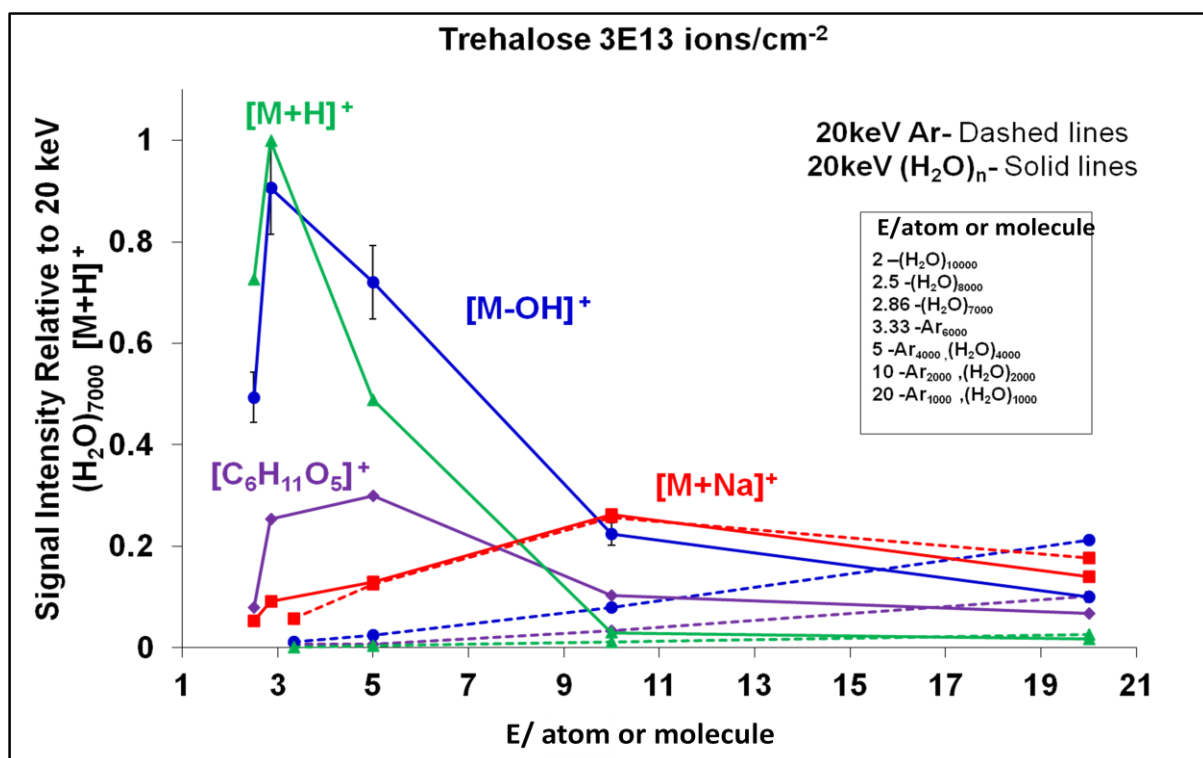


Figure 5.5: Trehalose secondary ion signal plot after an accumulated primary ion dose of  $3 \times 10^{13}$  ions  $\text{cm}^{-2}$ . The plots were normalised to the  $[M+H]^+$  signal obtained with 20 keV  $(\text{H}_2\text{O})_{7000}^+$ . The signal intensity is plotted against  $E/\text{atom}$  or molecule.. The plots include 20 keV  $\text{Ar}_n^+$  (dashed lines) and  $(\text{H}_2\text{O})_n^+$  (solid lines) clusters. Signal variation of the trehalose quasi-molecular ion  $[M+H]^+$  is represented with green lines;  $[M-OH]^+$  signal is plotted with blue lines; the sodiated molecular ion adduct  $[M+Na]^+$  is highlighted with red lines and the fragment  $[\text{C}_6\text{H}_{11}\text{O}_5]^+$  at  $m/z$  163 is denoted by purple lines. Error bars are included to show the variation ( $\sim 10\%$ ) in measurements from multiple experiments.

Ion protonation is clearly enhanced by water clusters with  $E/\text{molecule} \leq 10$  eV, reaching its maximum at  $\sim 3$  eV ( $\sim 6000$  cluster size). The same tendency is observed in Figure

5.5, after reaching the steady-state of the  $[M+H]^+$  trehalose ion. While depth-profiling, there was not significant degradation of the quasi-molecular ion as a function of depth, indicating removal of chemical damage as it forms.

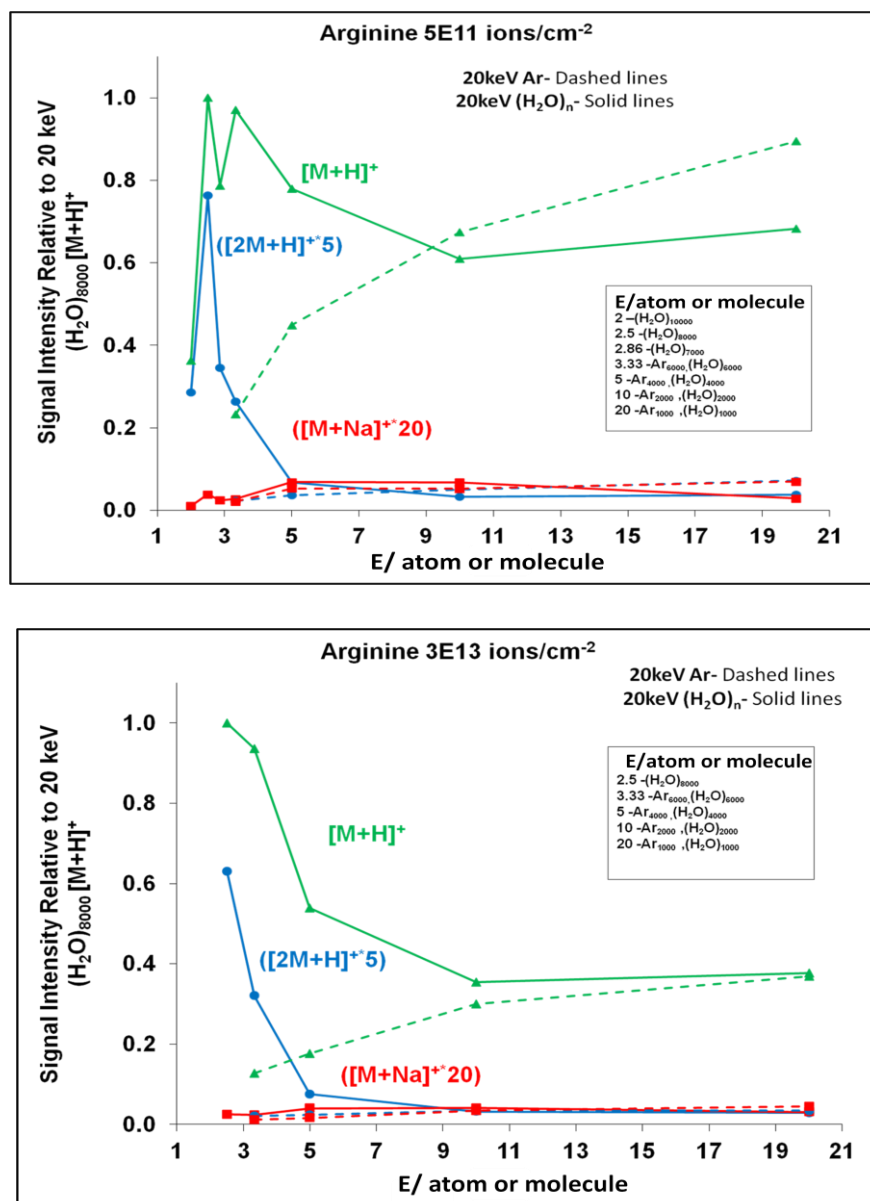


Figure 5.6: Plot of the secondary ion signal from the arginine film after a primary ion dose of  $5 \times 10^{11}$  ions  $\text{cm}^{-2}$  and  $3 \times 10^{13}$  ions  $\text{cm}^{-2}$ , respectively. Signal intensities from  $[M+H]^+$  at  $m/z$  175,  $[2M+H]^+$  at  $m/z$  349 and  $[M+Na]^+$  at  $m/z$  197 ions are plotted against their  $E/\text{atom}$  or molecule. Argon cluster experiments are denoted by dashed lines whereas water cluster are plotted with solid lines. The signal values are normalised to the  $[M+H]^+$  signal acquired with  $(\text{H}_2\text{O})_{8000}^+$ . Error bars are omitted since the level of uncertainty is the same to that observed in trehalose ( $\sim 10\%$ ).

After trehalose was analysed, arginine, angiotensin II and DPPC were also studied under the same primary ion dose conditions. Figure 5.6 illustrates the signal intensity

of arginine  $[M+H]^+$  at  $m/z$  175.2,  $[2M+H]^+$  at  $m/z$  349.4 and  $[M+Na]^+$  at  $m/z$  197.2 under two primary ion doses:  $5 \times 10^{11}$  and  $3 \times 10^{13}$  ions  $\text{cm}^{-2}$ .

In the same manner as trehalose, ion yield enhancement for the quasi-molecular ion and dimeric ion seem to be optimum when the water cluster possesses  $E/\text{molecule} = 2-3$  eV. Both plots were normalised to the highest  $[M+H]^+$  secondary ion signal obtained with 20 keV  $(\text{H}_2\text{O})_{8000}^+$ .

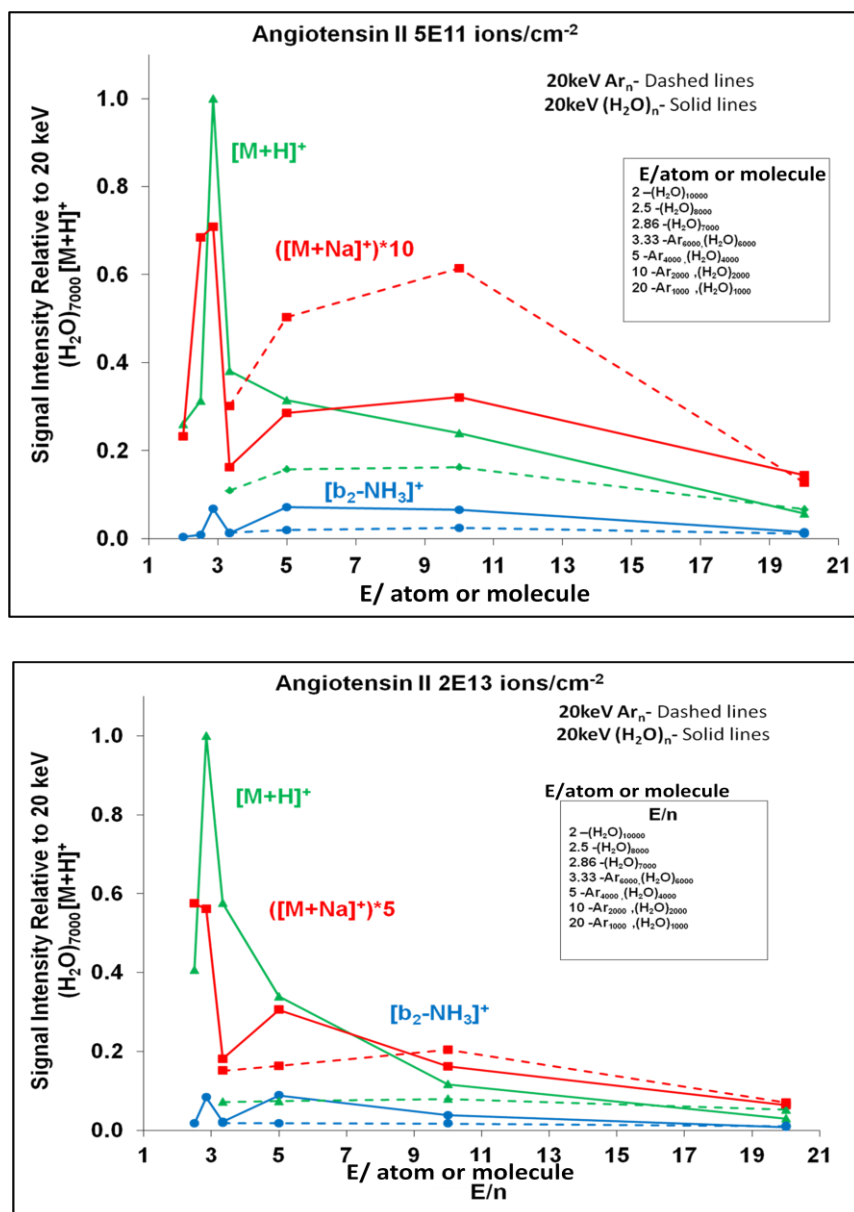


Figure 5.7: Secondary ion yield plot for Angiotensin II after a primary ion dose of  $5 \times 10^{11}$  ions  $\text{cm}^{-2}$  and  $2 \times 10^{13}$  ions  $\text{cm}^{-2}$ , respectively. The experiments acquired with 20 keV  $\text{Ar}_n^+$  are highlighted with dashed lines) and those acquired with 20 keV  $(\text{H}_2\text{O})_n^+$  are represented with solid lines. The secondary ion signal from ions  $[M+H]^+$  at  $m/z$  1031,  $[M+Na]^+$  at  $m/z$  1053 (multiplied by 10) and the fragment  $[b_2-\text{NH}_3]^+$  at  $m/z$  254 were normalised to the  $[M+H]^+$  signal obtained with 20 keV  $(\text{H}_2\text{O})_{7000}$ . Error bars are omitted since the level of uncertainty is the same to that observed in trehalose ( $\sim 10\%$ ).

Human angiotensin II was also analysed under argon and water cluster bombardment. Primary ion doses corresponding to  $5 \times 10^{11}$  ions  $\text{cm}^{-2}$  and  $2 \times 10^{13}$  ions  $\text{cm}^{-2}$  (for steady-state region) were used to quantify secondary ion yields.

The plot displayed in Figure 5.7 shows the ion intensity of  $[\text{M}+\text{H}]^+$ ,  $[\text{M}+\text{Na}]^+$  and the fragment  $[\text{b}_2\text{-NH}_3]^+$  relative to  $[\text{M}+\text{H}]^+$  obtained with  $(\text{H}_2\text{O})_{7000}^+$ . The structure of the fragment  $\text{b}_2$  can be visualised in Figure 4.2. There are many similarities in the behaviour of this peptide when compared to trehalose and arginine. The highest  $[\text{M}+\text{H}]^+$  ion signal is delivered by water clusters with  $E/\text{molecule} \sim 3$  eV.

The ion yield obtained under water cluster bombardment with  $E/\text{molecule} \sim 3$  eV is ten times higher than the highest yield observed with  $\text{Ar}_{2000}^+$ . The ion signal of the quasi-molecular ion obtained with  $\text{Ar}_{1000}^+$  is similar to that observed with  $(\text{H}_2\text{O})_{1000}^+$  ( $E/\text{atom or molecule}=20$  eV). However, the secondary ion signal obtained with water clusters increases with the cluster size, reaching its maximum somewhere between  $(\text{H}_2\text{O})_{6000}^+$  and  $(\text{H}_2\text{O})_{7000}^+$ . On the other hand, the maximum signal observed with argon clusters is that generated with  $\text{Ar}_{2000}^+$  ( $E/\text{atom}=10$  eV) and it decreases when using a larger argon cluster.

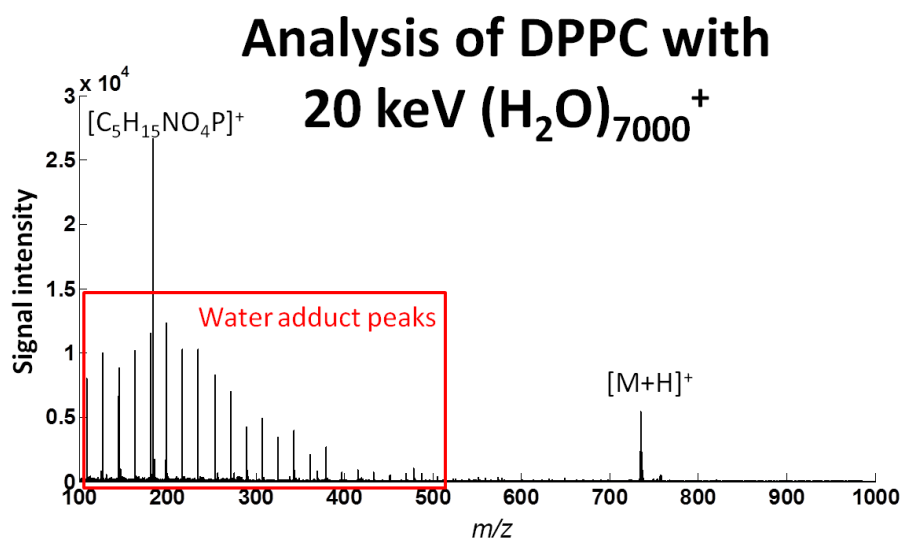


Figure 5.8: Analysis of DPPC with 20 keV  $(\text{H}_2\text{O})_{7000}^+$  showing the presence of water peak adducts in the red rectangle. This water peaks are only observed in DPPC spectra analysed with cluster sizes  $> 7000$ .

Secondary ion yields obtained with DPPC (Figure 5.8 and Figure 5.9) have a similar tendency to trehalose, arginine and angiotensin II. Here, the main phosphocholine ion fragment  $[\text{C}_5\text{H}_{15}\text{NO}_4\text{P}]^+$  derived from the  $[\text{M}+\text{H}]^+$  ion, is the base peak in the spectra. As the size of the water cluster for analysis increases, the detection the phosphocholine



ion fragments decreases, presumably due to less structural fragmentation. Here, the formation of  $[M+H]^+$  species is optimum when water clusters are used, especially when they have  $E/\text{molecule} \approx 3\text{--}5\text{ eV}$ .

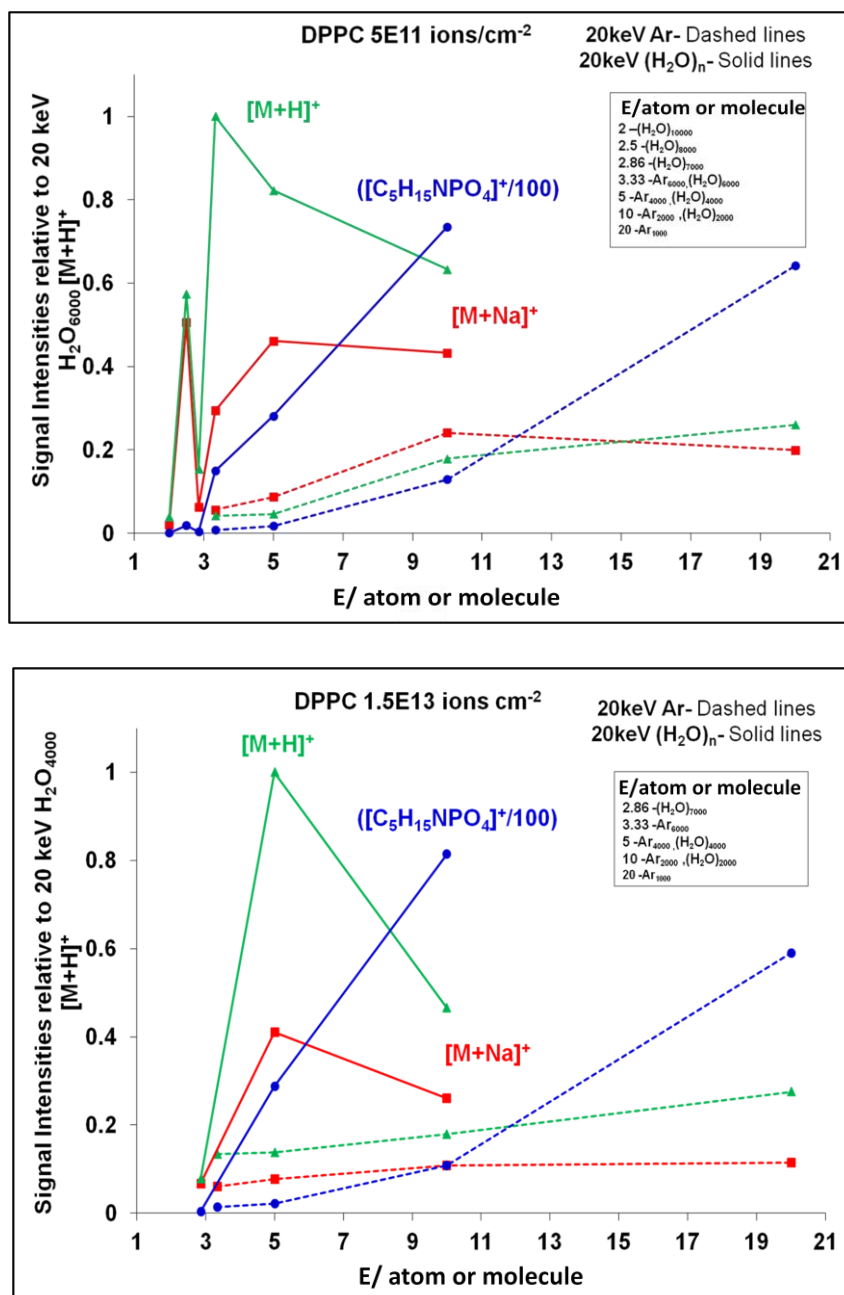


Figure 5.9: Secondary ion signal from DPPC with a total primary ion dose of  $5 \times 10^{11}$  ions cm<sup>-2</sup> and  $1.5 \times 10^{13}$  ions cm<sup>-2</sup>. The experiments were carried out using 20 keV Ar<sub>n</sub><sup>+</sup> (dashed lines) and 20 keV (H<sub>2</sub>O)<sub>n</sub><sup>+</sup> (solid lines). The ion signal from  $[M+H]^+$  at  $m/z$  735 (green lines),  $[M+Na]^+$  at  $m/z$  757 (red line) and the phosphocholine fragment  $[C_5H_{15}NO_4P]^+$  at  $m/z$  184 /100 (blue line) were normalised to the maximum signal  $[M+H]^+$  with 20 keV (H<sub>2</sub>O)<sub>6000</sub><sup>+</sup>. The level of uncertainty is the same to that observed in trehalose ( $\sim 10\%$ ).



The detection of  $[M+H]^+$  at  $m/z$  735,  $[C_5H_{15}NO_4P]^+$  at  $m/z$  184 and  $[M+Na]^+$  at  $m/z$  757 are all enhanced when using  $(H_2O)_n^+$  for cluster bombardment with  $E/molecule \approx 3-10$  eV. It is not clear why water clusters with  $E/molecule < 3$  eV produce such a low secondary ion signal. One possible explanation is the formation of water adduct peaks in the ion spectra. The formation of water adducts was observed in the DPPC spectra only. In this set of experiments, attachment of water to the sample was observed when using water clusters with more than 7000 molecules, as shown in Figure 5.8.

This phospholipid is an important model when analysing brain tissue since the brain is composed by a large amount of phospholipids. Thus, we would expect the presence of similar lipids to DPPC in brain. Therefore, DPPC along with total brain lipid extract will be studied further in the following chapters.

The proton-attachment observed in the four biorelated compounds (trehalose, arginine, angiotensin II and DPPC) seems to be optimum with energy per molecule of  $\sim 3$  eV.

#### 5.4.2 Ionisation mechanisms and the influence of the cluster size

Besides of the protonation of  $[M]$  species in all model compounds, a different ionisation mechanism was also observed to be interesting: formation of  $[M+Na]^+$  ions. The behaviour of  $[M+Na]^+$  ions was compared to the tendency observed in the formation of  $[M+H]^+$  ions. This comparison is included in Figure 5.10. The presence of inorganic salts in the samples leads to sodiation as an alternative ionisation mechanism to protonation.

The plot in Figure 5.10 displays the ratio  $[M + Na]^+ / [M + H]^+$  as a function of  $E/atom$  or  $molecule$ . If the graph is read with the  $E/atom$  or  $molecule$  decreasing, the signal of  $[M+Na]^+$  increases as the  $[M+H]^+$  signal falls under argon bombardment. In contrast, under water cluster analysis the  $[M + Na]^+ / [M + H]^+$  ratio falls to a very low level due to the rise of the  $[M+H]^+$  ion signal.

Results obtained from the experiments performed also demonstrate that there is a variation in the ion yield from fragment ions when the cluster size changes. There are two types of generated fragments in SIMS: fragments derived from damage and structural related ions. The first type refers to ions produced from a high-energy emission zone do not have any structural information. These fragments would be expected to decrease in secondary ion yield as the  $E/atom$  or  $molecule$  also falls [9], [10].

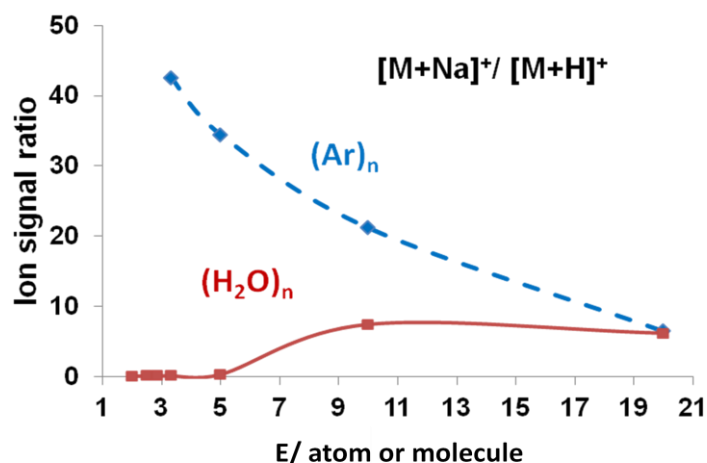


Figure 5.10: Plot of the signal ratio  $[M + Na]^+/[M + H]^+$  in trehalose as a function of  $E/\text{atom or molecule}$ . The plots include analysis with 20 keV  $Ar_n^+$  (dotted blue line) and 20 keV  $(H_2O)_n^+$  clusters (red solid line).

The second type of fragments dissociates from the precursor (parent) ion and are structurally related fragments resulting from its metastable decay. These fragments are related to a unique state of the precursor ion, its excitation and stability. For trehalose, two of the most evident structural-related ions are  $[M-OH]^+$  at  $m/z$  325 and  $[C_6H_{11}O_5]^+$  at  $m/z$  163. Figure 5.11 displays the ratio of these two ions to  $[M+H]^+$  under water cluster bombardment. Here, the ratio of  $[M-OH]^+$  and  $[C_6H_{11}O_5]^+$  obtained with  $(H_2O)_{1000}^+$ , is 14 and 7 respectively. When  $E/\text{atom or molecule}$  decreases (cluster size increases), the ratios fall down to  $\sim 1$  with  $(H_2O)_{7000}^+$  analysis. The signal decay is especially sharp with  $E/\text{atom or molecule} \sim 5-10$ . These results indicate a fall in fragmentation of about 50% when water clusters have  $E/\text{atom or molecule} < 10$  eV, thus the protonation enhancement is combined with reduced fragmentation.

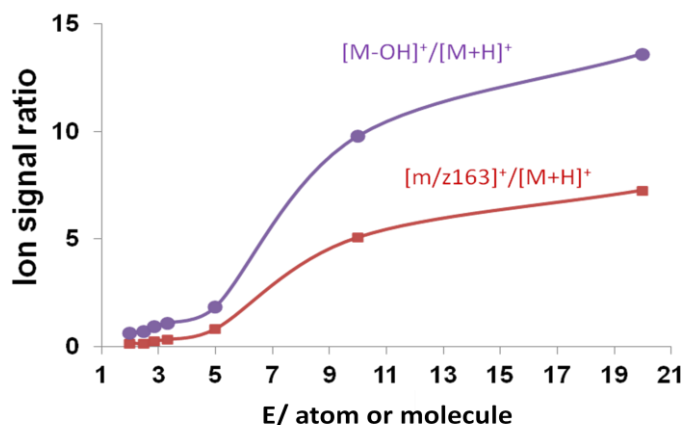


Figure 5.11: Ratio of  $[M-OH]^+$  at  $m/z$  325 and  $[C_6H_{11}O_5]^+$  at  $m/z$  163 to  $[M+H]^+$  at  $m/z$  379 as a function of  $E/\text{atom or molecule}$  for trehalose using  $(H_2O)_n^+$  clusters as primary ion beams.

This effect could be explained by considering that the  $[M+H]^+$  ions are left in a low state energy level as a result of the ionisation process. If the precursor ions are closer to the ground state, there will be less dissociation of fragment ions. The same effect is also observed in the other studied biomolecules (arginine, angiotensin II and DPPC). Under argon cluster bombardment, the ratios do not vary significantly, especially for  $E/atom < 10$  eV as shown in Figure 5.12.

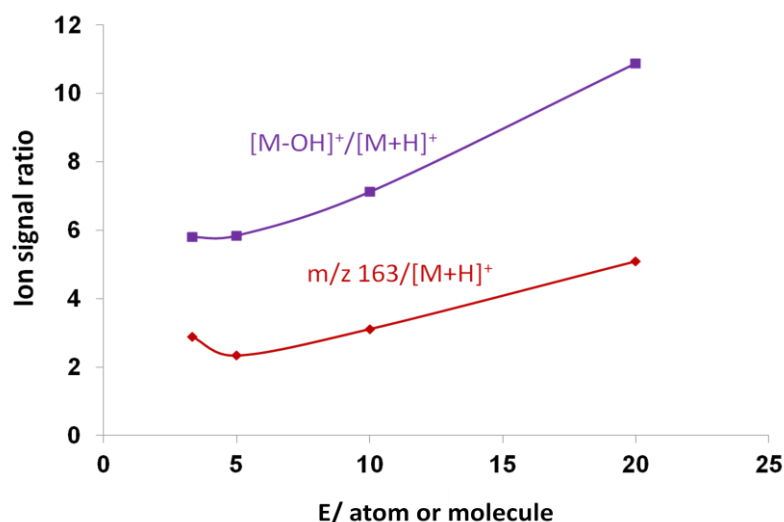


Figure 5.12: Ratio of  $[M-OH]^+$  at  $m/z\ 325$  and  $[C_6H_{11}O_5]^+$  at  $m/z\ 163$  to  $[M+H]^+$  at  $m/z\ 379$  as a function of  $E/atom$  or  $molecule$  for trehalose using  $(Ar)_n^+$  clusters as primary ion beams.

Looking at Figure 5.4 to Figure 5.9, there is an optimum energy regime for the secondary ion yields of quasi-molecular ions for both argon and water clusters. Secondary ion yield seems optimum with energy per atom  $\sim 10$  eV in analysis with argon whereas the best yield obtained with water clusters is with  $E/molecule \approx 2.5 - 5$  eV. However, one question that arises from these results is whether it is possible to maximise the secondary ion signal by increasing the cluster size but keeping an optimum  $E/atom$  or  $molecule$ . Angerer and co-workers [11] increased the cluster size from 2000 to 4000 argon atoms with a beam energy of 40 keV, keeping an energy per atom of 10 eV. This result indicates that by increasing the number of atoms and beam energy in argon clusters such that  $E/atom$  or  $molecule$  remains constant, it is possible to obtain doubled secondary ion yields.

This effect is demonstrated in our own data with the water beam by Figure 5.13, where the signal level of  $[M + H]^+$  and  $[M - OH]^+$  ions was monitored with larger cluster sizes and different beam energies such that  $E/atom$  or  $molecule \sim 3$  eV. 10 keV  $(H_2O)_{3300}^+$ , 15 keV  $(H_2O)_{5000}^+$ , and 20 keV  $(H_2O)_{7000}^+$  cluster ion beams were applied for analysis. It is

clear that the secondary ion yield produced by 15 keV  $(\text{H}_2\text{O})_{7000}^+$  is around x 2 when compared to 10 keV  $(\text{H}_2\text{O})_{3300}^+$ . Higher secondary ion yield is achievable by doubling the cluster size from 3300 to 7000 atoms, keeping an  $E/\text{atom or molecule}$  constant at  $\sim 3$  eV. Larger cluster sizes can be generated when increasing the beam energy and higher secondary ion signal is produced when  $E/\text{atom or molecule}$  is kept in its optimum regime.

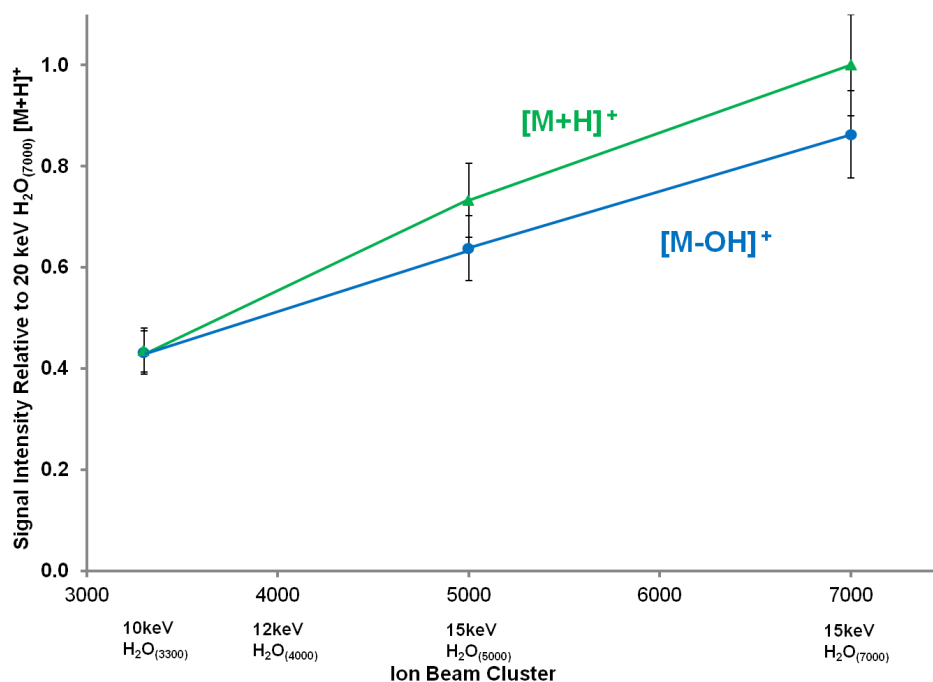


Figure 5.13:  $[\text{M}+\text{H}]^+$  (green line) and  $[\text{M}-\text{OH}]^+$  (blue line) ion signal from trehalose, generated by water beam analysis. The ion yield obtained with clusters having  $E/\text{atom or molecule} \sim 3$  eV was plotted as a function of cluster size and normalised to  $[\text{M}+\text{H}]^+$  yield obtained with 20 keV  $(\text{H}_2\text{O})_{7000}^+$ .

#### 5.4.3 Study of the $(\text{H}_2\text{O})_n^+$ mechanism: $\text{D}_2\text{O}$ studies on trehalose and DPPC

In an attempt to try to understand the ionisation mechanism of water clusters, a deuterated cluster beam was applied to the analysis of trehalose and DPPC. ToF-SIMS studies with deuterium have been performed in the past on polymers like polypropylene and polyethylene [24].

The chemical structure of trehalose (as illustrated in Figure 4.3) is composed of a disaccharide with four exchangeable hydrogens in each sugar ring; three in the OH groups and one in each  $\text{CH}_2\text{OH}$ . Proton attachment might occur at any of these OH groups. On the other hand, DPPC does not contain any exchangeable hydrogens.

These two different molecules were analysed with 20 keV  $(\text{D}_2\text{O})_n^+$ , where  $n = 1000, 2000$  and 4000. The produced spectra were compared to spectra acquired with argon

and water clusters of similar sizes. Secondary ion yield enhancement was observed with deuterated clusters and was close to that obtained with water clusters. DPPC and trehalose samples were exposed to a neutral  $(\text{D}_2\text{O})_{4000}$  beam for a period equivalent to a normal experiment and analysed with  $\text{C}_{60}^+$  to check for deuteration. In this way, it was ensured that the deuteration was from the  $\text{D}_2\text{O}$  ion beam and not from deuterated gas phase exposure. There was no evidence of deuterated secondary ions detected under  $\text{C}_{60}^+$  analysis.

Under  $(\text{D}_2\text{O})_n^+$  bombardment, two ions from the DPPC sample were affected by the deuterated ion beam:  $[\text{M}+\text{H}]^+$  at  $m/z$  734.5 and the phosphocholine fragment  $[\text{C}_5\text{H}_{15}\text{NO}_4\text{P}]^+$  at  $m/z$  184. The  $[\text{M}+\text{H}]^+$  ion with chemical formula  $[\text{C}_{40}\text{H}_{80}\text{NO}_8\text{P}+\text{H}]^+$  is generated from the protonation of the negative phosphate present in the choline molecule. The chemical structure of DPPC can be seen in Figure 4.5. The  $[\text{M}+\text{H}]^+$  ion was detected with its associated  $^{13}\text{C}$  isotope at  $m/z$  735.5. The mass resolution of the instrument does not allow the separation between the  $^{13}\text{C}$  and the  $[\text{M}+\text{D}]^+$  ion peaks.

The relative intensity of the natural abundance of the  $^{13}\text{C}$  isotope was 44%. The fragment ion phosphocholine head group at  $m/z$  184 and its  $^{13}\text{C}$  isotope at  $m/z$  185 with 5.5% of relative intensity were also present in the mass spectra. The formation of this fragment arises from neutral phosphocholine fragment dissociated from the molecule by intramolecular hydrogen transfer [12]. This neutral particle is protonated at the phosphate group, generating the  $m/z$  184 ion.

The deuteration results are displayed in Figure 5.14. The ‘expected’ ratios were obtained from the natural  $^{13}\text{C}$  abundance for  $m/z$  735/734 and  $m/z$  185/184 which is 0.44 and 0.05, respectively. The secondary ion yield ratios included for  $\text{Ar}_{2000}$  and  $(\text{H}_2\text{O})_{1000}^+$  are quite similar to those expected.

The ratios obtained with  $(\text{D}_2\text{O})_{1000}^+$  are slightly higher but they can still be within experimental error. It was mentioned before that water clusters with  $E/\text{molecule} > 5$  eV behave in a similar way to argon clusters. This observation applies to 20 keV  $(\text{H}_2\text{O})_{1000}^+$  and  $(\text{D}_2\text{O})_{1000}^+$  with  $E/\text{molecule} = 20$  eV, which show similar results to 20 keV  $\text{Ar}_{2000}^+$ . Nevertheless, the ratio produced by  $(\text{D}_2\text{O})_{2000}^+$  results in twice the yields for ion  $m/z$  735.5 (ratio  $> 1$ ) which clearly reflects the generation of  $[\text{M}+\text{D}]^+$ . Likewise, the experiment acquired with  $(\text{D}_2\text{O})_{4000}^+$  suggests a great increase in the detection of the  $[\text{M}+\text{D}]^+$  ion, with a signal intensity four times higher than the intensity recorded for the  $[\text{M}+\text{H}]^+$  ion. This result indicates that under  $(\text{D}_2\text{O})_{4000}^+$  bombardment, more ion deuteration takes place instead of protonation.

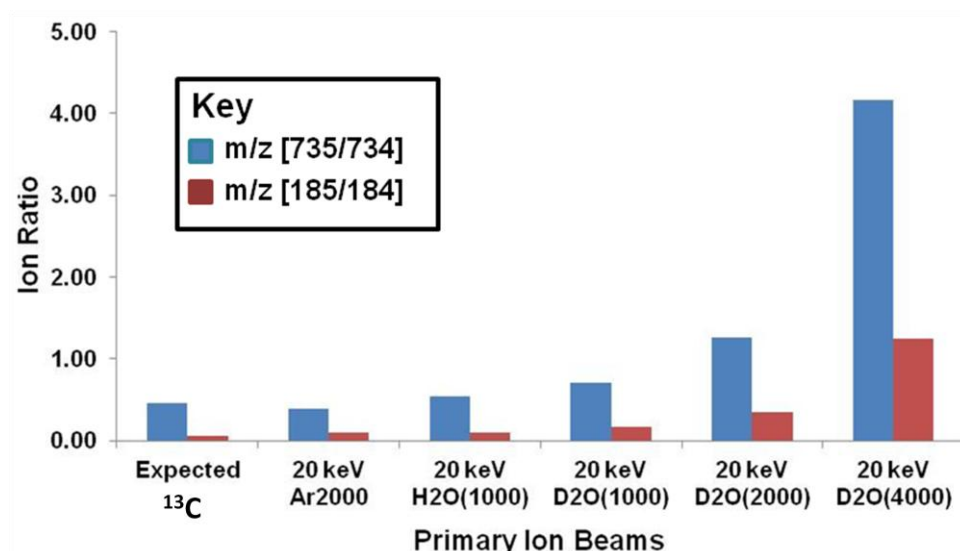


Figure 5.14: DPPC isotope ratios for the DPPC  $[M+H]^+$  ion and its related  $^{13}\text{C}$  isotope at  $m/z$  735/734 (blue columns) and the phosphocholine fragment ion  $[\text{C}_5\text{H}_{15}\text{NO}_4\text{P}]^+$  and its related  $^{13}\text{C}$  isotope at  $m/z$  185/184 (red columns). The expected ratios were calculated from the natural abundance of  $^{13}\text{C}$  isotopes and are compared to the ratios obtained with  $(\text{D}_2\text{O})_n^+$  and  $(\text{H}_2\text{O})_n^+$ . The primary ion dose used in these experiments was  $5 \times 10^{11}$  ions  $\text{cm}^{-2}$ .

Looking at the  $m/z$  185/184 ratios, the  $(\text{D}_2\text{O})_{2000}^+$  study indicated that the yield from the deuterated phosphocholine fragment  $[\text{C}_5\text{H}_{15}\text{NO}_4\text{P}+\text{D}]^+$  at  $m/z$  185 was doubled when compared with  $(\text{D}_2\text{O})_{1000}^+$ ,  $\text{Ar}_{2000}^+$  and  $(\text{H}_2\text{O})_{1000}^+$ , indicating some degree of deuteration. However, the  $(\text{D}_2\text{O})_{4000}^+$  cluster ion beam produced the same amount of  $[\text{C}_5\text{H}_{15}\text{NO}_4\text{P}+\text{D}]^+$  and  $[\text{C}_5\text{H}_{15}\text{NO}_4\text{P}+\text{H}]^+$  (ratio = 1). As anticipated, there was no deuteration of  $[\text{M}+\text{Na}]^+$  ions. These results demonstrate that ionisation with water clusters occurs by proton attachment, especially with clusters with  $E/\text{atom or molecule} < 10$  eV. Moreover, these experiments confirm that protons come from the water molecules carried in the ion beam and not from the sample.

On the other hand, trehalose showed a different behaviour under deuterated cluster bombardment. Results obtained with  $(\text{D}_2\text{O})_{1000}^+$  were similar to those observed with DPPC. Under  $(\text{D}_2\text{O})_{2000}^+$  and  $(\text{D}_2\text{O})_{4000}^+$  bombardment,  $[\text{M}+\text{H}]^+$  at  $m/z$  343,  $[\text{M}-\text{OH}]^+$  at  $m/z$  325 and the  $[\text{C}_6\text{H}_{11}\text{O}_5]^+$  fragment at  $m/z$  163 exhibit the formation of new +1, +2, +3 and +4 ions. Figure 5.15 displays the secondary ion yield obtained from the new ions. 10 keV  $(\text{D}_2\text{O})_{4000}^+$  is the beam that yields the highest secondary ion signal with  $E/\text{atom or molecule} = 2.5$  eV. When looking at the ions generated by this cluster in a mass range between  $m/z$  343 and 348 relative to  $[\text{M}+\text{H}]^+$ , it is possible to observe that there is  $\sim 25\%$  of  $[\text{M}+\text{D}]^+$  and  $\sim 16\%$  of  $[\text{M}-\text{H}+2\text{D}]^+$ . This result indicates the exchange of one hydrogen in addition to deuteration.

Another observation can be made when observing the protonation generated with 10 keV  $(D_2O)_{4000}^+$ ; the signal obtained from the  $[M+H]^+$  ion is about 50% when compared to 10 keV  $(H_2O)_{4000}^+$  (Figure 5.15).

From Figure 5.15 we can conclude that the activation of hydrogen results from the cluster impact on the specimen. However, the degree of deuteration is reduced due to the hydrogen exchange happening in trehalose, which leads to protonation. Deuteration can also be affected by the kinetic isotope effect, which in principle can be a slower process than protonation.

Furthermore, by increasing the  $(D_2O)_n^+$  cluster size, the hydrogen-deuterium exchange process is also increased. This mechanism might be a joint process between the  $(D_2O)_n^+$  cluster and the sputtered molecules in the emission zone. Ion peaks in the mass range  $m/z$  362-364 and  $m/z$  381-385 also appeared in the mass spectra; these ions can be assigned to  $[M+H \text{ or } +D, +H_2O \text{ or } D_2O]^+$  and  $[M+H \text{ or } D+2D_2O]^+$ .

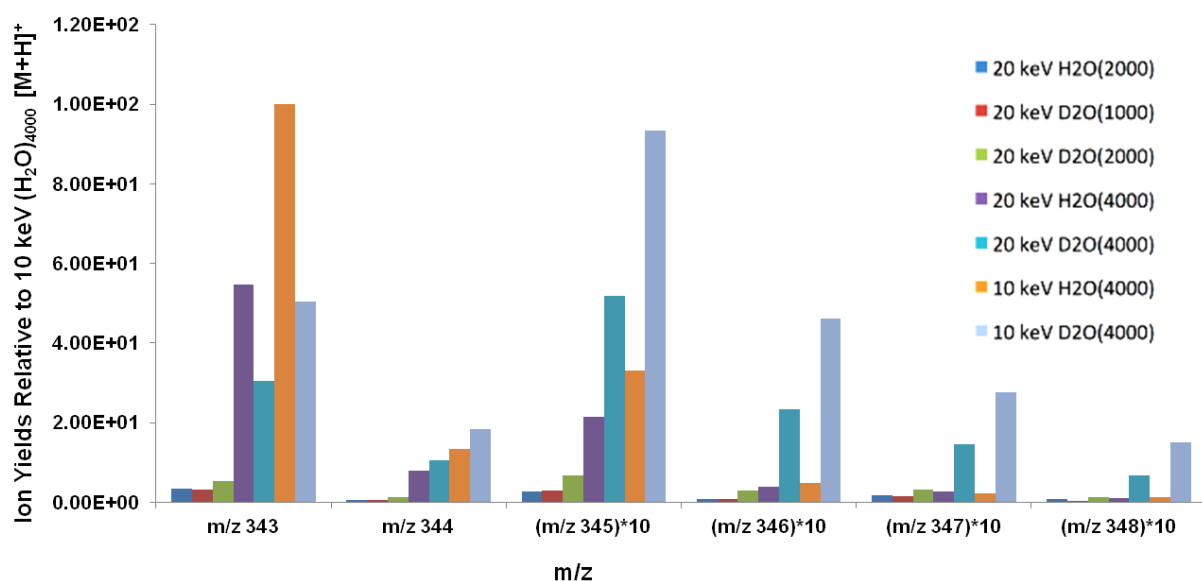


Figure 5.15: Trehalose secondary ion yields obtained with  $(H_2O)_n^+$  and  $(D_2O)_n^+$  analysis with a total primary ion dose of  $5 \times 10^{11}$  ions  $cm^{-2}$ . All yields were normalised to  $[M+H]^+$  obtained with 10 keV  $(H_2O)_{4000}^+$ . The secondary ion yields were calculated from  $[M+H]^+$  at  $m/z$  343 and the isotopes at  $m/z$  344, 345, 346, 347 and 348.

Comparing these results with previous hypothesis [13], [14], it is suggested that protonation with water clusters occurs when a high energy primary ion beam impacts a sample and produces protons. These protons travel outside the collision zone to the low energy periphery, where they encounter and attach to intact molecules [15]–[17].

This theory would suggest that protonation and emission of ion species might happen following the primary impact. According to our observations, the beam energy

required to emit protons via primary impact would be  $E/\text{atom or molecule} \geq 10$  eV, which is the case for argon clusters. If  $E/\text{atom or molecule}$  is  $< 10$  eV, there is a decay in  $[\text{M}+\text{H}]^+$  secondary ion yield maybe because more energy is required for proton formation. In contrast, the optimum energy regime for water clusters is  $E/\text{molecule} < 10$  eV and the yield of  $[\text{M}+\text{H}]^+$  is significantly enhanced by the cluster size, reaching a maximum with  $E/\text{molecule} \sim 3$  eV. These energy regime observations for water clusters indicate that proton-attachment is a process which requires low energy. It might be the case that at low energy, water clusters may maintain their geometry [15]–[17]. The latter statement could implicate the generation of craters on the sample's surface with the size of the cluster dimension, causing the combination of the primary ion beam clusters with the analyte molecules. As a consequence, a hydrated environment is created for sputtered particles. This hypothesis is supported by the results from the experiments with deuterated cluster, where a similar process takes place.

In order for the water clusters to ionise the sample via proton transfer, an optimum  $E/\text{molecule}$  is needed to activate the ionisation mechanism; this will happen either by molecular dissociation or by reaction with energised molecules and fragments leaving the surface region.

#### 5.4.4 Secondary ion detection per $1 \mu\text{m}^2$

The ultimate goal of evaluating the secondary ion yields obtained with each cluster ion beam is to assess the feasibility of biological imaging and detection of intact lipid molecules. Figure 5.16 displays the extrapolated detected secondary ion signal from  $1 \mu\text{m}^2$  analysis area under static and steady-state ion dose conditions ( $5 \times 10^{11}$  and  $1.5 \times 10^{13}$  ions  $\text{cm}^{-2}$ , respectively). The analysis beams used in the experiments were  $20 \text{ keV Ar}_{2000}^+$  and  $(\text{H}_2\text{O})_{4000}^+$  or  $(\text{H}_2\text{O})_{7000}^+$ .

The chart for arginine (Figure 5.16, (a)) shows a significant enhancement (by a factor of 14) of secondary ion detected signal for the dimeric ion  $[\text{2M}+\text{H}]^+$  when analysed with water clusters under static primary ion dose conditions when compared to argon cluster analysis. With the same primary ion dose, the  $[\text{M}+\text{H}]^+$  ion is slightly enhanced when compared to argon ( $\times 1.5$ ). However, the secondary ion signal from  $[\text{M}+\text{H}]^+$  and  $[\text{2M}+\text{H}]^+$  ions in the steady-state region detected with water clusters was enhanced by a factor of 3 and 19, respectively, when compared to the signal produced by argon.

Looking at trehalose (Figure 5.16, (b)), the detected signal from the  $[\text{M}+\text{H}]^+$  ion with water clusters is 80 times higher than the signal intensity recorded with argon clusters



when applying a primary ion dose of  $5 \times 10^{11}$  ions  $\text{cm}^{-2}$ . With an accumulated primary ion dose of  $1.5 \times 10^{13}$ , the water primary ion beam yields 87 times more signal than argon clusters.

The  $[\text{M}+\text{H}]^+$  secondary ion signal detected with DPPC is enhanced 5 to 6 times under  $(\text{H}_2\text{O})_{4000}^+$  bombardment, under static and steady-state primary ion dose conditions. Despite the enhancement, the secondary ion yield is still low. The reason for this low yield could be due to the dissociation of the DPPC molecule into phosphocholine ion fragments. The phosphocholine ion produces a high secondary ion signal, enhanced by a factor of 3 when analysed with water clusters in the steady-state and enhanced little in static conditions. The detection of phosphocholine fragments under  $(\text{H}_2\text{O})_{4000}^+$  bombardment could be a consequence of the increasing protonation due to the low  $E/\text{molecule}$  of the water cluster (5 eV) and the decreasing formation of neutral phosphocholine fragments.

The signal level observed with angiotensin II (Figure 5.16, (d)) shows an enhancement by a factor of 6 in static conditions, and 12 in steady-state conditions when  $(\text{H}_2\text{O})_{7000}^+$  are used for analysis.

With the J105-3D Chemical Imager, analyses are not restricted to static conditions. One of the instrument's main characteristics is the accumulation of signal from the sample. This instrumental feature can be combined with water cluster ion beam analysis to obtain accumulated secondary ion signal from  $1 \mu\text{m}^2$  area beyond the static limit. Secondary ion signal obtained from all compounds in static conditions and steady-state were assessed in Figure 5.16, (e). The ratios between secondary ion signals detected in the steady-state region with water clusters relative to the secondary ions obtained using argon clusters in static conditions are presented.

There is a significant improvement when analysing the samples in the steady-state with water clusters. The signal increases by a factor of 77 for arginine, 100 for DPPC, 120 for angiotensin II and 1750 for trehalose. The chemistry of each analyte is obviously different and that fact might have a direct influence in the ion yield. Nevertheless, this study shows encouraging results for sub-micron analysis and biological imaging applications, provided the beams can be focused accordingly.

Further instrumentation developments involving higher energy water beams and larger cluster sizes could deliver higher yields, as long as the  $E/\text{atom or molecule} \sim 3$  eV remains constant.

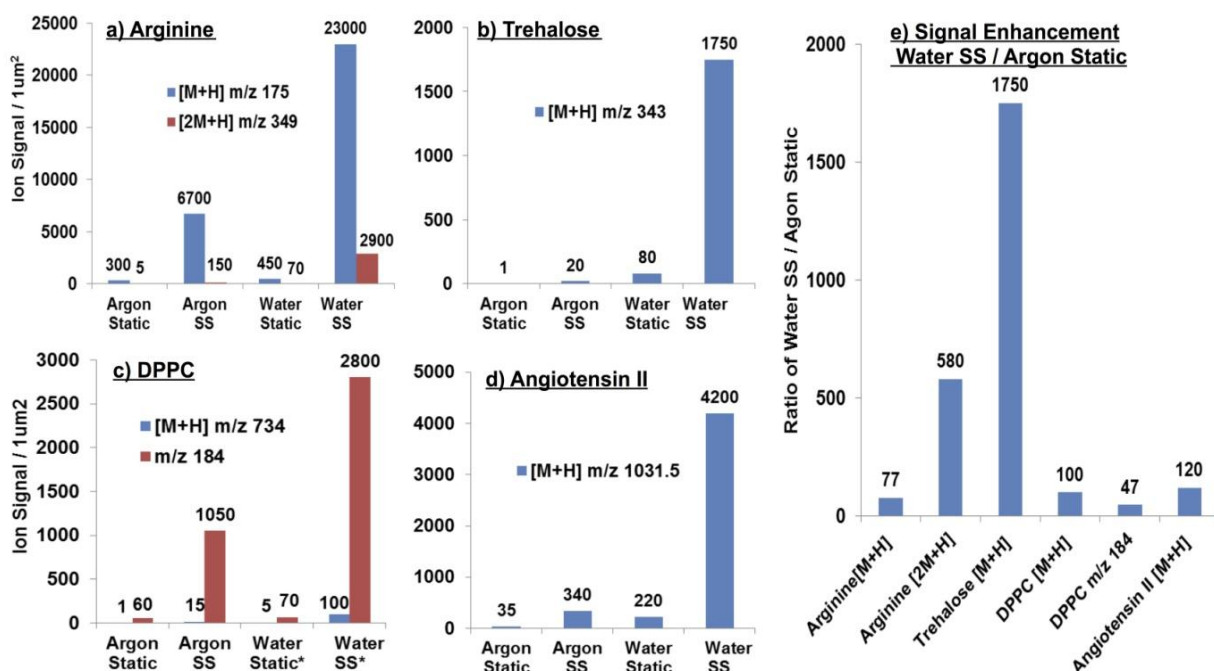


Figure 5.16: Detected secondary ion signal per  $1 \mu\text{m}^2$  area with  $20 \text{ keV Ar}_{2000}^+$  and  $(\text{H}_2\text{O})_{7000}^+$  under static primary ion dose conditions ( $5 \times 10^{11} \text{ ions cm}^{-2}$ ) and in the steady-state ( $1.5 \times 10^{13} \text{ ions cm}^{-2}$ ). The results from the experiments are displayed for (a) Arginine  $[\text{M}+\text{H}]^+$  and  $[2\text{M}+\text{H}]^+$ , (b) Trehalose  $[\text{M}+\text{H}]^+$ , (c) DPPC  $[\text{M}+\text{H}]^+$  and fragment  $m/z$  184 and (d) Angiotensin II  $[\text{M}+\text{H}]^+$ . (e) Secondary ion signal enhancement specified by the ratio of the signal detected with water is steady state divided by the signal detected with argon clusters in static. \* In the DPPC chart specifies that the data was acquired with  $20 \text{ keV } (\text{H}_2\text{O})_{4000}^+$ . The values are rounded to a 10 % error.

On this basis, with a  $40 \text{ keV } (\text{H}_2\text{O})_{13000}^+$  cluster ion beam would allow us to double the yields observed in Figure 5.16. One of the main technological challenges will be the improvement of the spatial resolution for the  $(\text{H}_2\text{O})_n^+$  cluster ion beam. The current obtainable spatial resolution is  $\sim 10 \mu\text{m}$  for  $20 \text{ keV } (\text{H}_2\text{O})_{6000}^+$ ; hence, sub-micron analysis still remains a challenge.

In the following section, the application of water-doped argon clusters and to selected standard biomolecules will be discussed and compared to the results obtained with pure water clusters.

## 5.5 Generation of water-doped argon clusters for analysis of biomolecular systems: comparative studies on trehalose and DPPC

The application of  $(\text{H}_2\text{O})_n^+$  clusters to analysis is limited to the lifetime of the ion source, which depending on the cluster size, is around  $\sim 3 - 4$  hours due to the limited volume of water that can be introduced in the boiler assembly (section 3.5.2.1). This is a major limitation when doing experiments beyond the static limit, which usually require a long analysis time. Hence, the application of  $(\text{H}_2\text{O})\text{Ar}_n^+$  clusters is explored.

The lifetime of water-doped clusters is around 8 hours and their formation was explained in section 3.5.2.

In this section, we will compare the ion yields obtained from trehalose and DPPC analysed with 20 keV  $C_{60}^+$ ,  $Ar_n^+$ ,  $(H_2O)_n^+$  and  $(H_2O)Ar_n^+$ . We will focus on the results from these model compounds and their potential impact on tissue imaging. The following chapter will focus on the analysis of a biomimetic brain model (lipid mouse brain extract) and mouse brain.

The results presented in previous sections demonstrated that argon clusters can be successfully applied to analysis of biomolecules with different chemistry, being optimally effective when the energy per molecule is  $\sim 10$  eV. With similar energy, water clusters produce similar results to those observed with argon. However, secondary ion signal of quasi-molecular (protonated) ions is significantly enhanced when water clusters hold energy per molecule of  $\sim 3$  eV. The increase in secondary ion yield will also vary according to the sample's chemical structure; secondary ion signal enhancement by a factor of 10-100 was observed in the experiments from section 5.4.

Experiments to study the ionisation mechanism of water-doped argon clusters were also performed. Results from experiments will be presented in section 5.5.1.

### 5.5.1 Results and discussion

Successful experiments from other SIMS groups explored the application of doped-argon clusters for molecular ToF-SIMS imaging [18]. Tian *et al.* acquired images from a mouse brain section using a mixed cluster ion beam, composed by 98.9 % argon and 1.1% methane (20 keV  $(CH_4)Ar_{4000}^+$ ). Their results demonstrated secondary ion signal enhancement of 1.5x when compared to  $Ar_{4000}^+$  and 13.8x more signal when compared to  $C_{60}^+$  during the analysis of a mouse brain section. The increased secondary ion yield was specifically observed in the mass range 600-900 Da, where many intact lipids can be found [18]. Considering these results, we have explored the possibility of doping argon clusters with other hydrogen containing molecules to increase protonation i.e. water.

$(H_2O)Ar_n^+$  clusters with  $n = 1000-6000$  atoms can be generated in the GCIB-boiler assembly with a beam energy of 20 keV. These water-doped argon clusters were applied to the analysis of trehalose and DPPC.

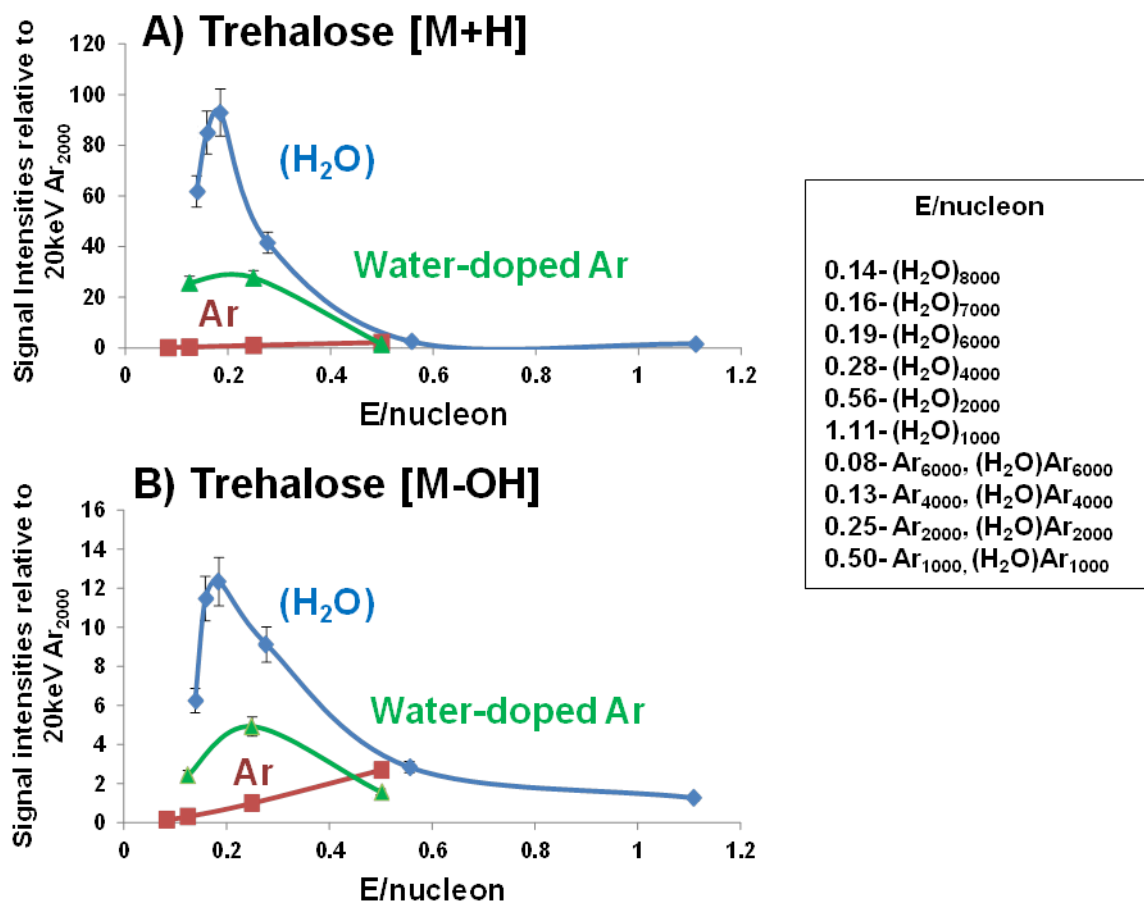


Figure 5.17: Secondary ion signal comparison from the analysis of trehalose.  $(\text{H}_2\text{O})_n^+$  (blue line),  $\text{Ar}_n^+$  (red line) and  $(\text{H}_2\text{O})\text{Ar}_n^+$  (green line) cluster ion beams were used for analysis. Secondary ion signal intensities are plotted against  $E/\text{nucleon}$ . Intensity values were normalised to the signal of the  $[\text{M}+\text{H}]^+$  ion produced by 20 keV  $\text{Ar}_{2000}^+$ . The two plots presented correspond to the ions: A)  $[\text{M}+\text{H}]^+$  at  $m/z$  343 and B)  $[\text{M}-\text{OH}]^+$  at  $m/z$  325.

Figure 5.17 summarises the secondary ion signal obtained with trehalose. The two plots from Figure 5.17 show the signal intensities of  $[\text{M}+\text{H}]^+$  and  $[\text{M}-\text{OH}]^+$  ions, analysed with 20 keV  $(\text{H}_2\text{O})_{1000-8000}^+$ ,  $\text{Ar}_{1000-6000}^+$  and  $(\text{H}_2\text{O})\text{Ar}_{1000-6000}^+$ . The results from water and argon experiments are those previously obtained and presented in section 5.4.1. The accumulated primary ion dose for steady-state experimental conditions was  $1 \times 10^{13}$  ions  $\text{cm}^{-2}$ . It was suggested previously that water clusters with  $E/\text{atom}$  or  $\text{molecule}$  of 10 eV (2000 size), behave similar to argon clusters of the same size. If water clusters have low  $E/\text{molecule}$ , they keep their geometry due to the hydrogen bonds and enhance protonation with minimum fragmentation when they interact with the sample on the impact zone. It was also shown in Figure 5.13 that nuclearity (i.e. the number of constituent atoms or molecules [19], [20]) of the projectile is important for water clusters since the yield is increased by changing the number of water molecules with a constant  $E/\text{molecule}$  or  $E/\text{nucleon}$ . The mechanism of water-doped argon clusters might

be very similar when the data is visualised in terms of  $E/\text{nucleon}$  and not as a function of particle nuclearity.

In Figure 5.17,  $(\text{H}_2\text{O})\text{Ar}_{2000}^+$  clusters with  $E/\text{nucleon} \sim 0.25$  eV increased the secondary ion signal of  $[\text{M}+\text{H}]^+$  by a factor of 20 when compared to the yields generated with normal argon clusters. Pure water clusters with similar  $E/\text{nucleon}$  ( $\sim 0.2$  eV) i.e.  $\sim (\text{H}_2\text{O})_{6000}^+$ , exhibit an enhancement by a factor of 3 when compared to  $(\text{H}_2\text{O})\text{Ar}_{2000}^+$ . The trehalose  $[\text{M}-\text{OH}]^+$  ion shows a very close behavior to that observed with the  $[\text{M}+\text{H}]^+$  ion.

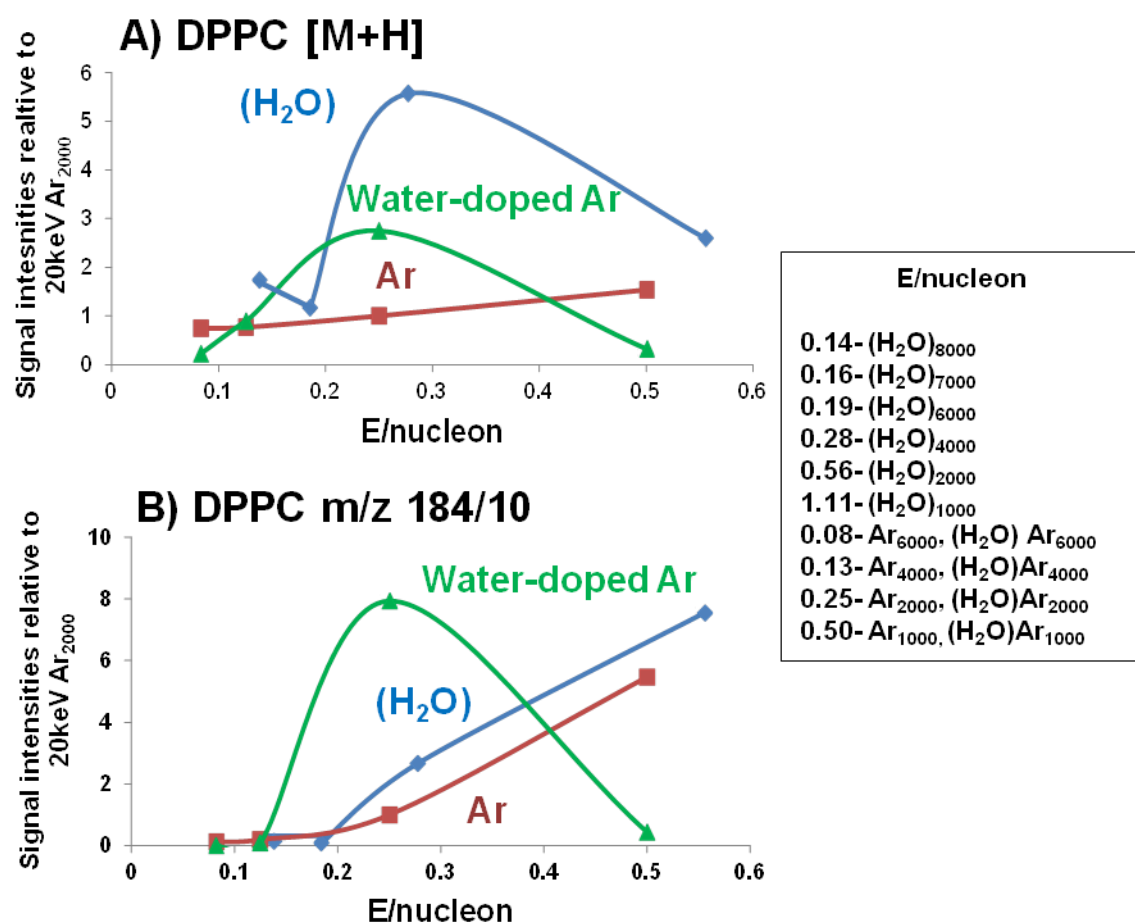


Figure 5.18: Secondary ion signal comparison from the analysis of DPPC.  $(\text{H}_2\text{O})_n^+$  (blue line),  $\text{Ar}_n^+$  (red line) and  $(\text{H}_2\text{O})\text{Ar}_n^+$  (green line) cluster ion beams were used for analysis. Secondary ion intensities from  $[\text{M}+\text{H}]^+$  at  $m/z$  735 and the phosphocholine fragment  $[\text{C}_5\text{H}_{15}\text{NO}_4\text{P}]^+$  at  $m/z$  184 are plotted against  $E/\text{nucleon}$ . The phosphocholine fragment was divided by ten to fit the plots and all ion intensities were normalised to the signal of the  $[\text{M}+\text{H}]^+$  ion produced by 20 keV  $\text{Ar}_{2000}^+$ .

The results obtained with DPPC are displayed in Figure 5.18. The maximum secondary ion signal obtained from the  $[\text{M}+\text{H}]^+$  ion is generated by  $(\text{H}_2\text{O})_{6000}^+$ , with  $E/\text{nucleon}$  of  $\sim 0.19$  eV. Looking at the same ion,  $(\text{H}_2\text{O})\text{Ar}_{2000}^+$  ( $E/\text{nucleon} = 0.25$  eV) generates half of

the secondary ion signal detected with water clusters. The signal intensity produced with  $\text{Ar}_n^+$  clusters is the lowest, three times lower than the signal observed with  $(\text{H}_2\text{O})\text{Ar}_{2000}^+$ . The detection of the phosphocholine fragment  $[\text{C}_5\text{H}_{15}\text{NO}_4\text{P}]^+$  decreases in a constant manner as the energy per nucleon reduces under water bombardment. A similar behaviour is observed under argon cluster bombardment. In contrast, the maximum yield for this phosphocholine fragment is delivered by water-doped argon clusters. The highest secondary ion signal is observed at  $E/\text{nucleon} \sim 0.25$  eV which corresponds to  $(\text{H}_2\text{O})\text{Ar}_{2000}$ .

The maximum yield of the  $[\text{M}+\text{H}]^+$  ion from both compounds, trehalose and DPPC, is observed with water clusters possessing an  $E/\text{nucleon}$  of  $\sim 0.2$  eV. Interestingly, water-doped argon clusters also deliver maximum secondary ion yields of the quasi-molecular ion at the same energy per nucleon ( $\sim 0.2$  eV). This result points out the fact that both cluster types may behave in a similar way. With energy per nucleon of  $\sim 0.2$  eV, argon clusters produce relatively low  $[\text{M}+\text{H}]^+$  secondary ion yield.

#### 4.5.2 Investigation of the ionisation mechanism with $(\text{D}_2\text{O})\text{Ar}_n^+$ clusters

A deuteration experiment was carried out with  $(\text{D}_2\text{O})\text{Ar}_n^+$  clusters to investigate the effect of  $(\text{H}_2\text{O})\text{Ar}_n^+$  clusters in the ionisation of sputtered molecules. The conditions to form the  $(\text{D}_2\text{O})\text{Ar}_n^+$  beam were the same as those described in the instrumentation chapter to generate a  $(\text{H}_2\text{O})\text{Ar}_n^+$  beam (see section 3.5.2.1). A 20 keV  $(\text{D}_2\text{O})\text{Ar}_{2000}^+$  cluster ion beam was applied to the analysis of DPPC and the results obtained were compared to previous data generated with  $(\text{D}_2\text{O})_{2000}^+$  and is close to that observed in  $(\text{D}_2\text{O})_{4000}^+$ . The 'expected' ratios are again calculated from the natural isotopic abundance of  $^{13}\text{C}$ . Figure 5.19 displays the ion signal ratios from ions  $m/z$  185/184 and 735/734 obtained from the analysis of DPPC. These ratios indicate a higher degree of deuteration with  $(\text{D}_2\text{O})\text{Ar}_{2000}^+$  when compared to  $(\text{D}_2\text{O})_{2000}^+$  or  $(\text{D}_2\text{O})_{4000}^+$ .

The maximum secondary ion yield delivered by water-doped argon clusters was observed with  $E/\text{nucleon}$  of  $\sim 0.2$  eV and the deuteration degree of  $(\text{D}_2\text{O})\text{Ar}_{2000}^+$  is similar to that observed with  $(\text{D}_2\text{O})_{4000}^+$  with  $E/\text{nucleon}$  of 0.25. These results suggest that the mechanism involved in the proton-attachment process with  $(\text{H}_2\text{O})\text{Ar}_n^+$  clusters is similar to that involved in  $(\text{H}_2\text{O})_n^+$  clusters.

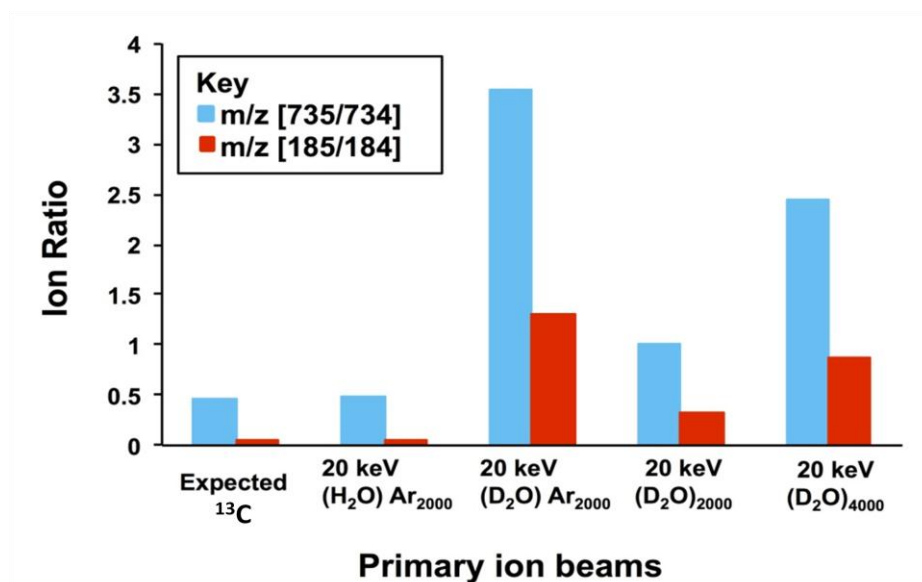


Figure 5.19: Ion signal ratios from the DPPC experiments. The ratios were calculated for  $m/z$  735/734 and  $m/z$  185/184. The expected ratios are calculated from the  $^{13}\text{C}$  isotopic abundance (44.36 % for the DPPC molecule and 5.54% for the phosphocholine fragment). The experiments we acquired with 20 keV  $(\text{H}_2\text{O})\text{Ar}_{2000}^+$ ,  $(\text{D}_2\text{O})\text{Ar}_{2000}^+$  and 20 keV  $(\text{D}_2\text{O})_{2000,4000}^+$  under static conditions ( $5 \times 10^{11}$  ions  $\text{cm}^{-2}$ ).

As discussed earlier, the optimum energy per atom for argon clusters is  $\sim 10$  eV, which corresponds to 20 keV  $\text{Ar}_{2000}^+$ . It was also mentioned that water molecules with energy per molecule of  $\sim 10$  eV result in secondary ion yields similar to those observed with argon clusters.  $(\text{H}_2\text{O})_n^+$  clusters with lower energy per molecule produce increased  $[\text{M}+\text{H}]^+$  secondary ion signal. Figure 5.18 indicates a maximum secondary ion signal obtained from the DPPC  $[\text{M}+\text{H}]^+$  ion with  $(\text{H}_2\text{O})_{4000}^+$ , with an energy of 5 eV/molecule or 0.28 eV/nucleon. The optimum  $E/\text{nucleon}$  for  $(\text{H}_2\text{O})\text{Ar}_n^+$  clusters is close to the optimum energy detected for  $(\text{H}_2\text{O})_{6000}^+$  which is at 0.185 eV/nucleon. Thus, the ionisation mechanism for water-doped argon clusters could be similar to pure water clusters if we consider that the secondary ion yields for  $[\text{M}+\text{H}]^+$  and  $[\text{M}+\text{D}]^+$  reach their maximum with an energy per nucleon of  $\sim 0.25$  eV.

Other SIMS groups have reported that large clusters are likely to keep their structure at low energy per nucleon ( $<1$  eV) [15]–[17]. Delcorte and co-workers reported experimental observations on the impact of large clusters as a function of their  $E/n$  [16], [21]. Their research concluded that clusters with  $E/\text{nucleon} > 1$  eV will cause sputter yield which becomes linearly dependant to the beam energy. The sputter yield is independent of the projectile's nuclearity. If the  $E/\text{nucleon}$  of the cluster is  $< 1$  eV, less energy density is deposited on the impact zone; hence, low levels of molecular fragmentation would be expected. The beam energy deposited outside the impact zone

is lower than the molecular binding energy from the molecules of the specimen such that more intact molecules are desorbed [16], [21].

These studies [16], [21] agree the results obtained from our experiments when water and water-doped argon clusters have  $E/\text{nucleon} \geq 0.5$  eV. However, when the energy per nucleon decreases, the protonation increases. In the experiments presented in this section, the maximum enhancement is observed with  $E/\text{nucleon} \sim 0.2$  eV. According to the investigations from Delcorte *et al.* [51], [54], clusters impacting the sample remain on the surface for hundreds of femtoseconds (fs), providing enough time for proton attachment as the molecules are desorbed.

## 5.6 Summary

Positive ion spectra from arginine, trehalose, angiotensin II and DPPC were acquired with  $\text{Ar}_n^+$ ,  $(\text{H}_2\text{O})_n^+$  and  $(\text{H}_2\text{O})\text{Ar}_n^+$ . Primary cluster ion beams of different sizes and energies were compared. Within the first set of experiments (Section 5.1), spectral differences between data obtained with 20 keV  $\text{Ar}_{4000}^+$  and  $(\text{H}_2\text{O})_{4000}^+$  were assessed, identifying differences in  $[\text{M}+\text{H}]^+$  and  $[\text{M}+\text{Na}]^+$  ion ratios. Results from the four biorelated molecules indicated higher secondary yields for  $[\text{M}+\text{H}]^+$  and related ions when compared to  $[\text{M}+\text{Na}]^+$  under  $(\text{H}_2\text{O})_{4000}^+$  bombardment. When using  $\text{Ar}_{4000}^+$  cluster for analysis, the secondary ion signal obtained from the  $[\text{M}+\text{Na}]^+$  ion was higher relative to the signal intensity of the quasi-molecular ion  $[\text{M}+\text{H}]^+$ .

Secondary ion yields from  $[\text{M}+\text{H}]^+$  and related ions from arginine, trehalose, angiotensin II and DPPC were also evaluated in static and steady-state primary ion dose conditions. It was concluded that water cluster ion beams enhance the generation of  $[\text{M}+\text{H}]^+$  ions while reducing structural fragmentation. The secondary ion signal obtained for  $[\text{M}+\text{H}]^+$  and related ions was maximised when the analysis was carried out with  $(\text{H}_2\text{O})_n^+$  clusters with energy per molecule of  $\sim 3$  eV, whereas the optimum energy regime for  $\text{Ar}_n^+$  clusters was  $\sim 10$  eV. If  $(\text{H}_2\text{O})_n^+$  clusters possess an energy per molecule of  $\sim 10$  eV, their behaviour is similar to that observed in  $\text{Ar}_n^+$  clusters of the same energy.

The secondary ion signal detected per  $1 \mu\text{m}^2$  was extrapolated using water clusters with  $E/\text{molecule}$  of  $\sim 3$  eV for analysis; the observed secondary ion signal was 100 to 1000 times higher than the signal detected in static conditions with argon clusters. These results demonstrate a clear benefit when applying large water clusters for analysis. Furthermore, if the primary ion dose is beyond the static limit, the secondary



ion signal can be accumulated and molecular imaging from biological samples can be enabled.

Results obtained with water clusters were validated with the formation of deuterium clusters. The deuterated experiments confirmed that that protonation enhancement is originated from the proton carried by the water cluster.

In a second set of experiments (Section 5.5), argon clusters were doped with water to explore their effect on the secondary ion yield. The water-doped argon clusters were applied to the analysis of trehalose and DPPC. Results showed that  $(\text{H}_2\text{O})\text{Ar}_n^+$  clusters deliver 4- 10 times more secondary ion signal than  $\text{Ar}_n^+$  clusters on their own. However, the signal intensity is still lower than the signal observed with  $(\text{H}_2\text{O})_n^+$ . This study also revealed that maximum secondary ion yields with water-containing clusters is observed when the clusters have an energy per nucleon of  $\sim 0.2$  eV. This is an indicator of the close behaviour denoted by  $(\text{H}_2\text{O})_n^+$  and  $(\text{H}_2\text{O})\text{Ar}_n^+$  clusters. Again, experiments with deuterated water-doped argon clusters on DPPC confirmed that the origin of the protons exchanged during ionisation is the cluster primary ion beam.

Although still under research, it is believed that the energised water molecules from the primary ion beam interact with the sample molecules resulting in protonation enhancement and increased  $[\text{M}+\text{H}]^+$  ion yields. In addition, the secondary yield results obtained with water clusters are supported by sputtering studies on L-arginine and Irganox 1010 (presented in Section 2.5.8) [23]. This plot illustrated with Figure 2.26 (by Kohn *et al.*) demonstrates that the sputtering obtained with water clusters is similar to that obtained with  $\text{C}_{60}$  and argon clusters of similar energy per atom or molecule. Therefore, the increase in secondary ion yields presented in this chapter can be attributed to protonation enhancement and not to an increase in sputter yields.

These results showed the potential of water-contained cluster ion beams for biological studies. The following chapters will discuss the application of pure water and water-doped argon clusters in total lipid brain extract and imaging of mouse brain tissue sections.

## 5.7 References

- [1] S. Sheraz, A. Barber, J. S. Fletcher, N. P. Lockyer, and J. C. Vickerman, "Enhancing secondary ion yields in ToF-SIMS using water cluster primary beams .," *Anal. Chem.*, pp. 2-3, 2013.

- [2] S. Sheraz née Rabbani, a. Barber, I. Berrueta Razo, J. S. Fletcher, N. P. Lockyer, and J. C. Vickerman, "Prospect of increasing secondary ion yields in ToF-SIMS using water cluster primary ion beams," *Surf. Interface Anal.*, no. November 2013, p. n/a–n/a, 2014.
- [3] A. G. Shard and I. S. Gilmore, "Molecular depth profiling," in *TOF-SIMS: Materials analysis by mass spectrometry*, J. C. Vickerman and D. Briggs, Eds. Manchester: IM Publications, 2013, pp. 311–334.
- [4] C. M. Mahoney, *Cluster Secondary Ion Mass Spectrometry: Principles and Applications*. Sons, John Wiley &, 2013.
- [5] A. G. Shard and I. S. Gilmore, *TOF-SIMS: Materials analysis by mass spectrometry*, 2nd ed. Manchester: IM Publications, 2013.
- [6] A. M. Piwowar, S. Keskin, M. O. Delgado, K. Shen, J. J. Hue, I. Lanekoff, A. G. Ewing, and N. Winograd, "C60-ToF SIMS imaging of frozen hydrated HeLa cells," *Surf. Interface Anal.*, vol. 45, no. February, pp. 302–304, 2013.
- [7] T. P. Roddy, D. M. Cannon, S. G. Ostrowski, N. Winograd, and A. G. Ewing, "Identification of cellular sections with imaging mass spectrometry following freeze fracture," *Anal. Chem.*, vol. 74, no. 16, pp. 4020–4026, 2002.
- [8] E. A. Jones, N. P. Lockyer, and J. C. Vickerman, "Mass spectral analysis and imaging of tissue by ToF-SIMS-The role of buckminsterfullerene, C60 +, primary ions," *Int. J. Mass Spectrom.*, vol. 260, no. 2–3, pp. 146–157, 2007.
- [9] M. P. Seah, R. Havelund, and I. S. Gilmore, "Universal equation for argon cluster size-dependence of secondary ion spectra in sims of organic materials," *J. Phys. Chem. C*, vol. 118, no. 24, pp. 12862–12872, 2014.
- [10] M. P. Seah, "Universal equation for argon gas cluster sputtering yields," *J. Phys. Chem. C*, vol. 117, no. 24, pp. 12622–12632, 2013.
- [11] T. B. Angerer, P. Blenkinsopp, and J. S. Fletcher, "High energy gas cluster ions for organic and biological analysis by time-of-flight secondary ion mass spectrometry," *Int. J. Mass Spectrom.*, vol. 377, pp. 591–598, 2015.
- [12] A. G. Sostarecz, D. M. Cannon, C. M. McQuaw, S. Sun, A. G. Ewing, and N. Winograd, "Influence of molecular environment on the analysis of phospholipids by

time-of-flight secondary ion mass spectrometry,” *Langmuir*, vol. 20, no. 12, pp. 4926–4932, 2004.

[13] D. Willingham, D. A. Brenes, N. Winograd, and A. Wucher, “Investigating the fundamentals of molecular depth profiling using strong-field photoionization of sputtered neutrals,” *Surf. Interface Anal.*, vol. 43, no. 1–2, pp. 45–48, 2011.

[14] B. J. Garrison, “Molecular ions in cluster bombardment: What clues do the molecular dynamics simulations provide?,” *Surf. Interface Anal.*, vol. 43, no. 1–2, pp. 134–136, 2011.

[15] Z. Postawa, R. Paruch, L. Rzeznik, and B. J. Garrison, “Dynamics of large Ar cluster bombardment of organic solids,” *Surf. Interface Anal.*, vol. 45, no. 1, pp. 35–38, 2013.

[16] A. Delcorte, B. J. Garrison, and K. Hamraoui, “Dynamics of molecular impacts on soft materials: From fullerenes to organic nanodrops,” *Anal. Chem.*, vol. 81, no. 16, pp. 6676–6686, 2009.

[17] B. Czerwinski, Z. Postawa, B. J. Garrison, and A. Delcorte, “Molecular dynamics study of polystyrene bond-breaking and crosslinking under C60 and Arn cluster bombardment,” *Nucl. Instruments Methods Phys. Res. Sect. B Beam Interact. with Mater. Atoms*, vol. 303, pp. 22–26, 2013.

[18] H. Tian, A. Wucher, and N. Winograd, “Molecular imaging of biological tissue using gas cluster ions,” *Surf. Interface Anal.*, vol. 46, no. S1, pp. 115–117, 2014.

[19] a V Samartsev and a Wucher, “Yields and ionization probabilities of sputtered In n particles under atomic and polyatomic Au m Å ion bombardment,” vol. 252, pp. 6474–6477, 2006.

[20] S. S. Johar and D. A. Thompson, “Sputtering yields of Ag, Au and Pt thin films,” vol. 90, pp. 319–330, 1979.

[21] A. Delcorte, O. A. Restrepo, B. Czerwinski, and B. J. Garrison, “Surface sputtering with nanoclusters: The relevant parameters,” *Surf. Interface Anal.*, vol. 45, no. 1, pp. 9–13, 2013.

[22] J. a Geurst and L. D. R. Philips, “Dynamics of of L-phenylalanine sputtering by argon cluster bombardment,” 1975.

[23] S. Sheraz née Rabbani, I. Berrueta Razo, T. Kohn, N. P. Lockyer, and J. C. Vickerman, "Enhancing Ion Yields in Time-of-Flight-Secondary Ion Mass Spectrometry: A Comparative Study of Argon and Water Cluster Primary Beams," *Anal. Chem.*, vol. 87, no. 4, pp. 2367–2374, 2015.

[24] H. Min, S. Wettmarshausen, J. F. Friedrich and W. E. S. Unger, "A ToF-SIMS study of the deuterium-hydrogen exchange induced by ammonia plasma treatment of polyolefins", *Journal of Analytical Atomic Spectrometry*, vol. 26, pp.-1157-1165, 2011.

## 6 Molecular imaging of mouse brain tissue sections using Cluster ToF-SIMS

Mouse brain is a well-established biological model for mass spectrometry [1]. It is estimated that the brain contains around 37% of lipid when considering its dry matter [2]. When a whole brain is cryo-sectioned and then analysed under vacuum, most of the ions detected from the surface correspond to lipids and lipid fragments [3]. Thus, ToF-SIMS is a well-suited platform for lipid imaging *in situ* [1]. However, the low number of secondary ion produced from biological samples is one of the main obstacles for molecular imaging.

Another significant challenge is the suppression or enhancement of ions in biological environments [4]. These two issues are studied with the application of giant water, argon and water-doped argon clusters on ToF-SIMS imaging of mouse brain tissue sections. These primary ion clusters were successfully applied to the study of standard biomolecules (chapter 5) and it was demonstrated that water clusters with  $E/n \sim 3$  eV produced the highest secondary ion signal. Water clusters in this energy regime along with water-doped argon clusters were compared to argon and fullerene clusters for molecular imaging. Lipid ionisation and spatial resolution were also assessed.

The first series of experiments present a comparison between water clusters and  $C_{60}^+$  for tissue imaging on a small area of the brain striatum. Subsequently, a larger area of the brain (cerebellum) was analysed with  $C_{60}^+$ ,  $Ar_n^+$ ,  $(H_2O)Ar_n^+$  and  $(H_2O)_n^+$  clusters. An evaluation including qualitative and semi-quantitative comparisons of the spectra obtained is presented. ROI-Principal component analysis (PCA) was applied to highlight the chemical differences between grey and white matter of the brain cerebellum. From the PCA separation of the two types of tissue, lipid peaks detected from both matters of the brain were identified and assigned.

Some of the results presented in this chapter, have been published in scientific journals and are included in Appendix II and Appendix III.

### 6.1 Overview of the mouse brain anatomy

The experiments presented in this section contemplate the mouse brain in a sagittal plane. In this brain orientation most of the anatomical features are exposed and many structures of the brain can be visualised.

Figure 6.1 shows the sagittal orientation in a mouse brain. Rodent brains are analysed with MSI mainly because of their reduced size and their high content of lipids, which ionise easily [1], [5]–[9]. Moreover, there are similarities between a mouse brain and a human brain.

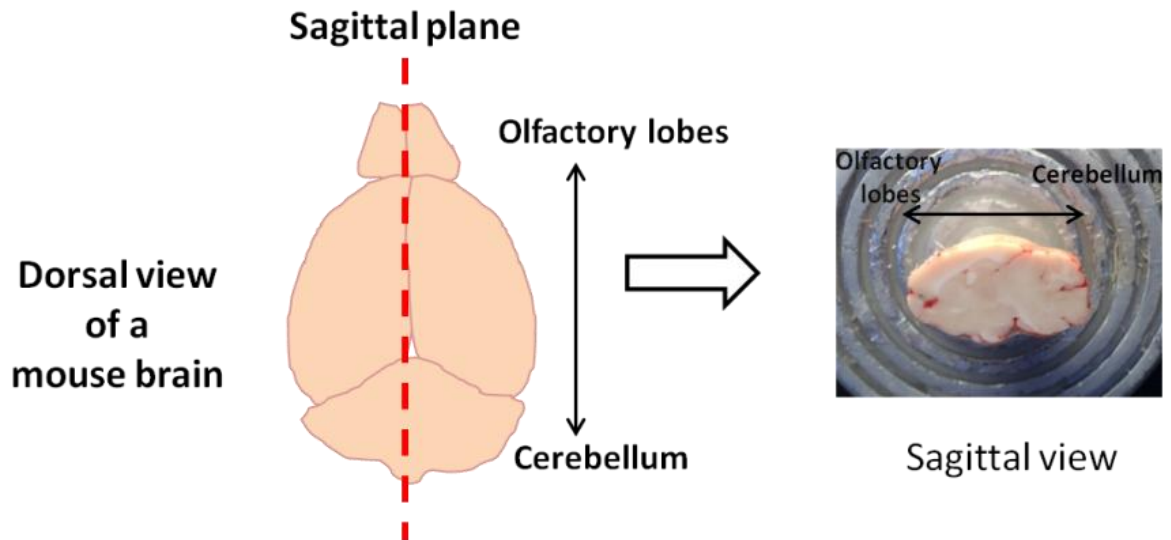


*Figure 6.1: Visualisation of the sagittal plane on a mouse brain.*

The main difference between them is the size of the cerebellum; the size of the cerebellum in mouse is bigger relative to the size of the frontal lobes and the cortex. Furthermore, the human cortex has folds on the surface whereas mice have smooth brains. Humans also possess more neurons per unit volume than any other animal [10].

If a mouse brain is sectioned in a sagittal plane, two symmetric hemispheres are obtained and most of the major brain structures can be easily identified from this perspective [10]. However, the visibility of different structures can be reduced or enhanced according to the thickness of each section and its proximity to the central brain axis.

Figure 6.2 displays the sections obtained from one of the hemispheres of the brain when sectioning a complete mouse brain in a sagittal plane [11], [12]. Figure 6.2 shows the sectioning of an adult mouse brain starting from the outer part of the left hemisphere up to the central axis.

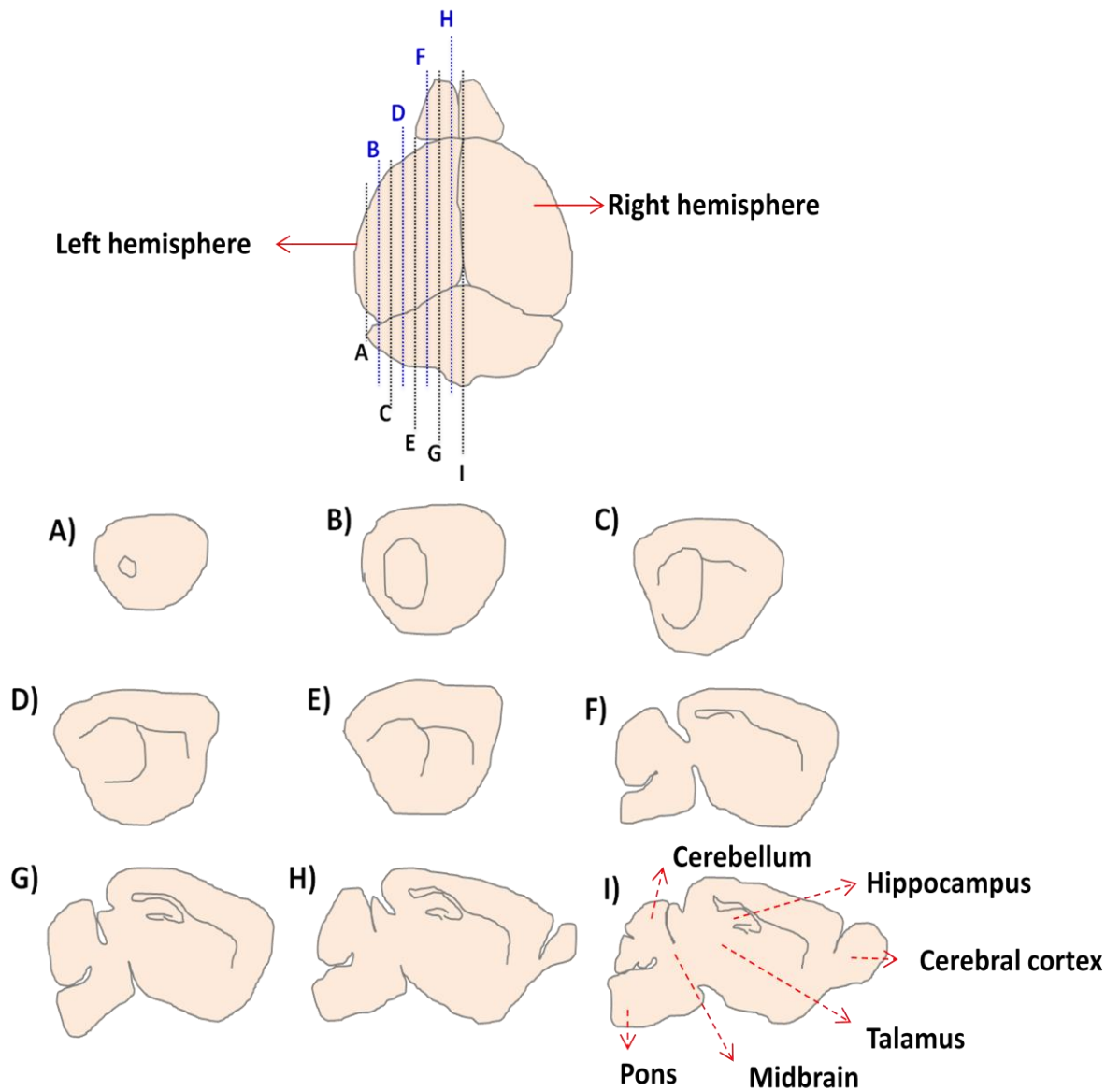


*Figure 6.2: Sagittal sections obtained from the left hemisphere of the mouse brain. This hemisphere is sectioned in nine sections from the outside (section A) up to the central axis (section I). Here, it is possible to locate many of the main brain structures: the cerebellum area with pons and medulla underneath, the midbrain, the cerebral cortex; the two hippocampal areas; caudate putamen; thalamus; internal capsule and amygdala [11].*

There are different mouse brain atlases available [11], [12] to identify the anatomical structures of sagittal mouse brain sections. Figure 6.3 illustrates the anatomical areas identified in a sagittal section taken from the central axis. More anatomical areas can be visualised when the section is closer to the central axis.

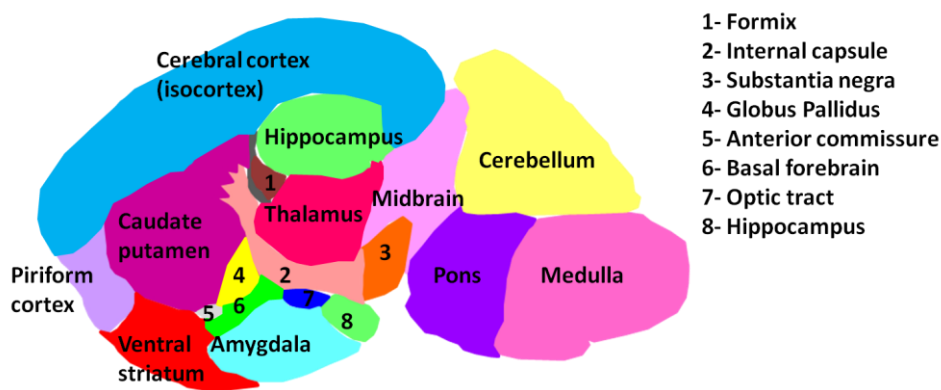


Figure 6.3: Mouse brain anatomy from a sagittal plane perspective. The identified anatomical structures from this sagittal section belong to the region close to the central axis [11].

The lipid composition of human and mouse brain was explained in the literature review, section 2.5.2.1. It was also mentioned that the brain is mainly composed of two types of tissue: grey matter and white matter. White matter contains mainly axons and myelin sheath; thus, it is rich in cholesterol. On the other hand, grey matter is built by cell bodies and contains a higher content of phospholipids [13].

## 6.2 Presence of cholesterol in the grey and white matter

ToF-SIMS has been applied to study the localisation of cholesterol in the brain [14]. Its localisation in the cerebellum is related to the function of nervous tissue [14]. However, this molecule has proven to be challenging since results obtained in past studies are highly influenced by tissue preparation and analytical conditions [14], [16].

Although cholesterol is mainly concentrated in the white matter, it is also located in the grey matter [2, 14]. 55 to 70% of the white matter's dry weight is composed of lipid, from which 27% is cholesterol and 45% relates to other phospholipid species. In the grey matter, 35% of the dry weight is lipids; 22% of these lipids are cholesterol whereas 60-70% corresponds to phospholipids of many classes. In the white matter, cholesterol is synthesized *in situ* in neurons and glial cells. This cholesterol production is destined to build the myelin sheath that wraps around the neuron's axon. In the grey matter, this sterol lipid is vital to maintain the integrity of all cell membranes [17], [18].

Figure 6.4 (A) displays the structure of the brain's grey matter and the localisation of cholesterol in it. This region is mainly composed of the nerve cell bodies with membranes built by phospholipids and cholesterol. Figure 6.4 (B) illustrates the localisation of cholesterol in the white matter. Cholesterol is a main structural part of the myelin which also contains phospholipids. Cholesterol molecules are more



abundant in this type of tissue (27.7 % of the dry weight in a human) when compared to the grey matter structure (22% of dry weight in a human) (See Table 2.2) [19], [20].

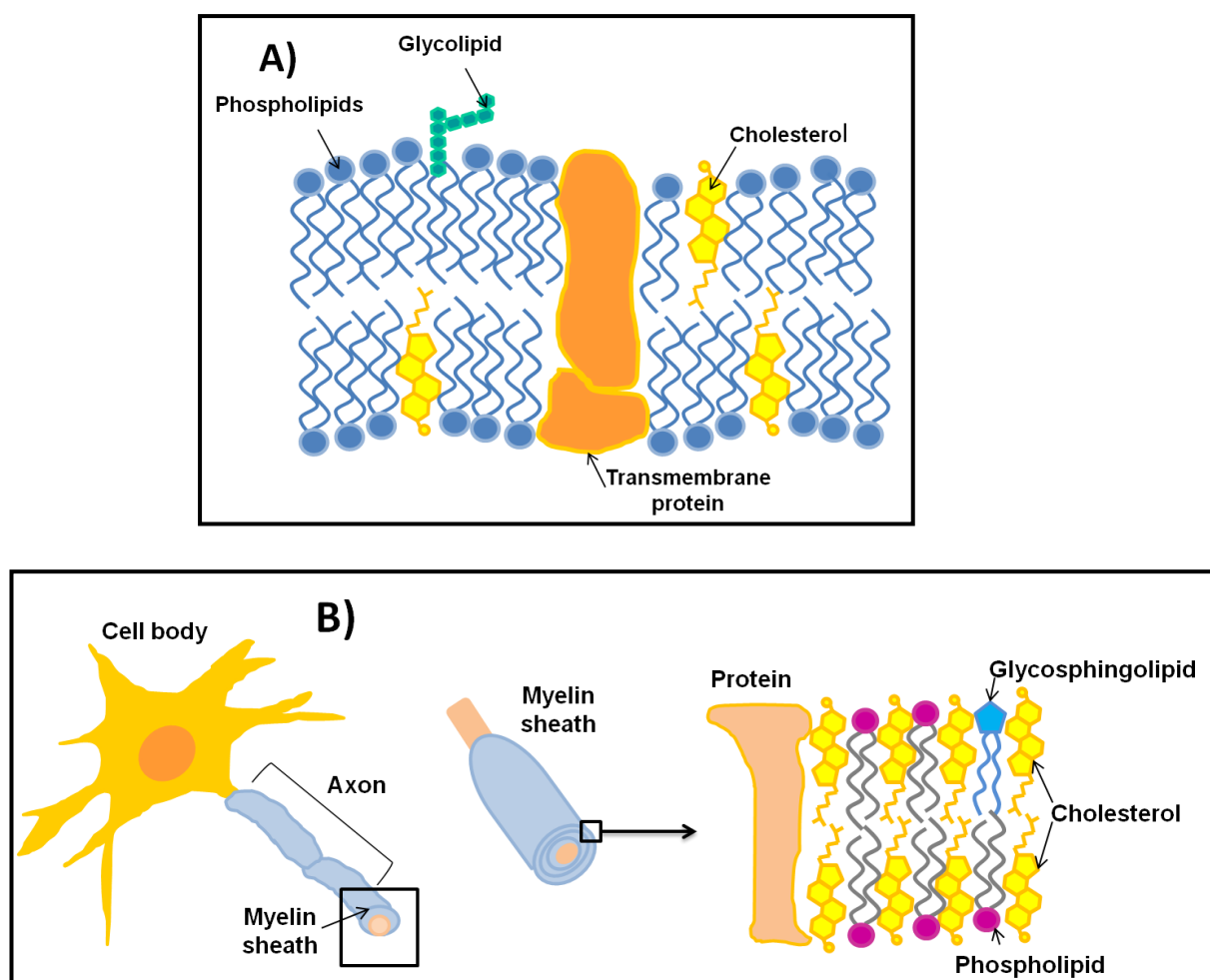


Figure 6.4: (A) Membrane structure found in the cell bodies located in the grey matter area of the brain. (B) Lipids located in the myelin sheath of the neuron's axons; the myelin sheath wraps up the axon. Axons are the main components of the white matter of the brain [19], [20].

### 6.3 Aim of the experiments

The experiments presented aim to develop an experimental protocol for biological tissue imaging using clusters as primary ion beams on the J105-3D Chemical Imager. Previous background studies on standards established that water cluster ion beams deliver the highest signal of protonated intact molecules when the beam has energy per nucleon of  $\sim 0.18$  eV. It was also mentioned that water-doped argon clusters with energy per nucleon of  $\sim 0.2$  eV show a similar behaviour to that observed in water clusters but producing lower secondary ion yield. Although the highest enhancement of secondary ion signal was observed with 20 keV  $(\text{H}_2\text{O})_{6000}^+$ , the lifetime of this ion source is limited to 2 hours. Depending of the primary ion beam current, an image

acquisition of the whole tissue section can take up to 6 hours. In contrast, 20 keV  $(\text{H}_2\text{O})\text{Ar}_n^+$  can produce steady ion current for about 8 hours and 20 keV  $\text{Ar}_n^+$  and is only restricted by the gas supply. All of these experimental factors are assessed for the analysis of brain total lipid extract and brain tissue imaging. The brain sections were analysed with different 20 keV  $(\text{H}_2\text{O})_n^+$ ,  $(\text{H}_2\text{O})\text{Ar}_n^+$ ,  $\text{Ar}_n^+$  and  $\text{C}_{60}^+$  cluster ion beam.

## 6.4 ToF-SIMS analysis

All experimental data was acquired with the J105 Chemical Imager (Ionoptika Ltd, Hampshire, UK), previously described in the instrumental section (section 3.4) in positive ion mode. The experimental conditions for brain extract analysis; lipid mixture analysis and brain imaging are described next.

### 6.4.1 Analysis of brain total lipid extract

Similarly to the comparative background studies presented in the previous chapter, brain total lipid extract was analysed with 20 keV pure water clusters, water-doped argon clusters and argon clusters of different sizes. The secondary ion yield and spectral changes were assessed in two sets of experiments: an initial acquisition of data obtained after the sample was exposed to a primary ion dose equivalent to  $5 \times 10^{11}$  ions  $\text{cm}^{-2}$ . This initial acquisition was followed by a second acquisition once  $3 \times 10^{13}$  ions  $\text{cm}^{-2}$  of primary ion dose were accumulated. 20 keV  $(\text{H}_2\text{O})_{1000-6000}^+$ , 20 keV  $(\text{H}_2\text{O})\text{Ar}_{1000-6000}^+$  and 20 keV  $\text{Ar}_{1000-4000}^+$  clusters were applied to this series of experiments.

### 6.4.2 Molecular imaging of mouse brain sections

ToF-SIMS images were acquired by analysing specific areas of sagittal mouse brain sections. The experimental parameters used on the images are described below:

*Molecular imaging of the brain striatum:* Images of the striatum of the brain from one single section were acquired using 20 keV  $\text{C}_{60}^+$ , 20 keV  $(\text{H}_2\text{O})_{3000}^+$  and 20 keV  $(\text{H}_2\text{O})_{4500}^+$ . All images cover a total area of  $650 \mu\text{m}^2$  with  $64 \times 64$  pixels. The initial primary ion dose used was  $5 \times 10^{11}$  ions  $\text{cm}^{-2}$  after which, a total of  $3 \times 10^{13}$  ions  $\text{cm}^{-2}$  was accumulated for subsequent image acquisitions. The beam diameter measured with 20 keV  $\text{C}_{60}$  was  $7 \mu\text{m}$  whereas the diameters obtained with 20 keV  $(\text{H}_2\text{O})_{3000}$  and  $(\text{H}_2\text{O})_{4500}$  were  $9 \mu\text{m}$  and  $10 \mu\text{m}$ , respectively. The pixel size in each image was adjusted to match to the beam diameter obtained with each analysis beam so that each pixel covered the same area than the actual spot size.

*Dual beam experiment on the brain's striatum:* a dual beam approach was studied to evaluate the possible secondary ion yield enhancement obtained from the application of 5 keV  $(\text{H}_2\text{O})_{3000}^+$  and 20 keV  $\text{C}_{60}^+$  simultaneously. A  $650 \mu\text{m}^2$  area of the brain's striatum was analysed with 20 keV  $\text{C}_{60}^+$  first, accumulating a total primary ion dose of  $5 \times 10^{12}$  ions  $\text{cm}^{-2}$ . After the first acquisition, a second image with the same 20 keV  $\text{C}_{60}^+$  ion dose was acquired on the same area, but this time a defocused 5 keV  $(\text{H}_2\text{O})_{3000}^+$  beam was applied on dc simultaneously.

*Molecular imaging of brain cerebellum:* Tiled images of the cerebellar area of the brain comprising cerebellum, medulla and pons were acquired on serial sagittal sections. Unless stated otherwise, all cerebellum images were acquired under a primary ion dose of  $1 \times 10^{12}$  ions  $\text{cm}^{-2}$ . Each image was acquired on a  $4\text{mm} \times 4\text{mm}$  area, which was enough to cover the complete cerebellar area. The cerebellum area was selected to acquire tiled images on a bigger area containing both white and grey matter tissues.

In the first sets of experiments, the primary cluster ion beams used for image acquisition were 20 keV  $\text{C}_{60}^+$ , 20 keV  $\text{Ar}_{2000}^+$ , 20 keV  $(\text{H}_2\text{O})_{2000}^+$  and 20 keV  $(\text{H}_2\text{O})_{4000}^+$ . The beam diameter obtained with 20 keV  $\text{C}_{60}$  was  $9 \mu\text{m}$ , with 20 keV  $\text{Ar}_{2000}$  was  $10 \mu\text{m}$  and with 20keV  $(\text{H}_2\text{O})_n$  was 10-11  $\mu\text{m}$ .

During the second set of experiments, the cerebellum from serial sections were analysed using 20 keV  $\text{C}_{60}^+$ , 20 keV  $\text{Ar}_{2000}^+$ , 20 keV  $(\text{H}_2\text{O})_{6000}^+$  and 20 keV  $(\text{H}_2\text{O})\text{Ar}_{2000}^+$ . The beam diameter obtained with 20 keV  $\text{C}_{60}$  was  $9 \mu\text{m}$ , with 20 keV  $\text{Ar}_{2000}$  was  $13 \mu\text{m}$ , with water clusters  $(\text{H}_2\text{O})_n$  was  $10 \mu\text{m}$  and with water-doped argon clusters  $(\text{H}_2\text{O})\text{Ar}_n$  was  $11 \mu\text{m}$ . Once again, the pixel size used for imaging matched the beam diameters of each cluster ion beam.

### **6.4.3 Matrix effect experiments**

The ion suppression effect observed in the mouse brain images was explored further with the analysis of lipid mixtures. In this experiment, the same cluster ion beams used for biological imaging were applied to the study of standard lipid mixtures of different concentrations.

The primary ion dose was kept  $1 \times 10^{12}$  ions  $\text{cm}^{-2}$  to try to mimic the tissue analysis conditions. A second spectrum was acquired with a primary ion dose equivalent to  $5 \times 10^{12}$  ions  $\text{cm}^{-2}$  to check the reproducibility of the first acquired spectrum and to discard any surface effects.

## 6.5 Results and discussion

### 6.5.1 Analysis of total lipid brain extract with 20 keV $C_{60}^+$ , $Ar_n^+$ , $(H_2O)_n^+$ and $(H_2O)Ar_n^+$ clusters

Previous results [21]–[23] obtained with the same prototype water cluster ion beam have proved the efficacy of water-containing beams to study model compounds such as arginine, trehalose, DPPC, haloperidol, cholesterol and angiotensin II. To explore the possible application of this prototype water cluster ion beam to mouse brain tissue imaging, water-containing clusters were applied first to the study of a sample that mimics the lipid composition of the brain: brain total lipid extract (BTLE). The lipid composition of BTLE is comparable to that found in the brain; thus, the cluster ion beams that demonstrate the best results could potentially be applied to brain imaging.

Spectra acquired with a total ion dose of  $5 \times 10^{11}$  ions  $cm^{-2}$  were compared. One of the major spectral differences is the secondary ion signal obtained from the cholesterol  $[M+H-H_2O]^+$  ion peak. The detection of the cholesterol ion was increased significantly when using  $(H_2O)_n^+$  clusters, especially with large cluster sizes ( $n = 6000$ ). This increase of secondary ion signal can be seen in Figure 6.5. Here, the cholesterol signal intensity at  $m/z$  369 is considerably higher with 20 keV  $(H_2O)_{6000}^+$  (Figure 6.5, B) when compared to 20 keV  $(H_2O)_{2000}^+$  Figure 6.5, (A).

The signal intensity obtained from the ion peaks found in the mass range  $m/z$  700-900 is also significantly higher with  $(H_2O)_{6000}^+$ . Of particular interest is the mass range (700-900 Da) since most intact phospholipids can be found there.

On the other hand, the signal intensity of the phosphocholine fragment  $[C_5H_{15}NO_4P]^+$  at  $m/z$  184 is lower with  $(H_2O)_{6000}^+$  in comparison to  $(H_2O)_{2000}^+$ . The phosphocholine molecule is the head group in the structure of phospholipids. Thus, less signal intensity from this ion may suggest that more intact phospholipids and less fragments are generated with  $(H_2O)_{6000}^+$ .

Similarly to the analysis of DPPC and biomolecules with water clusters, the detection of structural phosphocholine fragments highly depended on the  $E/molecule$  of the water cluster. There is a decrease in the detection of the phosphocholine ion when  $E/molecule < 10$  eV (<2000 clusters size).

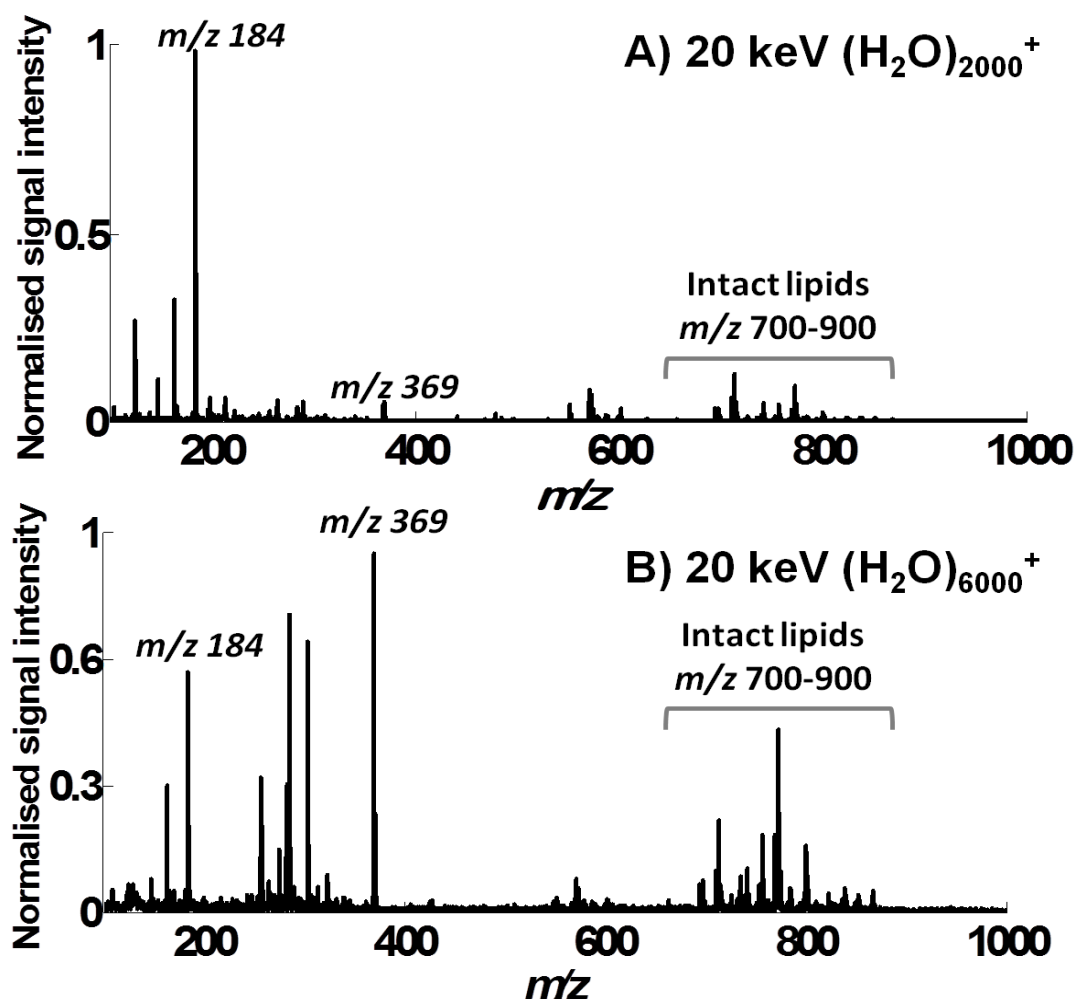


Figure 6.5: Secondary ion spectra of brain extract acquired with (A) 20 keV  $(\text{H}_2\text{O})_{2000}^+$  and (B) 20 keV  $(\text{H}_2\text{O})_{6000}^+$ . Both spectra were normalised to the total ion counts.

The behaviour of the lipids GPCho C32:0  $[\text{M}+\text{H}]^+$  at  $m/z$  734, GPCho C34:0  $[\text{M}+\text{H}]^+$  at  $m/z$  762, sphingolipid Ch 24:1 GalCer(d18:1/2-OH-24:1)  $[\text{M}+\text{H}]^+$  at  $m/z$  826 and cholesterol  $[\text{M}-\text{H}_2\text{O}+\text{H}]^+$  at  $m/z$  369 were studied further by monitoring the signal variations in the spectra. Figure 6.6 displays their secondary ion signal variation as a function of the energy per nucleon ( $E/\text{nucleon}$ ). All the experiments included acquisitions with 20 keV  $\text{C}_{60}$ , although this data is not included in the plots due to the low signal intensities for most ions.

In Figure 6.6, it is possible to see the similar trends for the selected lipids to those observed in previous model compounds e.g. DPPC, trehalose, angiotensin and arginine. The secondary yields obtained with  $\text{Ar}_n^+$  clusters are the lowest, especially for the cholesterol ion. The secondary ion signal for cholesterol obtained with  $(\text{H}_2\text{O})_n^+$  clusters was the highest. According to the plots, the optimum  $E/\text{nucleon}$  regime for  $(\text{H}_2\text{O})_n^+$  clusters is  $\sim 0.2$  eV which corresponds to a cluster size of  $\sim 6000$ . The 20 keV

$(\text{H}_2\text{O})\text{Ar}_n^+$  clusters exhibit increased signal intensity when compared to  $\text{Ar}_n^+$ , especially with an  $E/\text{nucleon}$  of  $\sim 0.2$  eV (2000 cluster size). With 20 keV  $(\text{H}_2\text{O})\text{Ar}_{2000}^+$ , the signal intensity is about half that of the signal obtained with 20 keV  $(\text{H}_2\text{O})_{6000}^+$ .

The cholesterol signal is enhanced by a factor of 10 with  $(\text{H}_2\text{O})\text{Ar}_{2000}$  analysis and by a factor of 35 under  $(\text{H}_2\text{O})_{6000}$  bombardment when compared to the signal intensity detected with  $\text{Ar}_n^+$  at  $m/z$  369. The formation of this ion requires the protonation of  $[\text{M}]$  and the removal of one molecule of water. The protonated molecular ion  $[\text{M}+\text{H}]^+$  at  $m/z$  385 was not observed, unlike in the case of 20 keV  $\text{C}_{60}$ .

The behaviour of the phospholipids GPCho C32:0 and GPCho C34:0 and the sphingolipid Ch 24:1  $[\text{M}+\text{H}]^+$  ions are very similar to that which is observed in the DPPC standard (Figure 5.18). The signal enhancement obtained with the cluster  $(\text{H}_2\text{O})_{6000}$  ranges from 10x to 100x, whereas the enhancement produced by  $(\text{H}_2\text{O})\text{Ar}_{2000}^+$  lies between 4x to 10x.

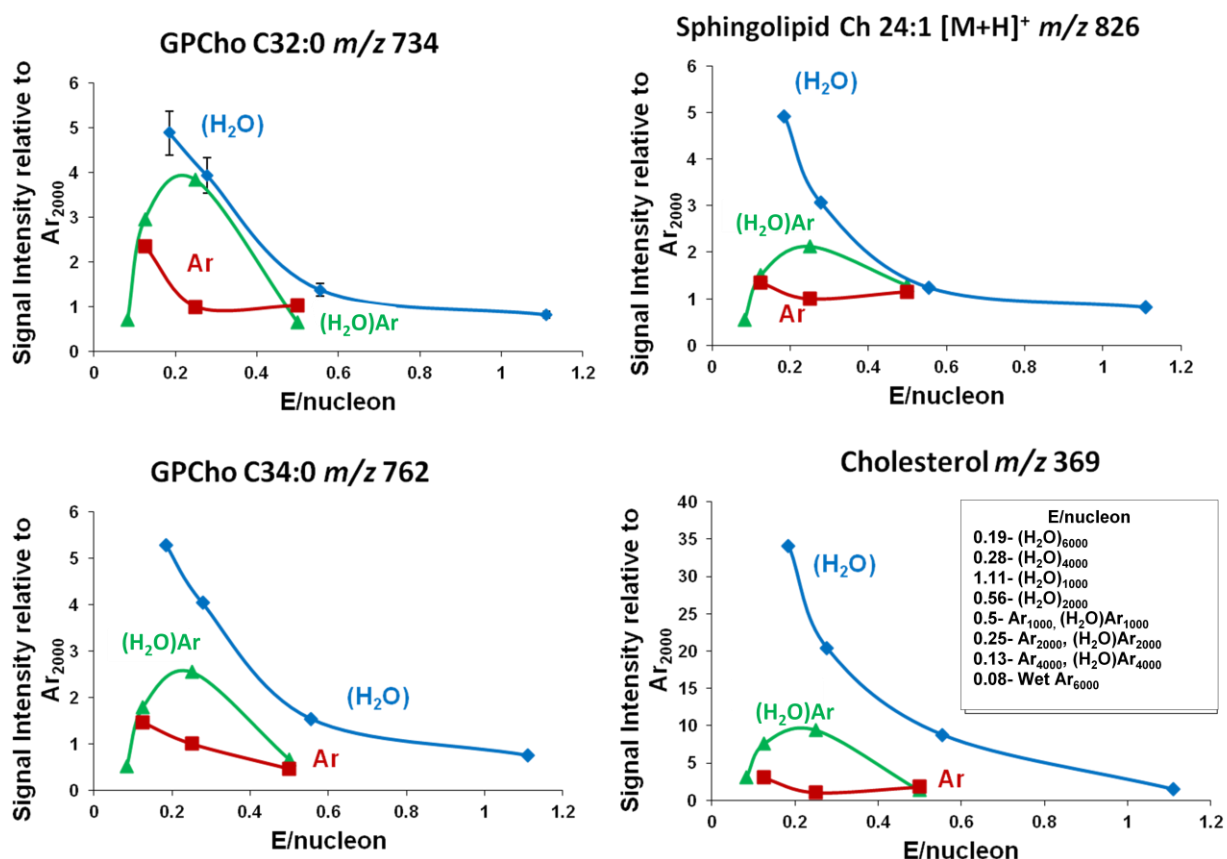
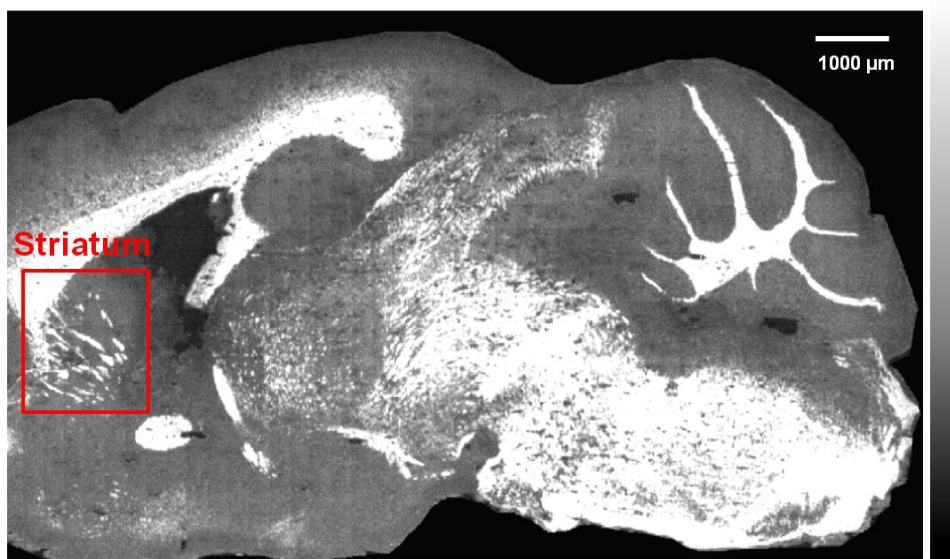


Figure 6.6: Plots of secondary ion signal of GPCho C32:0  $[\text{M}+\text{H}]^+$  at  $m/z$  734; GPCho C34:0  $[\text{M}+\text{H}]^+$  at  $m/z$  762; Sphingolipid Ch 24:1  $[\text{M}+\text{H}]^+$  at  $m/z$  826 and cholesterol  $[\text{M}-\text{H}_2\text{O}+\text{H}]^+$  ion at  $m/z$  369. The experiments were acquired using 20 keV  $(\text{H}_2\text{O})_n^+$  (blue line), 20 keV  $(\text{H}_2\text{O})\text{Ar}_n^+$  (green line) and 20 keV  $\text{Ar}_n^+$  (red line). All signal intensities are plotted relative to the ion signal observed with 20 keV  $\text{Ar}_{2000}^+$  and as a function of  $E/\text{nucleon}$ .

### 6.5.2 Cluster ToF-SIMS imaging of the brain striatum

The brain striatum, or striate nucleus, is a brain structure part of the forebrain, surrounded by the thalamus. In a sagittal section, it is located below the cerebral cortex and it is characterised by its striated appearance, as illustrated in Figure 6.7. Functionally, it controls and coordinates fine body movement and behaviour. Anatomically, it is divided by a tract of white matter tissue called internal capsule, which divides it into two sectors: cuate and putamen [24].



*Figure 6.7: Localisation of the brain striatum in a total ion SIMS image of a sagittal section of a mouse brain. This image was acquired with 20 keV  $C_{60}^+$  and a pixel size of 7  $\mu m$ . The mass range recorded was  $m/z$  100- 1000. The striated appearance is one of the main characteristics of this brain region.*

Images of the striatum of the mouse brain were acquired from a 650  $\mu m^2$  area with 20 keV  $C_{60}^+$  and 20 keV  $(H_2O)_{3000}^+$ . In Figure 6.8 (A), an image acquired with 20 keV  $C_{60}^+$  using a primary ion fluence of  $2.5 \times 10^{12}$  ions  $cm^{-2}$  is displayed. In the spectrum, it is possible to observe that the base peak is the phosphocholine fragment  $[C_5H_{15}NO_4P]^+$  at  $m/z$  184, which is mainly found in the grey matter of the brain [9]. The phosphocholine molecule is a part of the structure of phospholipids [25]. In an adult rat, 56% of the dry weight of the brain is phospholipid [13]. Hence, phospholipids and their fragments are expected to be notably present in the mass spectrum of mouse brain. The ion peak that exhibits the second highest secondary ion signal is cholesterol  $[M+H-H_2O]^+$  at  $m/z$  369. This sterol lipid is mainly found in the myelin sheathes of axons in the white matter of the brain [2]. Hence, cholesterol is mostly detected in the white matter of the brain. There are also several ion peaks observed in the mass range  $m/z$  500-1000, where intact lipid species can be detected. The signal intensity of the peaks in this mass range

is low, being almost 100 times lower than the signal detected from the phosphocholine head group ion. The fragmentation observed is consistent with the fragmentation of DPPC (Figure 5.18) and BTLE (Figure 6.5).

After analysis with  $C_{60}^+$ , a second image was acquired on the same area with 20 keV  $(H_2O)_{3000}^+$  and a primary ion fluence of  $5 \times 10^{11}$  ions  $cm^{-2}$ . Figure 6.8 (B) displays this image and the corresponding mass spectrum. Here, it is possible to observe an increase in secondary ion signal even after the potential surface damage caused by  $C_{60}^+$  analysis. The primary ion dose used for this experiment is 5 times lower than the dose used in the  $C_{60}^+$  experiment highlighting the increase in secondary ion yields achieved with water clusters. The ion peaks found in the mass range  $m/z$  500-1000 are increased by a factor of 5, suggesting the detection of more intact lipids. Moreover, the signal from the phosphocholine ion is  $\sim 3$  times lower relative to the lipid molecular ions observed in the mass range  $m/z$  500-1000 indicating less fragmentation of intact lipid molecules into phosphocholine fragments.

The larger spot size (9  $\mu m$ ) of the  $(H_2O)_{3000}^+$  has a lower spatial resolution, meaning smaller anatomical features are not so easily resolved. The striated features of this region of the brain can be identified easily with  $C_{60}^+$  as the beam diameter is smaller (7  $\mu m$ ) [26].

Two images of different areas of the brain striatum were acquired on 650  $\mu m^2$  regions using 20 keV  $(H_2O)_{3000}^+$  and 20 keV  $(H_2O)_{4500}^+$ . The primary ion fluence was kept constant  $5 \times 10^{11}$  ions  $cm^{-2}$ . The images obtained in this experiment are shown in Figure 6.9 (A) and (B). The ion distribution shows the same trend as the spectra in Figure 6.9 with the phosphocholine ion as the base peak, the cholesterol ion as the second highest peak and multiple significant ion peaks in the higher mass range (500-1000 Da).

The secondary ion signal obtained with  $(H_2O)_{3000}^+$  and  $(H_2O)_{4500}^+$  is also notably enhanced when compared to the signal produced with  $C_{60}^+$ , although there is less anatomical detail due to the lower spatial resolution. Even though the areas analysed with the two water clusters are different, they are both located right next to each other in the striatum region. Therefore, the chemical variation should not be significant.



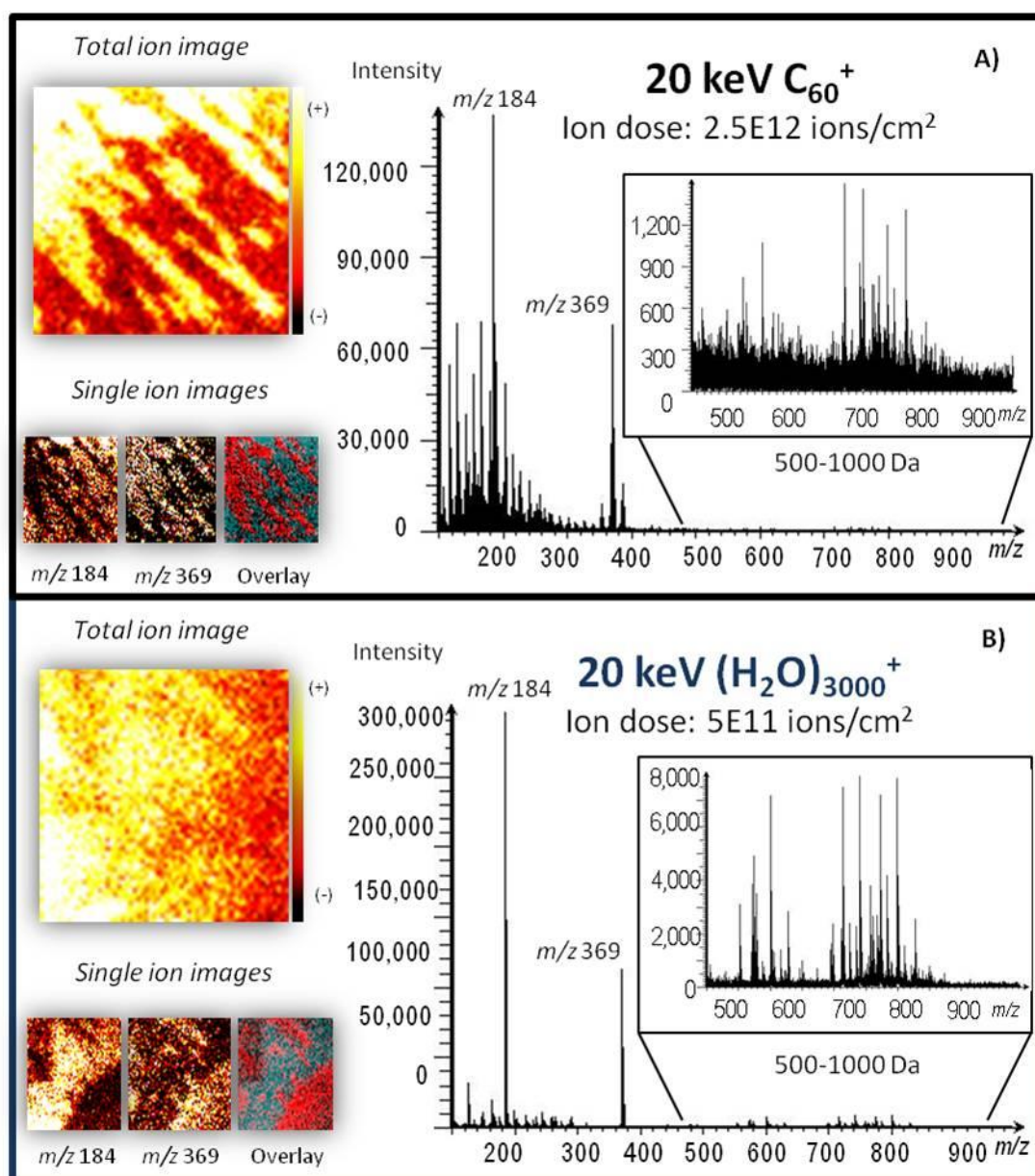


Figure 6.8: ToF-SIMS imaging of the brain striatum in positive ion mode. The same area was analysed with 20 keV  $C_{60}^+$  and 20 keV  $(H_2O)_{3000}^+$  with a  $650 \mu m^2$  field of view. (A) Total ion spectrum and image after a primary ion dose of  $2.5 \times 10^{12}$  ions  $cm^{-2}$  with 20 keV  $C_{60}^+$ . The beam diameter was  $7 \mu m$  and it is possible to observe the white matter striated features commonly found in this area of the brain. The ion peaks in mass range in which most intact phospholipids can be found (500-1000 Da) are zoomed in. (B) Same area analysed with 20 keV  $(H_2O)_{3000}^+$  after  $C_{60}$  bombardment. The accumulated ion dose was  $5 \times 10^{11}$  ions  $cm^{-2}$  with a spot size  $9 \mu m$ .

Under  $(H_2O)_{4500}^+$  bombardment, the secondary ion signal from the phosphocholine ion is lower than that obtained with  $(H_2O)_{3000}^+$ . Also, the ion peaks situated in the high mass range end of the  $(H_2O)_{4500}^+$  spectrum increase by a factor of two. This could suggest that the behaviour of the tissue under water bombardment is very similar to the standard samples, particularly DPPC and BTLE.

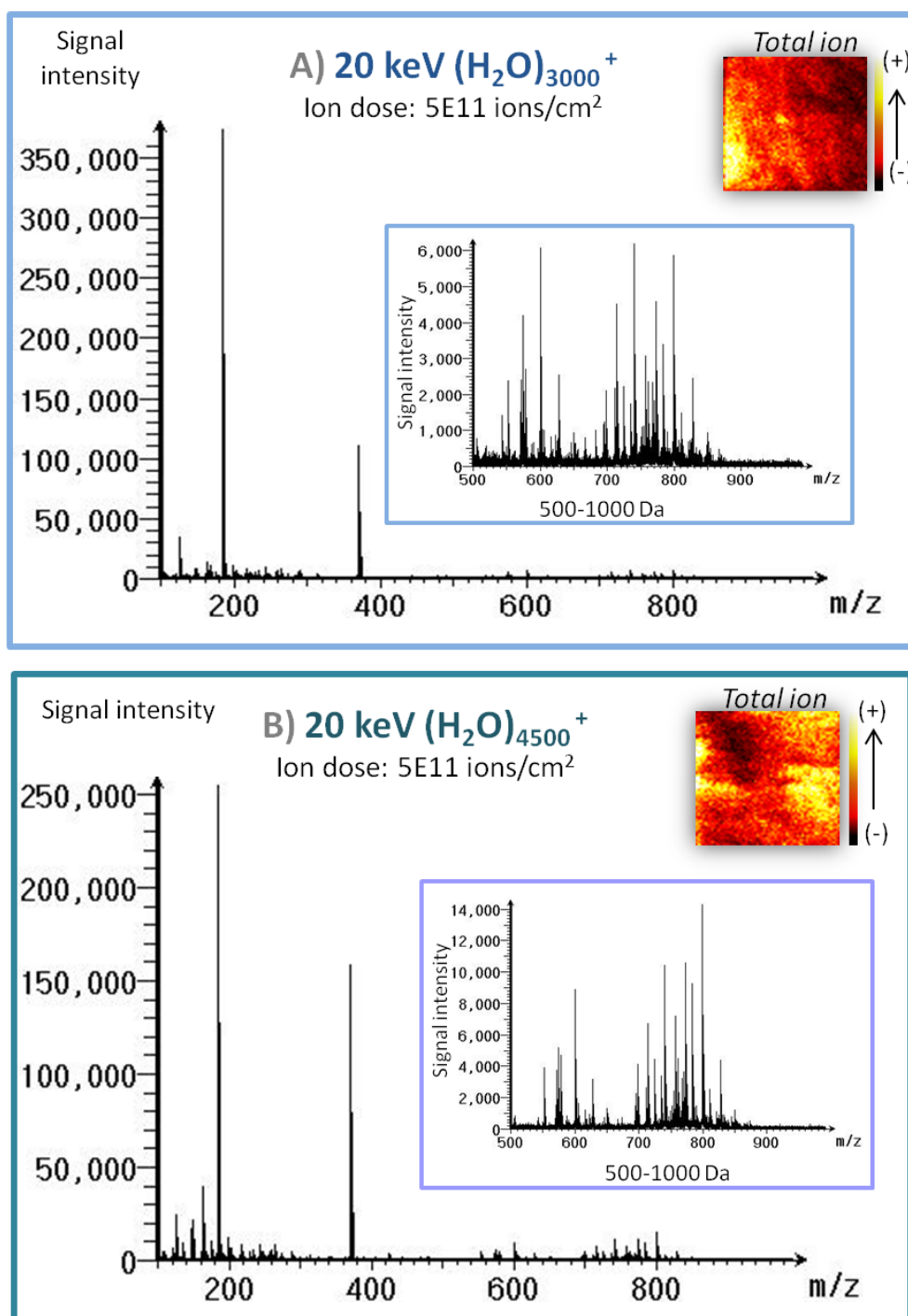


Figure 6.9: ToF-SIMS positive images of two different regions of the brain striatum using (A) 20 keV  $(\text{H}_2\text{O})_{3000}^+$  and (B) 20 keV  $(\text{H}_2\text{O})_{4500}^+$ . Both analysed were acquired over a  $650\ \mu\text{m}^2$  area with  $\sim 10\ \mu\text{m}$  of beam diameter.

As the energies per nucleon approach  $\sim 0.2$  eV, the water clusters will tend to ionise more of the lipids present in the tissue as  $[\text{M}+\text{H}]^+$  ions. In this experiment,  $(\text{H}_2\text{O})_{3000}^+$  possesses an  $E/\text{molecule}$  of  $\sim 6.6$  eV and  $E/\text{nucleon}$  of  $\sim 0.37$  eV;  $(\text{H}_2\text{O})_{4500}^+$  has an  $E/\text{molecule}$  of  $\sim 4.4$  eV and  $E/\text{nucleon}$  of  $\sim 0.24$  eV. Hence, the secondary ion signal

detected from the peaks located in  $m/z$  500-1000 region show higher secondary ion yields with 20 keV  $(\text{H}_2\text{O})_{4500}^+$  which has an energy per nucleon closer to 0.2 eV.

### 6.5.2.1 Dual beam approach

Another area of the brain striatum was analysed with a dual beam approach. This approach was carried out using the simultaneous application of semi continuous 20 keV  $\text{C}_{60}^+$  beam and a direct current 5 keV  $(\text{H}_2\text{O})_{3000}^+$  beam to the analysis area. The aim of this experiment was to exploit the spatial resolution provided by  $\text{C}_{60}^+$  clusters while using a defocused low energy water cluster ion beam to improve ionisation efficiency. The 20 keV  $\text{C}_{60}^+$  beam was used to probe the sample region ( $650 \times 650 \mu\text{m}^2$ ) and obtain an image, while a defocused direct current 5 keV  $(\text{H}_2\text{O})_{3000}^+$  beam bombarded the sample at the same time.

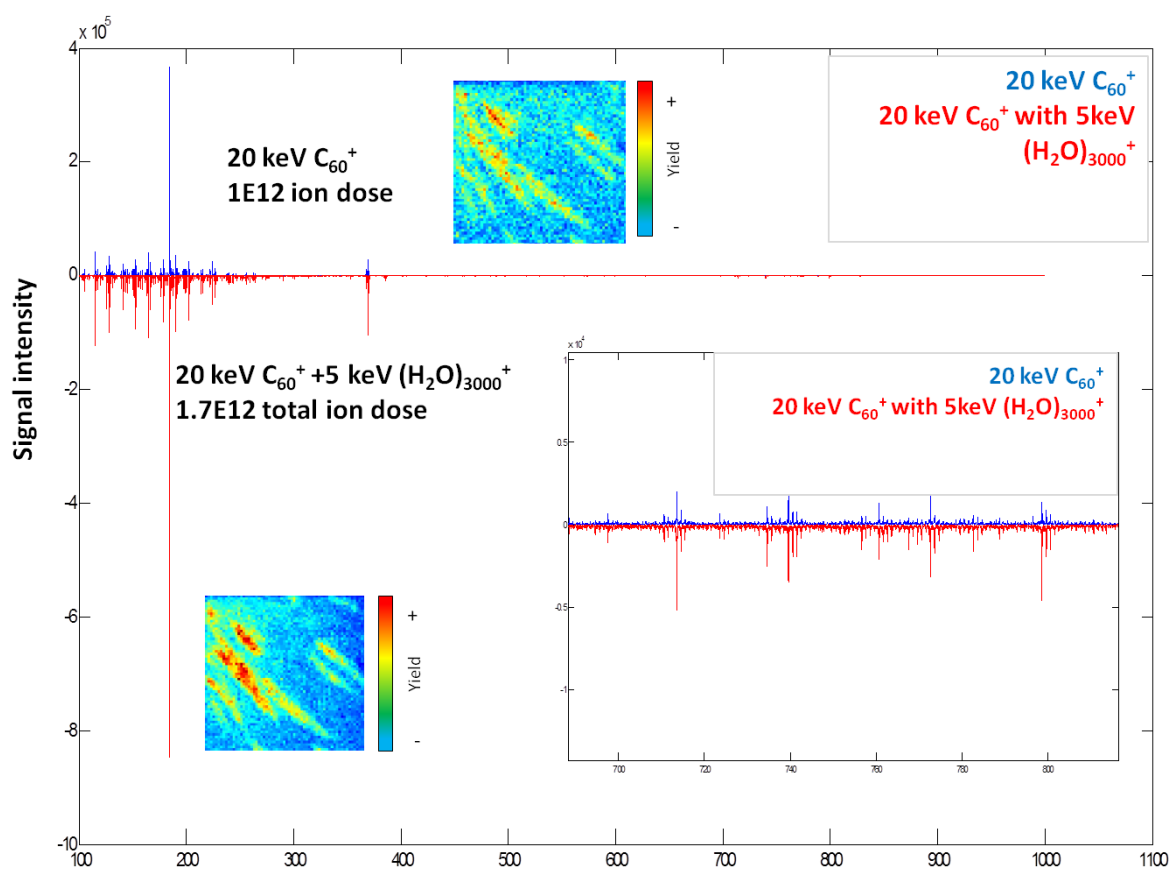


Figure 6.10: Total ion spectra comparison between the image acquired with 20 keV  $\text{C}_{60}^+$  only (top, blue line) and the image obtained from the same area with 20 keV  $\text{C}_{60}^+$  and 20 keV  $(\text{H}_2\text{O})_{3000}^+$  on dc simultaneously (bottom, red line). Total ion images are also displayed for comparison.

Figure 6.10 shows the total ion count (TIC) images and total ion spectra obtained first with 20 keV  $\text{C}_{60}^+$  only and then with the dual beam approach on the same analysis area.

The initial single beam analysis with 20 keV  $C_{60}^+$  was acquired with a primary ion dose of  $1 \times 10^{12}$  ions  $cm^{-2}$ . After this initial acquisition, a second image was obtained with 20 keV  $C_{60}^+$  and 5 keV  $(H_2O)_{3000}^+$ , with a combined ion dose of  $1.7 \times 10^{12}$  ions  $cm^{-2}$ .

From Figure 6.10, the secondary ion signal detected with  $C_{60}^+$  only (blue spectrum on the top) is significantly lower than the secondary ion signal obtained with the dual beam approach (red spectrum, bottom). It is clear that the combination of 5 keV  $(H_2O)_{3000}^+$  with 20 keV  $C_{60}^+$  enhances the total signal intensity, especially for ions such as cholesterol  $[M+H-H_2O]^+$  at  $m/z$  369 and phospholipid  $[M+H]^+$  ions e.g. GPCho 34:1  $m/z$  760 [1]. The signal enhancement was observed in all of the ion peaks from the mass spectrum and therefore, cannot be attributed to changes in the sample's chemistry as a function of depth [26].

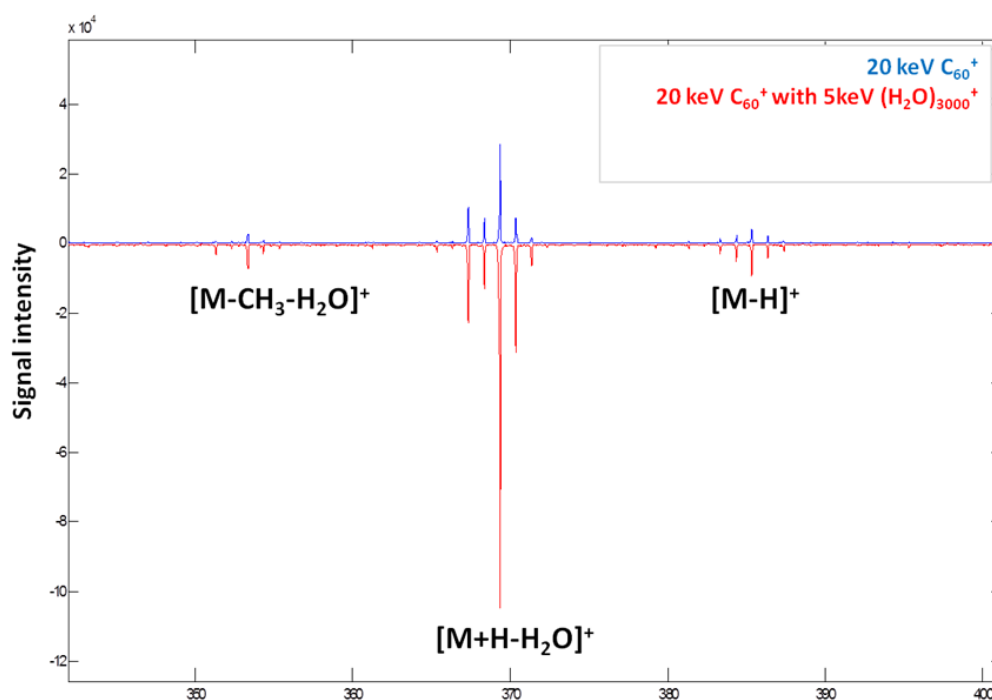


Figure 6.11: Cholesterol ion peak  $[M+H-H_2O]^+$  comparison between the image acquired with 20 keV  $C_{60}^+$  (top, blue line) and the image obtained from the same area with 20 keV  $C_{60}^+$  and 20 keV  $(H_2O)_{3000}^+$  on dc simultaneously (bottom, red line)[26].

To visualise the signal intensity of the ions derived from the cholesterol molecule, Figure 6.11 shows the comparison between spectra obtained in both experiments (single and dual beam). With both, single and dual beam experiments, three ions were derived from the cholesterol molecule.  $[M+H-H_2O]^+$  at  $m/z$  369,  $[M-H]^+$   $m/z$  386 and  $[M-$

$\text{CH}_3\text{-H}_2\text{O}^+$  at  $m/z$  353 [27] were detected; their signal intensities are increased by a factor of 3 - 4 when analysing with the dual beam method.

The results indicate that this dual beam approach could be used to enhance secondary the ion signal obtained from a biological sample, such as tissue. Currently, the main limitation is the lifetime of the water cluster ion source which is  $\sim 3\text{-}4$  hours for low-energy water clusters. This can limit the applicability of this approach to certain studies. For example, the analysis of a whole brain section could take significantly longer. For this reason, the water-doped argon clusters were tested for tissue imaging. The published journal paper containing the information and figures presented in this section is included in Appendix II.

### 6.5.3 Molecular imaging of the brain cerebellum with cluster ToF-SIMS

The effectiveness of water clusters in studying larger areas was assessed by analysing the cerebellar brain area. The cerebellum is the region of the brain responsible of basic functions like balance, movement, learning and cognition [28]. The cerebellum can be recognised because of its specific foliation pattern, as seen in Figure 6.12, (A).

The cerebellum is mainly composed of ten lobules (Figure 6.12, B) which comprise three main layers: the outer molecular layer, the intermediate Purkinje cell layer and the inner granular layer (Figure 6.12, C) [28].

In this set of experiments, complete cerebellum areas from serial sections were imaged with cluster ToF-SIMS to find the suitable experimental conditions using clusters of different size and nature.

The clusters 20 keV  $\text{C}_{60}^+$ ,  $\text{Ar}_{2000}^+$ ,  $(\text{H}_2\text{O})_{2000}^+$  and  $(\text{H}_2\text{O})_{4000}^+$  were used during these experiments. The resulting tiled images are presented in Table 6.1. The SIMS images presented in the table were acquired using a primary ion dose equivalent to  $1 \times 10^{12}$  ion  $\text{cm}^{-2}$ . The only exception is the  $(\text{H}_2\text{O})_{4000}^+$  image from the last column (Table 6.1) which was analysed under a primary ion fluence of  $2 \times 10^{12}$  ion  $\text{cm}^{-2}$ .

In Table 6.1, it is possible to observe the variation of ion counts per  $\mu\text{m}^2$  due to different primary ion analysis beam conditions. The ion counts per  $\mu\text{m}^2$  are extrapolated values to assess the level of signal that might be obtained from different cluster ion beams of the same current density (Table 6.1, first four columns) and an ion beam with more current density (Table 6.1, last column). The ion counts per  $\mu\text{m}^2$  are significantly higher when water clusters are used for analysis (Table 6.1, columns 3-5).



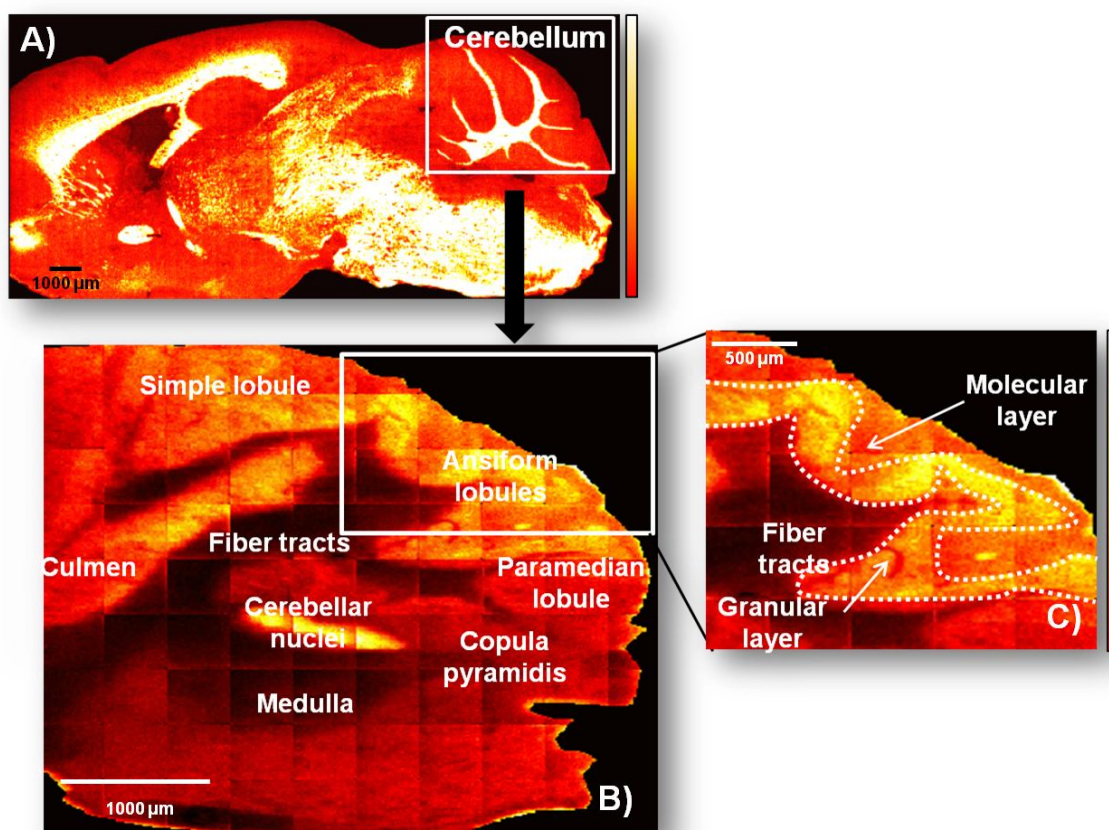


Figure 6.12: Total ion images of the mouse brain cerebellum acquired with 20 keV  $C_{60}^+$  and a mass range  $m/z$  100-1000. (A) Localisation of the cerebellum in a sagittal mouse brain section. (B) General anatomy and main regions within the cerebellar area. (C) Amplification of a small region of the anisform lobule to visualise the different cerebellum layers: the molecular layer; the granular layer; and the Purkinje layer (not shown), localised between the molecular and granular layers.

The first row of images in Table 6.1 was obtained using PCA to show the separation between grey and white matter tissue in the brain. As previously explained, a SIMS image contains multi-dimensional data that can be reduced with PCA (Figure 2.8). The resulting Principal Components (PCs) contain the relevant information of the data set. Imaging-PCA was applied to the images by selecting a Region-of-Interest (ROI) which only contained tissue and excluded the silicon substrate. This ROI was manually selected using MatLab® (The MathWorks Inc., Natick, Ma). Eight PCs were calculated with this approach; the spectral variance displayed with each PC was plotted as a score (contour plot) where pixels with similar chemistry are shown in the same colour. The score images from the first principal component (PC1) displayed the best separation between grey and white matter tissues in all experiments. These scores are included in the first row from Table 6.1.

Single ion images of the phospholipid GPCho C34:0  $[M+H]^+$  at  $m/z$  762, GPCho (38:4)  $[M+H]^+$  ion at  $m/z$  810 and the sphingolipid Ch24:1  $[M+H]^+$  at  $m/z$  826 are also illustrated in Table 6.1, rows 2-5. The  $C_{60}^+$  analysis displays just a few counts per  $\mu m^2$ , whereas the counts obtained with  $Ar_{2000}^+$  are 3 to 4 times higher when compared to  $C_{60}^+$ . Furthermore, the ion counts obtained with  $(H_2O)_{2000}^+$  are enhanced 2x when compared to  $Ar_{2000}^+$  and the ion count detected with  $(H_2O)_{4000}^+$  is three times higher when compared to argon. When a serial section is analysed with  $(H_2O)_{4000}^+$  and an increased primary ion dose ( $2 \times 10^{12}$  ions  $cm^{-2}$ ), the signal increased by a factor of 5 when compared to  $Ar_{2000}^+$ . This accumulation of secondary ions when applying more ions per  $cm^{-2}$  is possible when using a J105 instrument for analysis.

Single ion images showing the distribution of the cholesterol fragment  $[M-H_2O+H]^+$  is particularly interesting (Table 6.1, second row). This ion is observed across the white matter when the analysis is carried out with  $C_{60}^+$  or  $Ar_{2000}^+$ . However, under  $(H_2O)_n^+$  bombardment, this ion is also observed in the grey matter. This effect is especially visible when using larger water clusters i.e.  $(H_2O)_{4000}^+$ . The cholesterol molecule is a main component of myelin found in the white matter, but it also supports the cell membranes in the grey matter. Consequently, there is cholesterol that could be ionised in the grey matter [18], [29]–[31]. The cholesterol signal detected with  $(H_2O)_{4000}^+$  is 10 times higher than the signal recorded with  $C_{60}^+$  and 22 times higher when compared to  $Ar_{2000}^+$ . This result is particularly interesting since the analysis of BTLE showed similar cholesterol secondary ion yields with  $(H_2O)_{2000}^+$  and  $Ar_{2000}^+$  experiments.

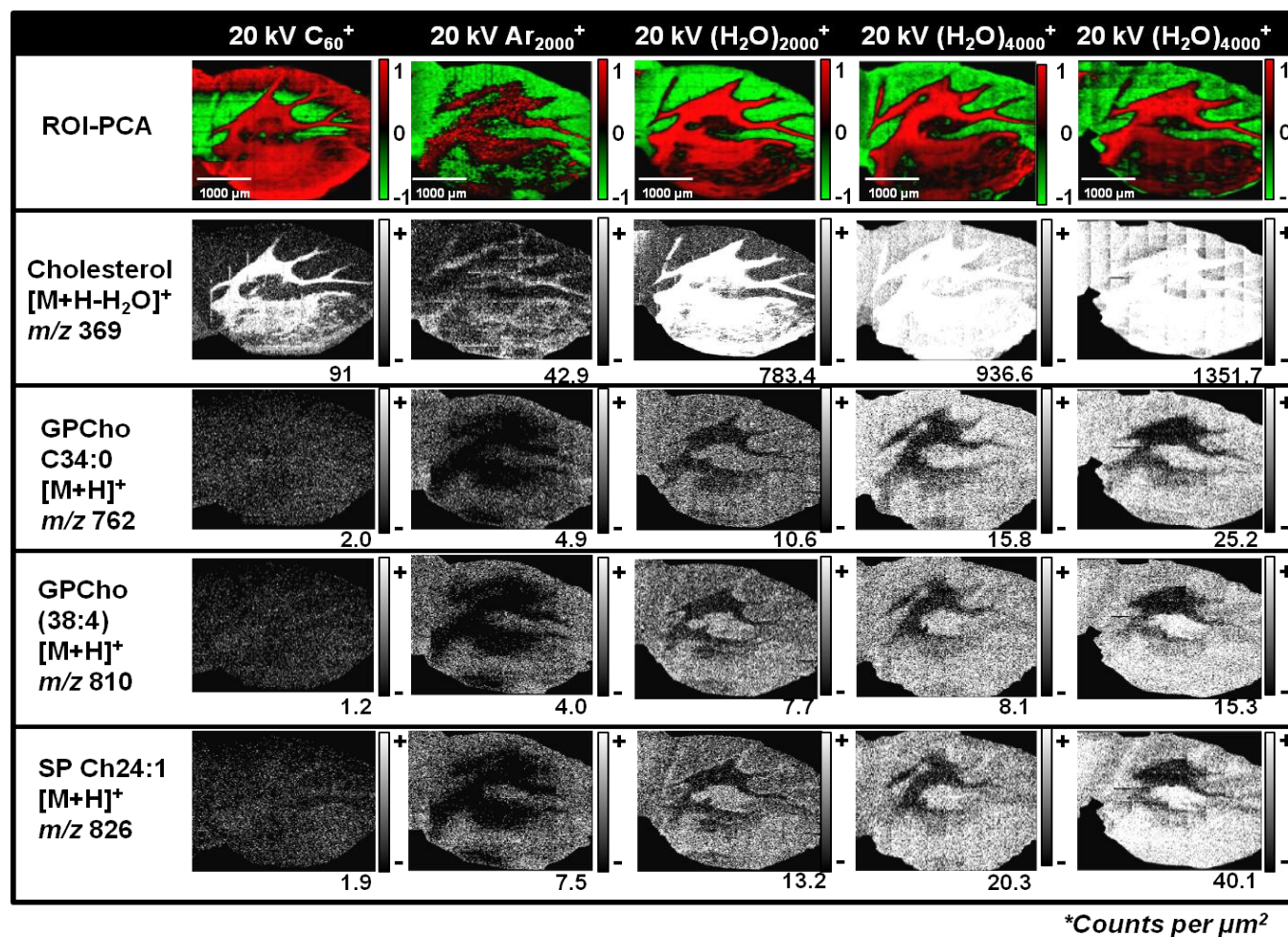


Table 6.1: ROI-PCA score images (top) showing the separation between grey and white matter tissue areas of the brain. The score from the first principal component (PC1) is shown for every experiment. Single ion images are also displayed for a cholesterol fragment, the phospholipid GPCho C34:0, a phosphorylethanolamine ion and the sphingolipid Ch24:1. All images were normalised to the total number of counts. The counts recorded per μm<sup>2</sup> are included under each image.



Total ion spectra obtained during  $(\text{H}_2\text{O})_{4000}^+$  and  $\text{Ar}_{2000}^+$  bombardment with  $1 \times 10^{12}$  ions  $\text{cm}^{-2}$  are compared in Figure 6.13. In both spectra, the phosphocholine ion at  $m/z$  184 is the base peak. The main difference is probably the total ion signal, which is enhanced by a factor of 5 with water cluster analysis. In the 500-1000 Da mass range, the signal obtained is 3 times higher than that obtained with argon.

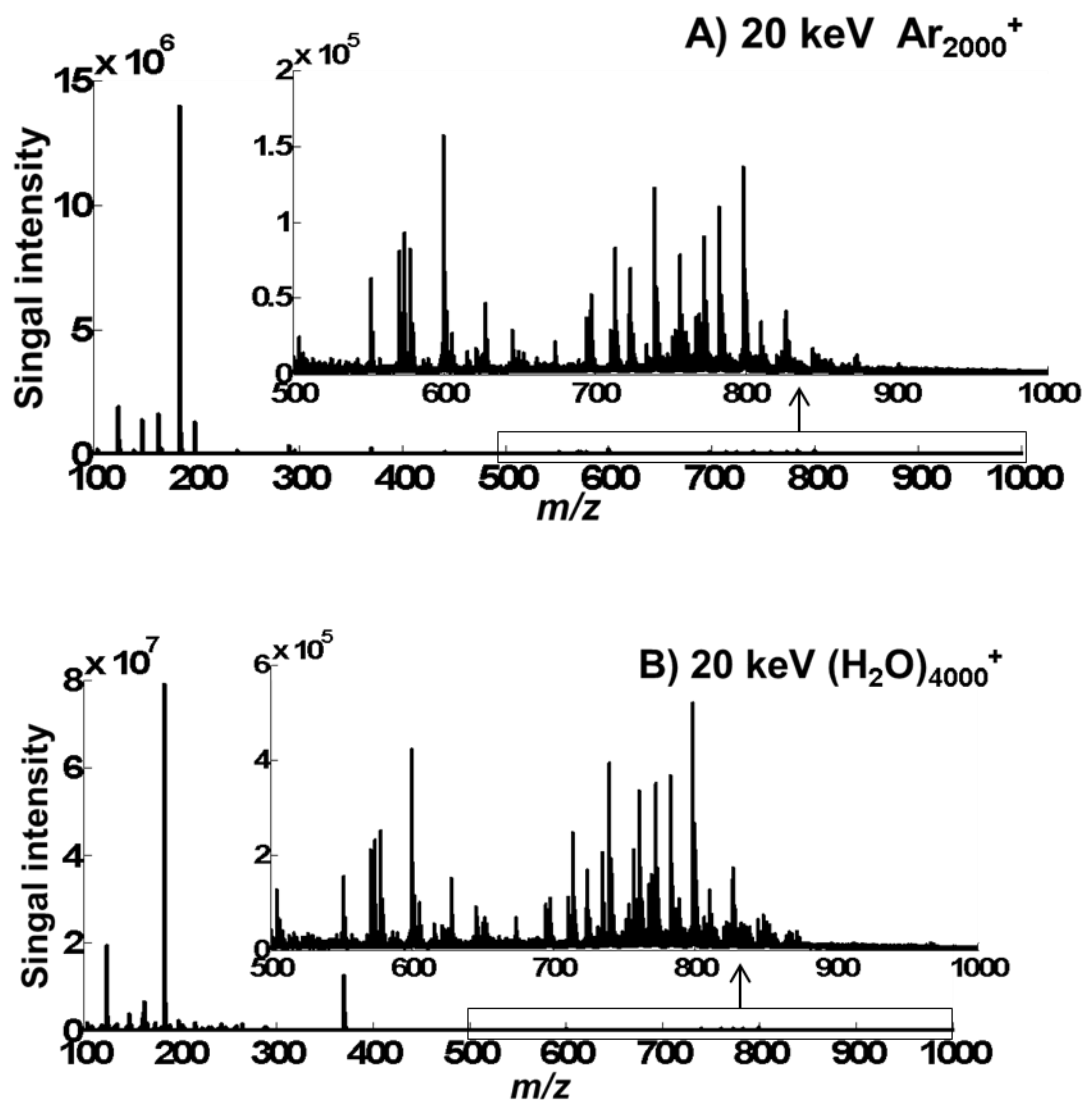


Figure 6.13: Total ion spectra from the tissue region (ROI), excluding the silicon substrate. (A) 20 keV  $\text{Ar}_{2000}^+$  spectrum and (B) 20 keV  $(\text{H}_2\text{O})_{4000}^+$  spectrum. Both experiments were run with  $1 \times 10^{12}$  ions  $\text{cm}^{-2}$  as the primary ion dose.

To visualise the spectral differences, the  $\text{Ar}_{2000}^+$  total ion spectrum was subtracted from the  $(\text{H}_2\text{O})_{4000}^+$  total ion spectrum. The resulting spectrum is displayed in Figure 6.14. This total ion spectrum demonstrates that secondary ion yield is enhanced in all ion peaks, and it is particularly intense for the cholesterol ion at  $m/z$  369.

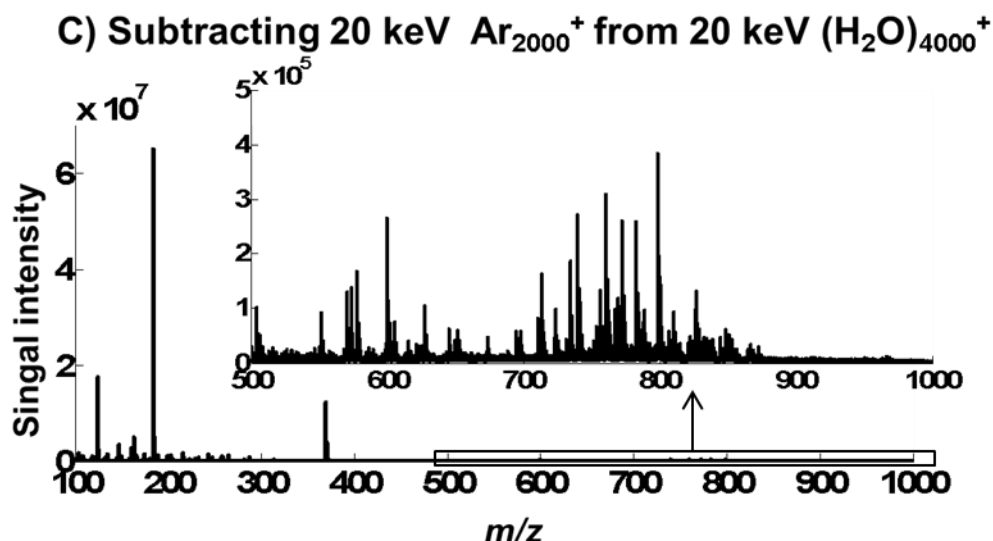


Figure 6.14: Spectrum derived from the subtraction of 20 keV  $\text{Ar}_{2000}^+$  from 20 keV  $(\text{H}_2\text{O})_{4000}^+$ . The total ion spectra used in the subtraction were obtained from the ROI of tissue area to exclude interference peaks from the substrate.

#### 6.5.4 Cluster ToF-SIMS imaging studies on the brain cerebellum with using 20 keV $\text{C}_{60}^+$ , $\text{Ar}_{2000}^+$ , $(\text{H}_2\text{O})\text{Ar}_{2000}^+$ and $(\text{H}_2\text{O})_{6000}^+$

A second study of the brain cerebellum was carried out to expand the application of water-containing beams to brain tissue imaging, in particular into the use of water doped argon cluster beams. For this set of experiments, images from the brain cerebellum were acquired with 20 keV  $\text{C}_{60}^+$ , 20 keV  $\text{Ar}_{2000}^+$ , 20 keV  $(\text{H}_2\text{O})_{6000}^+$  and 20 keV  $(\text{H}_2\text{O})\text{Ar}_{2000}^+$ . The cluster primary ion beams were selected according to the results obtained with the standard biomolecules and previous brain images (sections 6.4.1 and 6.4.2). The beam diameters were optimised to obtain the best possible spatial resolution: 3  $\mu\text{m}$  with  $\text{C}_{60}^+$ , 13  $\mu\text{m}$  with  $\text{Ar}_{2000}^+$ , 9  $\mu\text{m}$  with  $(\text{H}_2\text{O})_{6000}^+$  and 11  $\mu\text{m}$  with  $(\text{H}_2\text{O})\text{Ar}_{2000}^+$ .

The total ion images and total ion spectra from all four experiments are displayed in Figure 6.15. The images and spectra correspond only to the brain tissue, excluding the silicon substrate to avoid peak interference.

It is possible to observe that although 20 keV  $\text{C}_{60}^+$  (Figure 6.15, A) produces the highest total ion signal, it also generates the lowest signal intensity for the secondary ion peaks in the mass range  $m/z$  500-1000. The use of 20 keV  $(\text{H}_2\text{O})_{6000}^+$  (Figure 6.15, D) yields the highest secondary ion yield for this mass range, followed by 20 keV  $(\text{H}_2\text{O})\text{Ar}_{2000}^+$  (Figure 6.15, C) and 20 keV  $\text{Ar}_{2000}^+$  (Figure 6.15, B).

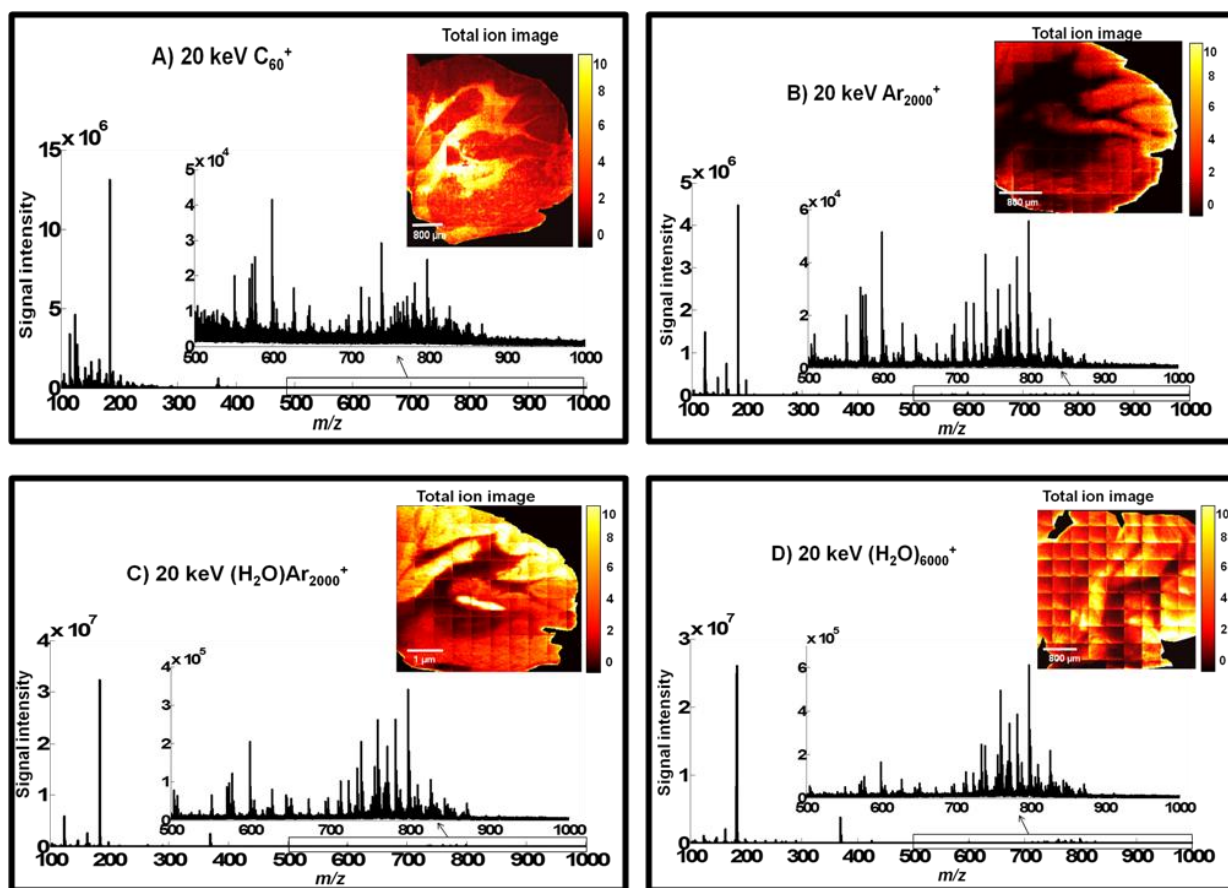


Figure 6.15: Total ion count (TIC) images and total ion spectra acquired from the cerebellar area of serial sagittal mouse brain sections. The primary ion dose applied was  $1 \times 10^{12}$  ions  $\text{cm}^{-2}$ . The cluster primary ion beams used are: (A) 20 keV  $\text{C}_{60}^+$ , (B) 20 keV  $\text{Ar}_{2000}^+$ , (C) 20 keV  $(\text{H}_2\text{O})\text{Ar}_{2000}^+$  and (D) 20 keV  $(\text{H}_2\text{O})_{6000}^+$ .

White matter and grey matter tissues were identified in each image using ROI-PCA to evaluate the detection of different lipids. This enabled the semi-quantitative analysis and characterisation of the ion peaks obtained from each type of tissue.

Figure 6.16 shows the score images from the ROI-PCA analysis on the four images. The scores displayed demonstrated the clearest distinction between grey and white matter. Prior to PCA analysis, all images were normalised to the total number of ion counts. The score images are composed of green or red pixels, according to the chemical similarity of the spectra. The PCs that drew the clearest distinction between grey and white matter were: PC1 for  $\text{C}_{60}^+$ , PC2 and PC3 for  $\text{Ar}_{2000}^+$  and  $(\text{H}_2\text{O})_{6000}^+$ , and PC5 for  $(\text{H}_2\text{O})\text{Ar}_{2000}^+$  analysis.

The cerebellum anatomy consists of grey and white matter tissues with a central core. Distinctive features such as the foliation pattern and the lobules can be seen in the score images (Figure 6.16). Medulla and pons regions are located below the cerebellum

nuclei and can also be visualised in each score. In addition, the fiber tracts located between the cerebellum and medulla can also be seen (as illustrated in Figure 6.12).

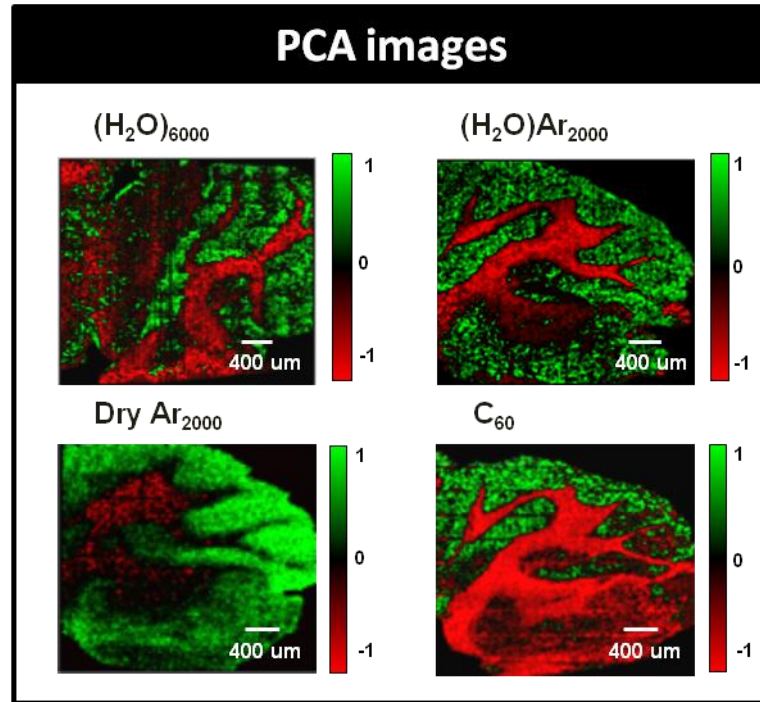


Figure 6.16: Score images generated with ROI-PCA applied to the normalised TIC images of the brain cerebellum. The images were normalised to the total ion counts prior to PCA analysis. (A) 20 keV (H<sub>2</sub>O)<sub>6000</sub><sup>+</sup> score image, (B) 20 keV (H<sub>2</sub>O)Ar<sub>2000</sub><sup>+</sup> score image, (C) 20 keV Ar<sub>2000</sub><sup>+</sup> score image and (D) 20 keV C<sub>60</sub><sup>+</sup>. These images show the grey and white matter areas in green and red, respectively.

The anatomical features visible in these images of the cerebellum indicate that all the serial sections were taken in a close proximity to the brain's midline (see Figure 6.17) [28].

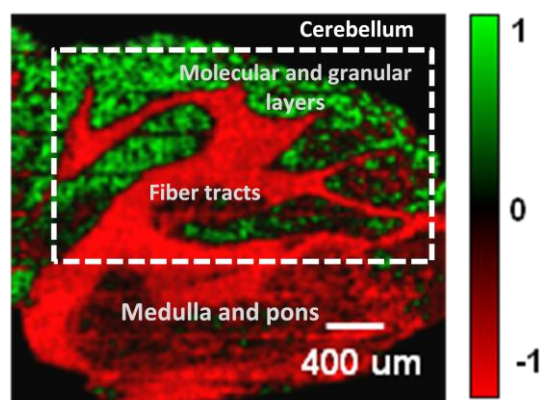


Figure 6.17: Anatomical features observed in the score image obtained from the 20 keV C<sub>60</sub><sup>+</sup> image on the cerebellar area.

Each score has a corresponding loading which contains the ion peaks plotted as positive or negative values, according to their chemical similarities. Positive loadings are visualised as green pixels in scores whereas negative loadings are represented by red pixels.

As expected, the loading plots corresponding to the score images previously displayed, showed that one of the main differences between the two tissue types is the presence of the cholesterol fragment  $[M-H_2O+H]^+$ . Counts for this fragment are mostly associated with the white matter.

Figure 6.18 presents the loading plot that matches the score image of the  $(H_2O)_{6000}^+$  experiment. One of the main features of the white matter (red pixels in the score image) is the presence of the cholesterol fragment  $[M-H_2O+H]^+$  at  $m/z$  369. The same result was observed in loadings from all experiments.

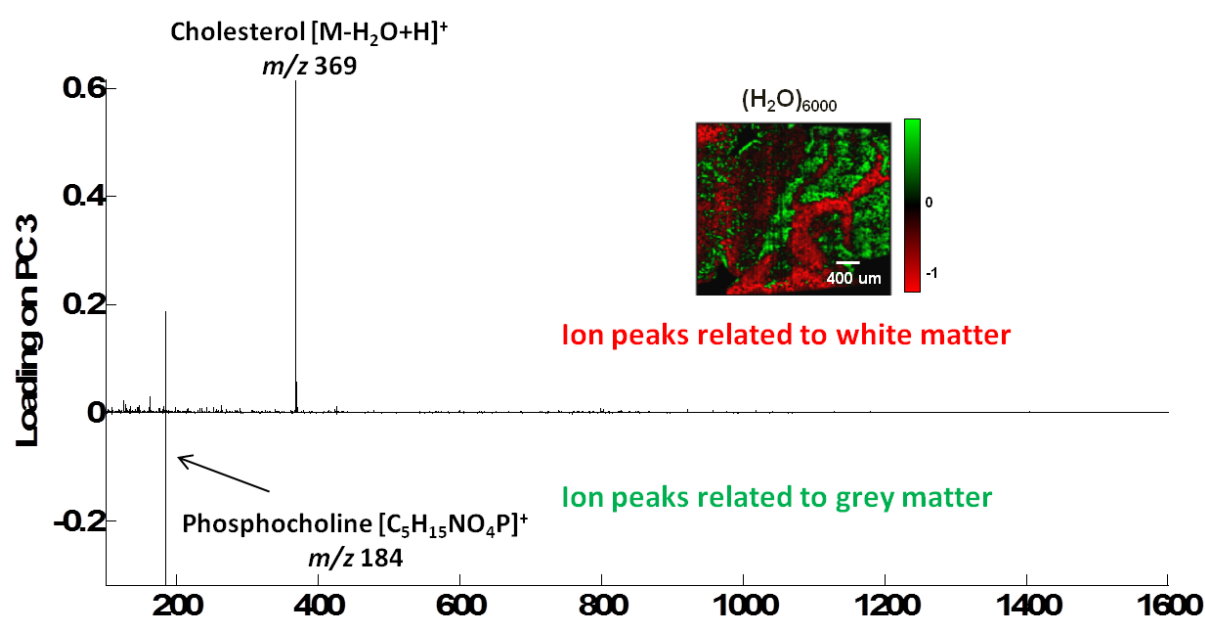


Figure 6.18: Loading plot corresponding to the image score obtained from the ROI-PCA analysis on the image analysed with 20 keV  $(H_2O)_{6000}^+$ . This loading was calculated for the 3<sup>rd</sup> principal component (PC3).

Under  $Ar_{2000}^+$  and  $C_{60}^+$  bombardment, there were less counts for the cholesterol ion  $[M-H_2O+H]^+$  in the grey matter. Contrastingly, the signal detected under water-containing cluster bombardment is considerably higher. The presence of cholesterol in brain sections has been studied by different groups [15], [16], [32]–[34]. It has been proven that cholesterol molecules migrate to the surface of the brain tissue under vacuum conditions when the analysis is performed at room temperature [16]. Another study

showed that cholesterol signal decays significantly during depth profiling of mouse brain tissue at room temperature [35]. This effect was avoided by analysing the brain sample in a frozen-hydrated state at cryogenic temperatures ( $-100^{\circ}\text{C}$ ). Under these conditions, the cholesterol signal did not decrease as dramatically as a function of depth, although signal decay was observed for other lipids [35].

Another recent study involved the exposure of brain tissue sections to *trifluoroacetic acid* (TFA), removing cholesterol from the tissue's surface. Moreover, crystalline structures attributed to the features of myelin sheath were removed after TFA exposure. The removal of cholesterol by chemical pre-treatment favoured the detection of other intact lipids [36]. This study included images acquired on the cerebellar area, demonstrating that TFA treatment was especially effective in the white matter, particularly in the granular and molecular layers.

The score images generated with ROI-PCA were used to localise separated areas corresponding to white or grey matter. The spectra acquired with  $\text{Ar}_{2000}^{+}$ ,  $(\text{H}_2\text{O})\text{Ar}_{2000}^{+}$  and  $(\text{H}_2\text{O})_{6000}^{+}$  from both matters were overlaid and compared. The summed spectra from each region selected covered a total area of  $400\text{ }\mu\text{m} \times 800\text{ }\mu\text{m}$  to allow qualitative and semi-quantitative comparisons.

Figure 6.19 presents the two spectra sets (white matter and grey matter regions). Intact lipids of different classes are detected in both regions of the brain, with more counts coming from the grey matter. The mass range displayed includes  $m/z$  500 to  $m/z$  900, and  $m/z$  369 separately. Figure 6.19 highlights the signal enhancement produced by with  $(\text{H}_2\text{O})_{6000}^{+}$  or  $(\text{H}_2\text{O})\text{Ar}_{2000}^{+}$  analysis, over  $\text{Ar}_{2000}^{+}$ . Some of the identified lipid peaks were labelled: black labels correspond to those ion peaks detected in both tissue areas, ions with red labels were only found in white matter and peaks labelled in blue refer to lipids detected in grey matter only. Total ion spectra collected with  $\text{C}_{60}^{+}$  clusters were excluded from this comparison due to the low secondary ion signal generated with this primary ion beam.

The signal intensity of the cholesterol fragment,  $[\text{M}-\text{H}_2\text{O}+\text{H}]^{+}$ , is also compared in Figure 6.19. Under  $\text{Ar}_{2000}^{+}$  bombardment, this ion is mainly detected in the white matter.

Cholesterol is detected with similar intensities in both grey and white matter when  $(\text{H}_2\text{O})_{6000}^{+}$  and  $(\text{H}_2\text{O})\text{Ar}_{2000}^{+}$  beams are used. In the white matter, the signal intensity produced by water containing clusters is increased by a factor of  $\sim 20$  when compared to signals produced using an argon beam.

Previous SIMS imaging experiments performed on mouse brain tissue sections have demonstrated that cholesterol is mainly detected in the white matter [37], [38]. However, according to the brain's chemical composition [17], [18], it is expected that cholesterol would be present in the grey matter since it is ~ 22% of its dry weight (Table 2.2). The results obtained with water-containing ion beams confirm the presence of cholesterol in both tissue types.

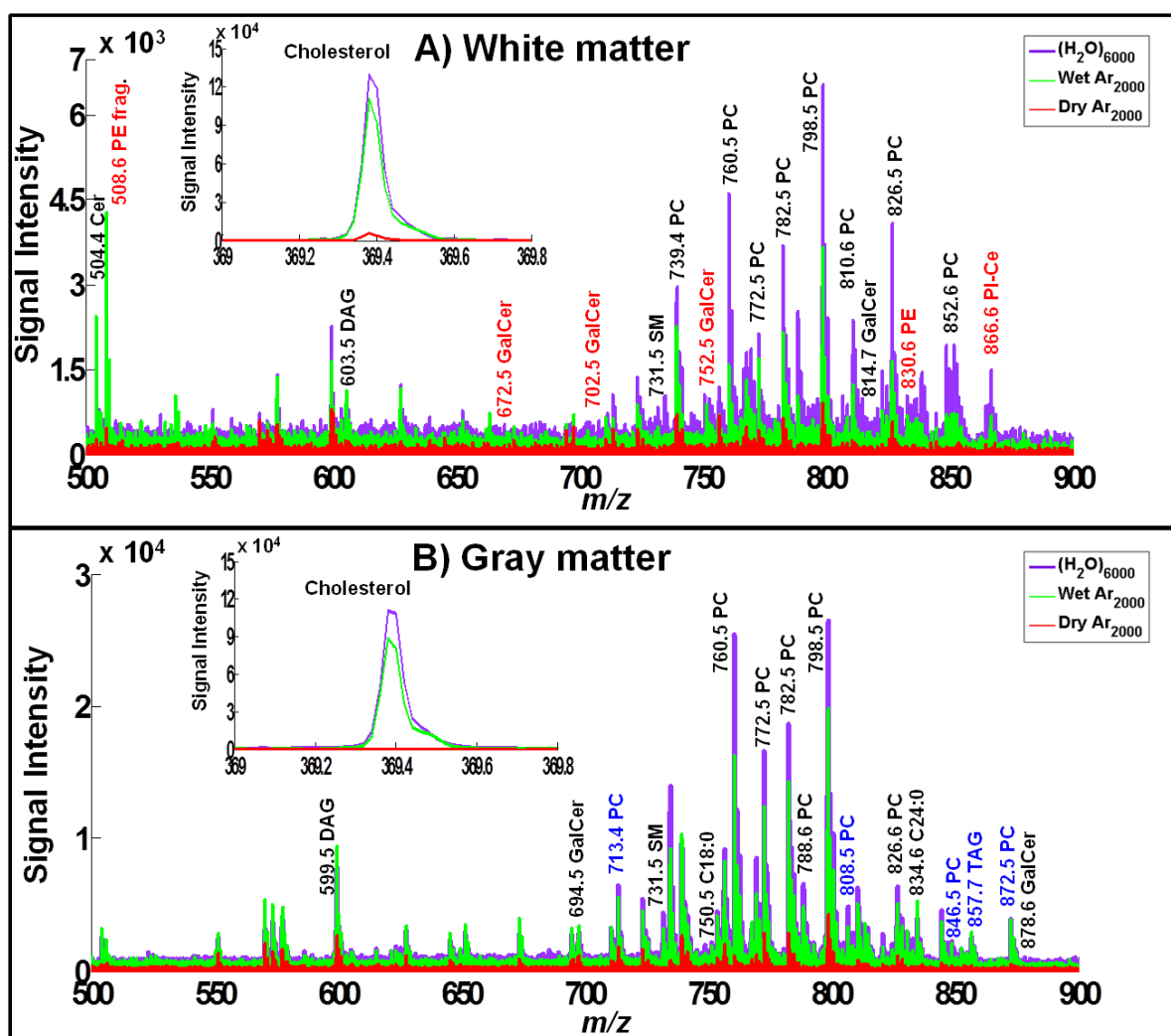


Figure 6.19: Overlaid spectra from images obtained with 20 keV  $(\text{H}_2\text{O})_{6000}^+$  (purple line),  $(\text{H}_2\text{O})\text{Ar}_{2000}^+$  (green line) and  $\text{Ar}_{2000}^+$  (red line). White matter (A) and grey matter (B) regions were identified according to the PCA analysis. The mass ranges included are 500-900 Da and 369-370 Da for intact lipid detection and cholesterol detection, respectively. Data collected with 20 keV  $\text{C}_{60}^+$  is not included due to the low secondary ion signal obtained. Some lipid ion peaks have been labelled as a reference for each region. Black labels refer to ion peaks observed in both brain regions, ion peaks with red labels were observed only in the white matter region and lipids with blue labels were only detected in the grey matter.

Ion suppression/enhancement effects may be the cause of the increase in cholesterol signal intensity with  $(\text{H}_2\text{O})_{6000}^+$  and  $(\text{H}_2\text{O})\text{Ar}_{2000}^+$  beams relative to the yield observed with  $\text{Ar}_{2000}$ .

Both tissue types are comprised of phospholipids and cholesterol. Published studies have shown the ionisation suppression effect of molecules caused by the presence of phospholipids with diverse spectrometric techniques [41], [43]. Furthermore, the formation of phospholipid  $[\text{M}+\text{H}]^+$  ions is favoured when cholesterol is present [44]. Thus, the behaviour observed for the cholesterol fragment ion could be related to the different proton affinities of cholesterol and phospholipids.

The proton affinity would cause an ion suppression effect which reflects on the high ionisation of phospholipids and poor ionisation of cholesterol in the grey matter when using  $\text{Ar}_{2000}^+$  for analysis.

Grey matter is composed of phospholipids (60-70%) and cholesterol (22%). With water-containing cluster beams, there are more protons available due to the presence of hydrogen and OH groups. A greater number of available protons could lead to a competition amongst cholesterol and other lipids, e.g. phospholipids, in the grey matter for protonation. This matrix effect was studied further with another series of experiments involving the analysis of lipid standard mixtures (Section 6.5.5).

During  $(\text{H}_2\text{O})\text{Ar}_{2000}^+$  and  $(\text{H}_2\text{O})_{6000}^+$  bombardment, the ion suppression effect on cholesterol seems to be reduced. Single ion images of cholesterol distribution are displayed in Figure 6.20 (A) and (B). The image acquired with  $(\text{H}_2\text{O})\text{Ar}_{2000}^+$  (A), shows the localisation of cholesterol across the whole tissue and its signal is more intense in the white matter. Data acquired with  $(\text{H}_2\text{O})_{6000}^+$  displayed in Figure 6.20 (B), demonstrates an evident distribution of cholesterol in grey matter and a more intense signal from this ion in white matter.

From these results, we can conclude that the low detection of the cholesterol  $[\text{M}-\text{H}_2\text{O}+\text{H}]^+$  ion in the grey matter can be a consequence of a matrix effect when using  $\text{C}_{60}^+$  and  $\text{Ar}_{2000}^+$  for analysis. Moreover, this ion suppression effect is less evident when  $(\text{H}_2\text{O})\text{Ar}_{2000}^+$  or  $(\text{H}_2\text{O})_{6000}^+$  are employed for image acquisition. When looking at the cholesterol signal intensity relative to other lipid peaks, this matrix effect does not seem to be affecting the white matter.

From our results, we can consider that there are two matrix effects occurring in each tissue type: first, cholesterol is suppressed by phospholipids in the grey matter and this



effect could be mediated by the proton affinity of cholesterol and phospholipids. In the white matter, cholesterol might be suppressing the ionisation of phospholipids which might be due to the anatomical structure found in myelin (Figure 6.4) where the spatial distribution of cholesterol molecules is different.

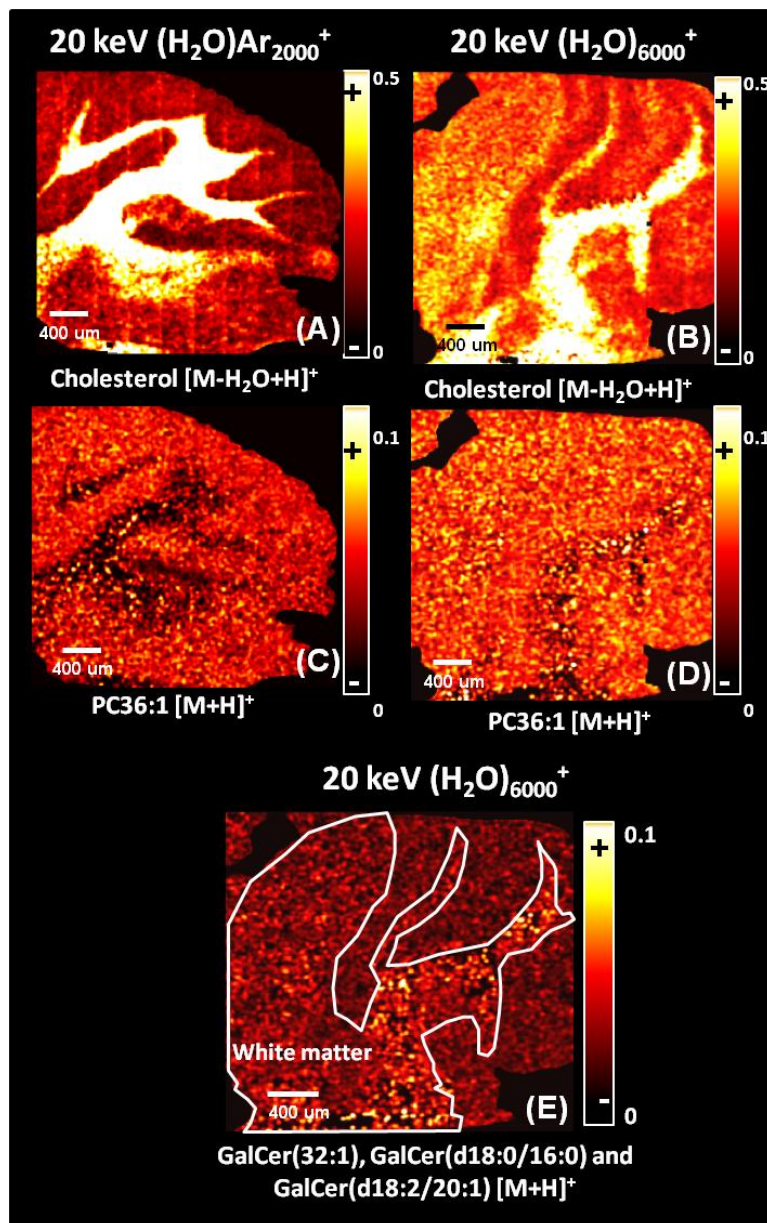


Figure 6.20: Single ion images from different lipids obtained from the tissue area (ROI). The total ion images were normalised to the total number of counts before generating the single ion images. Image showing the localisation of cholesterol  $[M-H_2O+H]^+$  at  $m/z$  369 with (A)  $(H_2O)Ar_{2000}$  and (B)  $(H_2O)_{6000}$ . Single ion image of the lipid PC36:1  $[M+H]^+$  at  $m/z$  788.6 obtained with (C)  $(H_2O)Ar_{2000}$  and (D)  $(H_2O)_{6000}$ . Image (E) displays the distribution of the glycosphingolipids GalCer(32:1  $[M+H]^+$  at  $m/z$  672.5, GalCer(d18:0/16:0)  $[M+H]^+$  at  $m/z$  702.5 and GalCer(d18:2/20:1)  $[M+H]^+$  at  $m/z$  752.5 with  $(H_2O)_{6000}$ . The white line was drawn to highlight the location of the white matter.

Some lipid ion peaks selected from the overlaid spectra (Figure 6.19) produced using different beams are compared in Table 6.2.

Lipid class	m/z	Assignment	Formula	White matter – signal ratio		Grey matter – signal ratio	
				(H <sub>2</sub> O)Ar <sub>2000</sub> /Ar <sub>2000</sub>	(H <sub>2</sub> O) <sub>6000</sub> /Ar <sub>2000</sub>	(H <sub>2</sub> O)Ar <sub>2000</sub> /Ar <sub>2000</sub>	(H <sub>2</sub> O) <sub>6000</sub> /Ar <sub>2000</sub>
<b>Sterol Lipids</b>	369.3	Chol. [M+H-H <sub>2</sub> O] <sup>+</sup>	C <sub>27</sub> H <sub>45</sub>	16.6	22.4	105.8	199.6
<b>Glycerophospholipids</b>	713.4	PC(32:0) [M+K-N(CH <sub>3</sub> ) <sub>3</sub> ] <sup>+</sup>	C <sub>37</sub> H <sub>71</sub> O <sub>8</sub> PK	ND	ND	2.7	4.6
	739.4	PC(34:1) [M+K-N(CH <sub>3</sub> ) <sub>3</sub> ] <sup>+</sup>	C <sub>39</sub> H <sub>73</sub> O <sub>8</sub> PK	2.8	6.3	2.8	5.3
	760.5	PC(34:1) [M+H] <sup>+</sup>	C <sub>42</sub> H <sub>82</sub> NO <sub>8</sub> PH	8.2	26.1	10.5	19.9
	772.5	PC(32:0) [M+K] <sup>+</sup>	C <sub>40</sub> H <sub>80</sub> NO <sub>8</sub> PK	3.7	9.8	4	8.1
	782.5	PC(34:1) [M+Na] <sup>+</sup>	C <sub>42</sub> H <sub>82</sub> NO <sub>8</sub> PNa	4.8	8.4	2.9	6.1
	788.6	PC(36:1) [M+H] <sup>+</sup>	C <sub>44</sub> H <sub>86</sub> NO <sub>8</sub> PH	8.5	19.1	8	19.4
	798.5	PC(34:1) [M+K] <sup>+</sup>	C <sub>42</sub> H <sub>82</sub> NO <sub>8</sub> PK	4	13.8	3.5	7.3
	808.5	PC(38:5) [M+H] <sup>+</sup>	C <sub>46</sub> H <sub>82</sub> NO <sub>8</sub> PH	(H <sub>2</sub> O) only	(H <sub>2</sub> O) only	5.8	10.4
	810.6	PC(36:1) [M+Na] <sup>+</sup>	C <sub>44</sub> H <sub>86</sub> NO <sub>8</sub> PNa	(H <sub>2</sub> O) only	(H <sub>2</sub> O) only	4.2	9.5
	826.5	PC(36:1) [M+K] <sup>+</sup>	C <sub>44</sub> H <sub>86</sub> NO <sub>8</sub> PK	4.5	13.2	4.1	10.4
	830.6	PE(42:1) [M+H] <sup>+</sup>	C <sub>47</sub> H <sub>92</sub> NO <sub>8</sub> PH	11.5	22.3	ND	ND
	846.5	PC(38:5) [M+K] <sup>+</sup>	C <sub>46</sub> H <sub>82</sub> NO <sub>8</sub> PK	(H <sub>2</sub> O) only	(H <sub>2</sub> O) only	ND	ND
	852.6	PC(41:4) [M+H] <sup>+</sup>	C <sub>49</sub> H <sub>90</sub> NO <sub>8</sub> PH	(H <sub>2</sub> O) only	(H <sub>2</sub> O) only	(H <sub>2</sub> O) only	(H <sub>2</sub> O) only
	866.6	PI-Cer(40:0) [M+H] <sup>+</sup>	C <sub>46</sub> H <sub>92</sub> NO <sub>11</sub> PH	(H <sub>2</sub> O) only	(H <sub>2</sub> O) only	ND	ND
	872.5	PC(18:0/22:6) [M+K] <sup>+</sup>	C <sub>48</sub> H <sub>84</sub> NO <sub>8</sub> PK	ND	ND	5	13
<b>Glycerolipids</b>	599.5	DAG(36:4) [M-OH] <sup>+</sup>	C <sub>39</sub> H <sub>67</sub> O <sub>4</sub>	3.6	7.9	2.7	2.5
	603.5	DAG(36:2) [M-OH] <sup>+</sup>	C <sub>39</sub> H <sub>71</sub> O <sub>4</sub>	(H <sub>2</sub> O) only	(H <sub>2</sub> O) only	(H <sub>2</sub> O) only	(H <sub>2</sub> O) only
	857.7	TAG(50:0) [M+Na] <sup>+</sup>	C <sub>53</sub> H <sub>102</sub> O <sub>6</sub> Na	(H <sub>2</sub> O) only	(H <sub>2</sub> O) only	5.8	16.9
<b>Sphingolipids</b>	672.5	GalCer(32:1) [M+H] <sup>+</sup>	C <sub>38</sub> H <sub>73</sub> NO <sub>8</sub> H	(H <sub>2</sub> O) only	(H <sub>2</sub> O) only	ND	ND
	694.5	GalCer(32:1) [M+Na] <sup>+</sup>	C <sub>38</sub> H <sub>73</sub> NO <sub>8</sub> Na	4.5	9.9	3.2	7.8
	702.5	GalCer(d18:0/16:0) [M+H] <sup>+</sup>	C <sub>40</sub> H <sub>79</sub> NO <sub>8</sub> H	(H <sub>2</sub> O) only	(H <sub>2</sub> O) only	ND	ND
	731.6	SM(36:1) [M+H] <sup>+</sup>	C <sub>41</sub> H <sub>83</sub> N <sub>2</sub> O <sub>6</sub> PH	(H <sub>2</sub> O) only	(H <sub>2</sub> O) only	(H <sub>2</sub> O) only	(H <sub>2</sub> O) only
	752.6	GalCer(d18:2/20:1) [M+H] <sup>+</sup>	C <sub>44</sub> H <sub>81</sub> NO <sub>8</sub> H	(H <sub>2</sub> O) only	(H <sub>2</sub> O) only	ND	ND
	814.7	GalCer(d18:0/24:0) [M+H] <sup>+</sup>	C <sub>48</sub> H <sub>95</sub> NO <sub>8</sub> H	(H <sub>2</sub> O) only	(H <sub>2</sub> O) only	3.4	8.7
	834.6	C24:0 [M+Na] <sup>+</sup>	C <sub>48</sub> H <sub>93</sub> NO <sub>8</sub> Na	(H <sub>2</sub> O) only	(H <sub>2</sub> O) only	(H <sub>2</sub> O) only	(H <sub>2</sub> O) only
	866.6	PI-Cer(40:0) [M+H] <sup>+</sup>	C <sub>46</sub> H <sub>92</sub> NO <sub>11</sub> PH	(H <sub>2</sub> O) only	(H <sub>2</sub> O) only	ND	ND

Table 6.2: Lipid ion peaks observed in the spectra from white matter and grey matter (Figure 6.19). Peak assignments were obtained using references [1], [36], [38] and were based on measurements with 10 ppm of precision. Columns on the right show the ratios result from the comparison of secondary ion yields between water-containing clusters and Ar<sub>2000</sub>. '(H<sub>2</sub>O) only' refers to peaks only detected with water-containing clusters such as (H<sub>2</sub>O)Ar<sub>2000</sub> and (H<sub>2</sub>O)<sub>6000</sub>; 'ND' refers to not- observed ion peaks. Lipid abbreviations included are: PE-Phosphatidylethanolamine, PC-Phosphatidylcholine, PI-Phosphatidylinositol, GalCer-Galactosylceramide, SM-Sphingomyelin, DAG-Diacylglyceride, TAG-Triacylglyceride, Cer-Ceramide and Chol-Cholesterol (Chol).

The secondary ion signal of peaks obtained with  $(\text{H}_2\text{O})\text{Ar}_{2000}^+$  and  $(\text{H}_2\text{O})_{6000}^+$  were compared to  $\text{Ar}_{2000}^+$ , and peak ratios were calculated. The detection of different lipid species was enhanced during  $(\text{H}_2\text{O})\text{Ar}_{2000}^+$  and  $(\text{H}_2\text{O})_{6000}^+$  bombardment. It is also possible to see that many ion species are not detected under  $\text{Ar}_{2000}^+$  or  $\text{C}_{60}^+$  analysis. Table 6.2 includes different ion species that were only detected with water-containing cluster ion beams. For example, most glycosphingolipids such as galactosylceramides and sphingomyelin were only detected with  $(\text{H}_2\text{O})\text{Ar}_{2000}^+$  and  $(\text{H}_2\text{O})_{6000}^+$ .

The total ion spectra obtained from the images are very complex (Figure 6.15). An extended list of lipid ion peaks observed in the total ion spectra is presented in Table 6.3. However, it is possible to observe that lipids found in the white matter in the mass range  $m/z$  500 - 900 are 2 to 4 times lower in intensity when compared to the grey matter intensities. The signal ratios included in Table 6.2 present a semi-quantitative analysis of the degree to which some lipid ions are enhanced by water-containing cluster ion beams. The detection of  $[\text{M}+\text{H}]^+$  lipid ions observed with  $\text{Ar}_{2000}^+$  in both grey and white matter such as PC(34:1) at  $m/z$  760.5 and PC(36:1) at  $m/z$  788.6 is increased by a factor of 5 to 10 when analysis is carried out with  $(\text{H}_2\text{O})\text{Ar}_{2000}^+$  and by a factor of 20 when the image is acquired with  $(\text{H}_2\text{O})_{6000}^+$ . These results correlate with the results obtained from the analysis of the model biomolecules and the total lipid brain extract reported earlier in this chapter (Figure 6.6) and in the previous chapter (Figure 5.18). Single ion images showing the co-localisation of PC(36:1)  $[\text{M}+\text{H}]^+$  at  $m/z$  788.6 showed in Figure 6.20 (C) and (D), prove that although this ion is present in the white matter, its intensity is significantly greater in the grey matter area.

There are a number of  $[\text{M}+\text{H}]^+$  lipids that are only detected with  $(\text{H}_2\text{O})\text{Ar}_{2000}^+$  or  $(\text{H}_2\text{O})_{6000}^+$ , such as PC(38:5) in white matter and PC(41:4) both regions. The increase in secondary ion signal seems to be more significant in the white matter than in the grey matter. For example, glycosphingolipids at  $m/z$  752.5, 814.7 and 866.6 are enhanced by a factor of 40 to 140. Single ion images of the sum of glycosphingolipids ions detected with  $(\text{H}_2\text{O})_{6000}^+$  are displayed in Figure 6.20 (E). These galactocerebrosides are components of the myelin sheath structure [39]. They interact with proteins to transport small proteins and enable cellular linking via signal transduction [40], [41]. They are only ionised by water-containing primary ion beams. These molecules have been previously identified with MALDI, Matrix-enhanced SIMS (ME-SIMS) and ToF-SIMS when the sample is chemically pre-treated by TFA exposure [36], [42], [43].

Unexpectedly, the formation of sodiated  $[M+Na]^+$  and potassiated  $[M+K]^+$  lipid adducts are also enhanced by water-containing beams. For example, the secondary ion yield of the lipid ion PC(34:1)  $[M+Na]^+$  at  $m/z$  782.5 and the  $[M+K]^+$  ion of PC(18:0/22:6) at  $m/z$  872.6 are enhanced between x3 and x10 times (Table 6.2). The presence of protons in the emission zone could mediate the attachment of alkali cations to the extracted ions, leading to the formation of adducts. This type of process has been identified in biological cellular structures including aqueous environments with lipids [44], [45]. Hence, during water cluster bombardment, ionisation occurs via protonation and adduct ion formation.

In summary, water-containing beams enhance lipid signal and reduce cholesterol ion suppression in the grey matter. Water-containing cluster ion beams can be applied to biological imaging such that the secondary ion signal from the spectrum of each pixel is maximised and the matrix effect reduced. Lipid imaging is now feasible, offering the opportunity to study them from a biological perspective. Moreover, with the J105-3D Chemical Imager, it is possible to accumulate a higher primary ion dose by courtesy of the increased duty-cycle to obtain more useful secondary ion signal from a sample.

We have observed that  $(H_2O)_{6000}^+$  can increase the secondary ion yield by a factor of 3-10 when compared to the yield delivered by  $(H_2O)Ar_{2000}^+$ . Therefore, pure water cluster ion beams produce the highest secondary ion signal and can provide more information about the chemical composition of a biological sample. In chapter 5, it was highlighted that the  $E/molecule$  or  $E/nucleon$  of pure water clusters significantly influence the secondary ion yield. Larger water clusters of higher beam energy will increase the secondary ion yield when keeping a constant  $E/molecule$  of  $\sim 3\text{eV}$  or  $E/nucleon$  of  $\sim 0.2\text{eV}$ . However, this effect is only observed with pure water clusters, unlike with water-doped argon clusters. The water-doped argon clusters have insufficient water to produce this effect. The proportion of water is limited to 5% since any further increase causes the argon cluster to break down and become a pure water cluster. The ion yield obtained depends on size/nucleon, with the optimum  $E/nucleon$  being  $\sim 0.2\text{eV}$ .

Since the best results from the brain tissue sections were obtained with  $(H_2O)_{6000}^+$ , it seems that this might be the best cluster primary ion beam for molecular imaging. The lifetime of the water clusters beam is limited by the boiler assembly's capacity. Water clusters can be generated for up to 3 hours. This limits the possibility of imaging large areas of tissue e.g. a whole brain section. When water-doped argon clusters are

produced, the lifetime of the ion beam is  $\sim 8$  hours, enough to acquire data from large areas.

In terms of spatial resolution, both pure water clusters and water-doped argon clusters beam diameters can be focused down to  $5\text{ }\mu\text{m}$ . As such, the technique cannot be used for applications that require sub-micron resolution such as cellular analysis. Further improvements will have to be made to obtain better spatial resolution, e.g. the implementation of higher energy beams with improved focusing capabilities. If sub-micrometer beam diameters can be achieved, then water-containing cluster ion beams could be a powerful tool for the chemical characterisation of biological tissues and cells.

Lipid class	Assignment	$m/z$	Grey matter			White matter		
			(H <sub>2</sub> O)Ar <sub>2000</sub>	(H <sub>2</sub> O) <sub>6000</sub>	Ar <sub>2000</sub>	(H <sub>2</sub> O)Ar <sub>2000</sub>	(H <sub>2</sub> O) <sub>6000</sub>	Ar <sub>2000</sub>
Sterol Lipids	Cholesterol fragment C <sub>8</sub> H <sub>13</sub>	109.1	✓	✓	ND	✓	✓	✓
	Cholesterol fragment C <sub>11</sub> H <sub>15</sub>	147.1	✓	✓	ND	✓	✓	✓
	Cholesterol fragment C <sub>12</sub> H <sub>17</sub>	161.1	✓	✓	ND	✓	✓	✓
	Cholesterol C <sub>27</sub> H <sub>45</sub> [M-OH] <sup>+</sup>	369.3	✓	✓	✓	✓	✓	✓
	Cholesterol C <sub>27</sub> H <sub>46</sub> O [M-H] <sup>+</sup>	385.3	✓	✓	✓	✓	✓	ND
	Chol.-2mer (C <sub>27</sub> H <sub>46</sub> O) <sub>2</sub> Na	795.6	✓	✓	✓	✓	✓	ND
	Chol.-3mer (C <sub>27</sub> H <sub>46</sub> O) <sub>3</sub> H	1160	✓	ND	✓	✓	✓	ND
Glycerophospholipids	PC fragment C <sub>5</sub> H <sub>14</sub> NO	104.1	✓	✓	✓	✓	✓	✓
	PC fragment C <sub>5</sub> H <sub>13</sub> NPO <sub>3</sub>	166	✓	✓	✓	✓	✓	✓
	PC fragment C <sub>5</sub> H <sub>15</sub> NPO <sub>4</sub>	184	✓	✓	✓	✓	✓	✓
	PC fragment C <sub>5</sub> H <sub>14</sub> PO <sub>4</sub> Na	206	✓	✓	✓	ND	ND	ND
	PC fragment C <sub>8</sub> H <sub>19</sub> NPO <sub>4</sub>	224.1	✓	✓	ND	✓	✓	ND
	PC [M+Na] <sup>+</sup> sodiated fragment	463.2	ND	ND	ND	✓	✓	✓
	PE fragment	508.6	ND	ND	ND	✓	✓	ND

PC sodiated fragment	652.6	✓	✓	ND	✓	✓	✓
PA(36:1) C <sub>39</sub> H <sub>75</sub> O <sub>8</sub> P [M+H] <sup>+</sup>	703.5	ND	ND	ND	✓	✓	ND
PC(30:1) C <sub>38</sub> H <sub>74</sub> NO <sub>8</sub> P [M+H] <sup>+</sup>	704.5	ND	ND	ND	ND	✓	ND
[PC32:0+K-N(CH <sub>3</sub> ) <sub>3</sub> ] <sup>+</sup>	713.5	ND	ND	ND	✓	✓	✓
PA(36:1) C <sub>39</sub> H <sub>75</sub> O <sub>8</sub> PNa [M+Na] <sup>+</sup>	725.5	✓	✓	✓	✓	✓	✓
PC(30:1) C <sub>38</sub> H <sub>74</sub> NO <sub>8</sub> PNa [M+Na] <sup>+</sup>	726.5	✓	✓	ND	✓	✓	✓
PC(32:1) C <sub>40</sub> H <sub>78</sub> NO <sub>8</sub> P [M+H] <sup>+</sup>	732.5	✓	✓	ND	✓	✓	ND
PC(32:0) C <sub>40</sub> H <sub>80</sub> NO <sub>8</sub> P [M+H] <sup>+</sup>	734.5	✓	✓	✓	✓	✓	✓
PC(34:1) [M+K- N(CH <sub>3</sub> ) <sub>3</sub> ] <sup>+</sup>	739.4	✓	✓	✓	✓	✓	✓
PA(36:1) C <sub>39</sub> H <sub>75</sub> O <sub>8</sub> PK [M+K] <sup>+</sup>	741.4	✓	✓	✓	✓	✓	✓
PC(30:1) C <sub>38</sub> H <sub>74</sub> NO <sub>8</sub> PK [M+K] <sup>+</sup>	742.4	✓	✓	✓	✓	✓	✓
PE(36:1) C <sub>41</sub> H <sub>81</sub> NO <sub>8</sub> P [M+H] <sup>+</sup>	747.5	ND	ND	ND	✓	✓	ND
PC fragment	751.5	✓	✓	✓	✓	✓	ND
PC(32:1) C <sub>40</sub> H <sub>78</sub> NO <sub>8</sub> PNa [M+Na] <sup>+</sup>	754.5	✓	✓	✓	✓	✓	ND
PC(32:0) C <sub>40</sub> H <sub>80</sub> NO <sub>8</sub> PNa [M+Na] <sup>+</sup>	756.5	✓	✓	✓	✓	✓	✓
PC(34:2) C <sub>42</sub> H <sub>80</sub> NO <sub>8</sub> P [M+H] <sup>+</sup>	758.5	✓	✓	ND	✓	✓	ND

PC(34:1) C <sub>42</sub> H <sub>82</sub> NO <sub>8</sub> P [M+H] <sup>+</sup>	760.5	✓	✓	✓	✓	✓	✓
PC(34:0) C <sub>42</sub> H <sub>84</sub> NO <sub>8</sub> P [M+H] <sup>+</sup>	762.5	✓	✓	ND	✓	✓	✓
PI(30:1) C <sub>39</sub> H <sub>76</sub> O <sub>12</sub> P [M+H] <sup>+</sup>	768.6	✓	✓	ND	✓	✓	✓
PC(32:1) C <sub>40</sub> H <sub>78</sub> NO <sub>8</sub> PK [M+K] <sup>+</sup>	770.5	✓	✓	✓	✓	✓	✓
PC(32:0) C <sub>40</sub> H <sub>80</sub> NO <sub>8</sub> PK [M+K] <sup>+</sup>	772.5	✓	✓	✓	✓	✓	✓
PC(34:3) C <sub>42</sub> H <sub>78</sub> NO <sub>8</sub> PNa [M+Na] <sup>+</sup>	778.5	✓	✓	ND	✓	✓	ND
PC(34:2) C <sub>42</sub> H <sub>80</sub> NO <sub>8</sub> PNa [M+Na] <sup>+</sup>	780.5	✓	✓	ND	✓	✓	ND
PC(34:1) C <sub>42</sub> H <sub>82</sub> NO <sub>8</sub> PNa [M+Na] <sup>+</sup>	782.5	✓	✓	✓	✓	✓	✓
PC(34:0) C <sub>42</sub> H <sub>84</sub> NO <sub>8</sub> PNa [M+Na] <sup>+</sup>	784.5	✓	✓	✓	✓	✓	✓
PC(36:1) C <sub>44</sub> H <sub>86</sub> NO <sub>8</sub> P [M+H] <sup>+</sup>	788.6	✓	✓	ND	✓	✓	ND
PC(34:3) C <sub>42</sub> H <sub>78</sub> NO <sub>8</sub> PK [M+K] <sup>+</sup>	794.5	ND	ND	ND	✓	✓	ND
PC(34:2) C <sub>42</sub> H <sub>80</sub> NO <sub>8</sub> PK [M+K] <sup>+</sup>	796.5	✓	✓	ND	✓	✓	ND
PC(34:1) C <sub>42</sub> H <sub>82</sub> NO <sub>8</sub> PK [M+K] <sup>+</sup>	798.5	✓	✓	✓	✓	✓	✓
PC(34:0) C <sub>42</sub> H <sub>84</sub> NO <sub>8</sub> PK [M+K] <sup>+</sup>	800.5	✓	✓	✓	✓	✓	✓
PC(36:3) C <sub>44</sub> H <sub>82</sub> NO <sub>8</sub> PNa [M+Na] <sup>+</sup>	806.5	✓	✓	ND	✓	✓	ND
PC(38:5) C <sub>46</sub> H <sub>82</sub> NO <sub>8</sub> P [M+H] <sup>+</sup>	808.5	✓	✓	ND	ND	ND	ND



	PC(36:1) C <sub>44</sub> H <sub>86</sub> NO <sub>8</sub> PNa [M+Na] <sup>+</sup>	810.6	✓	✓	✓	✓	✓	✓
	PC(38:4) C <sub>46</sub> H <sub>84</sub> NO <sub>8</sub> P [M+H] <sup>+</sup>	811.6	✓	✓	✓	✓	✓	✓
	PC(36:1) C <sub>44</sub> H <sub>86</sub> NO <sub>8</sub> PK [M+Na] <sup>+</sup>	826.6	✓	✓	✓	✓	✓	✓
	PE(42:1) C <sub>47</sub> H <sub>92</sub> NO <sub>8</sub> P [M+H] <sup>+</sup>	830.6	ND	ND	ND	✓	✓	ND
	PC(38:4) C <sub>46</sub> H <sub>84</sub> NO <sub>8</sub> PNa [M+Na] <sup>+</sup>	832.6	✓	✓	ND	✓	✓	ND
	PC(18:0/22:6) C <sub>48</sub> H <sub>84</sub> NO <sub>8</sub> P [M+H] <sup>+</sup>	834.5	✓	✓	ND	ND	ND	ND
	PC(40:4) C <sub>48</sub> H <sub>88</sub> NO <sub>8</sub> P [M+H] <sup>+</sup>	838.6	✓	✓	ND	✓	✓	ND
	PC(38:5) C <sub>46</sub> H <sub>82</sub> NO <sub>8</sub> PK [M+K] <sup>+</sup>	846.5	✓	✓	ND	ND	ND	ND
	PC(38:4) C <sub>46</sub> H <sub>84</sub> NO <sub>8</sub> PK [M+K] <sup>+</sup>	848.6	✓	✓	ND	✓	✓	ND
	PC(41:4) C <sub>49</sub> H <sub>90</sub> NO <sub>8</sub> P [M+H] <sup>+</sup>	852.6	✓	✓	ND	✓	✓	ND
	PC(18:0/22:6) C <sub>48</sub> H <sub>84</sub> NO <sub>8</sub> PNa [M+ Na] <sup>+</sup>	856.5	✓	✓	✓	ND	ND	ND
	PC(40:4) C <sub>48</sub> H <sub>88</sub> NO <sub>8</sub> PNa [M+Na] <sup>+</sup>	860.6	✓	✓	ND	ND	ND	ND
	PE(42:1) C <sub>47</sub> H <sub>92</sub> NO <sub>8</sub> PK [M+K] <sup>+</sup>	868.6	ND	ND	ND	✓	✓	ND
	PC(18:0/22:6) C <sub>48</sub> H <sub>84</sub> NO <sub>8</sub> PK [M+K] <sup>+</sup>	872.5	✓	✓	✓	ND	ND	ND
	PIP(38:4) C <sub>47</sub> H <sub>84</sub> O <sub>16</sub> P <sub>2</sub> [M+H] <sup>+</sup>	967.5	✓	ND	ND	ND	ND	ND
<b>Glycerolipids</b>	MAG(16:1) C <sub>19</sub> H <sub>35</sub> O <sub>3</sub> [M-OH] <sup>+</sup>	311.2	✓	✓	ND	ND	✓	ND

	MAG(16:0) C <sub>19</sub> H <sub>37</sub> O <sub>3</sub> [M-OH] <sup>+</sup>	313.2	✓	✓	ND	✓	✓	ND
	MAG(18:1) C <sub>21</sub> H <sub>39</sub> O <sub>3</sub> [M-OH] <sup>+</sup>	339.2	✓	✓	ND	✓	✓	✓
	MAG(18:0) C <sub>21</sub> H <sub>41</sub> O <sub>3</sub> [M-OH] <sup>+</sup>	341.3	✓	✓	ND	✓	✓	✓
	DAG(32:0) C <sub>35</sub> H <sub>67</sub> O <sub>4</sub> [M-OH] <sup>+</sup>	551.5	✓	✓	✓	✓	✓	✓
	DAG(34:3) C <sub>37</sub> H <sub>65</sub> O <sub>4</sub> [M-OH] <sup>+</sup>	573.4	✓	✓	✓	✓	✓	✓
	DAG(34:1) C <sub>37</sub> H <sub>69</sub> O <sub>4</sub> [M-OH] <sup>+</sup>	577.5	✓	✓	✓	✓	✓	✓
	DAG(34:0) C <sub>37</sub> H <sub>71</sub> O <sub>4</sub> [M-OH] <sup>+</sup>	579.5	✓	✓	✓	✓	✓	✓
	DAG(36:4) C <sub>39</sub> H <sub>67</sub> O <sub>4</sub> [M-OH] <sup>+</sup>	599.5	✓	✓	✓	✓	✓	✓
	DAG(36:3) C <sub>39</sub> H <sub>69</sub> O <sub>4</sub> [M-OH] <sup>+</sup>	601.5	✓	✓	✓	✓	✓	✓
	DAG(36:2) C <sub>39</sub> H <sub>71</sub> O <sub>4</sub> [M-OH] <sup>+</sup>	603.5	✓	✓	ND	✓	✓	ND
	DG(37:2) C <sub>40</sub> H <sub>74</sub> O <sub>5</sub> K [M+Na] <sup>+</sup>	673.5	✓	✓	✓	✓	✓	✓
	TAG(50:2) C <sub>53</sub> H <sub>98</sub> O <sub>6</sub> Na [M+Na] <sup>+</sup>	853.7	✓	✓	ND	✓	✓	ND
	TAG(50:1) C <sub>53</sub> H <sub>100</sub> O <sub>6</sub> Na [M+Na] <sup>+</sup>	855.7	✓	✓	ND	✓	✓	ND
	TAG(50:0) C <sub>53</sub> H <sub>102</sub> O <sub>6</sub> Na [M+Na] <sup>+</sup>	857.7	✓	✓	ND	ND	ND	ND
<b>Fatty acyls</b>	FA(16:0) fragment C <sub>16</sub> H <sub>31</sub> O <sub>2</sub>	255.2	✓	✓	ND	ND	✓	ND
	FA(18:0) fragment C <sub>18</sub> H <sub>35</sub> O <sub>2</sub>	283.2	ND	ND	ND	✓	✓	ND

Sphingolipids	Galactose headgroup fragment $C_6H_{12}O_6Na [M+Na]^+$	203	✓	✓	ND	✓	✓	ND
	Cer. fragment (d18:1) 4-sphingenine backbone $C_{18}H_{34}N$	264.2	✓	✓	✓	✓	✓	✓
	Cer. fragment	282.3	ND	ND	ND	✓	✓	ND
	Gal-sphing $C_{24}H_{47}NO_7Na [M+Na]^+$	484.3	ND	ND	ND	✓	✓	✓
	Cer(d18:1/12:0) $C_{48}H_{84}NO_8PNa [M+Na]^+$	504.4	✓	✓	✓	✓	✓	✓
	GalCer(32:1) $C_{38}H_{73}NO_8 [M+H]^+$	672.5	ND	ND	ND	✓	✓	ND
	GalCer(32:1) $C_{38}H_{73}NO_8Na [M+Na]^+$	694.5	✓	✓	✓	✓	✓	✓
	GalCer(d18:0/16:0) $C_{40}H_{79}NO_8 [M+H]^+$	702.5	ND	ND	ND	✓	✓	ND
	GalCer(32:1) $C_{38}H_{73}NO_8K [M+K]^+$	710.4	✓	✓	✓	✓	✓	✓
	GalCer(d18:1/18:0) $C_{42}H_{81}NO_8 [M+H]^+$	728.5	✓	✓	ND	✓	✓	ND
	SM(36:1) $C_{41}H_{83}N_2O_6P [M+H]^+$	731.5	✓	✓	ND	✓	✓	ND
	C18:0 $C_{42}H_{81}NO_8Na [M+Na]^+$	750.5	✓	✓	ND	✓	✓	✓
	GalCer(d18:2/20:1) $C_{44}H_{81}NO_8 [M+H]^+$	752.5	ND	ND	ND	✓	✓	ND
	SM(36:1) $C_{41}H_{83}N_2O_6PNa [M+Na]^+$	753.5	✓	✓	✓	✓	✓	✓
	GalCer(d18:1/18:0) $C_{42}H_{81}NO_8K [M+K]^+$	766.5	✓	✓	ND	✓	✓	✓

SM(36:1) C <sub>41</sub> H <sub>83</sub> N <sub>2</sub> O <sub>6</sub> PK [M+K] <sup>+</sup>	769.6	✓	✓	✓	✓	✓	✓
GalCer(d18:0/22:0) C <sub>46</sub> H <sub>91</sub> NO <sub>8</sub> [M+H] <sup>+</sup>	786.6	✓	✓	✓	✓	✓	ND
GalCer(d18:1/24:1) C <sub>48</sub> H <sub>91</sub> NO <sub>8</sub> [M+H] <sup>+</sup>	810.6	✓	✓	✓	✓	✓	✓
GalCer(d18:1/24:0) C <sub>48</sub> H <sub>93</sub> NO <sub>8</sub> [M+H] <sup>+</sup>	812.6	✓	✓	✓	✓	✓	ND
GalCer(d18:0/24:0) C <sub>48</sub> H <sub>95</sub> NO <sub>8</sub> [M+H] <sup>+</sup>	814.7	✓	✓	✓	✓	✓	ND
GalCer(d18:0/22:0) C <sub>46</sub> H <sub>91</sub> NO <sub>8</sub> K [M+K] <sup>+</sup>	824.6	✓	✓	ND	✓	✓	ND
GalCer(42:2) C <sub>48</sub> H <sub>91</sub> NO <sub>8</sub> Na [M+Na] <sup>+</sup>	832.6	✓	✓	ND	✓	✓	ND
C24:0 C <sub>48</sub> H <sub>93</sub> NO <sub>8</sub> Na [M+Na] <sup>+</sup>	834.6	✓	✓	ND	✓	✓	ND
GalCer(d18:0/24:0) C <sub>48</sub> H <sub>95</sub> NO <sub>8</sub> Na [M+Na] <sup>+</sup>	836.6	✓	✓	✓	✓	✓	ND
GalCer(42:2) C <sub>48</sub> H <sub>91</sub> NO <sub>8</sub> K [M+K] <sup>+</sup>	848.6	✓	✓	ND	✓	✓	ND
GalCer(d18:1/24:0(2-OH)) C <sub>48</sub> H <sub>93</sub> NO <sub>9</sub> Na [M+Na] <sup>+</sup>	850.6	✓	✓	ND	✓	✓	ND
C22 Sulfatide(3'-sulfo)Galβ-Cer(d18:1/22:0) C <sub>46</sub> H <sub>89</sub> NO <sub>11</sub> S [M+H] <sup>+</sup>	864.6	ND	ND	ND	ND	✓	ND
GalCer(d18:1/26:0) C <sub>50</sub> H <sub>97</sub> NO <sub>8</sub> K [M+K] <sup>+</sup>	878.6	ND	✓	ND	✓	✓	ND
C22(OH) Sulfatide (3'-sulfo)Galβ-Cer(d18:1/22:0(2OH)) C <sub>46</sub> H <sub>89</sub> NO <sub>12</sub> S	880.6	ND	✓	ND	ND	✓	ND

	[M+H] <sup>+</sup>							
	C24(OH) Sulfatide (3'-sulfo)Galβ- Cer(d18:1/24:0(2OH)) C <sub>48</sub> H <sub>93</sub> NO <sub>12</sub> S							
	[M+H] <sup>+</sup>	908.6	ND	ND	ND	ND	✓	ND
	FMC-5(d18:1/18:0) C <sub>52</sub> H <sub>91</sub> NO <sub>13</sub> [M+H] <sup>+</sup>	938.6	ND	ND	ND	ND	✓	ND
	FMC-5(d18:1/20:0) C <sub>54</sub> H <sub>95</sub> NO <sub>13</sub> [M+H] <sup>+</sup>	966.6	✓	ND	ND	✓	✓	ND

Table 6.3: List of lipids ion observed with (H<sub>2</sub>O)<sub>6000</sub><sup>+</sup>, (H<sub>2</sub>O)Ar<sub>2000</sub><sup>+</sup> and Ar<sub>2000</sub><sup>+</sup>. '✓' indicates a detected ion whereas 'ND' refers to not-observed species.

### 6.5.5 Study of the ion suppression effect on Cholesterol

In an attempt to investigate the ion suppression of cholesterol and phospholipids further, a series of experiments were performed on standard lipid mixtures. The cluster primary ion beams and ion doses applied to these experiments were the same as those applied to tissue imaging (section 6.5.4).

Figure 6.21 (A) and (B), show the total ion spectra obtained with 20 keV  $\text{Ar}_{2000}^+$  and 20 keV  $(\text{H}_2\text{O})_{6000}^+$  for the analysis of the 1:1 mixture of cholesterol with DPPC and SM.

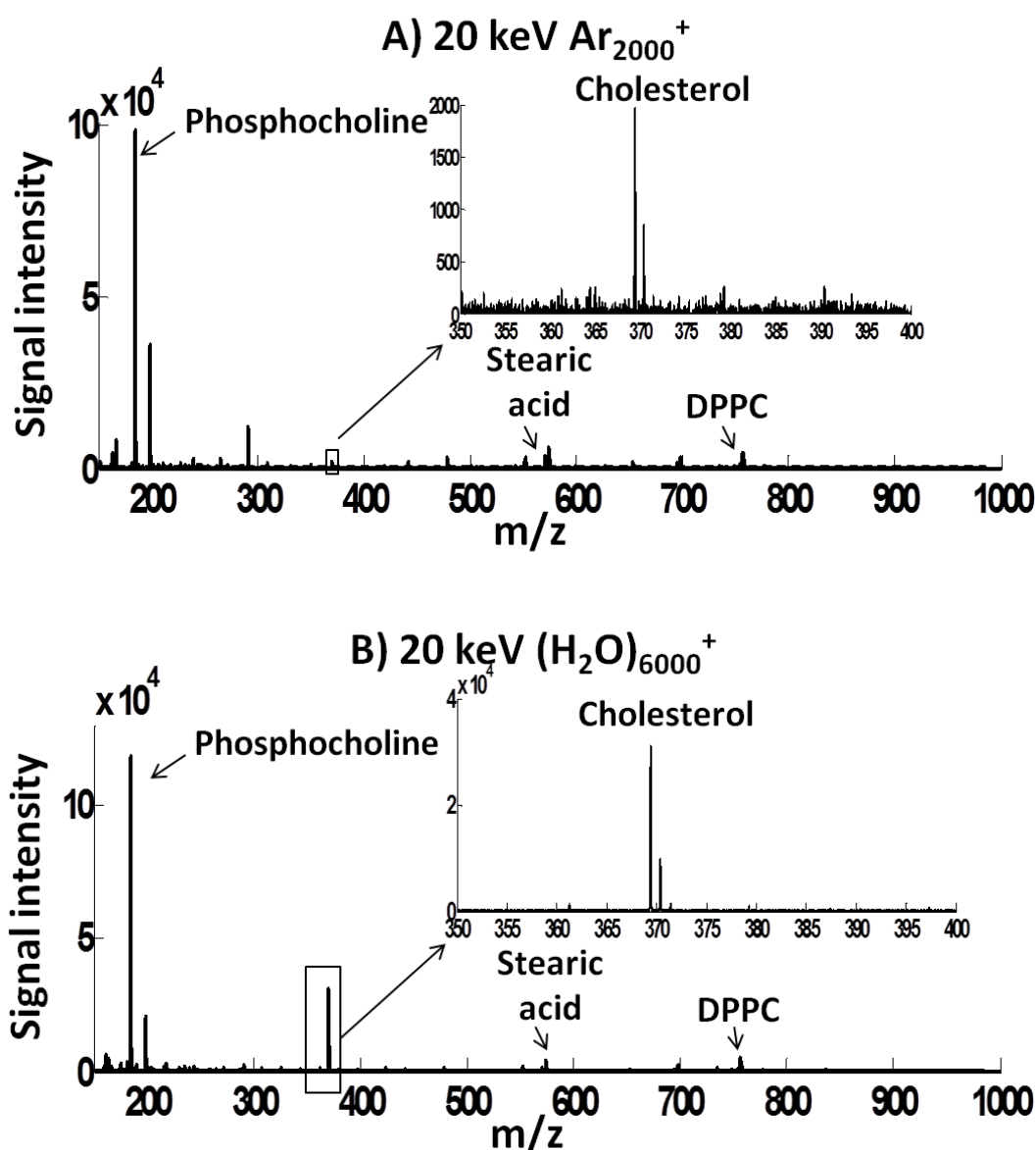


Figure 6.21: Total ion spectra obtained with (A) 20 keV  $\text{Ar}_{2000}^+$  and (B)  $(\text{H}_2\text{O})_{6000}^+$  from a cholesterol mixture of sphingomyelin/ DPPC (1:1). The total primary ion dose used was  $1 \times 10^{12}$  ions  $\text{cm}^{-2}$ .

In both spectra, the base peak is the phosphocholine fragment ion at  $m/z$  184 which is derived from the phosphocholine groups of DPPC and SM. The secondary ion signal intensity from this peak is similar for both argon and water clusters. However, the signal intensity from the cholesterol fragment  $[M-H_2O+H]^+$  at  $m/z$  369 is significantly different.

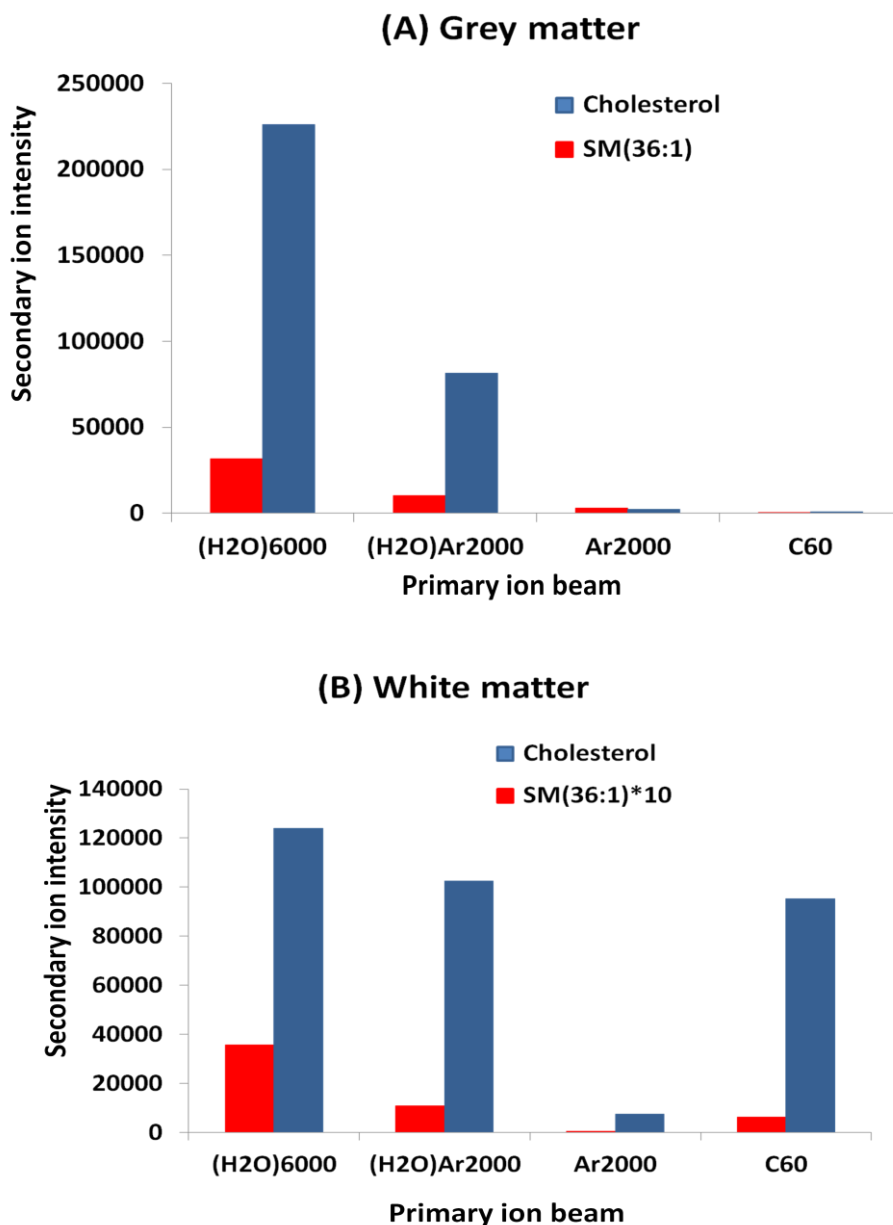


Figure 6.22: Secondary ion yields obtained from a  $400 \mu\text{m}^2$  area from the images previously presented. Secondary ion yields of stearic acid  $[M+H]^+$  ion from sphingomyelin and cholesterol  $[M-H_2O+H]^+$  ion from grey matter and white matter regions are presented. The primary ion beams used were 20 keV  $(\text{H}_2\text{O})_{6000}^+$ , 20 keV  $(\text{H}_2\text{O})\text{Ar}_{2000}^+$ , 20 keV  $\text{Ar}_{2000}^+$  and 20 keV  $\text{C}_{60}^+$  under a primary ion fluence of  $1 \times 10^{12}$  ions  $\text{cm}^{-2}$ . The presence of both lipids is in a ratio 1:0.3 (cholesterol/SM) [13]. The secondary ion yields of SM were multiplied by ten for better visualisation.

The secondary ion signal detected from cholesterol with  $(\text{H}_2\text{O})_{6000}^+$  is enhanced by 20x. The signal intensities produced by DPPC  $[\text{M}+\text{H}]^+$  at  $m/z$  735 and stearic acid from SM  $[2\text{M}+\text{H}]^+$  at  $m/z$  570 are similar to  $\text{Ar}_{2000}^+$ .

For better understanding of the effect of water-containing clusters on cholesterol detection in tissue, Figure 6.22 includes the comparison between the secondary ion yields obtained from the images from sphingomyelin (SM) and cholesterol in the white matter and grey matter (400  $\mu\text{m}^2$  area).

The native distribution of cholesterol/SM in the brain is 1:0.3 [13] in both tissue types. In the grey matter chart, the detection of cholesterol is considerably higher with  $(\text{H}_2\text{O})_{6000}^+$  and  $(\text{H}_2\text{O})\text{Ar}_{2000}^+$ , whereas the detection of cholesterol with  $\text{C}_{60}^+$  and  $\text{Ar}_{2000}^+$  is close to zero.

The detection of SM is also close to zero with  $\text{C}_{60}^+$  and  $\text{Ar}_{2000}^+$  and it is 5 and 10 times higher when analysing with  $(\text{H}_2\text{O})\text{Ar}_{2000}^+$  and  $(\text{H}_2\text{O})_{6000}^+$ , respectively. There is a higher detection of cholesterol in the white matter than SM with all beams (Figure 6.22). Moreover,  $\text{C}_{60}^+$  and  $\text{Ar}_{2000}^+$  more cholesterol in white matter than grey matter. The cholesterol recorded with  $\text{C}_{60}^+$  in the white matter is close to that observed with water-containing clusters. The detection of SM is close to zero with all beams in the white matter, thus, the secondary ion yields obtained were multiplied by ten to make then visible in the white matter chart.

To observe the effects of each beam in the detection of cholesterol and SM, the cholesterol/SM ratios were calculated for grey and white matter. The obtained ratios are presented in Figure 6.23. The effect observed on the grey matter is more secondary ion signal detected from cholesterol when compared to SM with  $(\text{H}_2\text{O})_{6000}^+$  and  $(\text{H}_2\text{O})\text{Ar}_{2000}^+$ . In the grey matter, the ratio of signal observed for cholesterol and SM with  $\text{C}_{60}^+$  and  $\text{Ar}_{2000}^+$  is close to one, which indicates similar number of counts recorded for both lipid types.

In the grey matter, water-containing beams are lifting the ion suppression effect observed for cholesterol with  $\text{C}_{60}^+$  and  $\text{Ar}_{2000}^+$ . Contrastingly,  $(\text{H}_2\text{O})_{6000}^+$  and  $(\text{H}_2\text{O})\text{Ar}_{2000}^+$  are detecting more SM in the white matter. Hence, another matrix effect might be taking place for SM in the white matter.



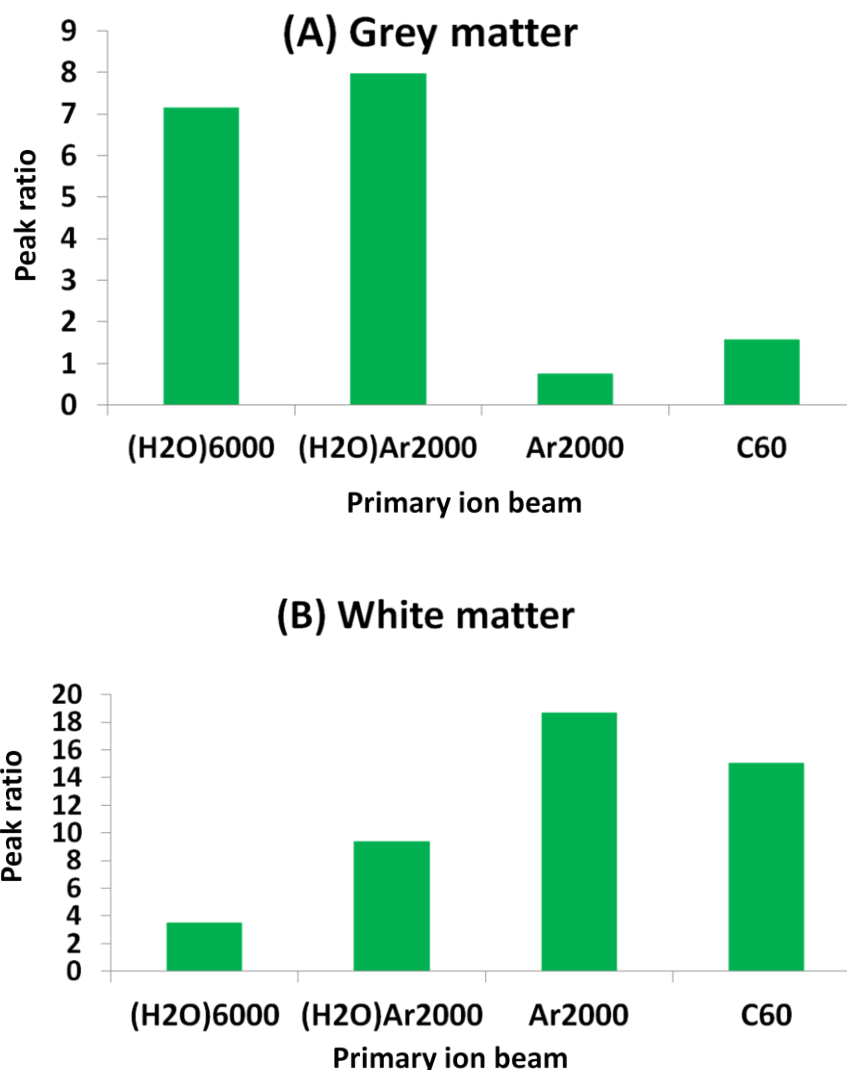


Figure 6.23: Cholesterol/SM ration obtained from the secondary ion yields from the analysis of the brain cerebellum. The primary ion beams used were 20 keV (H<sub>2</sub>O)<sub>6000</sub><sup>+</sup>, 20 keV (H<sub>2</sub>O)Ar<sub>2000</sub><sup>+</sup>, 20 keV Ar<sub>2000</sub><sup>+</sup> and 20 keV C<sub>60</sub><sup>+</sup> under a primary ion fluence of  $1 \times 10^{12}$  ions cm<sup>-2</sup>. The ratios are calculated for grey matter (top) and white matter (bottom).

A cholesterol/SM lipid mixture in the proportion 1:1 (v/v) was analysed. The ratios of cholesterol to stearic acid from SM are plotted in Figure 6.24. This chart shows a ratio tendency similar to that observed for the grey matter (Figure 6.23). The ratio of cholesterol/SM is close to 1 with C<sub>60</sub><sup>+</sup> and Ar<sub>2000</sub><sup>+</sup>. With (H<sub>2</sub>O)<sub>6000</sub><sup>+</sup> and (H<sub>2</sub>O)Ar<sub>2000</sub><sup>+</sup> analysis, the signal intensity for cholesterol is 5 and 4 times higher than SM, respectively. This could indicate an ion suppression effect on cholesterol in the white matter under Ar<sub>2000</sub><sup>+</sup> and C<sub>60</sub><sup>+</sup> bombardment. This ion suppression effect is ameliorated under water-containing ion beam bombardment.

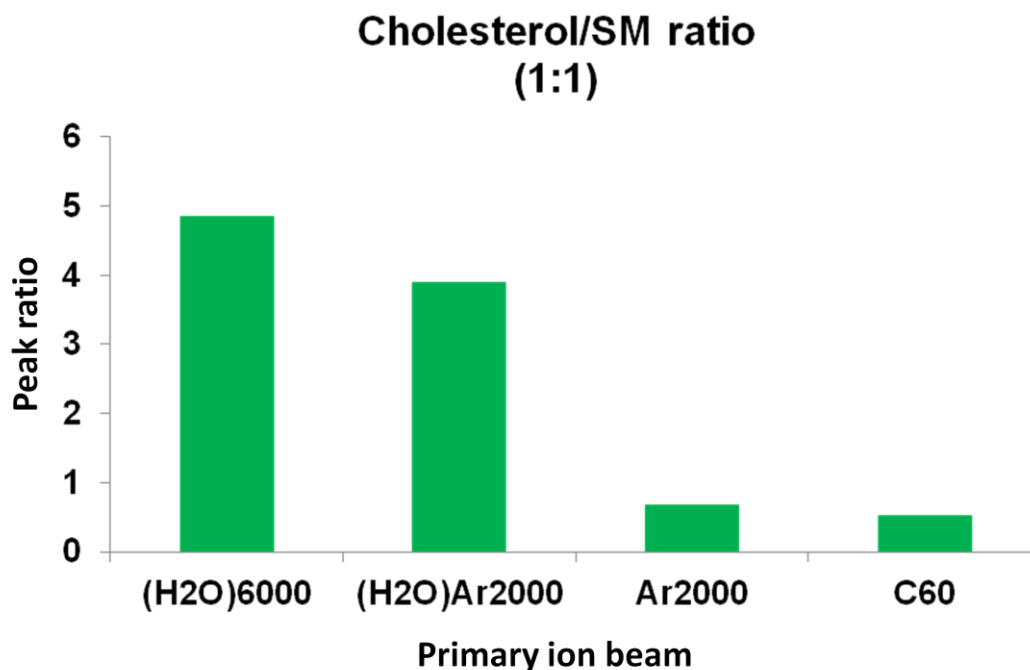


Figure 6.24: Cholesterol/sphingomyelin peak ratios from the analysis of a mixture of cholesterol/SM (1:1). The primary ion beams used were 20 keV (H<sub>2</sub>O)<sub>6000</sub><sup>+</sup>, 20 keV (H<sub>2</sub>O)Ar<sub>2000</sub><sup>+</sup>, 20 keV Ar<sub>2000</sub><sup>+</sup> and 20 keV C<sub>60</sub><sup>+</sup> under a primary ion fluence of  $1 \times 10^{12}$  ions cm<sup>-2</sup>.

This matrix effect was also clearly observed in the cerebellum images (Figure 6.20). The lipid composition of both grey and white matter might contribute to this matrix effect. The molecular structure might also play an important role, as observed in the ratios presented in Table 6.2. Grey and white matter have different membrane structures formed by cholesterol, phospholipids and glycosphingolipids that could influence the protonation of these molecules. These results also show that the matrix effects observed are very complex and have to be considered for image interpretation. The extent of this matrix effect remains unknown and is worth exploring in more detail in future experiments.

## 6.6 Summary

This chapter demonstrated the application of different cluster primary ion beams to biological tissue imaging with ToF-SIMS. The use of water-containing clusters for imaging seems beneficial for detecting of several lipid classes in the brain. This was demonstrated with the analysis of brain total lipid extract and brain tissue section imaging.

The energy regime for water containing clusters is optimum at an  $E/nucleon$  of  $\approx 0.2$  eV. Pure water clusters, particularly  $(H_2O)_{6000}^+$ , produced the highest secondary ion signal. Here, an enhancement of 10 - 100 over  $Ar_{2000}^+$  was observed. Additionally, water-doped argon clusters with the same  $E/nucleon$  generated an enhancement of 4- 10 when compared to argon-only clusters.

The enhancement of cholesterol detection was specific: during water-containing cluster bombardment, the detection of cholesterol in the white matter was similar to that recorded in the grey matter. The behaviour of this molecule, particularly in the grey matter, seemed to be highly influenced by a matrix effect. This ion suppression effect seems to be reduced when the sample is analysed with  $(H_2O)_{6000}^+$  or  $(H_2O)Ar_{2000}^+$ .

The ion suppression effect on cholesterol was studied further with experiments on standard cholesterol and lipid mixtures. Mixtures with concentrations similar to those found in the grey matter and white matter were analysed. The detection of cholesterol seems to be notably improved with  $(H_2O)_{6000}^+$  clusters.

In conclusion, the application of water-containing cluster ion beams is beneficial and enhances the useful secondary yields for the chemical characterisation of biological tissue. Moreover, instrumental improvements to the GCIB water cluster prototype, such as increased beam energy, could lead to higher yields and better spatial resolution. Currently, the best spatial resolution obtained with water-containing clusters is 4  $\mu m$ . This spot size restricts the application of water and water-doped argon clusters to micrometric samples e.g. tissue and does not apply to sub-micron imaging e.g. cells.

## 6.7 References

- [1] M. K. Passarelli and N. Winograd, "Lipid imaging with time-of-flight secondary ion mass spectrometry (ToF-SIMS)," *Biochim. Biophys. Acta - Mol. Cell Biol. Lipids*, vol. 1811, no. 11, pp. 976-990, 2011.
- [2] G. J. Siegel, B. W. Agranoff, R. W. Albers, S. K. Fisher, and M. D. Uhler., *Basic Neurochemistry Molecular, Cellular and Medical Aspects*, 6th ed. Philadelphia: Lippincott-Raven, 1999.
- [3] D. Touboul, O. Laprevote, and A. Brunelle, "Medical and biological applications of ToF-SIMS," in *TOF-SIMS: Materials analysis by mass spectrometry*, 2nd, Ed. Manchester: IM Publications, 2013, pp. 583-612.

- [4] A. M. Piwowar and N. Winograd, "Application of SIMS to study of biological systems," in *TOF-SIMS: Materials analysis by mass spectrometry*, 2nd ed., J. C. Vickerman and D. Briggs, Eds. Manchester: IM Publications, 2013, pp. 553–582.
- [5] B. Spengler, "Mass spectrometry imaging of biomolecular information.," *Anal. Chem.*, 2015.
- [6] J. Pól, M. Strohalm, V. Havlíček, and M. Volný, "Molecular mass spectrometry imaging in biomedical and life science research," *Histochem. Cell Biol.*, vol. 134, no. 5, pp. 423–443, 2010.
- [7] A. Römpp, J.-P. Both, A. Brunelle, R. M. a. Heeren, O. Laprévote, B. Prideaux, A. Seyer, B. Spengler, M. Stoeckli, and D. F. Smith, "Mass spectrometry imaging of biological tissue: an approach for multicenter studies," *Anal. Bioanal. Chem.*, pp. 2329–2335, 2015.
- [8] D. Gode and D. A. Volmer, "Lipid imaging by mass spectrometry - a review.," *Analyst*, vol. 138, no. 5, pp. 1289–315, 2013.
- [9] A. Brunelle and O. Laprévote, "Lipid imaging with cluster time-of-flight secondary ion mass spectrometry," *Anal. Bioanal. Chem.*, vol. 393, pp. 31–35, 2009.
- [10] N. (BRAIN) W. Group, "Brain 2025, a scientific vision," *NIH*, p. 146, 2014.
- [11] N. Heintz and L. Mamounas, "Gene Expression Nervous System Atlas (GENSAT)," 2004. [Online]. Available: <http://www.gensat.org/index.html>.
- [12] E. S. Lein, M. J. Hawrylycz, N. Ao, M. Ayres, A. Bensinger, A. Bernard, A. F. Boe, M. S. Boguski, K. S. Brockway, E. J. Byrnes, L. Chen, L. Chen, T.-M. Chen, M. C. Chin, J. Chong, B. E. Crook, A. Czaplinska, C. N. Dang, S. Datta, N. R. Dee, A. L. Desaki, T. Desta, E. Diep, T. a Dolbeare, M. J. Donelan, H.-W. Dong, J. G. Dougherty, B. J. Duncan, A. J. Ebbert, G. Eichele, L. K. Estin, C. Faber, B. a Facer, R. Fields, S. R. Fischer, T. P. Fliss, C. Frensley, S. N. Gates, K. J. Glattfelder, K. R. Halverson, M. R. Hart, J. G. Hohmann, M. P. Howell, D. P. Jeung, R. a Johnson, P. T. Karr, R. Kawal, J. M. Kidney, R. H. Knapik, C. L. Kuan, J. H. Lake, A. R. Laramée, K. D. Larsen, C. Lau, T. a Lemon, A. J. Liang, Y. Liu, L. T. Luong, J. Michaels, J. J. Morgan, R. J. Morgan, M. T. Mortrud, N. F. Mosqueda, L. L. Ng, R. Ng, G. J. Orta, C. C. Overly, T. H. Pak, S. E. Parry, S. D. Pathak, O. C. Pearson, R. B. Puchalski, Z. L. Riley, H. R. Rockett, S. a Rowland, J. J. Royall, M. J. Ruiz, N. R. Sarno, K. Schaffnit, N. V Shapovalova, T. Sivasay, C. R. Slaughterbeck, S. C. Smith, K. a Smith, B. I. Smith, A. J. Sodt, N. N. Stewart, K.-R. Stumpf, S. M. Sunkin, M. Sutram, A. Tam, C. D. Teemer, C. Thaller, C. L. Thompson,

L. R. Varnam, A. Visel, R. M. Whitlock, P. E. Wohnoutka, C. K. Wolkey, V. Y. Wong, M. Wood, M. B. Yaylaoglu, R. C. Young, B. L. Youngstrom, X. F. Yuan, B. Zhang, T. a Zwingman, and A. R. Jones, "Genome-wide atlas of gene expression in the adult mouse brain.," *Nature*, vol. 445, no. 7124, pp. 168–176, 2007.

[13] J. S. O'Brien and E. L. Sampson, "Lipid composition of the normal human brain: gray matter, white matter, and myelin.," *J. Lipid Res.*, vol. 6, no. 4, pp. 537–544, 1965.

[14] H. Nygren, K. Börner, P. Malmberg, and B. Hagenhoff, "Localization of cholesterol in rat cerebellum with imaging TOF-SIMS. Effect of tissue preparation," *Appl. Surf. Sci.*, vol. 252, no. 19, pp. 6975–6981, 2006.

[15] H. Nygren, C. Eriksson, P. Malmberg, H. Sahlin, L. Carlsson, J. Lausmaa, and P. Sjövall, "A cell preparation method allowing subcellular localization of cholesterol and phosphocholine with imaging TOF-SIMS," *Colloids Surfaces B Biointerfaces*, vol. 30, no. 1–2, pp. 87–92, 2003.

[16] P. Sjövall, B. Johansson, and J. Lausmaa, "Localization of lipids in freeze-dried mouse brain sections by imaging TOF-SIMS," *Appl. Surf. Sci.*, vol. 252, no. 19, pp. 6966–6974, 2006.

[17] E. Ikonen, "Cellular cholesterol trafficking and compartmentalization.," *Nat. Rev. Mol. Cell Biol.*, vol. 9, no. 2, pp. 125–138, 2008.

[18] M. Orth and S. Bellosta, "Cholesterol: Its regulation and role in central nervous system disorders," *Cholesterol*, vol. 2012, 2012.

[19] M. R. Krause and S. L. Regen, "The Structural Role of Cholesterol in Cell Membranes : From Condensed Bilayers to Lipid Rafts," no. iv, 2014.

[20] M. Podbielska, N. L. Banik, E. Kurowska, and E. L. Hogan, "Myelin recovery in multiple sclerosis: the challenge of remyelination.," *Brain Sci.*, vol. 3, no. 3, pp. 1282–324, 2013.

[21] S. Sheraz née Rabbani, a. Barber, I. Berrueta Razo, J. S. Fletcher, N. P. Lockyer, and J. C. Vickerman, "Prospect of increasing secondary ion yields in ToF-SIMS using water cluster primary ion beams," *Surf. Interface Anal.*, no. November 2013, p. n/a–n/a, 2014.

[22] S. Sheraz née Rabbani, I. Berrueta Razo, T. Kohn, N. P. Lockyer, and J. C. Vickerman, "Enhancing Ion Yields in Time-of-Flight-Secondary Ion Mass Spectrometry:

A Comparative Study of Argon and Water Cluster Primary Beams," *Anal. Chem.*, vol. 87, no. 4, pp. 2367–2374, 2015.

[23] S. Sheraz, A. Barber, J. S. Fletcher, N. P. Lockyer, and J. C. Vickerman, "Enhancing secondary ion yields in ToF-SIMS using water cluster primary beams .," *Anal. Chem.*, pp. 2–3, 2013.

[24] C. Gerfen and P. Bolam, "Multisensory Integration in the Mouse Striatum," in *Handbook of Basal Ganglia Structure and Function: A Decade of Progress*, H. Steiner and TsengKuei, Eds. San Diego: Academic Press, 2010, pp. 3–50.

[25] J. Berg, J. Tymoczko, and L. Stryer, "Structural Biochemistry and Organic Chemistry of Lipids," in *Biochemistry*, 6th ed., 2007.

[26] I. Berrueta Razo, S. Sheraz, A. Henderson, N. P. Lockyer, and J. C. Vickerman, "Comparing C 60 + and (H 2 O) n + clusters for mouse brain tissue analysis," *Surf. Interface Anal.*, no. November 2013, p. n/a–n/a, 2014.

[27] X. E. Wei, J. Korth, S. H. J. Brown, T. W. Mitchell, R. J. W. Truscott, S. J. Blanksby, M. D. P. Willcox, and Z. Zhao, "Rapid quantification of free cholesterol in tears using direct insertion/electron ionization-Mass spectrometry," *Investig. Ophthalmol. Vis. Sci.*, vol. 54, no. 13, pp. 8027–8035, 2013.

[28] E. Wright, L. Ng, and A. Guillozet-Bongarts, "Cerebral cortex and Purkinje cell layer," *Allen Bran Atlas Mouse Brain*, no. 118, pp. 1–14, 2007.

[29] M. a. Ward, B. B. Bendlin, D. G. McLaren, T. M. Hess, C. L. Gallagher, E. K. Kastman, H. a. Rowley, S. Asthana, C. M. Carlsson, M. a. Sager, and S. C. Johnson, "Low HDL cholesterol is associated with lower gray matter volume in cognitively healthy adults," *Front. Aging Neurosci.*, vol. 2, no. JUL, pp. 1–8, 2010.

[30] L. J. Whalley, R. T. Staff, a. D. Murray, S. J. Duthie, a. R. Collins, H. a. Lemmon, J. M. Starr, and I. J. Deary, "Plasma vitamin C, cholesterol and homocysteine are associated with grey matter volume determined by MRI in non-demented old people," *Neurosci. Lett.*, vol. 341, no. 3, pp. 173–176, 2003.

[31] C. Vitali, C. L. Wellington, and L. Calabresi, "HDL and cholesterol handling in the brain," *Cardiovasc. Res.*, vol. 103, no. 3, pp. 405–413, 2014.

[32] J. S. Fletcher, N. P. Lockyer, and J. C. Vickerman, "Molecular SIMS imaging; Spatial resolution and molecular sensitivity: Have we reached the end of the road? Is

there light at the end of the tunnel?," *Surf. Interface Anal.*, vol. 43, no. May 2010, pp. 253–256, 2011.

[33] P. Sjövall, J. Lausmaa, and B. Johansson, "Mass Spectrometric Imaging of Lipids on Single Cells," vol. 76, no. 15, p. 2, 2004.

[34] C. Bich, R. Havelund, R. Moellers, D. Touboul, F. Kollmer, E. Niehuis, I. S. Gilmore, and A. Brunelle, "Argon cluster ion source evaluation on lipid standards and rat brain tissue samples," *Anal. Chem.*, vol. 85, no. 16, pp. 7745–7752, 2013.

[35] E. A. Jones, N. P. Lockyer, and J. C. Vickerman, "Depth profiling brain tissue sections with a 40 keV C60 + primary ion beam," *Anal. Chem.*, vol. 80, no. 6, pp. 2125–2132, 2008.

[36] T. B. Angerer, M. P. Dowlathshahi, P. Malmberg, and J. S. Fletcher, "Improved Molecular Imaging in Rodent Brain with Time-of-Flight Secondary Ion Mass Spectrometry using Gas Cluster Ion Beams and Reactive Vapour Exposure," *Anal. Chem.*, p. 150323220819005, 2015.

[37] E. A. Jones, N. P. Lockyer, and J. C. Vickerman, "Mass spectral analysis and imaging of tissue by ToF-SIMS-The role of buckminsterfullerene, C60 +, primary ions," *Int. J. Mass Spectrom.*, vol. 260, no. 2–3, pp. 146–157, 2007.

[38] H. Tian, A. Wucher, and N. Winograd, "Molecular imaging of biological tissue using gas cluster ions," *Surf. Interface Anal.*, vol. 46, no. S1, pp. 115–117, 2014.

[39] R. H. Quarles, W. B. Macklin, and P. Morell, "Myelin Formation, Structure and Biochemistry," in *Basic Neurochemistry: Molecular, Cellular and Medical Aspects*, A. S. for Neurochemistry, Ed. Elsevier, Inc., 2006, pp. 51–73.

[40] J. M. Boggs, W. Gao, and Y. Hirahara, "Myelin glycosphingolipids, galactosylceramide and sulfatide, participate in carbohydrate-carbohydrate interactions between apposed membranes and may form glycosynapses between oligodendrocyte and/or myelin membranes," *Biochim. Biophys. Acta - Gen. Subj.*, vol. 1780, no. 3, pp. 445–455, 2008.

[41] N. Jackman, A. Ishii, and R. Bansal, "Myelin biogenesis and oligodendrocyte development: parsing out the role of glycosphingolipids," *Physiol.*, no. 860, pp. 290–297, 2009.

- [42] M. K. Passarelli, A. G. Ewing, and N. Winograd, "Measuring MALDI: Me-SIMS Reveals that Sublimation-based Samples Preparation Displaces Cholesterol and Enhances Galactocerebroside (GalCer) Signals," pp. 18–21.
- [43] E. E. Jones, S. Dworski, D. Canals, J. Casas, G. Fabrias, D. Schoenling, T. Levade, C. Denlinger, Y. a Hannun, J. a Medin, and R. R. Drake, "On-Tissue Localization of Ceramides and Other Sphingolipids by MALDI Mass Spectrometry Imaging," *Anal. Chem. (Washington, DC, United States)*, vol. 86, no. 16, pp. 8303–8311, 2014.
- [44] K. Venema, F. J. Quintero, J. M. Pardo, and J. P. Donaire, "The Arabidopsis  $\text{Na}^+/\text{H}^+$  exchanger AtNHX1 catalyzes low affinity  $\text{Na}^+$  and  $\text{K}^+$  transport in reconstituted liposomes," *J. Biol. Chem.*, vol. 277, no. 4, pp. 2413–2418, 2002.
- [45] X. Chen, W. Hua, Z. Huang, and H. C. Allen, "Interfacial water structure associated with phospholipid membranes studied by phase-sensitive vibrational sum frequency generation spectroscopy," *J Am Chem Soc*, vol. 132, no. 32, pp. 11336–11342, 2010.



## **7 Application of cluster ToF-SIMS imaging to the analysis of a transgenic mouse model infected with Alzheimer's disease**

With the analysis of wild type (WT) mouse brain tissue sections, it was concluded that  $(\text{H}_2\text{O})_{6000}^+$  and  $(\text{H}_2\text{O})\text{Ar}_{2000}^+$  clusters produced the highest secondary ion yields and reduced the matrix effect on cholesterol in the grey matter. It was also mentioned that there are technical and instrumental drawbacks to the application for pure water clusters and water-doped argon clusters to tissue imaging, such as life-time of the ion beam and the limited spatial resolution.

Considering the benefits and limitations of the assessed cluster ion beams, the possibility of studying an Alzheimer's disease case has been explored. Analysis of sections from a transgenic mouse model infected with Alzheimer's disease is reported in this chapter. The main indicator of the presence of this disease in the brain is the accumulation of extracellular amyloid beta (amyloid- $\beta$ ) protein in plaques [1], [2]. Such plaques were localised and analysed by registering images obtained with two techniques: fluorescence microscopy and ToF-SIMS. Multi-modal imaging studies offer the advantage of obtaining complementary information about a specimen. In this case, fluorescence microscopy and ToF-SIMS were correlated to identify and localise the senile plaques in mirror sections of brain tissue.

The histological staining dye Thioflavin S (ThioS) was used to localise amyloid- $\beta$  ( $\text{A}\beta$ ) plaques on specific brain regions with fluorescence microscopy. The identified regions containing plaques were localised in a mirror section for ToF-SIMS imaging. For this purpose, a series of images were acquired with 40 keV  $\text{C}_{60}^+$  and 20 keV  $(\text{H}_2\text{O})\text{Ar}_{2000}^+$ . Multivariate analysis techniques were also applied to ToF-SIMS images for the chemical characterisation of the areas with  $\text{A}\beta$  plaques.

### **7.1 Amyloid- $\beta$ plaques in Alzheimer's disease**

Alzheimer's disease (AD) is a neurodegenerative disease, responsible for about 60-70% cases of elderly dementia around the world. According to the Alzheimer's society in the UK, 1 in every 14 persons aged 65 years and over suffers from this condition [3]. This illness involves severe loss of memory, language, learning and perception of time and space, among other symptoms. It is a chronic illness that usually progresses for about 5-10 years, leading to death [4], [5]. The causes of this neurodegenerative

disorder are unknown. Some hypotheses have related the causes of AD to other diseases like hypertension or other genetic conditions. Scientists have been trying to find biomarkers that could lead to the early diagnosis of AD [4]–[7].

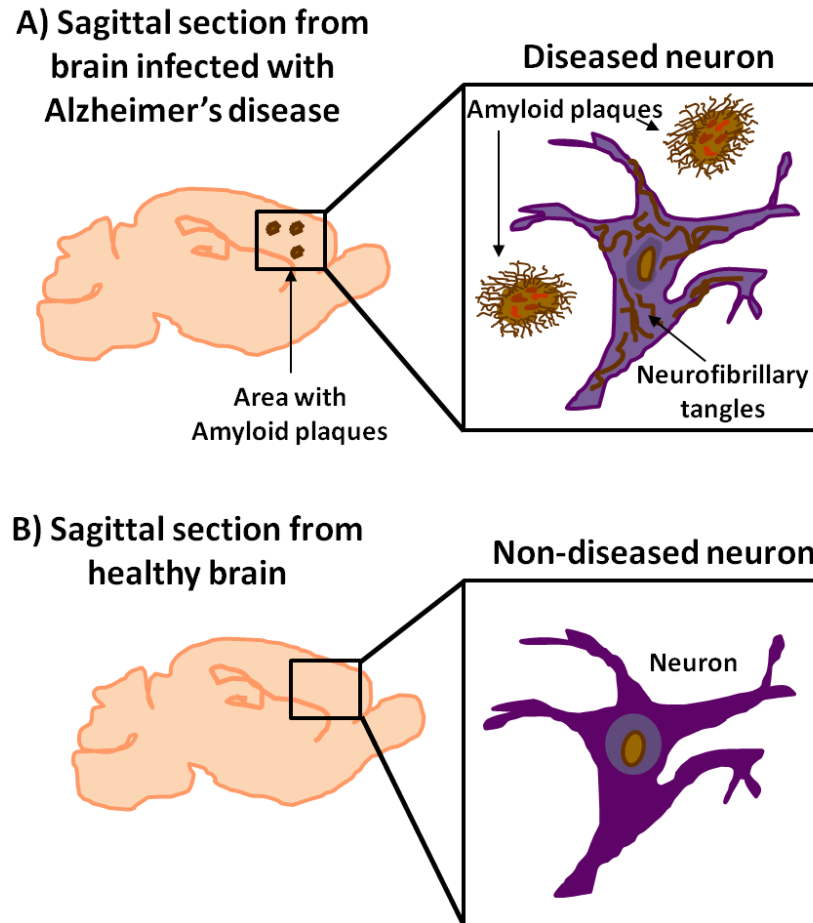


*Figure 7.1: (A) Diseased neuron with Alzheimer's disease (AD). (B) Non-diseased (healthy) neuron. Illustration (A) displays the effects of the disease on the generation of neurofibrillary tangles inside the neuron and the extracellular deposition of  $A\beta$  protein in plaques around the cortical and hippocampal regions [10].*

One of the main features of the advance of AD is the presence of amyloid aggregates and neurofibrillary tangles in the brain. Amyloid plaques are extracellular accumulations of fibrous protein, as displayed by Figure 7.1. These amyloid plaques are mainly composed of  $A\beta$  which is a fragment of the integral membrane amyloid precursor protein (APP) [1]. In a healthy organism, this  $A\beta$  protein fragment is eliminated. In a diseased brain,  $A\beta$  accumulates in insoluble plaques (Figure 7.1., A). Neurofibrillary tangles are protein fibres accumulated inside the neurons. These tangles are composed of tau protein, which is the responsible of building microtubules. In a normal brain, microtubules are the main internal transport system of nutrients and other substances across the neurons. In a sick brain, these microtubule structures

are damaged (Figure 7.1, B). Both, A $\beta$  plaques and neurofibrillary tangles interfere with normal neuronal functions and lead to disruption of neurons. Diseased neurons disconnect from each other, leading to memory loss and neuronal death [8], [9]. The reasons why these proteins are processed differently during AD and the precise mechanism of aggregation of amyloid plaques and neurofibrillary tangles are not fully understood yet [1], [2], [6], [8].

Post-mortem studies of patients with AD have shown that the areas of accumulation of A $\beta$  protein in senile plaques are the regions responsible of memory, attention and language. The first region affected by A $\beta$  plaques is the brain cortex (cortical and subcortical regions) including amygdala and nucleus basalis, followed by the hippocampal region and the striate area [11].

## 7.2 Transgenic mouse models in Alzheimer's disease

The unknown origins and poor prognosis of AD has lead to the development of transgenic mouse models to study this condition [12]. Animal models help to study the pathogenic mechanism of the disease.

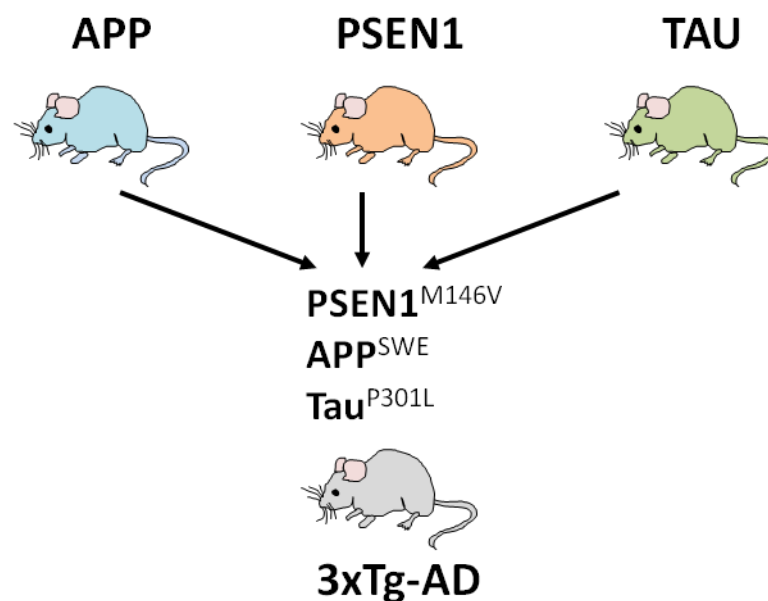


*Figure 7.2: The 3xTg-AD mouse model is generated from the expression of three mutant genes identified in AD: APP, PSEN1 and Tau. The name of each mouse strain is also included next to the gene: M146V for PSEN1, SWE for APP and P301L for Tau. [12].*

Less than 1% of the AD cases have been identified as hereditary. These cases are known as familial AD (FAD). In FAD, inherited mutations in three genes have been identified: APP, presenilin 1 (PSEN 1) and presenilin 2 (PSEN 2).

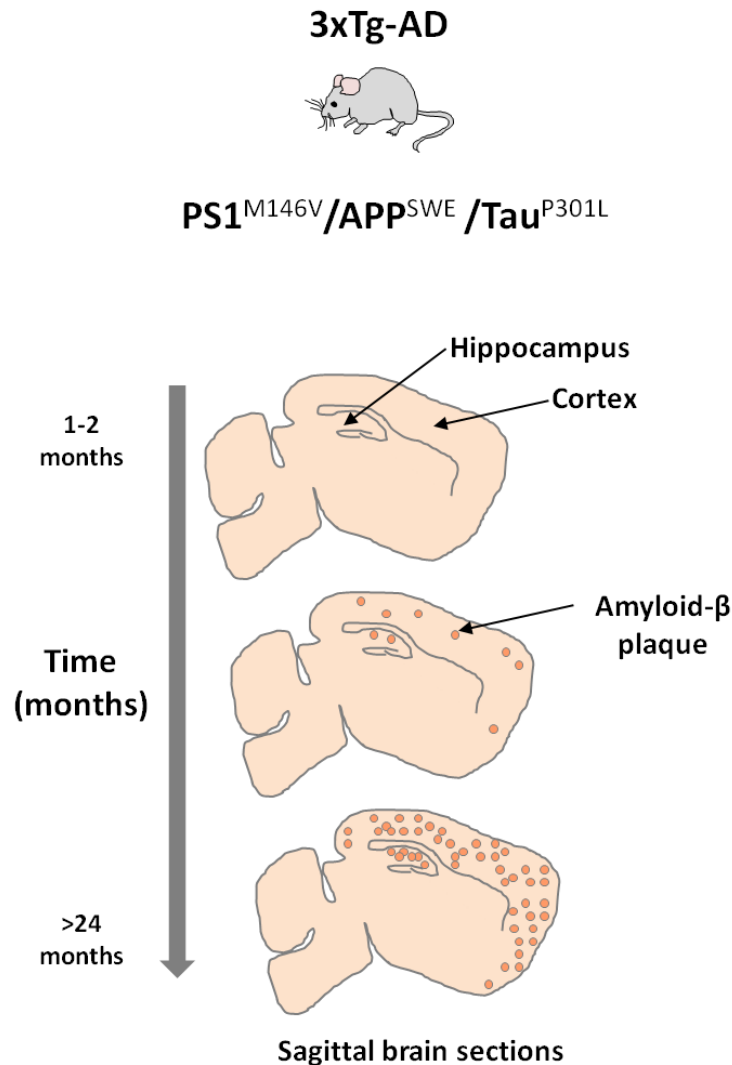


*Figure 7.3: Progression of AD in a mouse model brain. This mouse model is the combination of three genetic mutations: APP, PS1 and Tau. APP and PS1 have been identified as the genes responsible of encoding the proteins deposited in A $\beta$  plaques. The tau mutant mouse model reproduces the formation of neurofibrillary tangles. The combination of the three mutant genes leads to the generation of a 3xTg-AD mouse model. This mouse model develops plaques and tangles in hippocampus and cortex areas. These brain lesions get more prominent with the progression of the disease [12].*

Some of the pathogenic mutations of APP and the *gene* encoding the microtubule-associated protein tau (*MAPT*) have been expressed in transgenic mice. The genes APP and MAPT encode the proteins that are aggregated in A $\beta$  plaques. [13], [14]. In a transgenic mouse, the genome of the animal is modified by the artificial insertion of modified DNA (trans-gene). In the 3xTg-AD mouse model, the A $\beta$  plaques are

reproduced by expressing the mutation in APP and PSEN1, whereas the neurofibrillary tangles are induced by expressing the tau mutant [15]. Figure 7.2 shows the mutations of these three genes and the mice strains that are used for the gene expression [12]. In the 3xTg-AD mouse model, the progression of the disease occurs in hippocampus and cortex. A $\beta$  plaques and neurofibrillary tangles can be found mainly in hippocampus, amygdala and cortical areas, as shown in Figure 7.3. The generation of A $\beta$  plaques and neurofibrillary tangles reflects to some extent the development of AD in human patients [12].

### 7.3 Detection of neuritic plaques with ThioS labelling and fluorescence microscopy

Thioflavin T, Thioflavin S and congo red are histochemical dyes believed to interact with amyloid deposits. This interaction leads to the stain of the  $\beta$ -sheet structures from the amyloid protein, resulting in an increase in the fluorescence emission of those areas [16], [17].

ThioS is widely used to identify and classify the amyloid aggregates present in brain samples infected with AD. Stained neuritic plaques with thioS can be studied with fluorescence microscopy since the fluorochrome contained in thioS is excited by wavelengths of 430 nm, emitting a lower energy green light with wavelengths at 550 nm [18]. Neuritic plaques labelled by thioS appear as green fluorescent cores on the tissue, as illustrated in Figure 7.4.

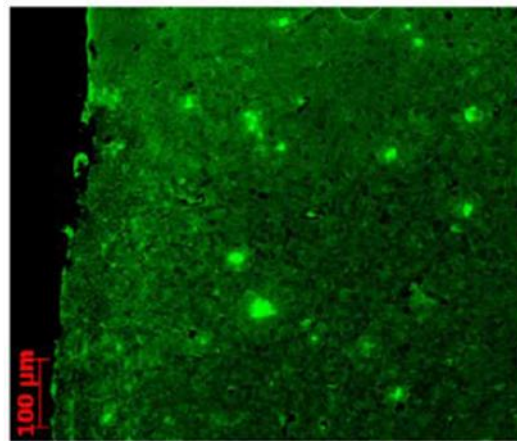


*Figure 7.4: Fluorescence microscopy image from a mouse brain section labelled with Thioflavin S. From the scale, it is possible to observe that the A $\beta$  plaques are less than 30  $\mu$ m in diameter. Modified and reprinted with permission from [19].*

They are recognised from the background tissue due to their contrasting brightness [19]. Morphological differences between plaques such as defined cores or diffused fibrils in senile plaques have different pathogenic significance for the development of treatments [2], [20].

#### **7.4 Aim of the experiments**

This series of experiments aim to study the identification and co-localisation of the A $\beta$  neuritic plaques in sagittal sections of 3xTg-AD mice with a multi-modal imaging approach. The neuritic plaques will be identified with thioS and examined with fluorescence microscopy. Once identified in a mirror section, the areas containing A $\beta$  plaques will be characterised with ToF-SIMS imaging.

ToF-SIMS images acquired with 40 keV C<sub>60</sub><sup>+</sup> and 20 keV (H<sub>2</sub>O)Ar<sub>2000</sub><sup>+</sup> will be registered with fluorescence microscopy images. The correlation of these two techniques will allow the specific localisation of the A $\beta$  plaques to obtain their chemical information. The information obtained will be validated with the analysis of a synthetic amyloid- $\beta$  peptide (1-40).

#### **7.5 ToF-SIMS imaging conditions**

SIMS images were acquired on 3xTg-AD sections with 40 kV C<sub>60</sub><sup>+</sup> and 20 keV (H<sub>2</sub>O)Ar<sub>2000</sub><sup>+</sup>. The experimental parameters were:

- Images from the complete tissue sections were acquired with 40 kV C<sub>60</sub><sup>+</sup> and a primary ion dose of  $1 \times 10^{12}$  ions cm<sup>-2</sup>. The spatial resolution was 7  $\mu$ m per pixel.
- High spatial resolution images of 1.5  $\mu$ m per pixel were acquired with 40 kV C<sub>60</sub><sup>+</sup> on specific cortical and hippocampal areas. The areas with neuritic plaques were determined by the localisation of A $\beta$  accumulations according to fluorescence microscopy. These images were acquired with  $2 \times 10^{12}$  ions cm<sup>-2</sup> primary ion dose.
- Analysis with 20 keV (H<sub>2</sub>O)Ar<sub>2000</sub><sup>+</sup> was performed on specific regions of the cerebral cortex and hippocampus. The primary ion dose applied to these images was  $2 \times 10^{12}$  ions cm<sup>-2</sup> and the spatial resolution was 4-5  $\mu$ m per pixel.

SIMS analyses of the synthetic peptide Amyloid-Beta (1 - 40), human were acquired with 40 kV C<sub>60</sub><sup>+</sup> and 20 keV (H<sub>2</sub>O)Ar<sub>2000</sub><sup>+</sup>. The primary ion dose used with both primary ion beams was  $2 \times 10^{12}$  ions cm<sup>-2</sup>.

### 7.5.1 *In-situ* localisation of Amyloid- $\beta$ plaques in brain sections from a triple transgenic mouse model infected with Alzheimer's disease

Mirror section 1 was stained with 1% ThioS and inspected with fluorescence microscopy (Figure 7.5). A tiled fluorescence image was acquired from the complete brain section to find the localisation of the A $\beta$  plaques. The identified areas with A $\beta$  plaques are highlighted with white rectangles and with white arrows. As expected in a 15 month old mouse, the A $\beta$  plaques are observed as brighter fluorescent cores located across the cerebral cortex. All A $\beta$  plaques found have specific location and were not localised outside the cortex and hippocampus.

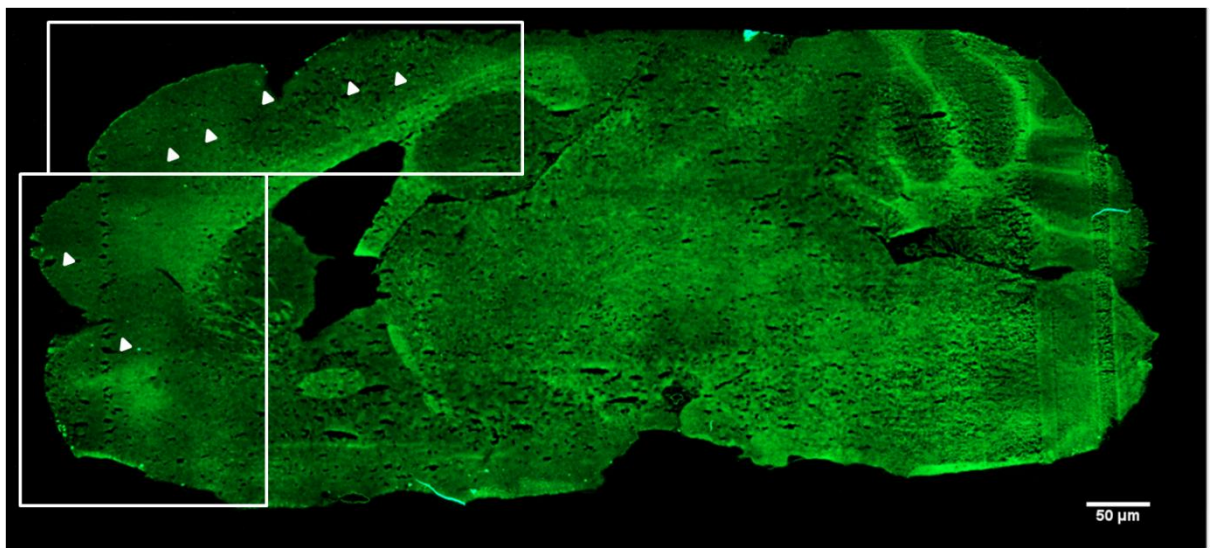


*Figure 7.5: Fluorescence microscopy image of a complete 3xTg-AD sagittal section labelled with 1% thioflavin S. The sample was imaged with fluorescence microscopy with magnification of x10 and a spatial resolution of 0.86  $\mu\text{m}$  per pixel.*

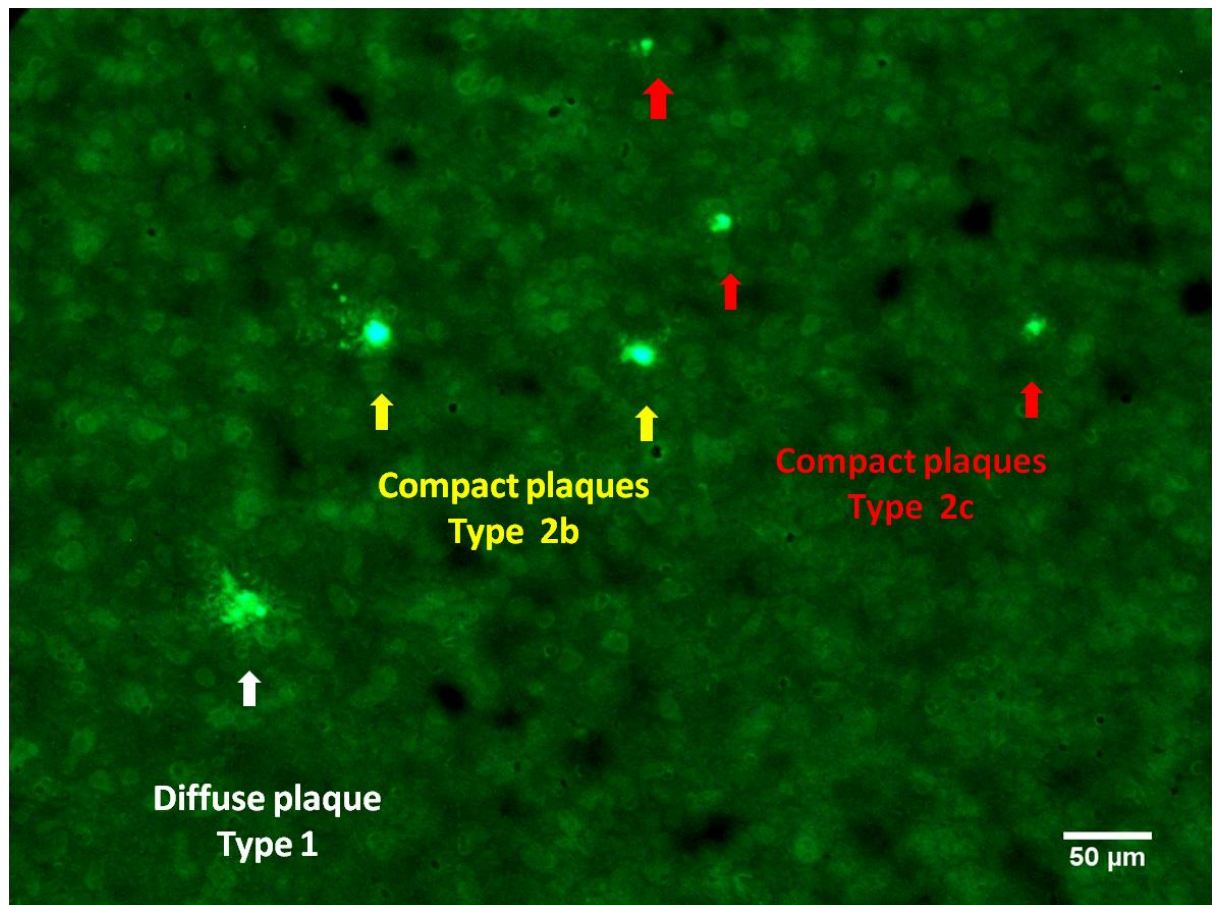
Cortical and hippocampal areas with neuritic plaques were explored further with a higher magnification of x20 and x40 to estimate the size and morphology classification of the A- $\beta$  plaques.

Figure 7.6 and Figure 7.7 display some of the plaques located on frontal and superior cortex. The morphology exposed by this neuritic plaques is in agreement with morphological classification of A $\beta$  plaques stained with thioS [2]. The identified plaques can be classified as follows:

- Type 1: diffuse plaques, mainly composed of a mesh of stained fibrils.
- Type 2a: plaques with small central cores, surrounded by fibrils simulating a corona.



- Type 2b: plaques with a dense central core and only a few fibrils around it
- Type 2c: burned-out plaques or very compact plaques are the brightest under fluorescence microscopy and do not have any fibrils around them.



*Figure 7.6: Neuritic plaques labelled with thioS found on the frontal brain cortex. The plaques are classified as: type 1, type 2b and 2c with an average diameter of 10-20  $\mu\text{m}$ . The image was obtained using a fluorescent microscope with x20 magnification and 0.53  $\mu\text{m}$  per pixel resolution.*

The neuritic plaques observed have different shapes and sizes. On average, the cored (types 2b and 2c) A $\beta$  plaques observed were 10  $\mu\text{m}$  (Figure 7.7). Some of the bigger aggregates were plaques with diffuse fibrils (types 1 and 2a) were about 20-30  $\mu\text{m}$  (Figure 7.7, A, B, C and D).

Mirror section 2 was analysed with ToF-SIMS and stained afterwards. Here, the neuritic plaques were localised on the same cortical areas identified in section 1. The fluorescence microscopy image obtained from section 2 was used to register with ToF-SIMS images, as described below.



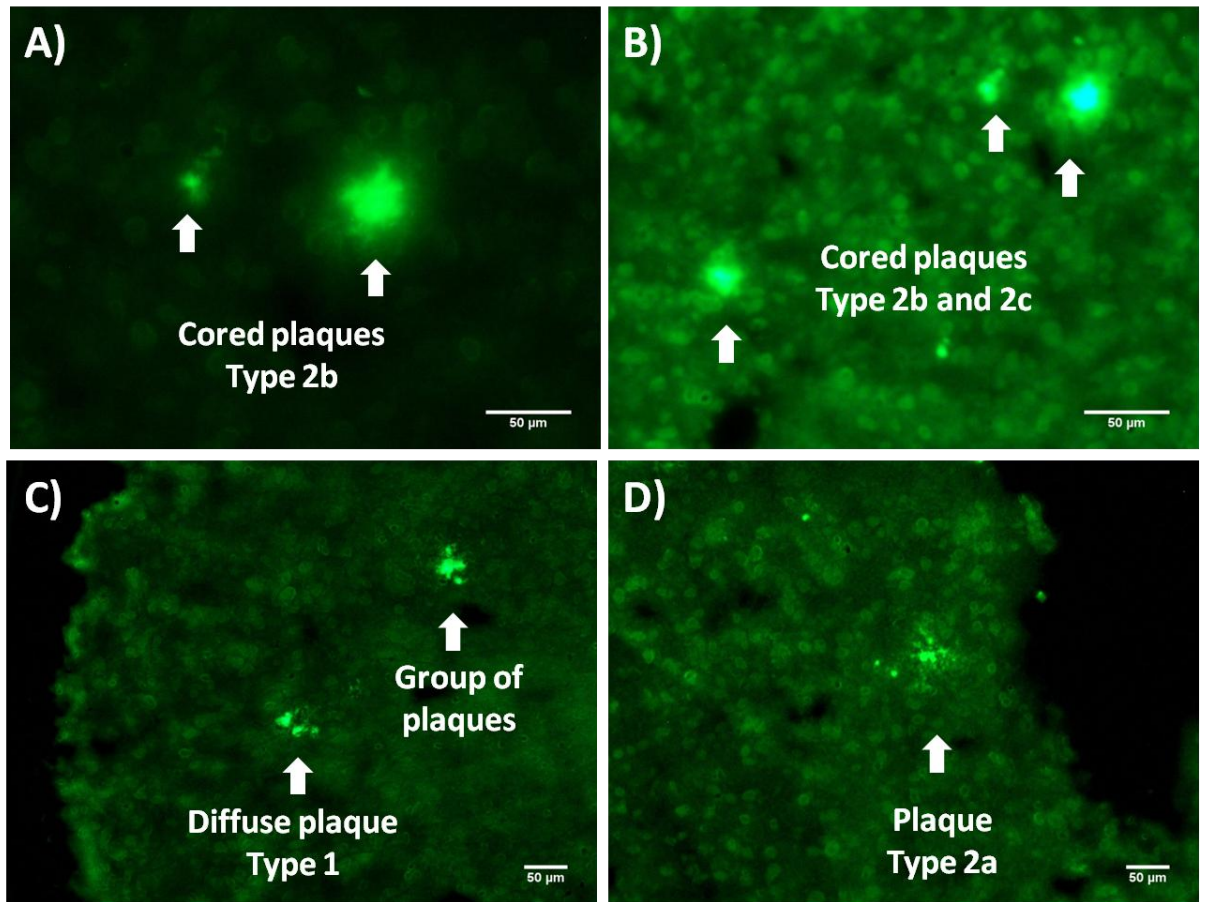


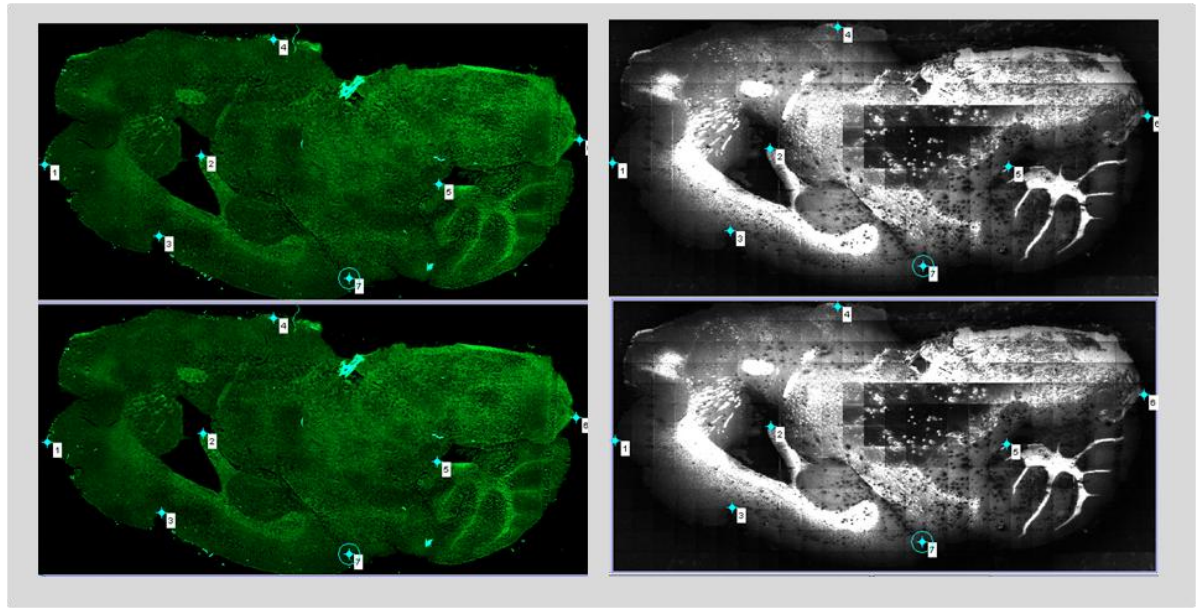
*Figure 7.7: A $\beta$  plaques dyed with 1% thioS and localised in frontal and superior (above hippocampus) brain cortex. (A) Cored plaques type 2b localised in superior cortex. (B) Cored plaques (Type 2b and 2c) localised above hippocampus. (C) Diffuse plaque type 1 and a group of 3 plaques type 2b localised in frontal cortex. (D) Plaque type 2a found in superior cortex. These images were acquired in a fluorescent microscope with the following magnification: (A) x40, (B) x40, (C) x 20 and (D) x20. Images with x40 magnification have 0.27  $\mu\text{m}$  per pixel spatial resolution and x20 images have 0.53  $\mu\text{m}$  per pixel spatial resolution.*

### 7.5.2 Fluorescence microscopy and ToF-SIMS image registration

Image registration is the process of aligning two (or more) images. In this process, one of the images is fixed and is the reference. The second image is transformed geometrically to align with the reference image. With brain section images, the registration is achieved by control point registration in MatLab® (The MathWorks Inc., Natick, Ma.).

This process starts by loading the images and identifying similar features from both data sets. In this case, images from the complete brain section show the anatomical features of the brain very clearly.

### A) Control points registration



### B) Registered image

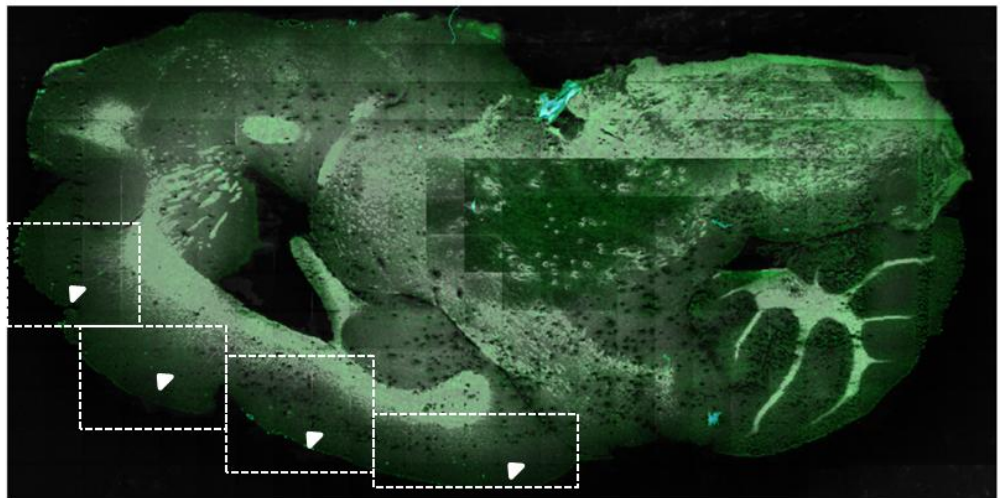


*Figure 7.8: (A) Selection of control points for the geometric transformation according to specific features of the brain's anatomy: foliation patterns in the cerebellum, superior cortex, inferior cortex and internal capsule. The points selected on the microscopy image are fixed points and the points selected on the SIMS fixed are moving points. (B) Registered image generated by overlapping of the fixed image (SIMS) and the image geometrically transformed (microscopy). The areas containing neuritic plaques are highlighted with white boxes and arrows.*

For example, the foliation patterns of the cerebellum, the localisation of the cerebral cortex and hippocampus can be used as regions of reference. With the *Control Point*

*Selection Tool* in MatLab®, it is possible to manually specify control points in a pair of images, as shown in Figure 7.8, (A). In the image presented, five pairs of control points were selected.

The control points selected on the fixed image are defined as fixed points, whereas the points determined for the moving image are moving points. A transformation matrix is created with the pairs of control points; this matrix is used to infer the geometric transformation. Thus, the transformation type needs to be specified i.e. an affine transformation. An affine transformation preserves co-linearity which refers to the preservation of points, lines and planes. Affine transformations include: translation, rotation, isotopic scaling, reflection and shear [22], [23].

The transformation matrix is then applied to the microscopy image (moving image) with the function 'imwarp'. The transformed image is then overlapped with the fixed image to generate one single registered image, as displayed in Figure 7.8, (B).

Image registration is just a preliminary step for the characterisation of the A $\beta$  plaques. Image registration (Figure 7.8, B) will lead to the co-localisation of the neuritic plaques in the SIMS image.

### 7.5.3 Study of Amyloid- $\beta$ plaques *in situ*

In the registered image (Figure 7.8, B) the neuritic plaques were localised in the frontal and superior cortex. In the SIMS image, the secondary ion signal detected from regions with plaques is less intense than the signal detected from the surrounding tissue. This results in the visualisation of the A $\beta$  plaques as dark areas in the total ion image. This effect was previously reported by Solé-Domènech *et al.* [24].

Following the identification, higher spatial resolution images (1.5  $\mu\text{m}/\text{pixel}$ ) from the brain cortex were acquired with 40 keV C $_{60}^{+}$ . This is the only primary ion beam currently in the J105-3D Chemical Imager that can be focused down to 1-2  $\mu\text{m}/\text{pixel}$ . The total ion images obtained were registered with fluorescence microscopy images. Regions-of-interest (ROI) containing plaques were identified and compared to regions that did not show the presence of plaques (control).

Figure 7.9 shows two ROIs and the spectra from both regions. Although the mass range of these spectra was recorded up to 1000 Da, most ion peaks were detected in the mass range 50-300 Da.

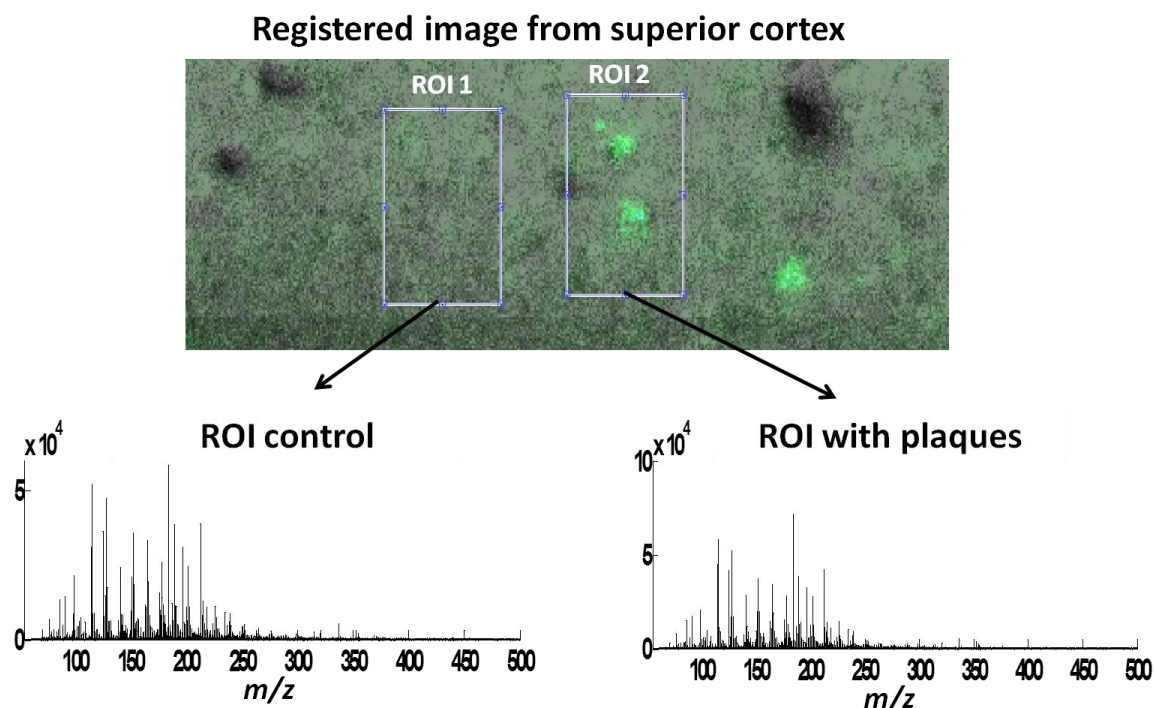


Figure 7.9: Selected regions-of-interest of areas from the cortex with and without the presence of A $\beta$  plaques. The areas of interest were selected on the registered image (SIMS and fluorescence microscopy) and total ion spectra were extracted from both regions. The regions-of-interest are identical in size and were deliberately selected in close proximity to minimise the chemical variation caused by different anatomical features.

Ions with masses higher than 400 Da were not detected. The absence of ion peaks from high masses can be attributed to the fragmentation caused by the high energy of the C<sub>60</sub><sup>+</sup> beam.

The spectra from Figure 7.9 are very similar and it is difficult to recognise any obvious differences between them. To visualise any differences more clearly, the spectrum taken from the region without plaques (control) was subtracted from the spectrum from the ROI with plaques. The spectral subtraction only highlights the changes in ion peaks from both regions. Figure 7.10 displays the spectrum result from this subtraction. This spectrum resulting from the subtraction could potentially indicate some ions present in the A $\beta$  plaques. From Figure 7.10, the ion peaks plotted as positive in the Y axis belong to the ROI with plaques. Some of the peaks observed are lipid fragments, such as phosphocholine [C<sub>5</sub>H<sub>15</sub>NO<sub>4</sub>P]<sup>+</sup> at  $m/z$  184 and the phosphocholine fragment [C<sub>2</sub>H<sub>6</sub>PO<sub>4</sub>]<sup>+</sup> at  $m/z$  125. Other peaks observed such as  $m/z$  86.1, 128.1, 156.1 and 222.2 could be assigned as amino acid fragments derived from the A $\beta$  protein.



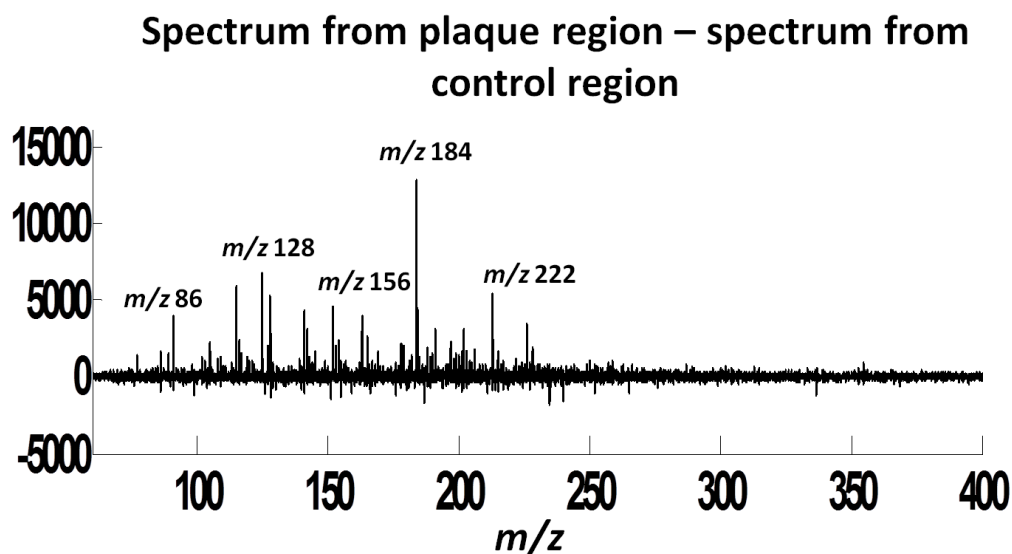


Figure 7.10: Spectrum resulting from the spectra from ROI with plaques minus the ROI without plaques. The labels refer to possible ions identified: phosphocholine ion  $[C_5H_{15}NO_4P]^+$  at  $m/z$  184, Leu or Ile at  $m/z$  86, Ala-Gly, Gln or Lys at  $m/z$  128, Gly-Val at  $m/z$  156 and Asp-Al at  $m/z$  222.

Four different ROIs including single A $\beta$  plaques were studied. The area of these new regions was selected so that the plaques studied without selecting much of the surrounding tissue. The overlaid spectra from these regions are displayed in Figure 7.11.

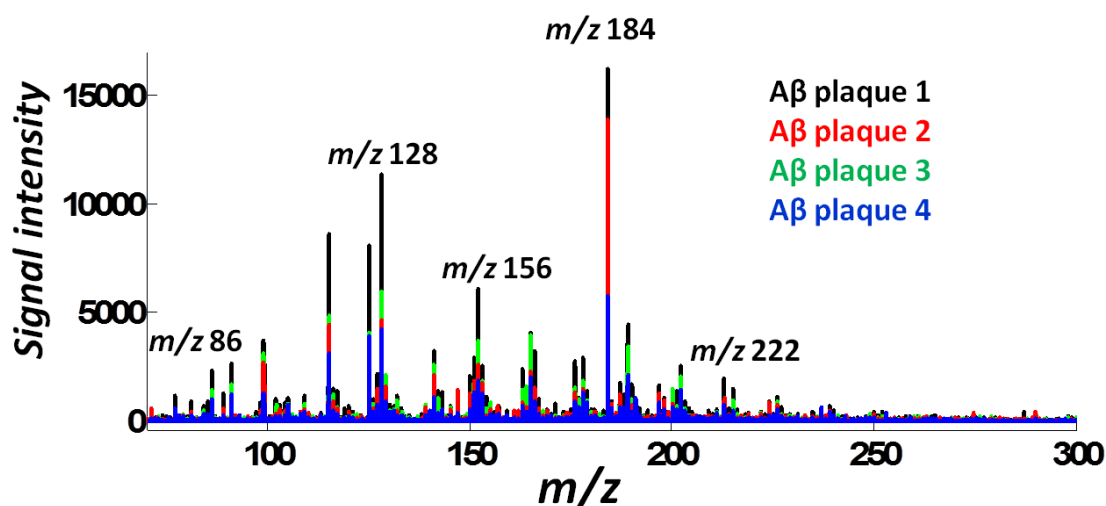


Figure 7.11: Overlaid spectra obtained from four different ROIs with A $\beta$  plaques. The areas were selected to cover the plaques and the least possible amount of surrounding tissue. The observed ions peaks are similar than those observed in the subtracted spectrum (Figure 7.10). The labels refer to possible ions identified: phosphocholine ion  $[C_5H_{15}NO_4P]^+$  at  $m/z$  184, Leu or Ile at  $m/z$  86, Ala-Gly, Gln or Lys at  $m/z$  128, Gly-Val at  $m/z$  156 and Asp-Al at  $m/z$  222.

The ion peaks observed are similar to those found in the subtracted spectrum (Figure 7.10) and are included in Table 7.1. The same peaks that could be assigned A $\beta$  fragments ( $m/z$  86.1, 128.1, 156.1 and 222.2) were found in this four plaque regions.

To validate the peak assignment of ions observed in tissue, the synthetic A $\beta$  peptide which is a fragment (1-40) of the A $\beta$  protein was analysed with 40 keV C<sub>60</sub><sup>+</sup> and 20 keV (H<sub>2</sub>O)Ar<sub>2000</sub><sup>+</sup>. The spectrum result from the analysis with 40 keV C<sub>60</sub><sup>+</sup> is shown in Figure 7.12, together with the amino acid sequence of the peptide.

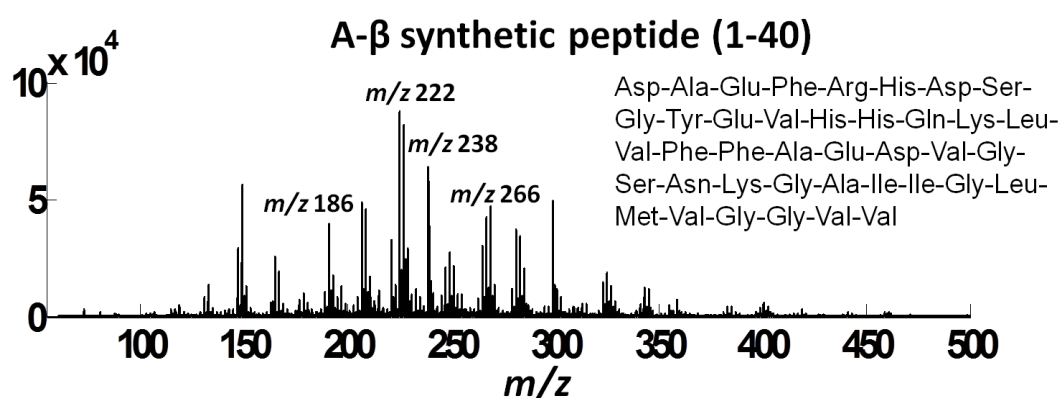


Figure 7.12: Total ion spectrum of Amyloid- $\beta$  synthetic peptide (1-40) acquired with 40 keV C<sub>60</sub><sup>+</sup>. The primary ion dose used was  $2 \times 10^{12}$  ions cm<sup>-2</sup>.

The total ion spectrum shows many fragments from the peptide, most of them with masses below 500 Da. The possible amino acid fragments and dipeptides obtained from the A $\beta$  spectrum and observed on the spectra from tissue with both 40 keV C<sub>60</sub><sup>+</sup> and 20 keV (H<sub>2</sub>O)Ar<sub>2000</sub><sup>+</sup>, are listed in Table 7.1.

In Figure 7.12, the ion  $m/z$  86.1 is assigned as a leucine or isoleucine fragment,  $m/z$  128.1 as glutamine, lysine or the dipeptide alanine-glycine, the ion  $m/z$  156.1 as the dipeptide glycine-valine and  $m/z$  222.2 as aspartic acid-alanine dipeptide [25]–[27].

Figure 7.11 indicates the presence of small amino acid fragments and dipeptides possibly derived from the A $\beta$  protein on tissue. Tripeptides were not identified in the tissue spectra with either 40 keV C<sub>60</sub><sup>+</sup> or 20 keV (H<sub>2</sub>O)Ar<sub>2000</sub><sup>+</sup>, thus they are not included in the peak list.

The comparison between control regions and regions with plaques was also done for analyses acquired with (H<sub>2</sub>O)Ar<sub>2000</sub><sup>+</sup>.

Amino acid fragments obtained from synthetic A $\beta$ peptide (1-40)	<i>m/z</i>	Primary ion beam used for tissue analysis in which the ion was observed
Leu or Ile	86.1	C <sub>60</sub> , (H <sub>2</sub> O)Ar <sub>2000</sub>
Asn or Gly	87.1	C <sub>60</sub>
Glu	102.1	C <sub>60</sub> , (H <sub>2</sub> O)Ar <sub>2000</sub>
Met	104.1	C <sub>60</sub> , (H <sub>2</sub> O)Ar <sub>2000</sub>
Gly-Gly or Asn	114.1	C <sub>60</sub> , (H <sub>2</sub> O)Ar <sub>2000</sub>
Ala-Gly, Gln or Lys	128.1	C <sub>60</sub> , (H <sub>2</sub> O)Ar <sub>2000</sub>
Gly-Val	156.1	C <sub>60</sub> , (H <sub>2</sub> O)Ar <sub>2000</sub>
Gly-Ala	164.16	C <sub>60</sub> , (H <sub>2</sub> O)Ar <sub>2000</sub>
Gly-Ser	180.14	C <sub>60</sub> , (H <sub>2</sub> O)Ar <sub>2000</sub>
Ala-Asp or Glu-Gly	186.1	C <sub>60</sub> , (H <sub>2</sub> O)Ar <sub>2000</sub>
Gly-Val	192.22	C <sub>60</sub>
Gly-Leu	206.25	C <sub>60</sub> , (H <sub>2</sub> O)Ar <sub>2000</sub>
Ala-Ile	220.28	C <sub>60</sub> , (H <sub>2</sub> O)Ar <sub>2000</sub>
Gly-Lys	221.26	C <sub>60</sub> , (H <sub>2</sub> O)Ar <sub>2000</sub>
Asp-Al	222.21	C <sub>60</sub> , (H <sub>2</sub> O)Ar <sub>2000</sub>
Ala-Glu	236.23	C <sub>60</sub> , (H <sub>2</sub> O)Ar <sub>2000</sub>
Ser-Asn	237.21	C <sub>60</sub> , (H <sub>2</sub> O)Ar <sub>2000</sub>
Asp-Ser	238.2	C <sub>60</sub> , (H <sub>2</sub> O)Ar <sub>2000</sub>

Leu-Val	248.33	$C_{60}, (H_2O)Ar_{2000}$
Asp-Val	250.26	$C_{60}, (H_2O)Ar_{2000}$
His-Asp	254.28	$C_{60}, (H_2O)Ar_{2000}$
Gly-Tyr	256.26	$C_{60}, (H_2O)Ar_{2000}$
Glu-Val	264.28	$C_{60}, (H_2O)Ar_{2000}$
Met-Val	266.36	$C_{60}, (H_2O)Ar_{2000}$
Lys-Leu	277.37	$C_{60}, (H_2O)Ar_{2000}$
Asn-Lys	278.31	$C_{60}, (H_2O)Ar_{2000}$
Glu-Asp	280.23	$(H_2O)Ar_{2000}$
Met-Leu	280.38	$C_{60}, (H_2O)Ar_{2000}$
Val-Phe	282.34	$(H_2O)Ar_{2000}$
His-Asp	288.27	$C_{60}, (H_2O)Ar_{2000}$
Gln-Lys	292.34	$C_{60}, (H_2O)Ar_{2000}$
His-Gln	301.31	$(H_2O)Ar_{2000}$
Glu-Phe	312.32	$(H_2O)Ar_{2000}$
Tyr-Glu	328.32	$(H_2O)Ar_{2000}$
Arg-His	329.36	$(H_2O)Ar_{2000}$
Phe-Phe	330.38	$(H_2O)Ar_{2000}$
Phe-Arg	339.39	$(H_2O)Ar_{2000}$

*Table 7.1: Possible amino acid fragments observed in the Amyloid- $\beta$  synthetic peptide (1-40) standard acquired with 40 keV  $C_{60}^+$  and 20 keV  $(H_2O)Ar_{2000}^+$  [25]–[27].*

Figure 7.13 shows two of the regions selected on the registered image for spectra comparison. One of the regions contains one A $\beta$  plaque whereas the second ROI is nearby but does not contain any visible plaques according to fluorescence microscopy. The spectrum resulting from the subtraction of both regions, it is possible to observe



the presence of more phosphocholine  $[C_5H_{15}NO_4P]^+$  at  $m/z$  184 and more cholesterol  $[M-H_2O+H]^+$  at  $m/z$  369 in the region containing A $\beta$  plaques. Peak ions at  $m/z$  104.1 relate to a glycine dipeptide or a fragment from asparagine. A peak at  $m/z$  236.2 could be assigned to the dipeptide alanine-glutamic acid, and  $m/z$  329.3 to the dipeptide arginine-histadine (all ion peaks observed are listed in Table 7.1).

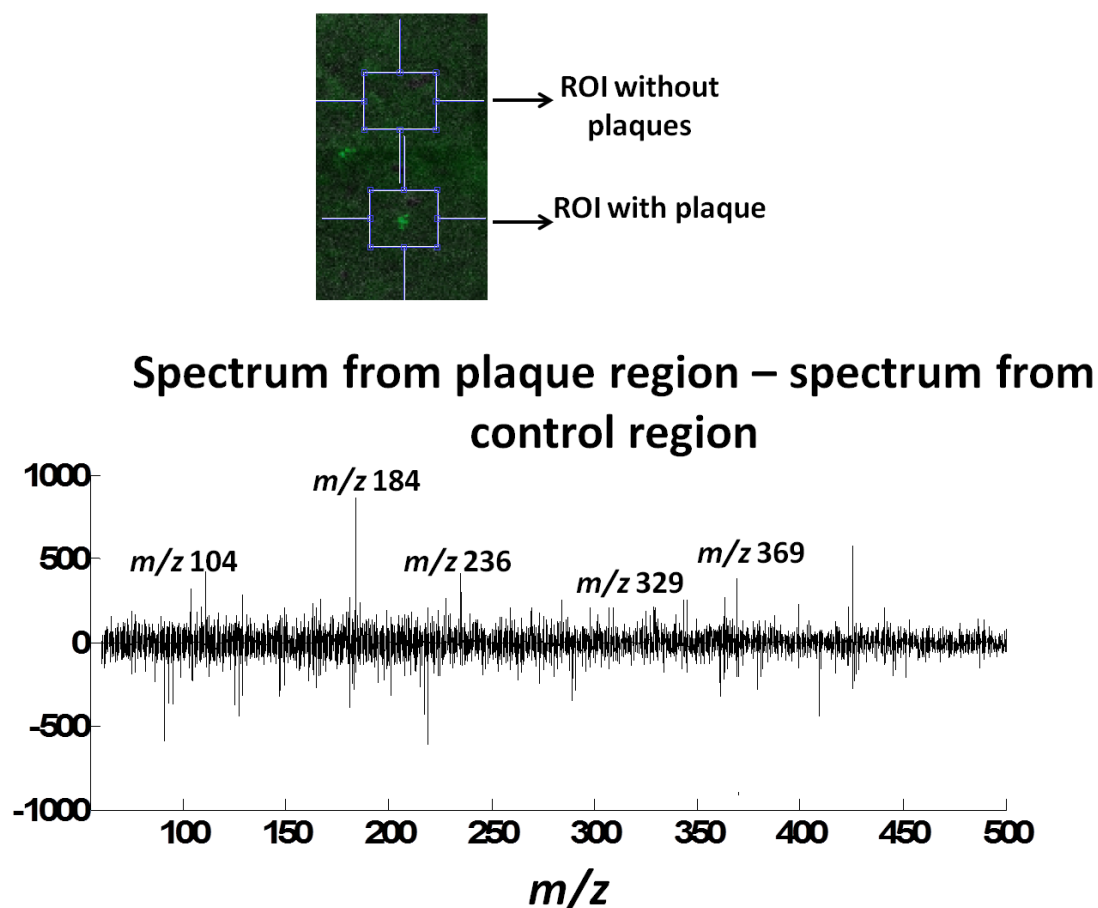


Figure 7.13: Spectrum resulting from the ROI with plaques minus the spectrum taken from the region without plaques. The areas of interest were selected on the registered image (SIMS and fluorescence microscopy) and total ion spectra were extracted from both regions. The labels refer to possible ions identified: phosphocholine ion  $[C_5H_{15}NO_4P]^+$  at  $m/z$  184, cholesterol fragment  $[M-H_2O+H]^+$  at  $m/z$  369], the ion  $m/z$  104.1 relates to a Gly-Gly or Asn, the peak at  $m/z$  236.2 is Ala-Glu and the ion at  $m/z$  329.3 could be assigned as Arg-His.

If 20 keV  $(H_2O)Ar_{2000}^+$  is used as the analysis beam, bigger ion species are detected, implying less fragmentation when compared to the results obtained with 40 keV  $C_{60}^+$ . As displayed in Figure 7.13, the detection of cholesterol  $[M-H_2O+H]^+$  is observed during  $(H_2O)Ar_{2000}^+$  bombardment. This matches the higher detection of cholesterol previously observed in brain cerebellum with water-containing ion beam (section 6.5.3). This

study illustrates a practical benefit of this phenomenon. This ion has higher secondary ion counts in the areas with A $\beta$  plaques.

This effect has been observed in previous studies on AD human and mice samples studied with ToF-SIMS [24], [28].

#### **7.5.4 Detection of cholesterol in areas with A $\beta$ plaques**

High levels of cholesterol in the grey matter have been linked to the A $\beta$  in the past, although the specific causes of the relationship between cholesterol and the A $\beta$  protein are yet to be established [26], [28], [29], [30].

Studies based in human trials showed that increased cholesterol levels present in neuronal membranes lead to the incorporation of A $\beta$  peptides in membranes. Cholesterol molecules in membranes have a binding affinity for A $\beta$  peptides. This binding produces neurotoxic oligomers, which eventually induces cell death [30]. Thus, the detection of cholesterol in the vicinity of the neuritic plaques has been matter of interest among the scientific community.

Cholesterol is distributed in cell membranes in specific subdomains called lipid rafts [31]. These lipid rafts are built of cholesterol and glycosphingolipids. These lipid rafts are present in a large fraction of the membranes and are involved in the regulation of signal transduction in cell signalling [31]. Hence, elevated levels of cholesterol in the brain could reflect the cholesterol changes in the lipid rafts. In addition to cholesterol levels, sphingolipids which are also present in lipid rafts, may also play an important role in the progression of AD [30], [32].

Previous ToF-SIMS experiments in cortical and hippocampal regions of transgenic mice [24] and human brain biopsies [28], have shown accumulations of cholesterol [M+H]<sup>+</sup> and [M-H<sub>2</sub>O+H]<sup>+</sup> surrounding the A $\beta$  deposits. However, the distribution of cholesterol in the cerebral cortex as the disease develops is still uncertain [28].

With 40 keV C<sub>60</sub><sup>+</sup> analysis on 3xTg-AD tissue, only a few counts of the cholesterol molecular ion [M+H]<sup>+</sup> at  $m/z$  385 or the cholesterol fragment [M-H<sub>2</sub>O+H]<sup>+</sup> at  $m/z$  369 were detected around the cortex. This low cholesterol signal intensity was not enough to generate single ion images of this molecule. ROI-PCA was then applied to the images to try to identify the localisation of cholesterol. The PCA results showed that PC2 identified the chemical differences between regions enriched with a cholesterol fragment and a phosphocholine fragment, as displayed in Figure 7.14. The cholesterol

fragment was observed as  $[C_{16}H_{21}]^+$  at  $m/z$  213 and the phosphocholine fragment as  $[C_2H_6PO_4]^+$  at  $m/z$  125. Figure 7.14 shows the distribution of the cholesterol fragment in red and the phosphocholine fragment in green. The concentration of cholesterol is visibly higher towards the white matter and lower in the pial surface. This is expected since there is more cholesterol concentrated in the white matter area due to the axons present in this region. The pial surface contains dendrites from neurons present in other cortical layers. The cortical internal layers in between the white matter and the pial surface are the layers. These multiform and pyramidal layers contain the cell bodies of pyramidal neurons, thus, high concentration of phosphocholine is expected in these regions [33].

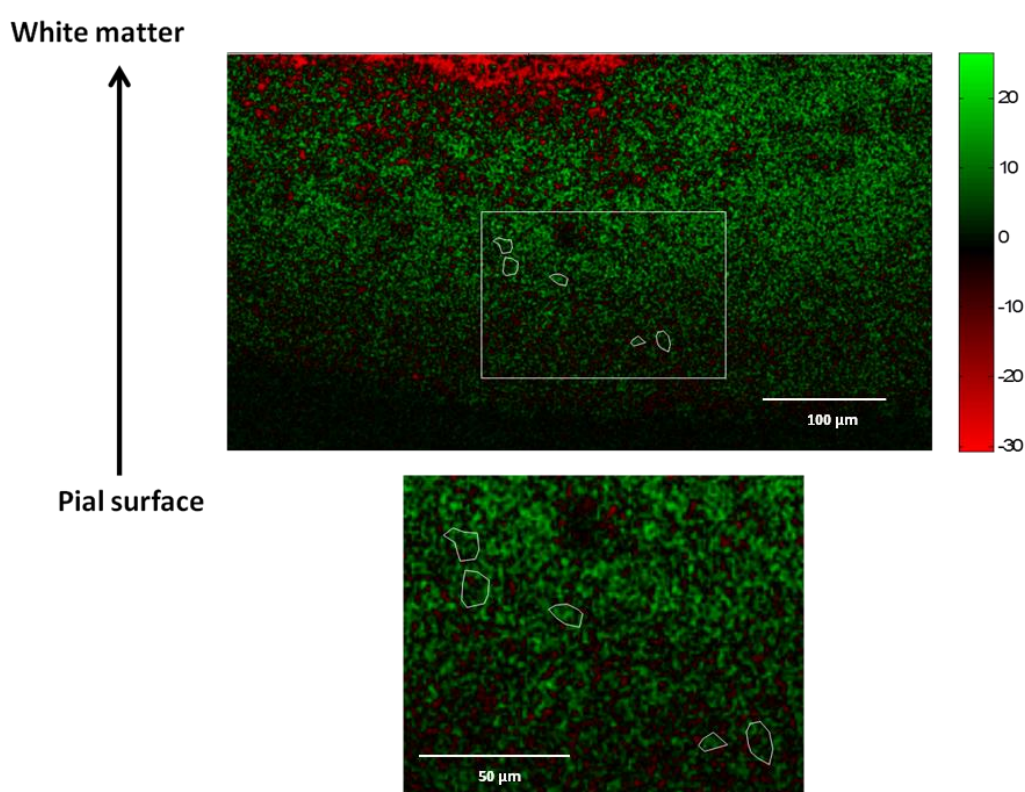


Figure 7.14: Score image from PC2 generated from the ROI-PCA analysis of a 40 keV  $C_{60}^+$  image. This image covers a  $500 \times 400 \mu m$  region of the cortex located above the hippocampus. The score shows the distribution of the cholesterol fragment  $[C_{16}H_{21}]^+$  at  $m/z$  213 in red and a phosphocholine fragment  $[C_2H_6PO_4]^+$  at  $m/z$  125. The localisation of the  $A\beta$  plaques is highlighted in white and magnified for better visualisation. The concentration of the cholesterol ions is higher towards the white matter. Cholesterol is not specifically localised around the plaques, as showed by Solé-Domènech et al. [24].

The localisation of  $A\beta$  plaques were drawn in Figure 7.14, taking the registered SIMS and microscopy image as reference. The few counts of cholesterol fragments are distributed close to the plaques but they are not specifically localised around them, like

the data shown by Solé-Domènech et al. [24]. It is likely that the sensitivity for cholesterol is low.

ROI-PCA analysis was also applied to the image acquired with  $(\text{H}_2\text{O})\text{Ar}_{2000}^+$  on the frontal cortex. PC2 also showed the distribution of cholesterol and phosphocholine, as shown in Figure 7.15.

The distribution of cholesterol and phosphocholine shown by the image score is opposite to the separation obtained for the 40 keV  $\text{C}_{60}^+$  image. Here, cholesterol is detected as the  $[\text{M}-\text{H}_2\text{O}+\text{H}]^+$  fragment at  $m/z$  369, whereas the phosphocholine head group is observed as  $[\text{C}_5\text{H}_{15}\text{NO}_4\text{P}]^+$  at  $m/z$  184. In the score image it is possible to observe that the distribution of cholesterol is not only in the vicinity of the  $\text{A}\beta$  plaques, but also throughout the cortex. If we consider that the cortex in the brain is composed of grey matter [33], this result could be directly related to the ion suppression on cholesterol in the grey matter observed in the analysis of the brain's cerebellum (Section 6.5.3). This matrix effect might be reduced by using 20 keV  $(\text{H}_2\text{O})\text{Ar}_{2000}^+$  for analysis.

This suppression effect can be demonstrated with the detection of cholesterol at  $m/z$  369 with 20 keV  $(\text{H}_2\text{O})\text{Ar}_{2000}^+$ , which is significantly higher than the smaller cholesterol fragment  $m/z$  213 detected with 40 keV  $\text{C}_{60}^+$ . In relation to AD, this could mean that cholesterol is not only present around the  $\text{A}\beta$  plaques but also all over the tissue. Moreover, an elevated presence of cholesterol, would lead to more production of neurotoxic oligamers, thus, more extracellular accumulation of  $\text{A}\beta$  plaques [30]. There could also be interaction between cholesterol and  $\text{A}\beta$  peptides, although further experimentation is needed to validate this theory.

For example, after the acquisition of ToF-SIMS images, the sample could be stained Filipin [34] which is specific for cholesterol in addition to ThioS for amyloid aggregates. A fluorescence microscopy image can be obtained and registered with ToF-SIMS images for the accurate co-localisation and characterisation *in situ* of both cholesterol and  $\text{A}\beta$  plaques.

The analysis the cortical region of a wild type (non-transgenic) brain with 20 keV  $(\text{H}_2\text{O})\text{Ar}_{2000}^+$  could be used to quantify and compare the amount of cholesterol found in specific cortical regions. Up to now, only the cerebellum area has been analysed with 20 keV  $(\text{H}_2\text{O})\text{Ar}_{2000}^+$ , as presented in section 6.5.3. This could aid understanding of relationship between the distribution of cholesterol and the development of AD.

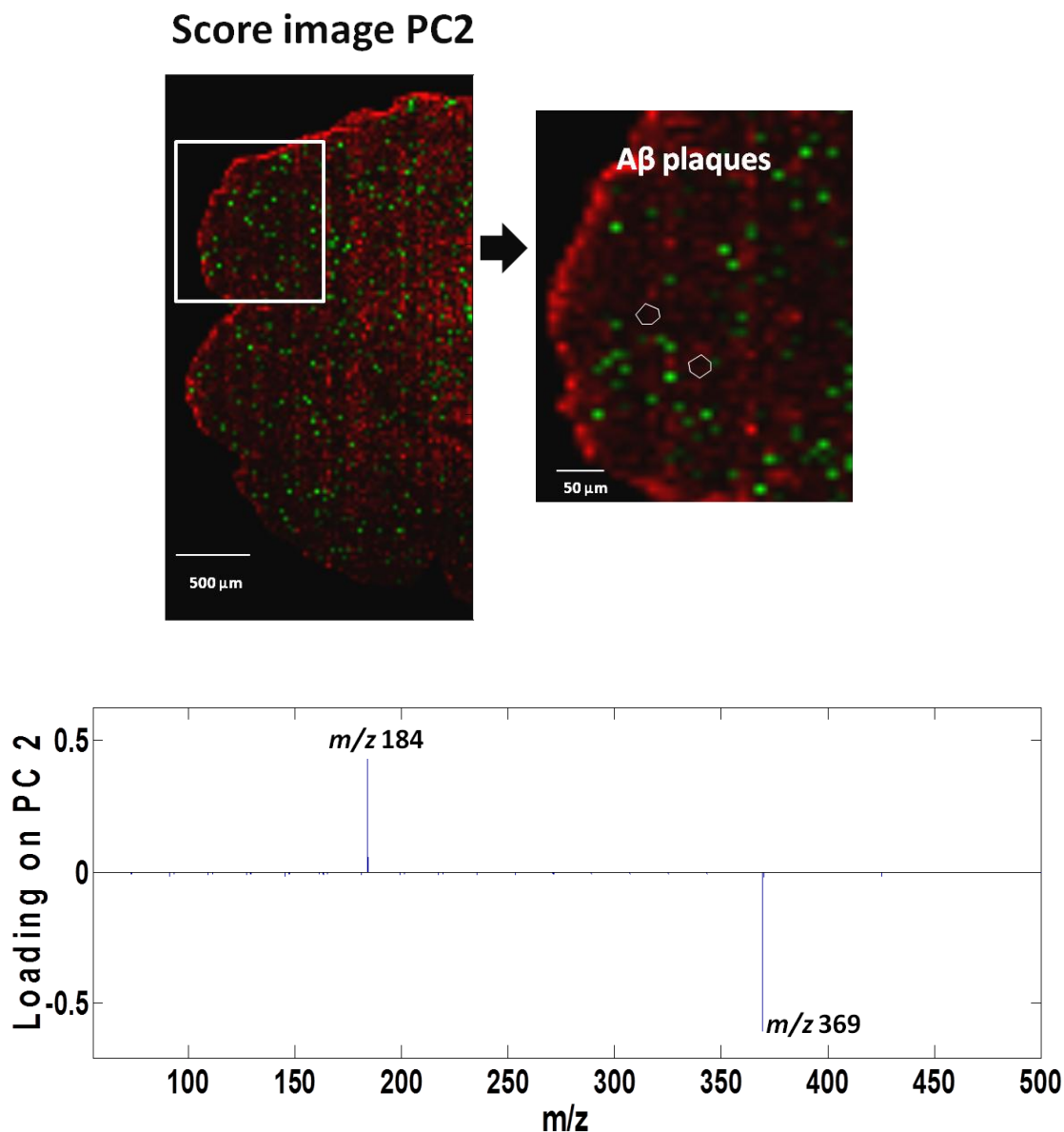


Figure 7.15: Score image and loading from PC2 on the 20 keV  $(\text{H}_2\text{O})\text{Ar}_{2000}^+$  image from a region of the frontal cortex. The score shows the distribution of the cholesterol fragment  $[\text{M}-\text{H}_2\text{O}+\text{H}]^+$  at  $m/z$  369 in red and the phosphocholine fragment  $[\text{C}_5\text{H}_{15}\text{NO}_4\text{P}]^+$  at  $m/z$  184 in green. The localisation of the  $\text{A}\beta$  plaques is drawn in white according to the registered SIMS-microscopy image and it is highlighted in white circles.

To verify the results from PC2, a single ion image of the cholesterol ion  $[\text{M}-\text{H}_2\text{O}+\text{H}]^+$  was generated for the frontal cortical area with  $(\text{H}_2\text{O})\text{Ar}_{2000}^+$ , as illustrated in Figure 7.16. As shown in the score image from PC2 (Figure 7.15) the distribution of cholesterol is more uniform across the cortex when compared to  $\text{C}_{60}^+$ . There is not clear separation of the grey matter (cortex) and white matter (corpus callosum).

### Cholesterol single ion image

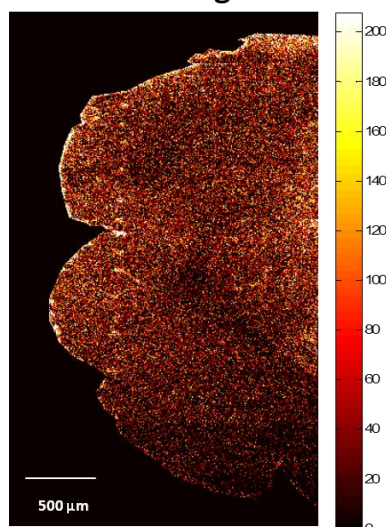


Figure 7.16: Single ion image of the cholesterol ion  $[M-H_2O+H]^+$  at  $m/z$  369. The area shown on this image is the frontal cortex of the brain. The distribution of this molecule is uniform across grey and white matter, thus, the anatomical structures are not visible.

## 7.6 Summary

Analysis of 3xTg-AD mouse brain tissue was performed with 40 keV  $\text{C}_{60}^+$  and 20 keV  $(\text{H}_2\text{O})\text{Ar}_{2000}^+$ . Parallel to the mass spectrometry analysis, mirror serial sections were stained with 1% thioflavin S and analysed with fluorescence microscopy. The resulting images from both techniques were registered to co-localise the  $\text{A}\beta$  plaques on the SIMS images.

Characterisation of the  $\text{A}\beta$  plaques *in situ* involved the analysis of spectra from regions-of-interest containing  $\text{A}\beta$  plaques and regions without plaques. The spectral subtraction from the two regions resulted in the identification of possible amino acid fragments derived from the  $\text{A}\beta$  peptide. The spectral subtraction was applied to images acquired with 40 keV  $\text{C}_{60}^+$  and 20 keV  $(\text{H}_2\text{O})\text{Ar}_{2000}^+$ . The ion peaks identified in tissue were compared to the ions observed in the analysis of synthetic  $\text{A}\beta$  peptide (1-40) with both primary ion beams. Possible fragments of amino acids, complete amino acids and dipeptides were identified and assigned. Larger amino acid fragments ( $> 300$  Da) were observed only with 20 keV  $(\text{H}_2\text{O})\text{Ar}_{2000}^+$ .

The presence of cholesterol was assessed in 40 keV  $\text{C}_{60}^+$  and 20 keV  $(\text{H}_2\text{O})\text{Ar}_{2000}^+$  images. During 40 keV  $\text{C}_{60}^+$  bombardment, only a few counts of the cholesterol fragment  $[M-H_2O+H]^+$  at  $m/z$  369 were detected, whereas the intensity of the

cholesterol fragment ion  $[C_{16}H_{21}]^+$  at  $m/z$  213 was considerably higher. With 20 keV  $(H_2O)Ar_{2000}^+$ , the cholesterol fragment  $[M-H_2O+H]^+$  at  $m/z$  369 was the cholesterol-related ion with the highest secondary ion intensity.

To identify the distribution of cholesterol in the tissue, the images were analysed with ROI-PCA. In both cases, the loading for PC2 showed chemical separation between phosphocholine and cholesterol. Analysis with 40 keV  $C_{60}^+$  indicated the presence of cholesterol in the vicinity of the A $\beta$  depositions but mainly towards the white matter. In the 20 keV  $(H_2O)Ar_{2000}^+$  image, the presence of cholesterol seemed to be more uniform across the cortex. A matrix effect previously observed on cholesterol in the grey matter might play an important role in the detection of cholesterol with both 40 keV  $C_{60}^+$  and, to a lesser extent, 20 keV  $(H_2O)Ar_{2000}^+$ . This effect can be observed in the distribution of cholesterol in specific areas with  $C_{60}^+$  and uniformly across the cortex with  $(H_2O)Ar_{2000}^+$ .

## 7.7 References

- [1] P. Fraser, L. Levesque, and D. McLachlan, "Biochemistry of Alzheimer's disease amyloid plaques," *Clin. Biochem.*, vol. 26, no. October, pp. 339–349, 1993.
- [2] T. Bussi re, F. Bard, R. Barbour, H. Grajeda, T. Guido, K. Khan, D. Schenk, D. Games, P. Seubert, and M. Buttini, "Morphological characterization of Thioflavin-S-positive amyloid plaques in transgenic Alzheimer mice and effect of passive Abeta immunotherapy on their clearance," *Am. J. Pathol.*, vol. 165, no. 3, pp. 987–995, 2004.
- [3] A. society Library, "Alzheimer's society demographics," *Dementia UK: second edition*, 2015. [Online]. Available: [http://www.alzheimers.org.uk/site/scripts/documents\\_info.php?documentID=412](http://www.alzheimers.org.uk/site/scripts/documents_info.php?documentID=412).
- [4] H. Braak and K. Del Tredici, "Introduction," in *Neuroanatomy and Pathology of Sporadic Alzheimer's Disease*, 1st ed., Springer International Publishing, 2015, pp. 3–14.
- [5] D. P. Perl, "Neuropathology of Alzheimer's Disease," *Mounts Sinai J. Med.*, vol. 70, no. 70, pp. 32–42, 2010.
- [6] G. W. Van Hoesen, J. Parvizi, and C. Chu, "Orbitofrontal Cortex Pathology in Alzheimer's Disease," *Cereb. cortex*, vol. 10, pp. 243–251, 2000.

- [7] D. Suzhen, D. Yale, G. Feng, H. Yinghe, and Z. Zheng, "Advances in the pathogenesis of Alzheimer's disease: a re-evaluation of amyloid cascade hypothesis," *Transl. Neurodegener.*, vol. 1, no. 1, p. 18, 2012.
- [8] I. Grundke-Iqbal, K. Iqbal, L. George, Y. C. Tung, K. S. Kim, and H. M. Wisniewski, "Amyloid protein and neurofibrillary tangles coexist in the same neuron in Alzheimer disease.," *Proc. Natl. Acad. Sci. U. S. A.*, vol. 86, no. 8, pp. 2853–2857, 1989.
- [9] K. Shoghi-Jadid, G. W. Small, E. D. Agdeppa, V. Kepe, L. M. Ercoli, P. Siddarth, S. Read, N. Satyamurthy, A. Petric, S.-C. Huang, and J. R. Barrio, "Localization of neurofibrillary tangles and beta-amyloid plaques in the brains of living patients with Alzheimer disease.," *Am. J. Geriatr. Psychiatry*, vol. 10, no. 1, pp. 24–35, 2002.
- [10] C. L. Masters and D. J. Selkoe, "Biochemistry of amyloid beta-protein and amyloid deposits in Alzheimer disease," *Cold Spring Harb Perspect Med*, vol. 2, no. 6, p. a006262, 2012.
- [11] H. Braak and E. Braak, "Neuropathological staging of Alzheimer-related changes.," *Acta Neuropathol.*, vol. 82, no. 4, pp. 239–259, 1991.
- [12] J. Götz and L. M. Ittner, "Animal models of Alzheimer's disease and frontotemporal dementia.," *Nat. Rev. Neurosci.*, vol. 9, no. 7, pp. 532–544, 2008.
- [13] J. Götz and L. M. Ittner, "Supplementary information-Animal models of Alzheimer's disease and frontotemporal dementia," *Nat. Rev. Neurosci.*, vol. 9, no. 9, 2008.
- [14] G. Elder, M. A. Gama Sosa, and Rita De Gasperi, "Transgenic Mouse Models of Alzheimer's Disease," *Mt. Sinai J. Med.*, vol. 77, pp. 69–81, 2010.
- [15] S. Oddo, A. Caccamo, J. D. Shepherd, M. P. Murphy, T. E. Golde, R. Kaye, R. Metherate, M. P. Mattson, Y. Akbari, and F. M. LaFerla, "Triple-transgenic model of Alzheimer's Disease with plaques and tangles: Intracellular A $\beta$  and synaptic dysfunction," *Neuron*, vol. 39, no. 3, pp. 409–421, 2003.
- [16] H. LeVine, "Thioflavine T interaction with synthetic Alzheimer's disease beta-amyloid peptides: detection of amyloid aggregation in solution.," *Protein Sci.*, vol. 2, no. 3, pp. 404–410, 1993.
- [17] P. T. T. Ly, F. Cai, and W. Song, "Detection of neuritic plaques in Alzheimer's disease mouse model.," *J. Vis. Exp.*, no. 53, pp. 10–12, 2011.



- [18] M. L. Schmidt, K. a Robinson, V. M. Lee, and J. Q. Trojanowski, "Chemical and immunological heterogeneity of fibrillar amyloid in plaques of Alzheimer's disease and Down's syndrome brains revealed by confocal microscopy," *Am. J. Pathol.*, vol. 147, no. 2, pp. 503–515, 1995.
- [19] Y. Yang, H. M. Jia, and B. L. Liu, "(E)-5-styryl-1H-indole and (E)-6-styrylquinoline derivatives serve as probes for beta-amyloid plaques," *Molecules*, vol. 17, no. 4, pp. 4252–4265, 2012.
- [20] A. Sun, X. V Nguyen, and G. Bing, "Comparative analysis of an improved thioflavin-s stain, Gallyas silver stain, and immunohistochemistry for neurofibrillary tangle demonstration on the same sections," *J. Histochem. Cytochem.*, vol. 50, no. 4, pp. 463–472, 2002.
- [21] G. Kelényi, "Thioflavin S fluorescent and congo red anisotropic stainings in the histologic demonstration of amyloid," *Acta Neuropathol.*, vol. 7, no. 4, pp. 336–348, 1967.
- [22] S. T. C. W. Jens Rittscher, Raghu Machiraju, "Registration of 3-D FMT and MicroCT Images," in *Microscopic Image Analysis for Life Science Applications*, Norwood, MA: Artech house, Inc, 2008, pp. 429–439.
- [23] J. Cui, N. Ray, S. T. Acton, and Z. Lin, "An affine transformation invariance approach to cell tracking," *Comput. Med. Imaging Graph.*, vol. 32, no. 7, pp. 554–565, 2008.
- [24] S. Solé-Domènech, P. Sjövall, V. Vukojević, R. Fernando, A. Codita, S. Salve, N. Bogdanović, A. H. Mohammed, P. Hammarström, K. P. R. Nilsson, F. M. Laferla, S. Jacob, P. O. Berggren, L. Giménez-Llort, M. Schalling, L. Terenius, and B. Johansson, "Localization of cholesterol, amyloid and glia in Alzheimer's disease transgenic mouse brain tissue using time-of-flight secondary ion mass spectrometry (ToF-SIMS) and immunofluorescence imaging," *Acta Neuropathol.*, vol. 125, no. 1, pp. 145–157, 2013.
- [25] S. Aoyagi, T. Shimanouchi, T. Kawashima, and H. Iwai, "ToF-SIMS observation for evaluating the interaction between amyloid  $\beta$  and lipid membranes," *Anal. Bioanal. Chem.*, pp. 2859–2863, 2015.
- [26] S. Solé-Domènech, B. Johansson, M. Schalling, J. Malm, and P. Sjövall, "Analysis of Opioid and Amyloid Peptides Using Time-of-Flight Secondary Ion Mass Spectrometry," *Anal. Chem.*, vol. 82, no. 5, pp. 1964–1974, 2010.

- [27] J. B. Lhoest, M. S. Wagner, C. D. Tidwell, and D. G. Castner, "Characterization of adsorbed protein films by time of flight secondary ion mass spectrometry.," *J. Biomed. Mater. Res.*, vol. 57, no. 3, pp. 432–440, 2001.
- [28] A. N. Lazar, C. Bich, M. Panchal, N. Desbenoit, V. W. Petit, D. Touboul, L. Dauphinot, C. Marquer, O. Lapr  vote, A. Brunelle, and C. Duyckaerts, "Time-of-flight secondary ion mass spectrometry (TOF-SIMS) imaging reveals cholesterol overload in the cerebral cortex of Alzheimer disease patients," *Acta Neuropathol.*, vol. 125, no. 1, pp. 133–144, 2013.
- [29] C. Di Scala, H. Chahinian, N. Yah, N. Garmy, and J. Fantini, "Interaction of Alzheimer ' s  $\beta$  - Amyloid Peptides with Cholesterol: Mechanistic Insights into Amyloid Pore Formation," 2014.
- [30] A. Y. Abramov, M. Ionov, E. Pavlov, and M. R. Duchon, "Membrane cholesterol content plays a key role in the neurotoxicity of ??-amyloid: Implications for Alzheimer's disease," *Aging Cell*, vol. 10, no. 4, pp. 595–603, 2011.
- [31] L. J. Pike, "Lipid rafts: bringing order to chaos.," *J. Lipid Res.*, vol. 44, no. 4, pp. 655–667, 2003.
- [32] C. Cecchi, D. Nichino, M. Zampagni, C. Bernacchioni, E. Evangelisti, A. Pensalfini, G. Liguri, A. Gliozzi, M. Stefani, and A. Relini, "A protective role for lipid raft cholesterol against amyloid-induced membrane damage in human neuroblastoma cells.," *Biochim. Biophys. Acta*, vol. 1788, no. 10, pp. 2204–2216, 2009.
- [33] D. Purves, A. G.J, and D. Fitzpatrick, "An overview of the cortical structure," in *Neuroscience*, Sunderland (Ma): Sinauer Associates, 2001.
- [34] F. R. Maxfield and D. W  stner, "Analysis of Cholesterol Trafficking with Fluorescent Probes," *Methods Cell Biol.*, vol. 108, no. 1, pp. 367–393, 2012.

## 8 Conclusions and future work

This study focused on molecular imaging of mouse brain tissue sections using cluster ion beams. In the first set of experiments, 20 keV  $C_{60}^+$ ,  $Ar_n^+$ ,  $(H_2O)Ar_n^+$  and  $(H_2O)_n^+$  cluster ion beams were applied to comparative background studies on four biorelated molecules: the amino acid L-arginine, the peptide angiotensin II, the lipid DPPC and the sugar trehalose. The same cluster ion beams were also applied to the analysis brain total lipid extract. The secondary ion yields obtained from the standard biomolecules and brain total lipid extract determined that 20 keV  $Ar_{2000}^+$ ,  $(H_2O)Ar_{2000}^+$  and  $(H_2O)_{6000}^+$  produced the highest secondary ion intensities of  $[M+H]^+$  type ions and the least structural fragmentation. Hence, the primary ion beams 20 keV  $Ar_{2000}^+$ ,  $(H_2O)Ar_{2000}^+$  and  $(H_2O)_{6000}^+$  were used to acquire ToF-SIMS images from the cerebellar area of serial mouse brain tissue sections. The images demonstrated that water-containing cluster ion beams produced the highest secondary ion yields in both grey and white matter, gaining a new level of insight into the lipid compositions of both types of tissue in the brain.

A clinical case was also evaluated with ToF-SIMS imaging, using 40 keV  $C_{60}^+$  and 20 keV  $(H_2O)Ar_{2000}^+$  as the primary ion beams. These cluster beams were applied to the analysis of 3xTg-AD mouse brain tissue. SIMS images were registered with fluorescence microscopy images for the identification and co-localisation of the Amyloid- $\beta$  plaques on the SIMS images. Spectra from regions of interest with A $\beta$  plaques were compared to regions without plaques, obtaining possible ion fragments derived from the A $\beta$  protein. Synthetic Amyloid- $\beta$  peptide (1-40) was analysed with keV  $C_{60}^+$  and 20 keV  $(H_2O)Ar_{2000}^+$  for validation of the ions identified *in situ*. The co-localisation of cholesterol was also studied from images obtained with both primary ion beams. ROI-PCA showed a discrete distribution of cholesterol around the A $\beta$  plaques in the  $C_{60}$  image, whereas with  $(H_2O)Ar_{2000}$  the distribution of cholesterol was uniform throughout the tissue.

Enhancement of the secondary ion signal was observed, specially for  $[M+H]^+$  type ions. This signal enhancement was observed when water-containing ion beams were applied to the analysis of biomolecules and tissue imaging. The enhancement was optimum when water-containing clusters had  $E/nucleon$  of 0.18-0.2 eV.

## 8.1 Comparative background studies on biomolecule models

- The cluster primary ion beams 20 keV  $\text{Ar}_n^+$ ,  $(\text{H}_2\text{O})_n^+$  and  $(\text{H}_2\text{O})\text{Ar}_n^+$  were applied to the analysis of arginine, trehalose, angiotensin II and DPPC in positive ion mode. The results from the spectral analysis in static and steady-state primary ion dose conditions of the four compounds indicated higher secondary ion yields of  $[\text{M}+\text{H}]^+$  and related ions during  $(\text{H}_2\text{O})_n^+$  bombardment when compared to  $\text{Ar}_n^+$  and  $(\text{H}_2\text{O})\text{Ar}_n^+$ . The structural fragmentation was also reduced when  $(\text{H}_2\text{O})_n^+$  clusters were used in the analysis.
- The secondary ion yield of  $[\text{M}+\text{H}]^+$  ions was optimum when the analysis was carried out with  $(\text{H}_2\text{O})_n^+$  clusters with energy per molecule of  $\sim 3$  eV. When the  $(\text{H}_2\text{O})_n^+$  clusters possess an energy per molecule of  $\sim 10$  eV, their behaviour is similar to that observed in  $\text{Ar}_n^+$  clusters of 10 eV/atom.
- The accumulated secondary ion signal per  $1 \mu\text{m}^2$  indicated that the signal enhancement obtained with  $(\text{H}_2\text{O})_n^+$  clusters with  $E/\text{molecule}$  of  $\sim 3$  eV was 100 to 1000 times higher the signal detected in static conditions with argon clusters of  $\sim 10$  eV/atom.
- $(\text{H}_2\text{O})\text{Ar}_n^+$  clusters were formed by doping argon clusters with 5% water. 20 keV  $(\text{H}_2\text{O})\text{Ar}_n^+$  clusters produced 4- 10 times more secondary ion yield than  $\text{Ar}_n^+$  clusters when applied to the analysis of trehalose and DPPC. The optimum energy regime observed for  $(\text{H}_2\text{O})\text{Ar}_n^+$  clusters is  $\sim 0.2$  eV of energy per nucleon.
- The optimum  $E/\text{nucleon}$  for  $(\text{H}_2\text{O})\text{Ar}_n^+$  clusters ( $\sim 0.2$  eV) is very close to that observed for  $(\text{H}_2\text{O})_n^+$  clusters ( $\sim 0.18$  eV). This is an indicator that the sputtering/ionisation mechanism of water-doped argon clusters is similar to that of the  $(\text{H}_2\text{O})_n^+$  clusters.
- Although the behaviour of  $(\text{H}_2\text{O})\text{Ar}_n^+$  and  $(\text{H}_2\text{O})_n^+$  clusters is similar, the secondary ion yield produced by pure  $(\text{H}_2\text{O})_n^+$  is higher.
- Deuterium oxide was incorporated to form  $(\text{D}_2\text{O})_n^+$  clusters to analyse DPPC and trehalose. The application of this beams proved that the protonation enhancement is induced by the hydrogen atoms present in the from the  $(\text{H}_2\text{O})_n^+$  analysis beam, although the detailed ionisation mechanism that is still unknown.
- The results from the comparative background studies demonstrated the benefit of applying water clusters of size  $n \sim 6000$  or water-doped argon clusters of size  $n \sim 2000$  to the analysis of biocompounds, especially when the analysis is

acquired beyond the static limit and more secondary ion signal can be accumulated.

## 8.2 Molecular imaging of mouse brain sections using cluster ToF-SIMS

- The analysis of BTLE with 20 keV  $C_{60}^+$ ,  $Ar_{2000}^+$ ,  $(H_2O)Ar_{2000}^+$  and  $(H_2O)_{6000}^+$  indicated similar results to those obtained with the standard biomolecules arginine, trehalose, angiotensin II and DPPC. The quantification of the secondary ion yields obtained from cholesterol  $[M-H_2O+H]^+$ , the sphingolipid SM (24:1)  $[M+H]^+$  and the phospholipids PC(32:0)  $[M+H]^+$  and PC(34:0)  $[M+H]^+$  demonstrated that water- containing clusters with  $E/nucleon$  of 0.18- 0.2 eV produce the highest secondary ion yields.
- For brain tissue imaging, 20 keV  $(H_2O)_{6000}^+$  with  $E/nucleon$  of 0.18 eV produced the highest secondary ion signal. An enhancement of 10 - 100 over 20 keV  $Ar_{2000}^+$  was observed.
- Brain tissue imaging with water-doped argon clusters with  $E/nucleon$  of 0.2 eV generated an enhancement of 4- 10 when compared to argon-only clusters.
- Several lipid classes were identified in the grey and white matter during 20 keV  $(H_2O)_{6000}^+$  and 20 keV  $(H_2O)Ar_{2000}^+$  bombardment. Lipid molecules such as sterol lipids, glycerophospholipids, glycerolipids, fatty acyls and sphingolipids were identified and assigned in both grey and white matter.
- There was specific enhancement of the detection of cholesterol during water- containing beam bombardment, which was detected almost with the same signal intensity in both grey matter and white matter, as shown in Figure 8.1.

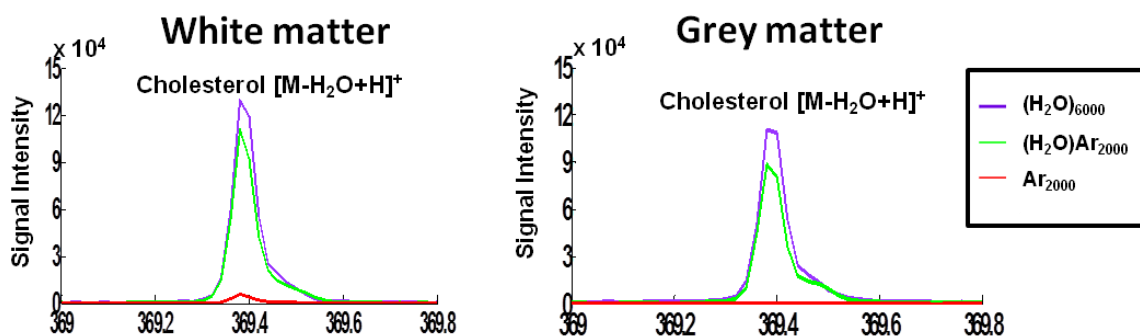


Figure 8.1: Cholesterol  $[M-H_2O+H]^+$  spectra comparison between 20 keV  $(H_2O)_{6000}^+$ ,  $(H_2O)Ar_{2000}^+$  and  $Ar_{2000}^+$  in the grey and white matter regions. The secondary ion signal intensity is similar in both regions with  $(H_2O)_{6000}^+$  and  $(H_2O)Ar_{2000}^+$ . With  $Ar_{2000}^+$ , the signal detected is considerably lower in the white matter and close to zero in the grey matter.

- The behaviour of cholesterol, particularly in the grey matter, seemed to be highly influenced by a matrix effect when the sample was analysed with  $C_{60}^+$  or  $Ar_{2000}^+$ . This ion suppression effect was reduced when the sample was analysed with  $(H_2O)_{6000}^+$  or  $(H_2O)Ar_{2000}^+$ .
- The ion suppression effect on cholesterol was studied further with a series of experiments on standard cholesterol and lipid mixtures. In these series of experiments, as in the tissue images, the ion suppression effect on cholesterol was reduced when the samples was analysed with  $(H_2O)_{6000}^+$  clusters.
- From the results obtained in imaging analysis of lipid mixtures, it is concluded that water-containing clusters with  $E/nucleon$  of 0.18- 0.2 eV enhance the formation of  $[M+H]^+$  ions and reduce the matrix suppression effects on cholesterol.
- It is possible than the amount of cholesterol present in the white matter induces the suppression of other lipids e.g. phospholipids whereas the phospholipids suppress the ionisation of cholesterol in the grey matter, when the analysis is performed with  $C_{60}^+$  or  $Ar_{2000}^+$ .
- The physical and chemical structure of the membranes of cells present in both white and grey matters might also play a significant role in the suppression effect of cholesterol. The distribution of cholesterol in the neuronal and glial cell membranes is dispersed between phospholipids in the grey matter. The predominant presence of cholesterol in the myelin sheath of the white matter over phospholipid molecules could reduce the ionisation of phospholipids during SIMS. This effect can be observed in Figure 8.2, where the distribution of cholesterol detected with  $(H_2O)_{6000}^+$  are  $(H_2O)Ar_{2000}^+$  is shown in grey matter and white matter.

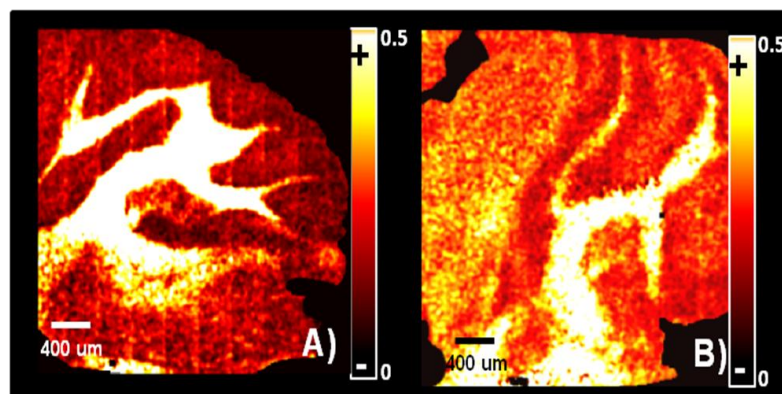


Figure 8.2: Single ion images of the distribution of cholesterol  $[M-H_2O+H]^+$  at  $m/z$  369 with (A)  $(H_2O)Ar_{2000}$  and (B)  $(H_2O)_{6000}$ .

### 8.2.1 Application of cluster ToF-SIMS imaging to the analysis of a clinical case: a transgenic mouse model infected with Alzheimer's disease

- Sagittal sections from 15 months 3xTg-AD mice were successfully stained with 1% thioflavin S and analysed with fluorescence microscopy. A $\beta$  plaques were localised in the frontal cortex and hippocampus areas.
- The observed A $\beta$  plaques were about 5-20  $\mu\text{m}$  in diameter. According to the established morphological classification of A $\beta$  plaques [1], the plaques observed were type 1, type 2a, 2b and 2c.
- Fluorescence microscopy images from the whole tissue were successfully registered with SIMS images acquired with 40 keV  $\text{C}_{60}^+$ .
- Specific areas of the cerebral cortex with A $\beta$  plaques were identified in the registered images. Such areas were analysed with 40 keV  $\text{C}_{60}^+$  (1.5  $\mu\text{m}/\text{pixel}$  resolution) and 20 keV  $(\text{H}_2\text{O})\text{Ar}_{2000}^+$  (5  $\mu\text{m}/\text{pixel}$  resolution).
- Single A $\beta$  plaques were identified on the  $\text{C}_{60}$  and  $(\text{H}_2\text{O})\text{Ar}_{2000}^+$  images. Spectra from regions without plaques were subtracted from spectra of regions with plaques, allowing the identification of amino acid fragments derived from the A $\beta$  protein.
- For validation purposes, all the fragments assigned to amino acids and dipeptides detected *in situ* were compared to spectra obtained from synthetic A $\beta$  peptide (1-40).
- The distribution of cholesterol was also studied in the images acquired with 40 keV  $\text{C}_{60}^+$  and 20 keV  $(\text{H}_2\text{O})\text{Ar}_{2000}^+$ . Due to extensive fragmentation with 40 keV  $\text{C}_{60}^+$ , the ion  $[\text{C}_{16}\text{H}_{21}]^+$  at  $m/z$  213 was the cholesterol fragment with the highest intensity. With 20 keV  $(\text{H}_2\text{O})\text{Ar}_{2000}^+$ , the fragment  $[\text{M}-\text{H}_2\text{O}+\text{H}]^+$  at  $m/z$  369 was the main ion detected for cholesterol.
- The distribution of cholesterol fragments in the tissue was assessed with ROI-PCA. With  $\text{C}_{60}^+$ , cholesterol was localised in the vicinity of the A $\beta$  deposits, with most of the cholesterol found towards the white matter. With 20 keV  $(\text{H}_2\text{O})\text{Ar}_{2000}^+$ , the distribution of cholesterol was uniform across the cortex area.
- The ion suppression effect on cholesterol influences the signal intensity detected for this ion in the cortex, which is mainly composed by grey matter. This ion suppression effect is considerably reduced when the analysis is acquired with  $(\text{H}_2\text{O})\text{Ar}_{2000}^+$ .
- Although still under research, there are a few theories that relate the presence of cholesterol with the progression of AD [2]–[4]. An elevated presence of

cholesterol, would lead to more production of oligomers, thus, more extracellular accumulation of A $\beta$  plaques [5]. Another hypothesis suggests that cholesterol plays an important role in the homeostasis of the brain [6], [7]. Hence, the specific detection of cholesterol with C<sub>60</sub><sup>+</sup> in the same areas where the A $\beta$  plaques are found agrees with these theories. The higher detection of cholesterol throughout the cerebral cortex with (H<sub>2</sub>O)Ar<sub>2000</sub><sup>+</sup> confirms that there is an ion suppression effect on cholesterol and suggests that the cholesterol is not only found in the vicinity of the plaques but all over the tissue, including the areas where the A $\beta$  plaques are found.

- If cholesterol and A $\beta$  are found in the same areas during the development of AD, it is possible that there could be interaction between cholesterol and A $\beta$  peptides. However, understanding the complexity of that mechanism goes beyond this project and would require further experimentation.

### 8.3 Future work

#### 8.3.1 Cluster ToF-SIMS imaging of mouse brain sections

Instrumental improvements are needed to increase the beam energy of water cluster ion beams. If larger water clusters of higher beam energy can be obtained with a constant  $E/molecule$  of  $\sim 3$  eV, higher secondary ion yield will be generated. This effect can be observed in Figure 8.3. By doubling the beam energy and the cluster size, the secondary ion yield obtained will increase 2x. Biological imaging could be benefited from the higher detection of useful secondary ion yields.

Improvements in the beam's optics and focusing capacity e.g. increasing the beam's energy would enable new imaging applications. Currently, the best spatial resolution obtained with water-containing clusters is 4  $\mu$ m. This spot size restricts the application of water and water-doped argon clusters to samples such as tissue. Sub-micron resolution is needed to enable cell imaging. With higher spatial resolution, the cells present in the cerebellum cellular layers such as neurons and Purkinje cells could be characterised *in situ*, providing specific information about the lipid components of the brain.

More experiments exploring the matrix effect observed on cholesterol in the grey matter are needed to fully understand this suppression effect. Higher spatial resolution imaging with higher energy water-containing clusters exploring the white matter and



the Purkinje and molecular layers in the grey matter of the cerebellum would provide more information about the cholesterol composition in specific regions of the brain.

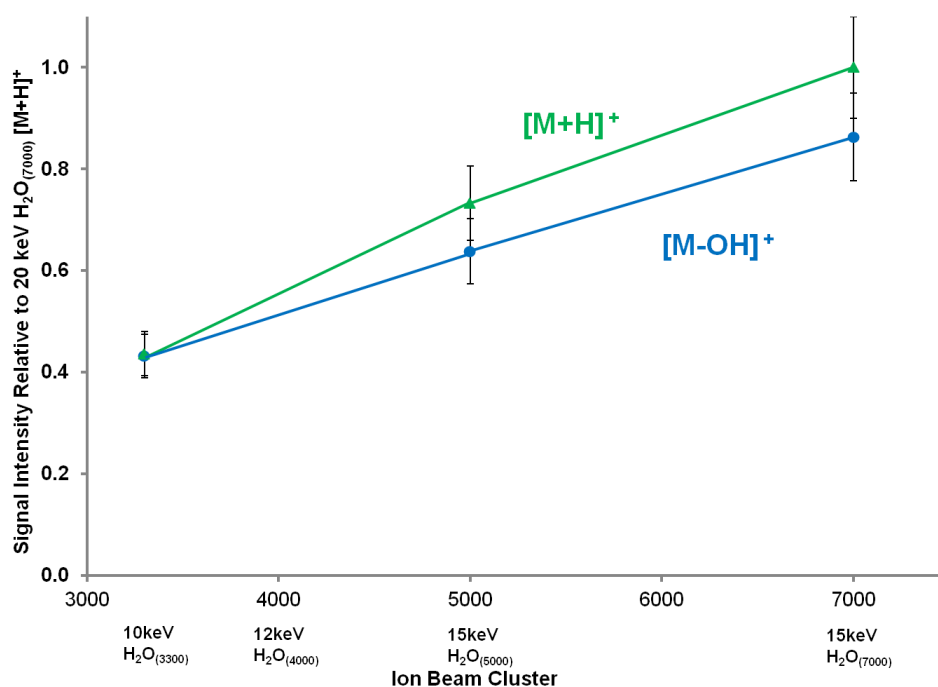


Figure 8.3:  $[M+H]^+$  (green line) and  $[M-OH]^+$  (blue line) ion signal from trehalose, generated by water beam analysis. The ion yield obtained with clusters having  $E/\text{molecule} \sim 3 \text{ eV}$  was plotted as a function of cluster size and normalised to  $[M+H]^+$  yield obtained with  $20 \text{ keV } (H_2O)_{7000}^+$ .

### 8.3.2 Analysis of AD brain tissue

Higher secondary ion yield and less structural fragmentation are needed for better characterisation of the  $A\beta$  plaques. If  $20 \text{ keV } (H_2O)_{6000}^+$  is applied to the analysis of 3xTg-AD brain sections, more  $[M+H]^+$  ions and less structural fragmentation would be produced. This would allow the detection of bigger fragments from the  $A\beta$  peptide.

Expansion of the GCIB water reservoir is needed to increase the lifetime. Improvement of the beam spot size is also necessary to enable imaging of 3xTg-AD with pure cluster ion beams.

Cholesterol has been detected in the vicinity of the  $A\beta$  plaques with  $25 \text{ keV Bi}_3^+$  [2], [8] and  $40 \text{ keV C}_{60}^+$ . However, when analysing with  $20 \text{ keV } (H_2O)Ar_{2000}^+$ , the matrix effect suppressing cholesterol was observed in the brain cortex. Thus, to study in a more accurate way the distribution of cholesterol and its relation with  $A\beta$  plaques, the experimental design could involve the acquisition of ToF-SIMS images with  $20 \text{ keV } (H_2O)Ar_{2000}^+$  and  $(H_2O)_{6000}^+$  and the subsequent staining of the sample with Filipin [9]

for cholesterol and with ThioS for amyloid aggregates. A fluorescence microscopy image can be obtained and registered with ToF-SIMS images for the co-localisation and characterisation *in situ* of cholesterol and A $\beta$  plaques.

The application of different analytical techniques suitable for the characterisation of single A $\beta$  plaques, could lead to the registration of images of the same sample with different techniques. For example, high-resolution Fourier-transform infrared imaging could provide complementary information about the beta-amyloid proteins from the sample [10], [11]. FTIR analysis does not require extensive sample preparation and could be applied to the same sample after ToF-SIMS imaging and before staining the sample.

Images acquired with  $(\text{H}_2\text{O})\text{Ar}_n^+$  and  $(\text{H}_2\text{O})_n^+$  from transgenic tissue could be compared to images of wild-type brain sections. Studying the distribution of A $\beta$  fragments, cholesterol molecules and intact sphingolipids could provide more information about the development of AD in specific regions such as cortex and hippocampus.

The results presented show that cluster ToF-SIMS can be successfully applied to brain tissue imaging. Current technologies allow us to acquire data with more useful secondary ion yield for clinical applications and biological research. Nevertheless, future technological improvements are required for specialised applications e.g. cellular imaging. Moreover, processing the data obtained is still challenging and more data processing tools are also needed for interpretation.

## 8.4 References

- [1] T. Bussi re, F. Bard, R. Barbour, H. Grajeda, T. Guido, K. Khan, D. Schenk, D. Games, P. Seubert, and M. Buttini, "Morphological characterization of Thioflavin-S-positive amyloid plaques in transgenic Alzheimer mice and effect of passive Abeta immunotherapy on their clearance.," *Am. J. Pathol.*, vol. 165, no. 3, pp. 987–995, 2004.
- [2] A. N. Lazar, C. Bich, M. Panchal, N. Desbenoit, V. W. Petit, D. Touboul, L. Dauphinot, C. Marquer, O. Lapr v te, A. Brunelle, and C. Duyckaerts, "Time-of-flight secondary ion mass spectrometry (TOF-SIMS) imaging reveals cholesterol overload in the cerebral cortex of Alzheimer disease patients," *Acta Neuropathol.*, vol. 125, no. 1, pp. 133–144, 2013.

- [3] S. Solé-Domènech, B. Johansson, M. Schalling, J. Malm, and P. Sjövall, "Analysis of Opioid and Amyloid Peptides Using Time-of-Flight Secondary Ion Mass Spectrometry," *Anal. Chem.*, vol. 82, no. 5, pp. 1964–1974, 2010.
- [4] C. Di Scala, H. Chahinian, N. Yah, N. Garmy, and J. Fantini, "Interaction of Alzheimer's  $\beta$  - Amyloid Peptides with Cholesterol: Mechanistic Insights into Amyloid Pore Formation," 2014.
- [5] A. Y. Abramov, M. Ionov, E. Pavlov, and M. R. Duchon, "Membrane cholesterol content plays a key role in the neurotoxicity of  $\beta$ -amyloid: Implications for Alzheimer's disease," *Aging Cell*, vol. 10, no. 4, pp. 595–603, 2011.
- [6] I. . Martins, T. Berger, M. Sharman, G. Verdile, S. Fuller, and R. Martins, "NoCholesterol metabolism and transport in the pathogenesis of Alzheimer's disease," *Journal Neurochem.*, vol. 111, pp. 1275–1308, 2009.
- [7] W. G. Wood, L. Li, W. E. Müller, and G. P. Eckert, "Cholesterol as a causative factor in Alzheimer's disease: A debatable hypothesis," *J. Neurochem.*, vol. 129, no. 4, pp. 559–572, 2014.
- [8] S. Solé-Domènech, P. Sjövall, V. Vukojević, R. Fernando, A. Codita, S. Salve, N. Bogdanović, A. H. Mohammed, P. Hammarström, K. P. R. Nilsson, F. M. Laferla, S. Jacob, P. O. Berggren, L. Giménez-Llort, M. Schalling, L. Terenius, and B. Johansson, "Localization of cholesterol, amyloid and glia in Alzheimer's disease transgenic mouse brain tissue using time-of-flight secondary ion mass spectrometry (ToF-SIMS) and immunofluorescence imaging," *Acta Neuropathol.*, vol. 125, no. 1, pp. 145–157, 2013.
- [9] F. R. Maxfield and D. Wüstner, "Analysis of Cholesterol Trafficking with Fluorescent Probes," *Methods Cell Biol.*, vol. 108, no. 1, pp. 367–393, 2012.
- [10] L. M. Miller, M. W. Bourassa, and R. J. Smith, "FTIR spectroscopic imaging of protein aggregation in living cells," *Biochim. Biophys. Acta*, vol. 1828, no. 10, pp. 2339–46, 2013.
- [11] L. P. Choo, D. L. Wetzel, W. C. Halliday, M. Jackson, S. M. LeVine, and H. H. Mantsch, "In situ characterization of beta-amyloid in Alzheimer's diseased tissue by synchrotron Fourier transform infrared microspectroscopy," *Biophys. J.*, vol. 71, no. 4, pp. 1672–1679, 1996.





## Enhancing Ion Yields in Time-of-Flight-Secondary Ion Mass Spectrometry: A Comparative Study of Argon and Water Cluster Primary Beams

Sadia Sheraz née Rabbani,<sup>†,‡</sup> Irma Berrueta Razo,<sup>†,§</sup> Taylor Kohn,<sup>†,‡</sup> Nicholas P. Lockyer,<sup>†,§</sup> and John C. Vickerman<sup>\*,†,‡</sup>

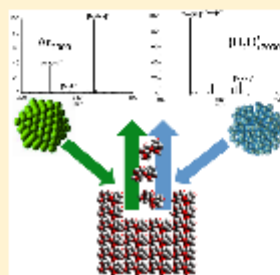
<sup>†</sup>Manchester Institute of Biotechnology, The University of Manchester, Manchester, U.K.

<sup>‡</sup>School of Chemical Engineering and Analytical Science, The University of Manchester, Manchester, U.K.

<sup>§</sup>School of Chemistry, The University of Manchester, Manchester, U.K.

### Supporting Information

**ABSTRACT:** Following from our previous Letter on this topic, this Article reports a detailed study of time-of-flight-secondary ion mass spectrometry (TOF-SIMS) positive ion spectra generated from a set of model biocompounds (arginine, trehalose, DPPC, and angiotensin II) by water cluster primary ion beams in comparison to argon cluster beams over a range of cluster sizes and energies. Sputter yield studies using argon and water beams on arginine and Irganox 1010 have confirmed that the sputter yields using water cluster beams lie on the same universal sputtering curve derived by Seah for argon cluster beams. Thus, increased ion yield using water cluster beams must arise from increased ionization. The spectra and positive ion signals observed using cluster beams in the size range from 1000 to 10000 and the energy range 5–20 keV are reported. It is confirmed that water cluster beams enhance proton related ionization over against argon beams to a significant degree such that enhanced detection sensitivities from 1  $\mu\text{m}^2$  in the region of 100 to 1000 times relative to static SIMS analysis with  $\text{Ar}_{3000}$  cluster beams appear to be accessible. These new studies show that there is an unexpected complexity in the ionization enhancement phenomenon. Whereas optimum ion yields under argon cluster bombardment occur in the region of  $E/n \geq 10$  eV (where  $E$  is the beam energy and  $n$  the number of argon atoms in the cluster) and fall rapidly when  $E/n < 10$  eV; for water cluster beams, ion yields increase significantly in this  $E/n$  regime (where  $n$  is the number of water molecules in the cluster) and peak for 20 keV beams at a cluster size of 7000 or  $E/n \sim 3$  eV. This important result is explored further using  $\text{D}_2\text{O}$  cluster beams that confirm that in this low  $E/n$  regime protonation does originate to a large extent from the water molecules. The results, encouraging in themselves, suggest that for both argon and water cluster beams, higher energy beams, e.g., 40 and 80 keV, would enable larger cluster sizes to be exploited with significant benefit for ion yield and hence analytical capability.



It is now widely accepted that time-of-flight-secondary ion mass spectrometry (TOF-SIMS) has great potential as one of a number of mass spectrometric techniques for 2D and 3D imaging of the distribution of molecular chemistry in organic and biological systems.<sup>1–4</sup> While it is limited to molecules of mass below about 2000 Da, compared to matrix-assisted laser desorption ionization (MALDI), desorption electrospray ionization (DESI), and related techniques, it has higher spatial resolution capabilities that offer the promise of submicrometer, and hence use in biology subcellular analysis.<sup>5</sup> However, as is common with all desorption mass spectrometries, ion yields are very low. Ionization probabilities below  $10^{-5}$  are very common.<sup>6</sup> As a result, the molecular ion useful yields from a 1  $\mu\text{m}^2$  pixel area are less than 0.01 under static conditions (<1% of surface removed to minimize ion beam induced chemical damage). The advent of  $\text{C}_{60}$  and more recently argon cluster ions beams has lifted the static restriction on TOF-SIMS, but even under these more advantageous conditions, signal levels from 1  $\mu\text{m}^2$  are at most only a few ions, certainly too few to

make submicrometer imaging a useful technique. There is therefore a very strong impetus to find ways of raising the ion yield.

Although it is possible to enhance the secondary ion yields from organic and bio-organic analytes by adding compounds or metals to the surface,<sup>7–12</sup> these methods are usually system specific, and the addition of further chemistry to what are frequently quite complex materials is not always to be recommended. Additionally they are not readily applicable in 3D analytical applications.

Ideally it would be preferable to enhance ion yield via developments in primary ion beam technology. There have been a number of these over the last 20 years. The use of gold and bismuth cluster beams based on liquid metal technology enhanced yields of ions around  $m/z$  300–800 although still

Received: November 17, 2014

Accepted: January 14, 2015

Published: January 14, 2015

# Comparing $C_{60}^+$ and $(H_2O)_n^+$ clusters for mouse brain tissue analysis

Irma Berrueta Razo, Sadia Sheraz, Alex Henderson,  
Nicholas P. Lockyer and John C. Vickerman\*

Time-of-flight SIMS is applied to the analysis of single cells and different types of biological tissue samples enabling the generation of images with high spatial resolution and chemical specificity. However, the low yield of secondary ions from this type of sample still remains a challenge. This low yield could potentially be increased by enhancing the protonation of ions with the presence of water. Here, we have explored the application of a prototype water cluster ion beam for the analysis of mouse brain tissue samples. A series of experiments acquired with 20 keV  $(H_2O)_{3000}^+$  and 20 keV  $(H_2O)_{4500}^+$  were compared with 20 keV  $C_{60}^+$ , showing ion yield enhancement when a  $(H_2O)_n^+$  cluster ion is employed in the analysis. The results have demonstrated the potential benefits provided by the use of  $(H_2O)_n^+$  clusters for the analysis of mouse brain tissue samples. © 2014 The Authors. *Surface and Interface Analysis* published by John Wiley & Sons Ltd.

**Keywords:** SIMS; tissue analysis; cluster comparison;  $H_2O$ ;  $C_{60}$ ; imaging

## Introduction

SIMS imaging is a desorption-ionisation technique capable of generating images of biological surfaces with chemical specificity and high spatial resolution without the need for sample staining or labelling.<sup>[1–3]</sup> SIMS has been used in a variety of biological applications including the analysis of single cells and tissue samples<sup>[4]</sup> to study the distribution of different compounds *in situ*. Images from endogenous and exogenous molecules from tissue samples have proved to be important in the study of biochemical mechanisms, the development of a disease, targeted drug delivery, and so on.

With the introduction of liquid metal ion guns, it was possible to image biological samples with good spatial resolution, but significant bombardment-induced damage to the sample can be a downside of the approach.<sup>[5]</sup> The use of polyatomic ion beams such as  $SF_5^+$  and  $C_{60}^+$  can significantly reduce this damage. Using  $C_{60}^+$ , it has been possible to image a biological sample without extensive sample preparation and with micrometer spatial resolution without inducing major sample damage.<sup>[3,4]</sup> Argon cluster beams offer imaging with even less damage but with lower spatial resolution. These polyatomic beams make analysis beyond the static limit possible such that increasing the ion dose results in more signal from each pixel volume or voxel. This also makes possible the generation of 3D images by depth profiling the sample.<sup>[4]</sup> 3D imaging of single cells and mouse brain tissue has been reported using 20 keV and 40 keV  $C_{60}^+$  clusters.<sup>[3]</sup>

When a tissue section is analysed with time-of-flight SIMS, most of the ions recorded in the mass spectrum correspond to lipids and their fragments.<sup>[6]</sup> Most of the peaks from the mass spectrum above  $m/z$  200 can be assigned to fragments or molecular ions from diverse lipid species.<sup>[6]</sup> Nowadays, it is possible to detect intact molecular ions up to 1000 Da although the low secondary ion yield still remains a challenge.<sup>[3]</sup> There have been efforts to enhance secondary ion yields by adding metallic

nanoparticles or matrix-assisted laser desorption/ionization type matrices to the sample.<sup>[5,12]</sup> Successful attempts to increase secondary ion yields involved the enhancement of the protonation of ions with the presence of water during the analysis.<sup>[8–11]</sup> There have been attempts to analyse the sample in a frozen hydrated state (instead of freeze-drying the sample)<sup>[9–11,13]</sup> or to inject water vapour at the sample's surface.<sup>[14]</sup> Another approach proposed the use of a water vapour electrospray beam as the primary ion beam to explore its effect on secondary ion yields.<sup>[15]</sup> In our lab in Manchester, a prototype water cluster ion beam developed by Ionoptika Ltd has been investigated and was successfully applied to the analysis of standard compounds as shown by Sheraz *et al.*<sup>[16]</sup> Herein, we discuss the application of this newly developed water cluster ion beam prototype for mouse brain tissue analysis and its effect on ionisation efficiency. The principles of its operation can be found elsewhere.<sup>[16]</sup>

## Experimental

A whole mouse brain was obtained using ethically approved procedures from the Faculty of Life Sciences, the University of Manchester. It was sectioned in a Cryo-Microtome (Wolfson Molecular Imaging Centre, The University of Manchester, UK) at

\* Correspondence to: J. C. Vickerman, Chemical Engineering and Analytical Science, University of Manchester, Manchester, UK.  
E-mail: john.vickerman@manchester.ac.uk

Manchester Institute of Biotechnology (MIB), The University of Manchester, Manchester, UK

This is an open access article under the terms of the Creative Commons Attribution License, which permits use, distribution and reproduction in any medium, provided the original work is properly cited.



# Appendix III

## Research Article



Received: 30 May 2015

Revised: 14 July 2015

Accepted: 15 July 2015

Published online in Wiley Online Library

*Rapid Commun. Mass Spectrom.* 2015, 29, 1843–1854  
(wileyonlinelibrary.com) DOI: 10.1002/rcm.7285

## Mass spectrometric imaging of brain tissue by time-of-flight secondary ion mass spectrometry – How do polyatomic primary beams $C_{60}^+$ , $Ar_{2000}^+$ , water-doped $Ar_{2000}^+$ and $(H_2O)_{6000}^+$ compare?

Irma Berrueta Razo<sup>1,3</sup>, Sadia Sheraz (née Rabbani)<sup>1,2</sup>, Alex Henderson<sup>1,2</sup>, Nicholas P. Lockyer<sup>1,3</sup> and John C. Vickerman<sup>1,2\*</sup>

<sup>1</sup>Manchester Institute of Biotechnology, The University of Manchester, Manchester M13 9PL, UK

<sup>2</sup>School of Chemical Engineering and Analytical Science, The University of Manchester, Manchester, UK

<sup>3</sup>School of Chemistry, The University of Manchester, Manchester, UK

**RATIONALE:** To discover the degree to which water-containing cluster beams increase secondary ion yield and reduce the matrix effect in time-of-flight secondary ion mass spectrometry (TOF-SIMS) imaging of biological tissue.

**METHODS:** The positive SIMS ion yields from model compounds, mouse brain lipid extract and mouse brain tissue together with mouse brain images were compared using 20 keV  $C_{60}^+$ ,  $Ar_{2000}^+$ , water-doped  $Ar_{2000}^+$  and pure  $(H_2O)_{6000}^+$  primary beams.

**RESULTS:** Water-containing cluster beams where the beam energy per nucleon ( $E/nucleon$ )  $\approx 0.2$  eV are optimum for enhancing ion yields dependent on protonation. Ion yield enhancements over those observed using  $Ar_{2000}^+$  lie in the range 10 to  $>100$  using the  $(H_2O)_{6000}^+$  beam, while with water-doped  $(H_2O)Ar_{2000}^+$  they lie in the 4 to 10 range. The two water-containing beams appear to be optimum for tissue imaging and show strong evidence of increasing yields from molecules that experience matrix suppression under other primary beams.

**CONCLUSIONS:** The application of water-containing primary beams is suggested for biological SIMS imaging applications, particularly if the beam energy can be raised to 40 keV or higher to further increase ion yield and enhance spatial resolution to  $\leq 1 \mu m$ . © 2015 The Authors. *Rapid Communications in Mass Spectrometry* Published by John Wiley & Sons Ltd.

Mass spectrometric imaging of biological tissue and cells is being widely explored by the main desorption techniques.<sup>[1–6]</sup> Many practitioners are beginning to regard the technique as a routine methodology for determining the spatial distribution of chemistry in tissue samples. However, the related issues of molecular sensitivity and the matrix effect are severe constraints to the confident application of imaging mass spectrometry to the analysis of complex samples, especially those related to medical conditions.<sup>[7,8]</sup>

While a number of groups have sought to tackle the ion yield issue in time-of-flight secondary ion mass spectrometry (TOF-SIMS) by adding metals and other compounds that aid cationisation to the sample surfaces,<sup>[9–12]</sup> we have focused on the possibility of enhancing proton positive ion yield using water cluster beams.<sup>[13,14]</sup> The idea was based on the observations of a number of groups that the presence of

water, either adventitious or intentionally added, promoted the yield of protonated molecules and related secondary ions. It has been shown that there is a significant ion yield benefit to be obtained from the use of water clusters as primary ion beams in the analysis of bio-organic molecules. This benefit is particularly significant for TOF-SIMS if an instrument is used that can collect all the ions generated well beyond the static limit that previously constrained analysis using high energy small metal cluster primary ions.

Argon cluster beams can be used as very effective primary beams for the analysis of biological systems and it has been shown that they are optimally effective where the primary energy per argon atom,  $E/n$ , is below about 10 eV.<sup>[15–19]</sup> Although molecular fragmentation falls below this energy, yield does too. Water cluster beams behave in a similar manner to argon at  $E/n \sim 10$  eV; however, the yield of  $[M+H]^+$  ions rises significantly to a maximum at  $E/n \sim 3$  eV, or a cluster size of about 7000 at 20 keV beam energy.<sup>[14]</sup> The yield enhancement varies with the chemistry of the analyte. In the cases studied to date the increase is in the region of 10 to 100 times. There is also some evidence that the matrix effect is ameliorated, although this has still to be fully demonstrated.<sup>[13]</sup> Studies with  $(D_2O)_n$  cluster beams have shown that enhanced protonation in the low  $E/n$  regime does arise mainly from the water molecules in the cluster. The mechanism of water cluster ion yield enhancement is a matter

\* Correspondence to: J. C. Vickerman, Manchester Institute of Biotechnology, The University of Manchester, Manchester M13 9PL, UK.  
E-mail: john.vickerman@manchester.ac.uk

This is an open access article under the terms of the Creative Commons Attribution License, which permits use, distribution and reproduction in any medium, provided the original work is properly cited.